Conference Proceedings of the Society for Experimental Mechanics Series

Jay Carroll · Shuman Xia · Alison M. Beese
Ryan B. Berke · Garrett J. Pataky *Editors*

Fracture, Fatigue, Failure and Damage Evolution, Volume 7

Proceedings of the 2017 Annual Conference on Experimental and Applied Mechanics

SEM

Springer

Conference Proceedings of the Society for Experimental Mechanics Series

Series Editor

Kristin B. Zimmerman, Ph.D.
Society for Experimental Mechanics, Inc.,
Bethel, CT, USA

More information about this series at http://www.springer.com/series/8922

Jay Carroll • Shuman Xia • Alison M. Beese • Ryan B. Berke
Garrett J. Pataky
Editors

Fracture, Fatigue, Failure and Damage Evolution, Volume 7

Proceedings of the 2017 Annual Conference on Experimental and Applied Mechanics

Springer

Editors
Jay Carroll
Sandia National Laboratories
Albuquerque, NM, USA

Alison M. Beese
Pennsylvania State University
State College, PA, USA

Garrett J. Pataky
Department of Mechanical Engineering
Clemson University
Clemson, SC, USA

Shuman Xia
School of Mechanical Engineering
Georgia Institute of Technology
Atlanta, GA, USA

Ryan B. Berke
Department of Mechanical & Aerospace Engineering
Utah State University
Logan, UT, USA

ISSN 2191-5644 ISSN 2191-5652 (electronic)
Conference Proceedings of the Society for Experimental Mechanics Series
ISBN 978-3-319-62830-1 ISBN 978-3-319-62831-8 (eBook)
DOI 10.1007/978-3-319-62831-8

Library of Congress Control Number: 2015951232

Printed on acid-free paper

This Springer imprint is published by Springer Nature
The registered company is Springer International Publishing AG
The registered company address is: Gewerbestrasse 11, 6330 Cham, Switzerland

Preface

Fracture, Fatigue, Failure and Damage Evolution represents one of nine volumes of technical papers presented at the 2017 SEM Annual Conference and Exposition on Experimental and Applied Mechanics organized by the Society for Experimental Mechanics and held in Indianapolis, IN, June 12–15, 2017. The complete proceedings also includes volumes on *Dynamic Behavior of Materials; Challenges in Mechanics of Time-Dependent Materials; Advancement of Optical Methods in Experimental Mechanics; Mechanics of Biological Systems, Materials and Other Topics in Experimental and Applied Mechanics; Micro- and Nanomechanics; Mechanics of Composite, Hybrid and Multifunctional Materials; Residual Stress, Thermomechanics and Infrared Imaging, Hybrid Techniques and Inverse Problems; and Mechanics of Additive and Advanced Manufacturing.*

Each collection presents early findings from experimental and computational investigations on an important area within experimental mechanics, fracture and fatigue being one of these areas.

Fatigue and fracture are two of the most critical considerations in engineering design. Understanding and characterizing fatigue and fracture has remained as one of the primary focus areas of experimental mechanics for several decades. Advances in experimental techniques, such as digital image correlation, acoustic emissions, and electron microscopy, have allowed for deeper study of phenomena related to fatigue and fracture. This volume contains the results of investigations of several aspects of fatigue and fracture such as microstructural effects, the behavior of interfaces, the behavior of different and/or complex materials such as composites, and environmental and loading effects. The collection of experimental mechanics research included here represents another step toward solving the long-term challenges associated with fatigue and fracture.

Albuquerque, NM, USA — Jay Carroll
Atlanta, GA, USA — Shuman Xia
State College, PA, USA — Alison M. Beese
Logan, UT, USA — Ryan B. Berke
Clemson, SC, USA — Garrett J. Pataky

Contents

Chapter 1
Interface Mechanical Strength and Elastic Constants Calculations via Nano Impact and Nanomechanical Raman Spectroscopy

Devendra Verma and Vikas Tomar

Abstract Interfaces are ubiquitous in important natural and manmade materials. Research evidence has shown that interface chemistry, structure, and thickness together strongly influence material microstructure and mechanical properties. The focus of the present work is on presenting an experiment based theoretic advancement to predict thickness dependent elastic properties of materials interfaces by treating the interfaces and the area around them in a material as an elastic continuum. The experiments are based on the nanomechanical Raman spectroscopy (NMRS) developed by authors earlier with a capability to simultaneously measure stress components in orthogonal directions during an in-situ nanomechanical loading. An analytical model is developed based on boundary conditions of interface to predict thickness dependent interface elastic constants. The interface elastic constants are compared with the relations provided in literature.

Keywords Nanomechanical Raman spectroscopy • In-situ interface deformation • In-situ nanomechanical measurements • Interface thickness • Interface elastic constants

The first ever mention of interfaces is in the work of Gibbs [1] where he formulated thermodynamic foundations of interface excess energy. Gibbs definition of interfaces was a zero thickness mathematical entity. The focus of the present work is different from interface thermodynamics, interface chemistry, and interface structure characterization work available in literature. The interface in this study is considered to be of finite thickness with a non-zero volume. Emphasis is on deducing the influence of interfaces on mechanical deformation using a classical approach that incorporates interface multi-axial properties. The present work uses a nanomechanical Raman spectroscopy (NMRS) [2–7] based experimental framework to measure direct in-situ interface deformation properties.

In the classical work by Dingreville and Qu [8–10] the interfacial mismatch stress was related to the in-plane strain and applied stress in the case of a zero thickness interface. These formulations provide a way to calculate interfacial elastic properties based on the contribution of interfacial coherent surface stress, incoherent surface stress and transverse excess strain. The role of transverse direction properties of interfaces is accounted for mathematically. In an another formation, the interface is explicitly considered as a finite thickness entity to calculate the interface elastic constants in the case of heterogeneous thin interfaces by Ustinov et al. [11] showing the interface stiffness dependence on their thickness. The present work focuses on using NMRS based direct observations of multiaxial interface deformation to develop a theoretical framework for predicting interface elastic constants as a function of interface thickness.

Interfaces in composite materials are considered as a material phase confined between two separate grains or phases. In this experimental work, the interface elastic constants are measured in the case of an idealized epoxy interface between two glass plates. Single interface samples of glass and epoxy were prepared with an epoxy interface sandwiched between two glass plates. The thickness of the interface in samples was measured with a microscope to make sure that it was in the error margin of 10 ± 0.5 μm.

Considering different stiffness for the interface and the bulk phases, this boundary condition leads to a jump in the stresses. It has continuous strain distribution for the component in indentation direction while the stresses perpendicular to the interface must fulfill the condition of equilibrium. To solve this problem, a fictitious homogeneous isotropic elastic half space is assumed which for a given applied load through the indenter exhibits the same normal surface displacement as the material with interface. Figure 1.1 shows the schematic of solution procedure for this case. The key assumption of the analytical approach presented here is that the classical strain solution and the solution for the layered half space are similar for the applied loads. The assumptions for these components are therefore:

D. Verma • V. Tomar (✉)
School of Aeronautics and Astronautics, Purdue University, West Lafayette, IN, 47907, USA
e-mail: vermad@purdue.edu; tomar@purdue.edu

J. Carroll et al. (eds.), *Fracture, Fatigue, Failure and Damage Evolution, Volume 7*, Conference Proceedings of the Society for Experimental Mechanics Series, DOI 10.1007/978-3-319-62831-8_1

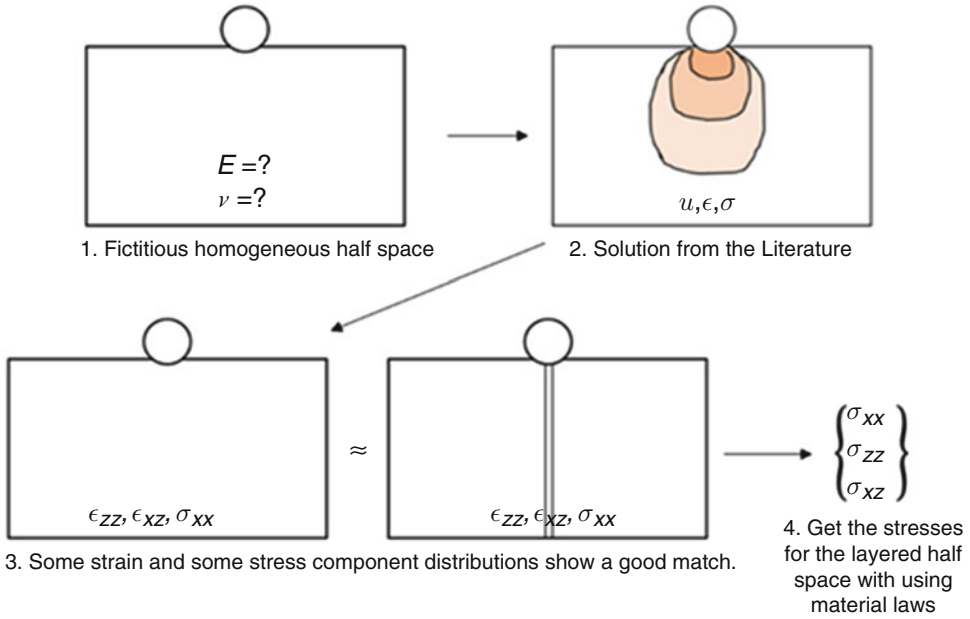

Fig. 1.1 Schematic illustration of the solution procedure

$$\begin{aligned} \sigma_{xx,fict} &\approx \sigma_{xx,lay}, \\ \sigma_{xz,fict} &\approx \sigma_{xz,lay}, \\ \sigma_{xy,fict} &\approx \sigma_{xy,lay}. \end{aligned} \tag{1.1}$$

The remaining strain components in interface plane direction, and must fulfill the conditions of compatibility and strain jumps cannot occur.

$$\begin{aligned} \epsilon_{yy,fict} &\approx \epsilon_{yy,lay}, \\ \epsilon_{yz,fict} &\approx \epsilon_{yz,lay}. \end{aligned} \tag{1.2}$$

Due to limitations of the stress measuring technique, it is not possible to obtain a full stress tensor for the interface in the current indentation setup. Nevertheless, an equivalent stress can be obtained, therefore the calculated stress tensors are transferred to an equivalent stress by:

$$\sigma_v = \sqrt{\sigma_{xx}^2 + \sigma_{yy}^2 + \sigma_{zz}^2 - \left(\sigma_{xx}\sigma_{yy} + \sigma_{yy}\sigma_{zz} + \sigma_{xx}\sigma_{zz}\right) + 3\left(\sigma_{xy}^2 + \sigma_{yz}^2 + \sigma_{xz}^2\right)}. \tag{1.3}$$

Here, σ_v is the von Mises equivalent stress. The flat punch corrections were then applied in the model. A flat ended and a spherical indenter produce different load distributions on the surface of the sample.

To validate the assumptions of the model, an interface FE model and a homogeneous isotropic half space model was simulated with 10 μm thick interface in the middle. Plane strain loading boundary conditions were applied and the loading was given in the displacement boundary condition. The strains were measured at the maximum displacement of 500 nm that was equivalent to the indentation depth in the actual experiments. The strains and stresses were compared for both models. The stresses showed the similar profile validating the stress assumptions given in Eq. (1.1).

Raman spectroscopy is an excellent tool to measure properties such as the crystalline structure, chemical signature without a necessity of sample preparation. The Raman spectroscopy has been used for other material systems such as epoxy in recent years to measure the curing state as well as the residual stresses in the sample44. We have used the Raman spectroscopy developed in our lab by Gan and Tomar to measure the stresses in the interface at different applied loads during nanomechanical loading to compare the stress distribution [3, 4]. The mechanical load was applied using the nanoindentation platform manufactured by Micro Materials Inc., UK, [12, 13] with load range from 0.1 to 500 mN, with the accuracy of 0.01 mN. The nanomechanical loading was performed using a flat punch indenter attached to the pendulum.

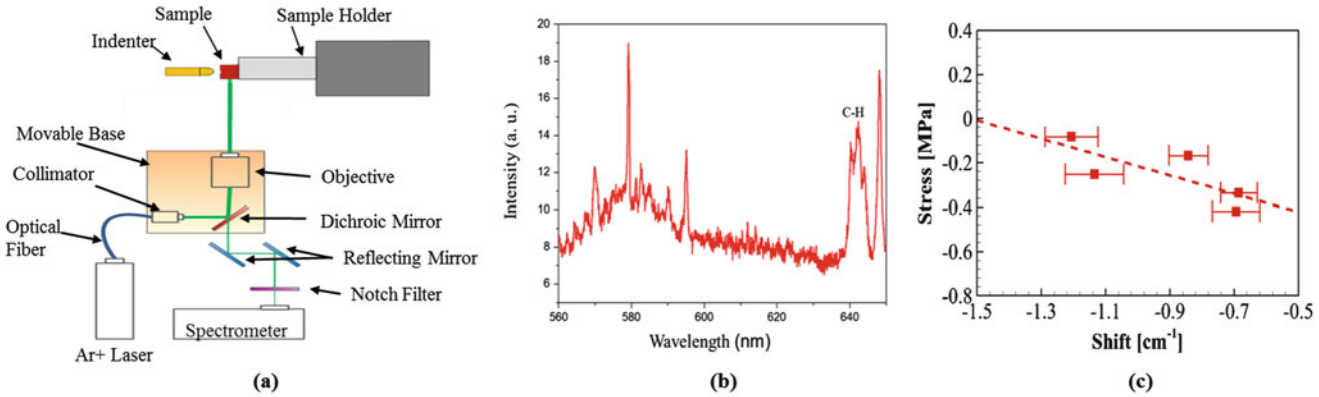

Fig. 1.2 (**a**) Setup of the nanomechanical Raman spectroscopy experiments. (**b**) Raman spectrum collected from epoxy showing the peak corresponding to C–H bond. (**c**) Raman shift versus stress calibration curve for epoxy

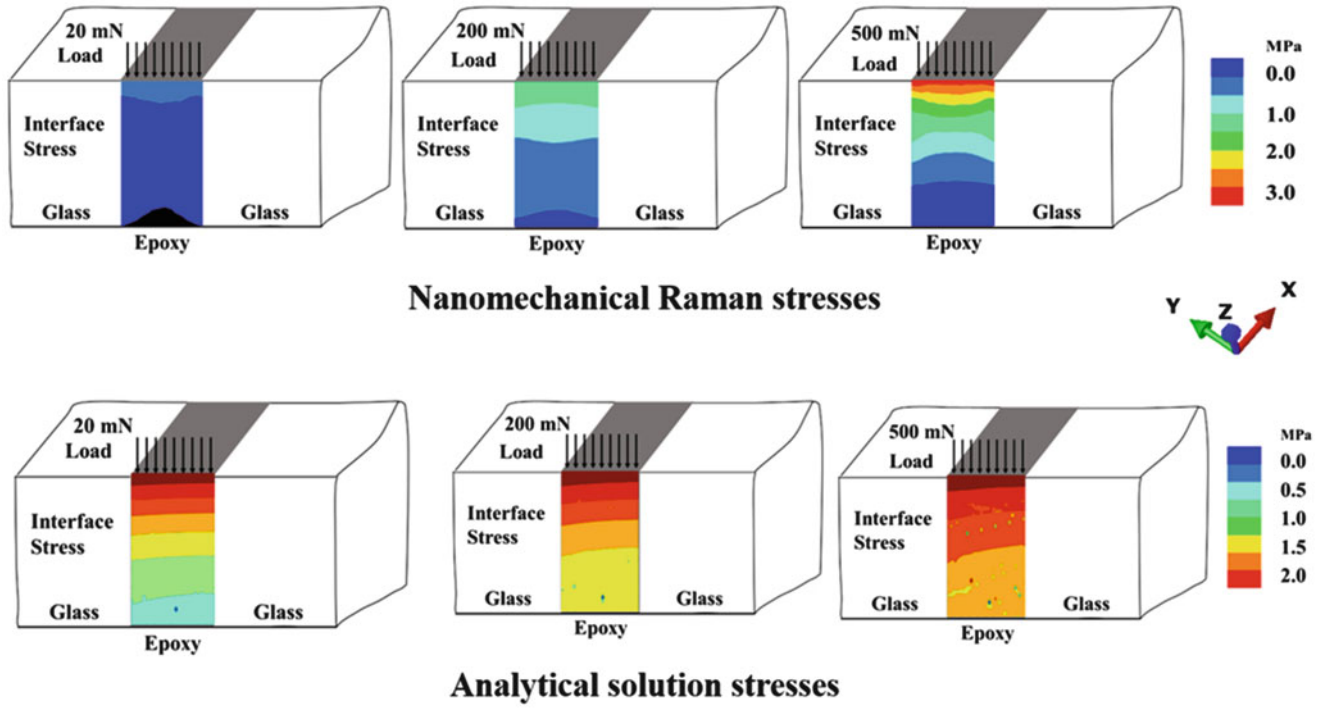

Fig. 1.3 Distribution of the equivalent stress for the indentation with a flat indenter for 20, 200, and 500 mN. The height in each map is 80 μm and width is 10 μm

The epoxy samples show Raman peaks in a wide range from 560 to 645 nm. The Raman signal at each wavelength depends on the mass of the atoms involved and the strength of the bonds between them. In the current system we measured the strongest signal around 641.1 nm as shown in Fig. 1.2b. The change in shift was obtained by subtracting the shift at the applied load for the shift at zero load. The calibration curve for shift versus load for epoxy is given in Fig. 1.2d. The Raman shift versus stress calibration curve was used to calculate the stress maps on the interfaces. The Raman maps were measured at 0, 6, 60, and 150 MPa. The measurements were performed while holding the load constant. The stress distribution across interfaces is shown in Fig. 1.3.

The Raman spectroscopy only provides the average stress at the interface but stress tensors in different directions are needed to fully understand the behavior of interfaces. Even in the experiments, it is difficult to measure the lateral stresses. An analytical solution is therefore developed to calculate the lateral stresses during indentation of interfaces. In the present analyses, the indentations are quasistatic and fully elastic which gives small indentation depths compared to the indenter

Table 1.1 Elastic constants *for glass/epoxy* interface

	A11 (Pa-m)	A22 (Pa-m)	A33 (Pa-m)	A13 (Pa)
This work	34,029	6821	2.03×10^{14}	2.80×10^{9}
Theoretical approximations [11]	53,571	53,571	5.35×10^{14}	3,571,428,571

radius. This condition allows for the simplifications of the loaded region. An analytical method to calculate the stresses in interfaces with vanishing thickness is presented by Ustinov et al. [11].

In this work, we replace the intermediate layer in the internal energy equation given in [11] by a layer of thickness *h,* which is less than the thickness of two original layers. A new two-layered system with additional interface elastic constants is obtained with its elastic energy as a function of the thickness of the intermediate layer. While the longitudinal strains stay the same as for the initial system, a new relation for the transverse strains are presented, by claiming that the surface displacements should coincide with the initial system. By substituting equation of elastic energy of the modified system expressed in terms of the strains of the initial system and solving the resulting equation system which results by equating after performing the limit transition the elastic properties of the interface with vanishing thickness can be obtained [14].

The abovementioned model was programmed in a MATLAB code to calculate the interface stresses for different scenarios, [14]. The stresses were then calculated for the quasistatic case for the same applied load as in the experiments. The values from the Nanomechanical Raman spectroscopy measurement and the analytical solution are of the same order showing the validity of the model to measure the stress components in the given case, Fig. 1.3. The stress and strains were then calculated in all direction using the analytical model to calculate the interface elastic constants.

The elastic constants were then calculated from these stress-strain data using the linear fit. These formulas were further used to calculate the interface elastic constants of the epoxy interfaces analyzed in the current study. The interface elastic constants for epoxy interface measured from the indentation experiments after conversion to surface constant is listed in the same Table 1.1 with the values obtained from theoretical approximation for comparison.

A new formulation based on the NMRS is presented to calculate the interface elastic constants using an analytical model. The measured and calculated elastic constants are compared with the strain energy frameworks provided in the literature. A comparison between the current and literature methods shows the dependence of the interface elastic constants on the interface thickness. The elastic constants calculated from the stress-strain data match the literature values after the thickness effect correction.

References

1. Gibbs, J.W.: The Collected Works of J. Willard Gibbs, Volume I: Thermodynamics. Yale University Press, New Haven (1928)
2. Gan, M., Samvedi, V., Tomar, V.: Raman spectroscopy-based investigation of thermal conductivity of stressed silicon Microcantilevers. J. Thermophys. Heat Transf. **29**(4), 845–857 (2014)
3. Gan, M., Tomar, V.: An in situ platform for the investigation of Raman shift in micro-scale silicon structures as a function of mechanical stress and temperature increase. Rev. Sci. Instrum. **85**(1), 013902 (2014)
4. Gan, M., Tomar, V.: Surface stress variation as a function of applied compressive stress and temperature in microscale silicon. J. Appl. Phys. **116**(7), 073502 (2014)
5. Zhang, Y., Gan, M., Tomar, V.: In-Situ Combined Sensing of Uniaxial Nanomechanical and Micromechanical Stress with Simultaneous Measurement of Surface Temperature Profiles by Raman Shift in Nanoscale and Microscale Structures. Purdue Research Foundation, West Lafayette (2016)
6. Zhang, Y., Gan, M., Tomar, V.: Small scale thermomechanics in Si with an account of surface stress measurements. In: Ralph, C., et al. (eds.) Mechanics of Composite and Multi-Functional Materials, Volume 7: Proceedings of the 2015 Annual Conference on Experimental and Applied Mechanics, pp. 247–250. Springer International Publishing, Cham (2016)
7. Zhang, Y., Gan, M., Tomar, V.: Raman thermometry based thermal conductivity measurement of bovine cortical bone as a function of compressive stress. J. Nanotechnol. Eng. Med. **5**(2), 021003 (2014)
8. Dingreville, R., Hallil, A., Berbenni, S.: From coherent to incoherent mismatched interfaces: a generalized continuum formulation of surface stresses. J. Mech. Phys. Solids. **72**(0), 40–60 (2014)
9. Dingreville, R., Qu, J.: Interfacial excess energy, excess stress and excess strain in elastic solids: planar interfaces. J. Mech. Phys. Solids. **56**(5), 1944–1954 (2008)
10. Dingreville, R., Qu, J., Mohammed, C.: Surface free energy and its effect on the elastic behavior of nano-sized particles, wires and films. J. Mech. Phys. Solids. **53**(8), 1827–1854 (2005)
11. Ustinov, K.B., Goldstein, R.V., Gorodtsov, V.A.: On the modeling of surface and interface elastic effects in case of eigenstrains. In: Altenbach, H., Morozov, F.N. (eds.) Surface Effects in Solid Mechanics: Models, Simulations and Applications, pp. 167–180. Springer Berlin Heidelberg, Berlin (2013)

12. Verma, D., Tomar, V.: Strain rate dependent failure of metallic interfaces at nano- microscale via nanoimpact experiments. In: 20th International Conference on Composite Materials, Copenhagen (2015)
13. Verma, D., Tomar, V.: An investigation into environment dependent nanomechanical properties of shallow water shrimp (Pandalus platyceros) exoskeleton. Mater. Sci. Eng. C Mater. Biol. Appl. **44**, 371–379 (2014)
14. Verma, D., et al.: A Combined Theoretic and Experimental Advancement to Measure Interface Stress-Strain Relations and Interface Elastic Constants using Nanomechanical Raman Spectroscopy. Manuscript in preparation (2017)

Chapter 2
Effect of Strain Rate and Interface Chemistry on Failure in Energetic Materials

Chandra Prakash, I. Emre Gunduz, and Vikas Tomar

Abstract We study the failure at interfaces between Hydroxyl-terminated polybutadiene (HTPB)-Ammonium Perchlorate (AP) based energetic material. In this work, interface mechanical strength of a set of HTPB-AP interfaces is characterized using nano-scale impact experiments at strain rates up to 100 s^{-1}. A power law viscoplastic constitutive model was fitted to experimental stress-strain-strain rate data in order to obtain constitutive behavior of interfaces, particle, and matrix. A mechanical Raman spectroscopy is used to analyze the effect of binding agent at different temperature. A tensile fracture experiment combined with In-situ Mechanical Raman Spectroscopy was used to obtain fracture properties. Stress maps are obtained near the interface using In-situ Mechanical Raman Spectroscopy to analyze the changes in the stress distribution around interfaces for different loads till failure. Cohesive zone model parameters were obtained from the consideration of local stress during failure and the cohesive energy required for delamination of AP from HTPB matrix. Effect of binding agent on the interface strength is found to be quite significant. The cohesive zone parameters and the viscoplastic model obtained from the experiment were then used in the cohesive finite element method to simulate the dynamic crack propagation as well as the delamination. Results show that interfacial properties are affected by the rate of loading and are also dependent upon the binding agent.

Keywords Energetic material • Stress/strain relationship • HTPB • AP • NRS

Energetic compounds are employed in a large number of applications, such as, explosive, propellant, and pyrotechnic formulations. An example of a heterogeneous solid propellant used in rocket industry is a crystalline oxidizer (e.g., ammonium perchlorate-AP) embedded in a polymeric binder (e.g., Hydroxyl-Terminated Polybutadiene or HTPB). Aluminum (Al) particles are sometimes added to enhance the propellant performance. A typical industrial solid propellant consists of 70% AP, 10% HTPB and around 20% Al by weight, [1]. Three main failure mechanisms in the composite material are identified as particle fracture, interfacial failure and the cavitation in the binder [2]. Palmer [2] investigated a number of polymer bonded explosives (PBXs) under tensile loading and observed finding a wide range of responses. They found that the crack propagation was mostly confined to binder and that the interface debonding was the dominant failure mode. Interface strength depends on the constituent material, i.e., particle, matrix and/or binding agents [3, 4].

Several experiments [5–7] have suggested a particle size effect on the performance of energetic materials. Yeager [8] has shown the effect of interface/interphase and the microstructure on the mechanical behavior of PBXs. Interfacial structure was altered by adding a plasticizer in the composite. The plasticizer was shown to inhibit the formation of a large interface/interphase and was more likely to have film delamination than the no-plasticized composite. The difference in interfacial properties was also shown to have significant effect on the crack initiation and explosive sensitivity.

Two samples were prepared for analyzing the effect of functionalization on the interface mechanical properties. One consist of ammonium perchlorate (AP) particles embedded in hydroxyl-terminated polybutadiene (HTPB). In the second sample, a surface binding agent (Tepanol) was added at a mass ratio of 0.5 to fabricate samples with higher surface adhesion, while keeping the same index ratio.

C. Prakash • V. Tomar (✉)
School of Aeronautics and Astronautics, Purdue University, West Lafayette, IN, 47907, USA
e-mail: cprakash@purdue.edu; tomar@purdue.edu

I. Emre Gunduz
School of Mechanical Engineering, Purdue University, West Lafayette, IN, 47907, USA

J. Carroll et al. (eds.), *Fracture, Fatigue, Failure and Damage Evolution, Volume 7*, Conference Proceedings of the Society for Experimental Mechanics Series, DOI 10.1007/978-3-319-62831-8_2

Table 2.1 Viscoelastic material parameters for AP, HTPB and the HTPB/AP interface

	χ (MPa)$^{-n}$		m		n	
	Sample-1	Sample-2	Sample-1	Sample-2	Sample-1	Sample-2
HTPB	25.52	13.13	−19	−13	25	30
AP	18	19.9	−16	−17	9	9
HTPB/AP interface	40.3	12.8	−30	−10	8	3

Energetic materials have been modeled using viscoelastic [9, 10] as well as elasto-viacoplastic [11, 12] model. For high strain rate loading viscoplastic models are used frequently [13–15]. Kalayciogly [12] et al. modeled an HTPB/AP composite propellant using Perzyna's viscoplastic model. In this work, following Tsai and Sun, [16], we assume an effective stress-effective viscoplastic strain curve by a power law model

$$\overline{\varepsilon}^{vp} = A(\overline{\sigma})^n, \tag{2.1}$$

where $\overline{\varepsilon}^{vp}$ and $\overline{\sigma}$ are the equivalent strain and equivalent stress respectively. A is a power law function of effective plastic strain rate given as,

$$A = \chi\left(\frac{\dot{\varepsilon}}{\dot{\varepsilon}^0}\right)^m. \tag{2.2}$$

The viscoplastic model then can be given as,

$$\dot{\overline{\varepsilon}}^{vp} = \chi\left(\frac{\dot{\varepsilon}}{\dot{\varepsilon}^0}\right)^m (\overline{\sigma})^n. \tag{2.3}$$

The values of χ, m and n are found from the stress strain data obtained during nano-scale impact test, [17].

Mechanical properties were obtained using a nano-scale impact experiment. The experimental procedure involves impacting the surface of material being tested by an indenter. The nano-scale impact were performed using the high strain rate impact schedule of Micro Materials, UK [18–21].

Table 2.1 shows that the viscoplastic model parameters for the interface, the matrix (HTPB) and the particle (AP) for two samples. These material parameters then further can be used to describe the material behavior at the interface as well as in the matrix and particle phase for high strain rates. The present analysis shows nano-scale impact as a tool to capture the material deformation behavior at micrometer scales.

As shown in Fig. 2.1a, the samples were loaded in tension at a loading rate of 0.1 mm/min till fracture. During the loading, a set of points on the sample near interface was scanned to get Raman shifts, [22]. These Raman shifts were obtained at different loads until the debonding occurred. The strength of the interface was evaluated from the stress map obtained using Raman spectroscopy by assuming the strength equal to the stress at the start of the delamination. The strength of the interface is the stress near the interface at the load during failure (Fig. 2.1b). Area under the load displacement curve, Fig. 2.1c, between the point where crack reaches the interface and the point where interface delaminates is the total energy required for delamination.

The dynamic behavior of the composite material system is modeled using the explicit finite element method (see e.g., [23, 24]). The average time step is of the order of 1 ns which is approximately one tenth of the time it takes for the longitudinal wave to traverse the smallest bulk element in the meshes in current research. The weak form of the governing equation is given as,

$$\int_V \tau : \delta\mathbf{F} dV - \int_{S_{int}} \mathbf{T}.\delta\boldsymbol{\Delta} dS = \int_{S_{ext}} \mathbf{T}.\delta\mathbf{u} dS - \int_V \rho \frac{\partial^2 \mathbf{u}}{\partial t^2} \cdot \delta\mathbf{u} dV, \tag{2.4}$$

To track complex crack/microcrack patterns, arbitrary crack paths, and crack branching, cohesive surfaces are specified along all finite element boundaries as an intrinsic part of the finite element model. The finite element meshes used have a uniform structure with "cross-triangle" elements of equal dimensions arranged in a quadrilateral pattern, Fig. 2.2. This type of triangulation is used since it gives the maximum flexibility for resolving crack extensions and arbitrary fracture patterns [25].

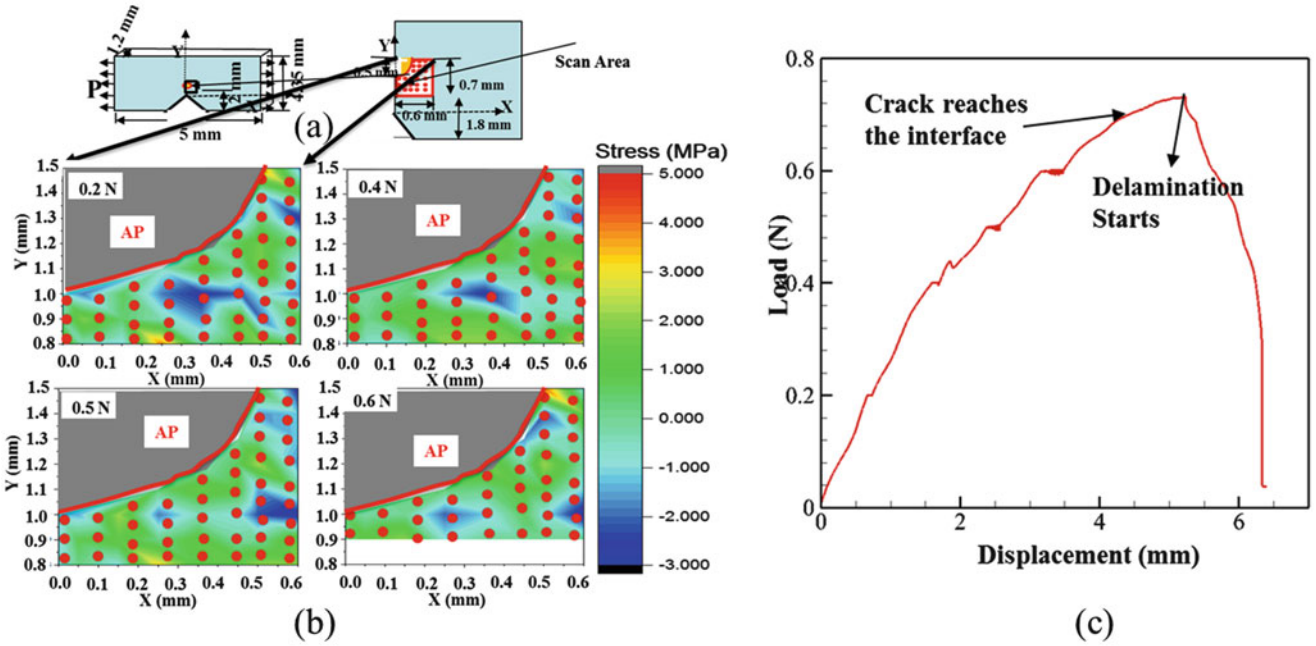

Fig. 2.1 (**a**) Loading configuration, (**b**) stress distribution around the interface for different load until failure and (**c**) Load-displacement curve

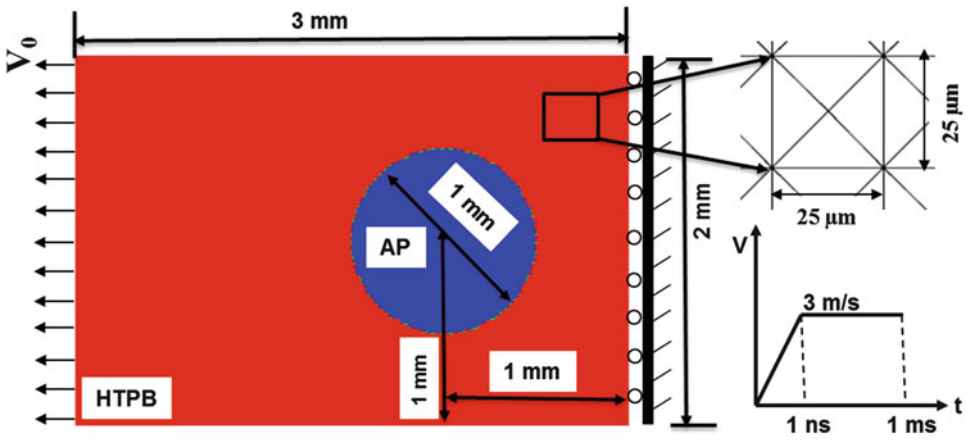

Fig. 2.2 Finite element mesh of the energetic material model being studied

We use the standard assumption for finite strain inelastic problems: the multiplicative decomposition of the deformation gradient $\boldsymbol{F}$ into an elastic and an inelastic part $\boldsymbol{F^e}$ and $\boldsymbol{F^p}$, i.e.,

$$F = F^e \cdot F^{vp} \tag{2.5}$$

In the cohesive model used, the traction T applied on material points coinciding at and occupying position x on cohesive surface in the reference configuration is work-conjugate to surface separation Δ. Reckoned in the reference configuration, the cohesive law is

$$T(x) = T\left[\Delta(x)\right], \tag{2.6}$$

and the work of separation under this traction at any stage of deformation is [26],

$$W_{sep} = \int_{S_0} \int_0^{\Delta} T\left(x, \Delta\right) .d\Delta dx. \tag{2.7}$$

Table 2.2 Cohesive zone parameters for constituents of HTPB/AP composite

Material/interface	Cohesive strength (MPa)	Critical displacement (mm)	Cohesive energy (N/mm)
HTPB	0.8	0.5	0.2
AP	200	1×10^{-6}	1×10^{-4}
Interface	0.5–6	0.11	0.02–0.33

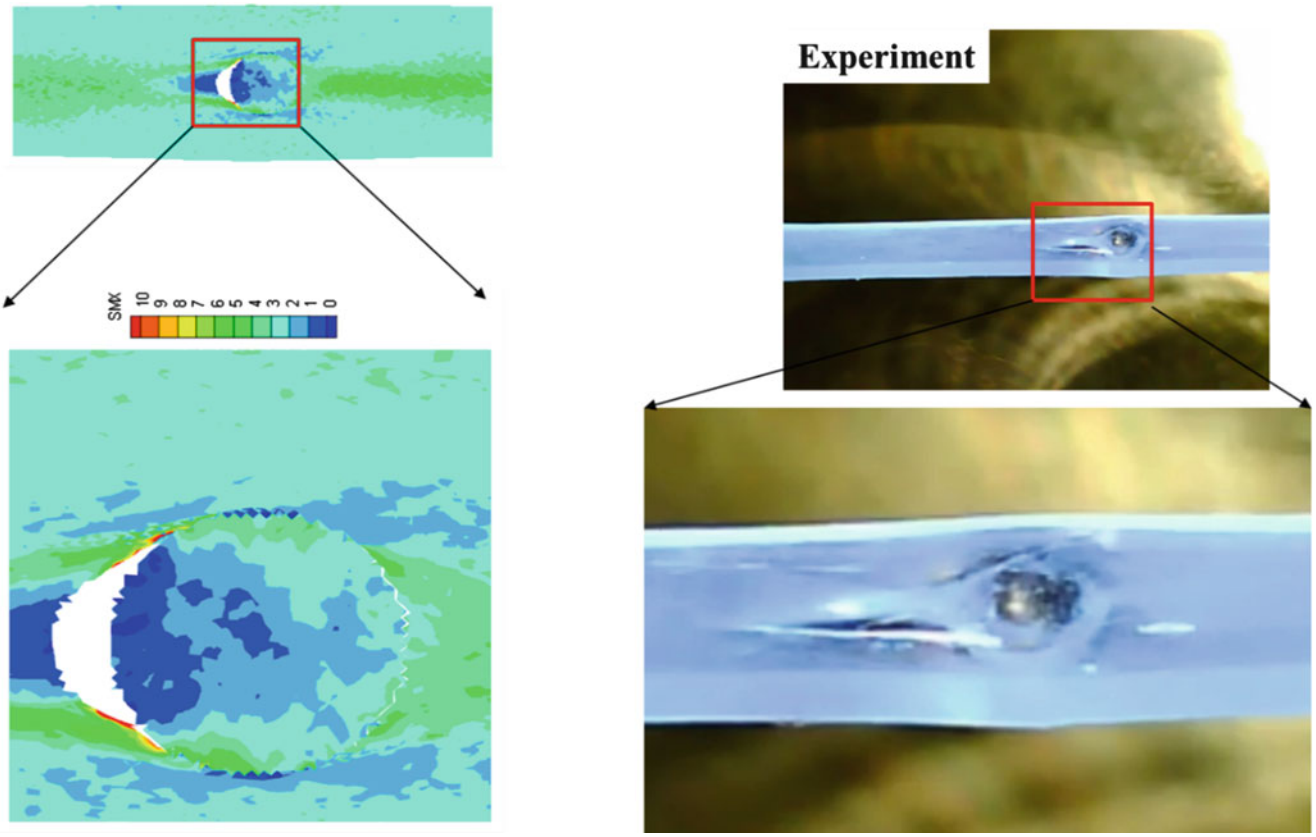

Fig. 2.3 Validation of delamination mode obtained using CFEM with experiment

The CFEM simulations are carried out under plane strain assumption. The plane strain assumption is therefore a major limitation of the framework. The irreversible bilinear law is used which is a generalized version of the cohesive laws with irreversibility [27, 28]. The current law is derived from a description φ of the surface energy dissipation per unit area which is a function of separation vector Δ through a state variable defined as that describes the effective instantaneous state of mixed-mode separations. The specific form for φ is taken as, [29].

A two dimensional numerical simulation is carried out for the AP-HTPB specimen with a single AP particle embedded in HTPB binder to simulate the failure. Figure 2.1 illustrates the geometry and boundary conditions employed in the numerical simulation. The AP particle is idealized as a circle with diameter D = 1 mm. The size of the element was chosen such that it satisfies the bounds given in [30], which is equal to 25 μm.

Local cohesive zone parameters used in the simulation were obtained from the Raman spectroscopy experiment, [17], and are given in Table 2.2. These parameters for HTPB and HTPB/AP interface were obtained from the Raman spectroscopy as explained above. For AP the cohesive strength is assumed to be $E/100$, [30], where E is the Young's modulus of AP. HTPB/AP interface cohesive strength was varied to study the effect of different interface. Figure 2.3 shows the similarity in the mode of delamination observed in both numerical and experimental observations.

Strain rates of 100, 200, 800, 1000, 2000, 3000 s^{-1} were applied in terms of the velocity boundary condition at the top boundary. Figure 2.4a shows the effect of strain rates on the cohesive energy of the system. Cohesive energy increases with the time as the deformation increases, even when the cohesive zone parameters are constant. This is because the material model used is a rate dependent viscoplastic material. The rate at which the cohesive energy increases also increase with strain rate. Delamination starts near the fix boundary at low strain rates (800 s^{-1} and 1000 s^{-1}). However, as the strain

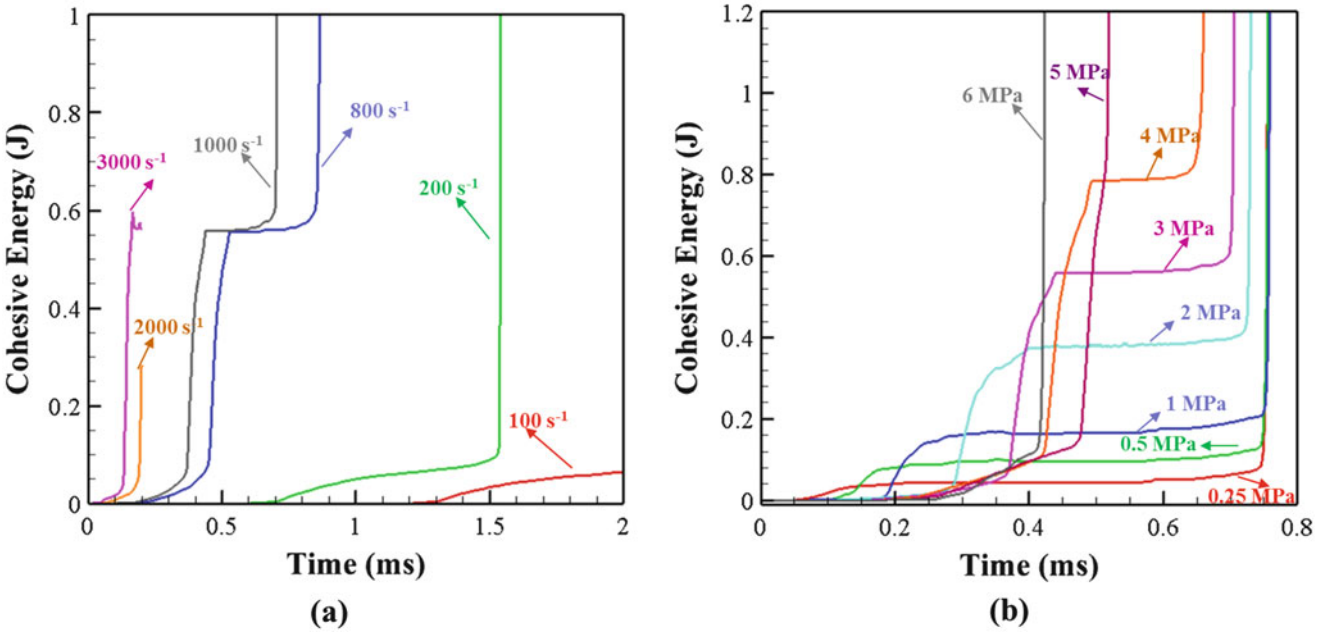

Fig. 2.4 Cohesive energy of the system (**a**) for different strain rates and (**b**) for different cohesive strength with time

rate increases the delamination occurs on the loading side (3000 s^{-1}). Figure 2.4b shows the effect of cohesive strength on the cohesive energy. The delamination occurs when the cohesive energy reaches the critical value. As can be seen in the Fig. 2.4b, time at which cohesive energy reaches its critical value, decreases with increasing cohesive strength.

This work shows the effect of interface strength and the strain rate on the debonding in HTPB/AP composite. We obtain a strain rate dependent mechanical properties of constituents of the HTPB/AP composite using a nano-scale impact experiment which allows us to obtain not only the properties of constituents but also of interface which is otherwise difficult to obtain. Cohesive parameters based on in-situ mechanical Raman spectroscopy based on change in interface chemistry by adding a binding agent into the composite propellant. We then use these experimentally obtained properties into our cohesive finite element model (CFEM) to simulate the delamination of HTPB-AP interface. The dynamic fracture behavior is simulated for the HTPB/AP sample with CFEM. The CFEM simulation accurately captures the evolution and mode of delamination. This has been confirmed by comparing it with the quasi-static tensile experiment also. Strain rate effects are considered and shown to affect the delamination in the sample. The effect of interface chemistry on delamination mode can eventually effect the possible hot-spots in the material. Further study would be needed to quantify this effect in multi-particle energetic materials.

Acknowledgments This research was supported by US-AFoSR Grant FA9550-15-1-0202 (Program Manager Dr. Martin Schmidt).

References

1. Gallier, S., Hiernard, F.: Microstructure of composite propellants using simulated packings and X-ray tomography. J. Propuls. Power. **24**(1), 154–157 (2008)
2. Palmer, S.J.P., Field, J.E., Huntley, J.M.: Deformation, strengths and strains to failure of polymer bonded explosives. Proc. R. Soc. A: Math. Phys. Eng. Sci. **440**, 399–419 (1993)
3. Stacer, R.G., Hubner, C., Husband, M.: Binder/filler interaction and the nonlinear behavior of highly-filled elastomers. Rubber Chem. Technol. **63**(4), 488–502 (1990)
4. Stacer, R.G., Husband, M.: Small deformation viscoelastic response of gum and highly filled elastomers. Rheol. Acta. **29**, 152–162 (1990)
5. Fleming, K.A., et al.: The influence of formulation variables on the growth of reaction in plastic bonded explosives. In: Proceedings of the 8th International Detonation Symposium, Albuquerque. Naval Surface Weapons Center (1985)
6. Kimura, E., Oyumi, Y.: Shock instability test for azide polymer propellants. J. Energ. Mater. **16**(2–3), 173–185 (1998)
7. Rae, P.J., et al.: Quasi-static studies of the deformation and failure of β-HMX based polymer bonded explosives. Proc. R. Soc. A: Math. Phys. Eng. Sci. **458**, 743–762 (2002)
8. Yeager, J.D.: Microstructural Characterization of Simulated Plastic Bonded Explosives, in Mechanical and Materials Engineering. Washington State University, Washington (2011)

9. Wang, Z., et al.: Tensile mechanical properties and constitutive model for HTPB propellant at low temperature and high strain rate. J. Appl. Polym. Sci. **132**, 42104 (2015)
10. Renganathan, K., et al.: Tensile fracture of HTPB based propellant specimens. Mater. Sci. Technol. **18**(11), 1408–1412 (2013)
11. Xu, F., Aravas, N., Sofronis, P.: Constitutive modeling of solid propellant materials with evolving microstructural damage. J. Mech. Phys. Solids. **56**(5), 2050–2073 (2008)
12. Kalaycioglu, B., Dirikolu, M.H., Çelik, V.: An elasto-viscoplastic analysis of direct extrusion of a double base solid propellant. Adv. Eng. Softw. **41**(9), 1110–1114 (2010)
13. Trumel, H., et al.: A constitutive model for the dynamic and high-pressure behaviour of a propellant-like material: part II: model development and applications. Int. J. Numer. Anal. Methods Geomech. **25**(6), 581–603 (2001)
14. Trumel, H., et al.: A constitutive model for the dynamic and high-pressure behaviour of a propellant-like material: part I: experimental background and general structure of the model. Int. J. Numer. Anal. Methods Geomech. **25**(6), 551–579 (2001)
15. Trumel, H., Fanget, A., Deragon, A.: A finite strain elastic-plastic model for the quasi-static behaviour of particulate composites. Int. J. Eng. Sci. **34**(6), 677–698 (1996)
16. Tsai, J., Sun, C.T.: Constitutive model for high strain rate response of polymeric composites. Compos. Sci. Technol. **62**, 1289–1297 (2002)
17. Prakash, C., et al.: Strain rate dependent failure of interfaces examined via nanoimpact experiments. In: Antoun, B. et al. (eds.) Challenges in Mechanics of Time Dependent Materials, vol. 2. Conference Proceedings of the Society for Experimental Mechanics Series. Springer, Cham, pp. 93–102 (2017)
18. Verma, D., Tomar, V.: An investigation into environment dependent nanomechanical properties of shallow water shrimp (Pandalus platyceros) exoskeleton. Mater. Sci. Eng. C Mater. Biol. Appl. **44**, 371–379 (2014)
19. Verma, D., Tomar, V.: A comparison of nanoindentation creep deformation characteristics of hydrothermal vent shrimp (Rimicaris exoculata) and shallow water shrimp (Pandalus platyceros) exoskeletons. J. Mater. Res. **30**(08), 1110–1120 (2015)
20. Verma, D., Tomar, V.: An investigation into mechanical strength of exoskeleton of hydrothermal vent shrimp (Rimicaris exoculata) and shallow water shrimp (Pandalus platyceros) at elevated temperatures. Mater. Sci. Eng. C Mater. Biol. Appl. **49**, 243–250 (2015)
21. Verma, D., Qu, T., Tomar, V.: Scale dependence of the mechanical properties and microstructure of crustaceans thin films as biomimetic materials. JOM. **67**(4), 858–866 (2015)
22. Prakash, C., et al.: An analysis of the influence of grain boundary strength on microstructure dependent fracture in polycrystalline tungsten. Int. J. Fract. **199**(1), 1–20 (2016)
23. Fish, J., et al.: AL 6061-T6-Elastomer impact simulation. Technical Report. Rensselaer Polytechnic Institute (2005)
24. Hui, T., Oskay, C.: Computational modeling of polyurea-coated composites subjected to blast loads. J. Compos. Mater. **46**(18), 2167–2178 (2012)
25. Tomar, V.: Insights into the effects of tensile and compressive loadings on microstructure dependent fracture of trabecular bone. Eng. Fract. Mech. **76**(7), 884–897 (2009)
26. Ortiz, M., Pandolfi, A.: Finite-deformation irreversible cohesive elements for three-dimensional crack-propagation analysis. Int. J. Numer. Methods Eng. **44**(9), 1267–1282 (1999)
27. Tvergaard, V.: Cohesive zone representations of failure between elastic or rigid solids and ductile solids. Eng. Fract. Mech. **70**(14), 1859–1868 (2003)
28. Camacho, G.T., Ortiz, M.: Computaional modeling of impact damage in brittle materials. Int. J. Solids Struct. **33**(20–22), 2899–2938 (1996)
29. Zhai, J., Tomar, V., Zhou, M.: Micromechanical simulation of dynamic fracture using the cohesive finite element method. J. Eng. Mater. Technol. **126**(2), 179 (2004)
30. Tomar, V., Zhai, J., Zhou, M.: Bounds for element size in a variable stiffness cohesive finite element model. Int. J. Numer. Methods Eng. **61**(11), 1894–1920 (2004)

Chapter 3
Characterization of Crack Tip Plasticity in IN-617 Using Indentation and Nano-Mechanical Raman Spectroscopy

Yang Zhang and Vikas Tomar

Abstract This research focuses on work with emphasis on direct measurements of stresses during mesoscale microstructural deformation of nickel based super alloys during 3-point bending tests at elevated temperatures. A novel nano-mechanical Raman spectroscopy measurement platform was designed for temperature, stress, and chemistry mapping at micro to nano-scale for different temperature and loading conditions. During the 3-point bending test, notch tip plastic stresses as a function of microstructure, load, and temperature, with micron scale resolution were measured. The temperature field distribution was correlated to stress distribution and residual microstructure stresses around the area of the notch tip. Grain boundaries are the stress concentrated area but with lower temperature due to the contact thermal resistant. Grain boundary slide or grain rotation can result in stress concentration but enhance the ability of heat conduction and result in lower temperature. The mechanical properties which include the elastic modulus, hardness and stress-strain relation at the plastic zone around the notch tip were also measured. Instead of considering actual grain structures with different material properties, a new FE method was adopted to predict stress distribution applying the material properties which were obtained from indentation experiments around the same notch area as scanning. Predictions from theory and simulations matched closely in stress concentration area with experimental measurements. However, away from notch area a slight deviation due to microstructural effects was observed.

Keywords Nano-mechanical Raman • Raman spectroscopy • Stress distribution • Temperature field • Nanoindentation

There are several existing experimental methods to measure stress distribution at small scale such as X-ray diffraction (XRD) [1] and cross-sectional transmission electron microscopy (XTEM) [2]. Raman spectroscopy method to measure the stress was first introduced by Anastassakis et al. in 1970 to measure the mechanical stress inside silicon [3]. From then on, this method has been used and developed extensively to investigate stress distribution in silicon structures. Compared to the other available methods for stress measurement, Raman spectroscopy method is a non-destructive technique, requires minimal sample preparation, and has spatial resolution of less than one micron that makes it suitable for microscale to nanoscale samples. Most importantly, this method is also suitable for the measurement of temperature [4–6] and thermal conductivity [7–11] along with stress. In this research, combined nanoindentation and nanomechanical Raman spectroscopy (NMRS) methods (developed by Gan and Tomar, [12–14]) were used to measure crack tip stress distribution. Through the relation between the Raman shift and stress, the stress or strain can be calculate at each scanning point and then be integrated to show the stress distribution around the area of crack tip. Through the relation between the Raman shift and Raman peak width, the Raman shift caused by the stress and temperature can be separated. As a result, stress distribution around the crack tip at different temperature will be shown.

The tested samples used in this research were subjected to 3-point bending based mechanical loading applied by a modified nano-scale loading platform. For the 3-point bending crack tests, the samples were cut into small pieces according to the ASTM D5045 standard with the dimension of 8.8 * 2.0 * 0.5 mm with the length of crack equal to 1.0 mm and the width 0.2 mm. After cutting, the samples were mechanically polished, electrolytically polished and etched. In order to detect the Raman signal, a 1.0 μm thick layer of silicon was deposited on the surface of metals that creates negligible Raman shift phenomenon. The schematic diagram of the experimental setup is shown in Fig. 3.1. As mechanical load is applied along one axis, the Raman laser is focused onto the side surface using an objective. Back-scattered Raman signal is collected by the same objective and sent to a spectrometer.

Y. Zhang (✉) • V. Tomar
School of Aeronautics and Astronautics, Purdue University, West Lafayette, IN, 47907, USA
e-mail: yangzhang@purdue.edu; tomar@purdue.edu

J. Carroll et al. (eds.), *Fracture, Fatigue, Failure and Damage Evolution, Volume 7*, Conference Proceedings of the Society for Experimental Mechanics Series, DOI 10.1007/978-3-319-62831-8_3

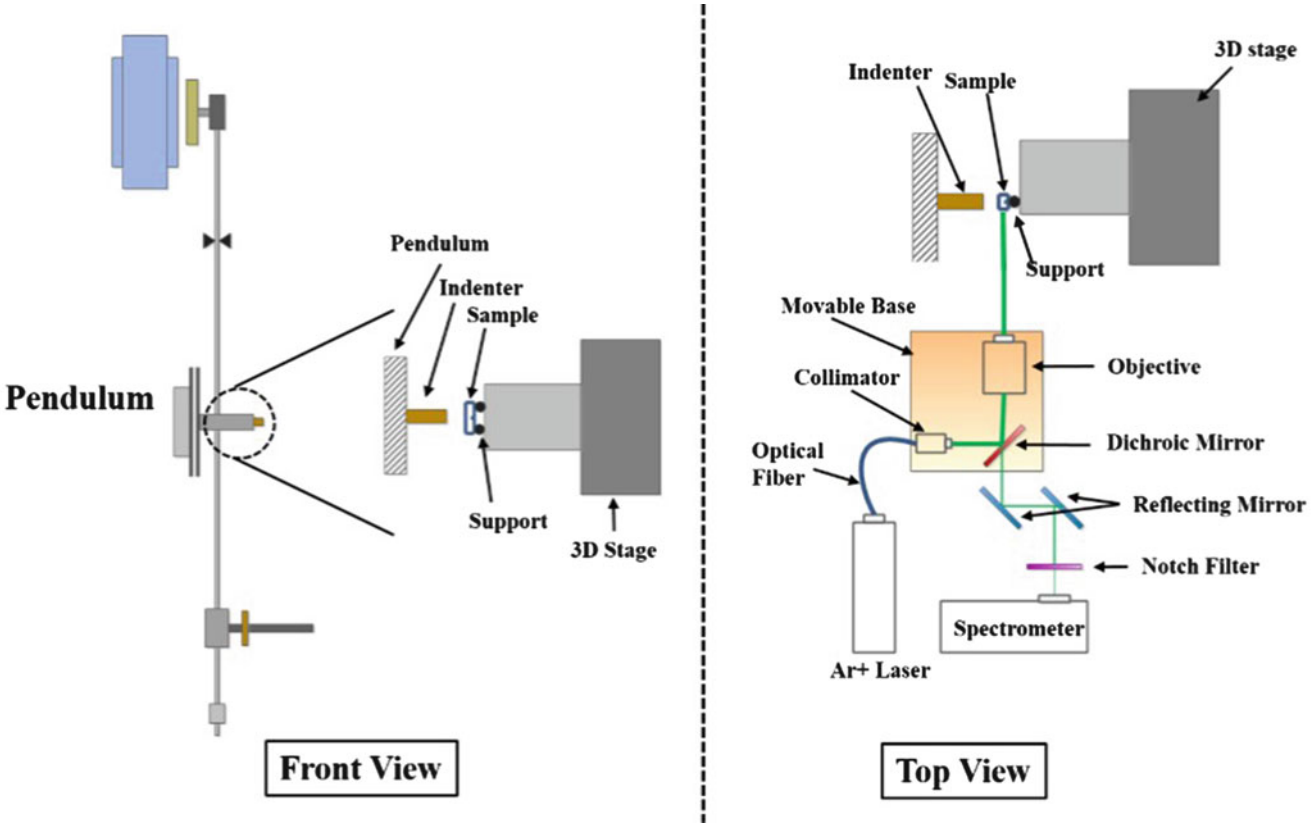

Fig. 3.1 Experimental set-up of nano-mechanical Raman spectroscopy

The temperature as well as stress change affect the position of Raman peak. In this work, both full width half maximum (FWHM) and Raman shift were detected and evaluated at different temperatures. The temperature of sample which was obtained from FWHM measurement is used to separate the temperature-induced Raman shift from the stress-induced Raman shift. The overall schedule had three steps for one set of experiments. The first step is to make indentations around the notch tip on the uncoated surface of sample before the bending. These tests are used to determine indentation based stress-strain curve in the area before 3-point bending. Thereafter, while applying load to bend the sample, Raman scanning was performed around the notch tip at the coated surface using the NMRS. After separating temperature effect on Raman shift and combining the stress information from each measuring point, a contour figure of stress distribution around the notch tip can be plotted. Overall 72 indentations (and corresponding Raman spectrums) were scanned to get the mechanical properties mapping, stress distribution and temperature field. For each spectrum, at least 3 repeated tests were performed to eliminate measurement error.

After combining all the stress information, contour figures that depicted stress distribution around the notch tip under loads of 500 mN, 2 N and 4 N at room temperature were generated in Fig. 3.2. As shown and discussed before, the stress distribution around the notch tip was not symmetric due to the asymmetry in the material microstructure around the notch tip. Grain boundary and grain structure played an important role in the mechanical property of polycrystalline material. In this research Orientation Image Microscopy (OIM) [15–17] which was an automated indexing of electron back-scattered diffraction (EBSD) pattern was used to obtain the characteristic of microstructure. The microstructural information obtained from the Raman scanned area using OIM was correlated to the stress distribution data that obtained from nano-mechanical Raman spectroscopy. The tip of notch was the stress concentrated area through the figures. Through the comparison of stress distribution mapping for different samples under different loads, it is known that the stress is concentrated and higher at the notch tip as expected for any kinds of microstructure. Additionally, notch tip stress increase with the bending load but not proportional to the load due to the plasticity at the notch tip. Plastic deformation will degrade the strength of material that result in lower stress. Correlation with microstructures of the notch area, it is clear that microstructures play a very important role in the stress distribution.

According to the relation between temperature and Raman peak, temperature at every point around the notch tip was measured. After combining all measured temperature information, contour figures that depicted temperature field around notch tip under loads of 500 mN, 2 N and 4 N at the overall temperature of 200 °C were shown in the Fig. 3.3. The average

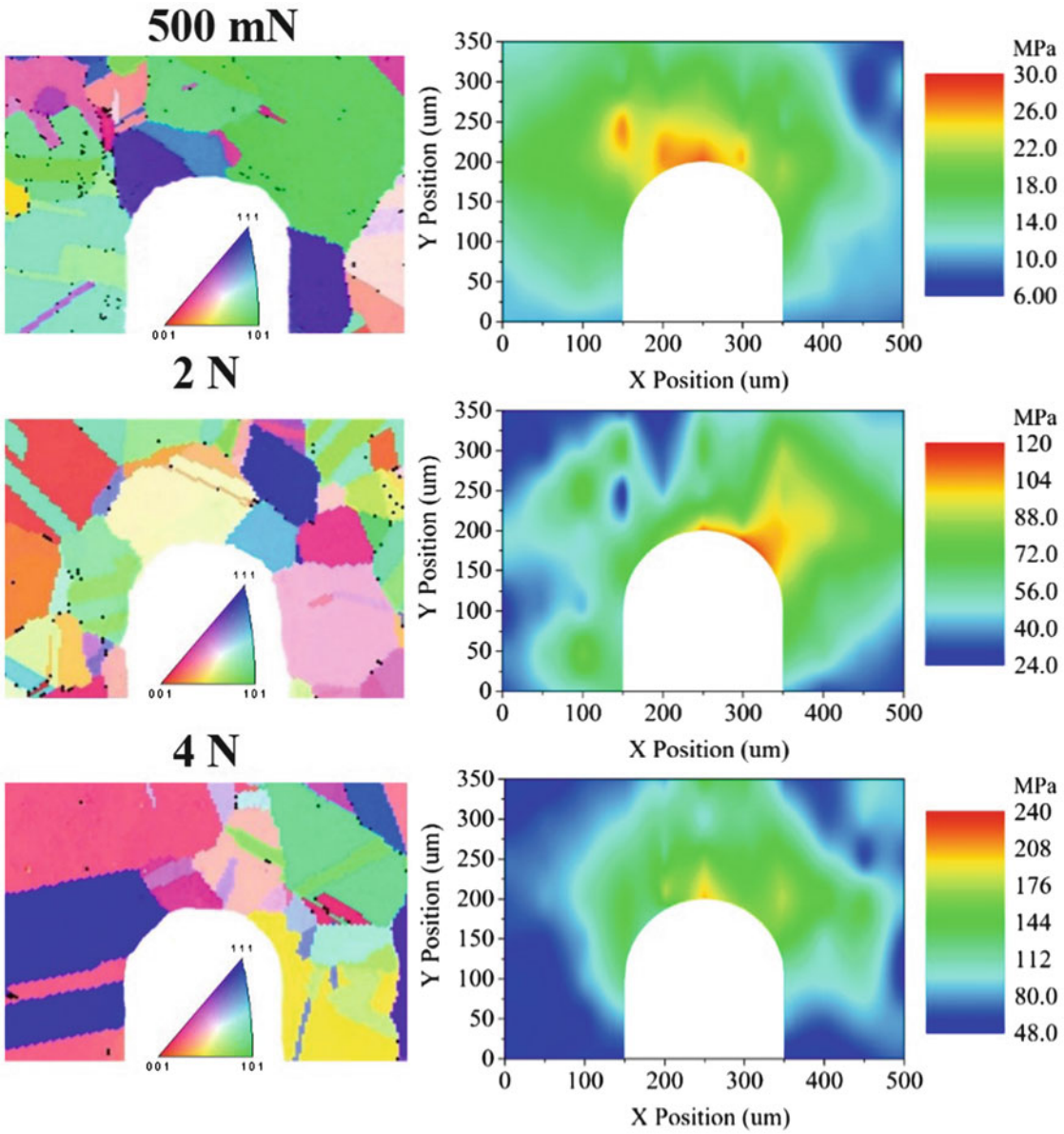

Fig. 3.2 Stress distribution with microstructures obtained from EBSD of the notch tip under different bending loads of 500 mN, 2 N and 4 N at room temperature

temperature of the sample during the test was 200 °C, which was monitored by thermocouples. However, the temperature along the notch edge was little lower due to heat convection to the ambient air with obvious lower temperature inside the notch. And the difference of temperature at different area was due to difference of thermal conductivity that was affected by the precipitates on the surface, microstructure of surface and the stress conditions. After subtracting the temperature-induced Raman shift contribution, the remaining Raman shift was used to calculate stress. Stress values at every points around the notch tip was measured. Contour plots that depicted stress distribution of around the notch tip under loads of 500 mN, 2 N and 4 N at the overall temperature of 200 °C were also shown in Fig. 3.3. The temperature field and stress distribution are affected by the microstructure of the notch area and the precipitates.

In order to consider microstructure influence one needs to perform crystal plasticity type of simulations. However, dislocation systems data is very limited in this case. Therefore, an alternate approach is pursued in this work. For the purpose of finite element simulations, boundary conditions are shown in Fig. 3.4a. Microstructure of Alloy 617 has average grain size of approximately 150 microns. For each grain using spherical indentation, elastic-plastic stress strain curves were obtained with spacing of 50 microns by converting the experimental load-displacement data [18]. Figure 3.4b shows the

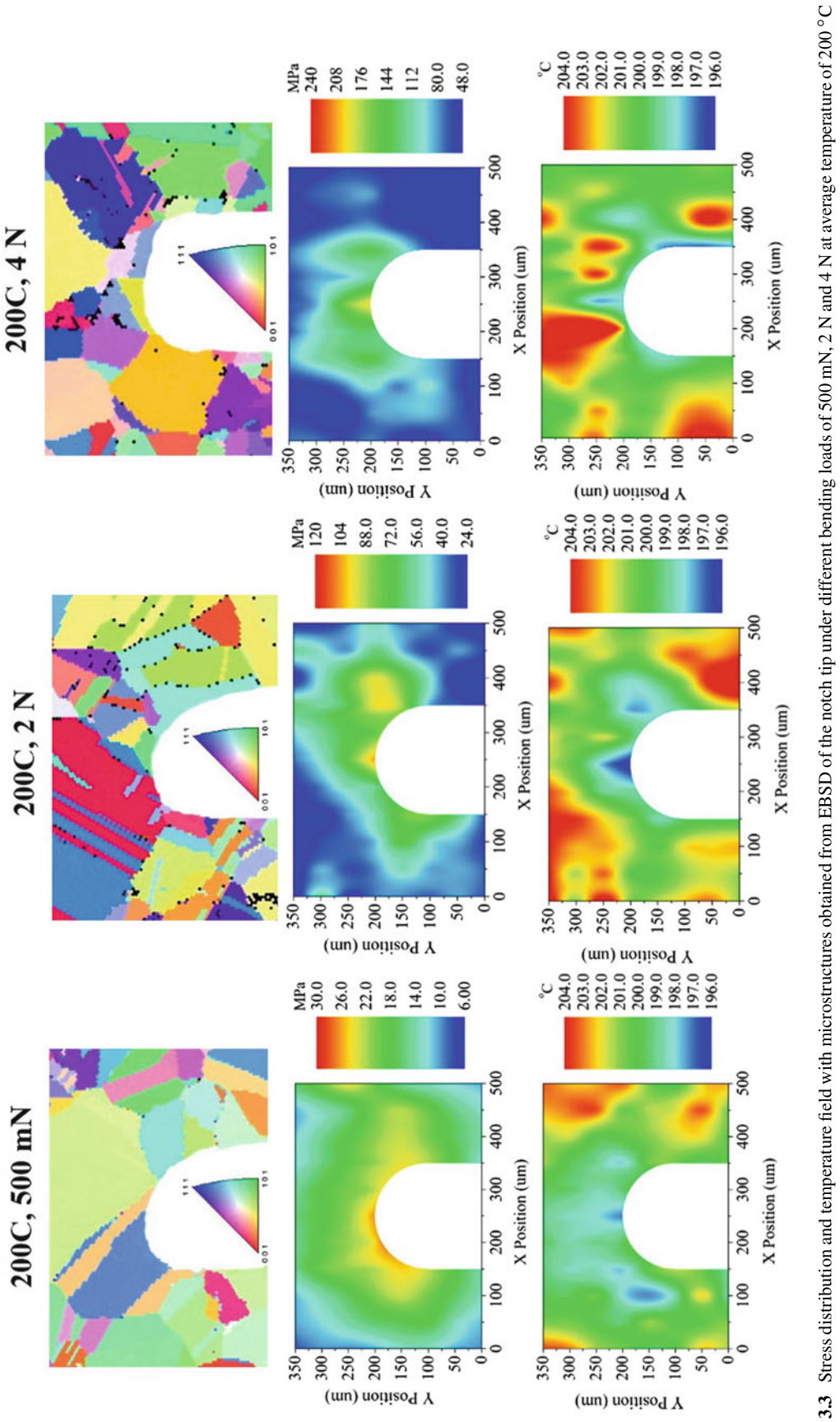

Fig. 3.3 Stress distribution and temperature field with microstructures obtained from EBSD of the notch tip under different bending loads of 500 mN, 2 N and 4 N at average temperature of 200 °C

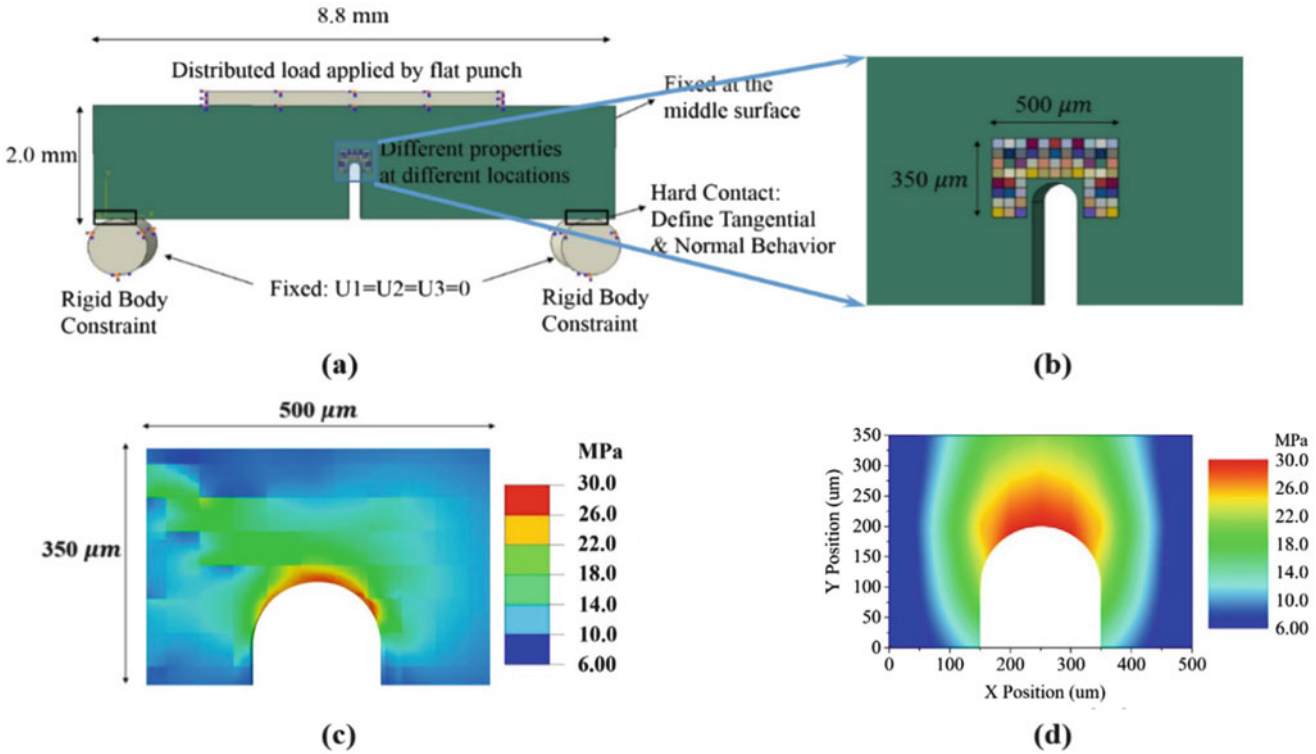

Fig. 3.4 (**a**) Overall setup and boundary conditions in FE simulation, (**b**) indentation stress-strain curve zones around notch area, (**c**) stress map around notch determined using FE simulation at 500 mN bending load, and (**d**) stress map around notch calculated theoretically at 500 mN bending load

grid used for such calculations. Instead of considering actual grain structures, different elastic and plastic material properties which were obtained from indentation experiments around the notch area were applied to the same area with 68 small rectangular zones of 50 by 50 microns. For each grain average stress-strain behavior was based on spatial average of such curves. These stress-strain curves were fitted to a J2 plasticity model. The validated J2 plasticity model for each grain was taken as a representative for its elastic-plastic deformation behavior. While performing the finite element deformation simulations in Fig. 3.4a, use of the grid shown in Fig. 3.4b leads to the incorporation of averaged microstructure effects and plasticity. In the rest of sample, average material properties that were also obtained from the experiments was applied. From the finite element simulation results shown in Fig. 3.4c it is clear that the average maximum principal stress at the notch tip matches closely with experimental measurements (Fig. 3.2, 500 mN). Difference between the experiments and simulations at other points in microstructure away from the notch can be attributed to the residual stresses due to grain boundaries and precipitates. Magnitude-wise, however, stresses are in the same range in the scanned area using NMRS bringing simulations and experiments close in terms of stress prediction. Theoretical calculations were also performed to predict stress distribution in notch area based on stress intensity factor calculations. The mapping of maximum principal stress obtained in this way around the crack tip is shown in Fig. 3.4d. The difference between the experiments and theoretical calculation can be attributed to crack tip plasticity as well as microstructure effect. However, crack-tip average stresses are in the same range as experiments.

In the current research, a novel NMRS measurement platform was used to measure crack (notch) tip stresses during *in-situ* mechanical deformation at elevated temperature. Notch tip of sample during 3-point bending tests with an initial notch was scanned. Temperature field and stress distribution in the notch tip area were generated by combining measurement results at each scan point through the relation between the stress, temperature and Raman shift. Based on the nanoindentation stress-strain curve, the yield strength at the notch tip was found to decrease after the 3-point bending. Instead of considering actual grain structures with different material properties, a new FE method was adopted to predict stress distribution around the same notch area as scanning. Predictions from theory and simulations matched closely in stress concentration area near notch with experimental measurements. However, away from notch area deviation in simulation and experimental predictions due to microstructural effects was observed. A significant effect of temperature change induced residual stress and its correlation with microstructure dependent temperature distribution was observed.

References

1. Flinn, P.A., Waychunas, G.A.: A new x-ray diffractometer design for thin-film texture, strain, and phase characterization. J. Vac. Sci. Technol. B. **6**(6), 1749–1755 (1988)
2. Armigliato, A., Barboni, R., Dewolf, I., Frabboni, S., Janssens, K.G.F., Vanhellemont, J.: Determination of lattice strain in local isolation structures by electron-diffraction techniques and micro-Raman spectroscopy. In: Cullis, A.G., StatonBevan, A.E., Hutchison, J.L. (eds.) Microscopy of Semiconducting Materials, CRC Press, Boca Raton, pp. 229–234 (1993)
3. Anastassakis, E., Pinczuk, A., Burstein, E., Pollak, F.H., Cardona, M.: Effect of static uniaxial stress on the Raman spectrum of silicon. Solid State Commun. **8**(2), 133–138 (1970)
4. Kim, S.H., Noh, J., Jeon, M.K., Kim, K.W., Lee, L.P., Woo, S.I.: Micro-Raman thermometry for measuring the temperature distribution inside the microchannel of a polymerase chain reaction chip. J. Micromech. Microeng. **16**(3), 526 (2006)
5. Phinney, L.M., Serrano, J.R., Piekos, E.S., Torczynski, J.R., Gallis, M.A., Gorby, A.D.: Raman thermometry measurements and thermal simulations for MEMS bridges at pressures from 0.05 Torr to 625 Torr. J. Heat Transf. **132**(7), 072402 (2010)
6. Ribeiro, L.A., Rosolem, J.B., Toledo, A.O.: Improving the dynamic range in distributed anti-Stokes Raman thermometry by means of susceptibility asymmetry. In: 21st International Conference on Optical Fibre Sensors (OFS21), International Society for Optics and Photonics, Ottawa, ON (2011)
7. Abel, M.R., Graham, S., ASME: Thermometry of polycrystalline silicon structures using Raman spectroscopy. In: Advances in Electronic Packaging, Pts A–C, American Society of Mechanical Engineers, New York, pp. 1695–1702 (2005)
8. Dou, Y.W., Hu, M., Cui, M., Zong, Y.: Experimental study of porous silicon thermal conductivity using micro-Raman spectroscopy. In: Wen, T.D. (ed.) ISTM/2005: 6th International Symposium on Test and Measurement, Conference Proceedings, Dalian, China, vols. 1–9, pp. 2094–2097 (2005)
9. Fang, Z.-Q., Hu, M., Zhang, W., Zhang, X.-R.: Micro-Raman spectroscopic investigation of the thermal conductivity of oxidized meso-porous silicon. Acta Phys. Sin. **57**(1), 103–110 (2008)
10. Perichon, S., Lysenko, V., Remaki, B., Barbier, D., Champagnon, B.: Measurement of porous silicon thermal conductivity by micro-Raman scattering. J. Appl. Phys. **86**(8), 4700–4702 (1999)
11. Xi, L., Xiaoming, W., Tianling, R.: A metrology of silicon film thermal conductivity using micro-Raman spectroscopy. In: SOI Conference (SOI), 2010 IEEE International, San Diego, CA (2010)
12. Gan, M., Tomar, V.: An in-situ platform for the investigation of Raman shift in micro-scale silicon structures as a function of mechanical stress and temperature increase. AIP Rev. Sci. Instrum. **85**, 013902 (2014.) (10 pp)
13. Gan, M., Tomar, V.: Surface stress variation as a function of applied compressive stress and temperature in microscale silicon. AIP J. Appl. Phys. **116**, 073502 (2014.) (10 pages)
14. Gan, M., Tomar, V.: Temperature dependent microscale uniaxial creep of silicon and surface dominated deformation mechanisms. ASME J. Nanotechnol. Eng. Med. **5**, 021004 (2014.) (9 pages)
15. Pathak, S., Michler, J., Wasmer, K., Kalidindi, S.R.: Studying grain boundary regions in polycrystalline materials using spherical nano-indentation and orientation imaging microscopy. J. Mater. Sci. **47**(2), 815–823 (2012)
16. Adams, B.L.: Orientation imaging microscopy: emerging and future applications. Ultramicroscopy. **67**(1), 11–17 (1997)
17. Adams, B.L., Wright, S.I., Kunze, K.: Orientation imaging: The emergence of a new microscopy. Metall. Trans. A. **24**(4), 819–831 (1993)
18. Kalidindi, S.R., Pathak, S.: Determination of the effective zero-point and the extraction of spherical nanoindentation stress–strain curves. Acta Mater. **56**(14), 3523–3532 (2008)

Chapter 4
The Two-Way Relationship Between Residual Stress and Fatigue/Fracture

Michael B. Prime

Abstract Most mechanicians are aware that residual stresses affect fatigue and fracture. Few are aware of the full extent of the effects residual stress have on myriad aspects of those and other structural processes AND of the reverse relationship: fracture concepts are hugely intertwined with residual stress measurements. This talk first reviews the straightforward effect that residual stress has: it acts just like an external load and, depending on the sign, accelerates or retards failure processes. The talk then describes one exemplar less well-known effect: residual stress can make it very difficult to measure true material properties like fracture toughness. The talk then describes the influence of fracture concepts, most notably the mode I stress intensity factor K_I, on residual stress measurement. A short and elegant derivation reveals that incremental slitting measurement strain data can be converted to residual stress profiles using a K_I analysis and a conceptually simple calibration factor that is independent of the stress distribution. The talk next shows that several error sources for slitting and contour method stress measurements can be directly correlated with the K_I caused by residual stress. The talk then lays out Bueckner's superposition principle, the most powerful but misunderstood and mistrusted tool for analyzing stress fields around cracks. Originally developed for fracture mechanics, Bueckner's is used to calculate the K_I from residual stresses and to calculate calibration coefficients for hole drilling and slitting. More notably, the contour method for measuring residual stress is a direct experimental embodiment of Bueckner's principle. In fact, we review an experimental demonstration that misfit measurements between mating fracture surfaces can be used to calculate the residual stresses that existed prior to the fracture.

Keywords Residual stress • Fracture mechanics • Superposition • Stress intensity factor

4.1 Residual Stress Influence on Fatigue and Fracture and Properties

Residual stresses are the stresses present in a part free from external load, and they are generated by virtually any manufacturing process [1, 2]. They can be particularly insidious because they are ubiquitous, offer no external evidence of their existence, and they are difficult to predict or measure.

The most straightforward relationship between residual stress and failure processes is that residual stresses add to applied loads and contribute to many material failure processes like fatigue, fracture, and stress corrosion cracking [3–8]. The relationship can illustrated using the mode I stress intensity factor K_I used for fatigue and fracture and the standard fracture criteria:

$$(K_I)_{applied} + K_{Irs} > K_{Ic} \tag{4.1}$$

where K_{Irs} is the residual stress contribution to K_I. For brittle fracture, the sum of the K_I's from residual stress and applied must exceed the fracture toughness K_{Ic}, a material property, for failure. The contribution may be beneficial in the case of compressive residual stress (negative K_{Irs}) or harmful in the case of tensile stress. For fatigue, residual stress acts as a mean stress as compared to an alternating stress and therefore has more impact in fatigue crack growth situations [9–11] than high-cycle fatigue.

A related but less well-known residual stress effect is the "contamination" of material property measurements [12–16]. We continue our example using fracture toughness. In fracture toughness testing, a load is applied to a test coupon and the applied K_I at fracture is assumed to be the fracture toughness:

M.B. Prime (✉)
Los Alamos National Laboratory, Los Alamos, NM, 87545, USA
e-mail: prime@lanl.gov

J. Carroll et al. (eds.), *Fracture, Fatigue, Failure and Damage Evolution, Volume 7*, Conference Proceedings of the Society for Experimental Mechanics Series, DOI 10.1007/978-3-319-62831-8_4

$$(K_{Ic})_{apparent} = (K_I)_{applied} \tag{4.2}$$

However, test coupons often contain residual stress. When the crack is introduced into a fracture coupon, the release and redistribution of residual stress results in a K_{Irs}. Combining and rearranging Eqs. 4.1, 4.2 we get

$$(K_{Ic})_{apparent} = (K_{Ic})_{actual} - K_{Irs} \tag{4.3}$$

Which shows that the apparent, "measured" fracture toughness can be significantly in error. Such results confound the development of fracture resistant alloys and transferring coupon data to the prediction of structural failure.

4.2 Influence of Fracture Concepts on Residual Stress Measurement

The incremental slitting method for measuring residual stress, also known as crack compliance, is a powerful and widely used method [17, 18]. By incrementally introducing a narrow slit and measuring relaxed strain at each increment of slit depth, it is possible to precisely determine a depth profile of residual stresses. Through a simple derivation, it can be shown that the incremental slitting data can be used to calculate the K_{Irs} more simply and directly than one can calculate the residual stress [19–21]:

$$K_{Irs}(a) = \frac{E'}{Z(a)} \frac{d\varepsilon}{da} \tag{4.4}$$

where Z(a) is a geometric calibration factor that is independent of the stress distribution. One can then calculate the residual stress from K_{Irs} as has been recognized for a long time [22].

Like all relaxation methods, slitting relies on the assumption that the stresses relax elastically after material removal [2]. It turns out that slitting method errors due to plasticity can be better analyzed and predicted using K_{Irs} than using simple stress magnitudes [23].

Maybe the most powerful and pervasive contribution of fracture mechanics to residual stress is a superposition principle that immensely simplifies calculations. A problem seemed intractable at the dawn of fracture mechanics before the wide availability of finite element modeling. In a body under stress (applied stress and/or residual), the growth of a crack (or in the introduction of a slit) causes stresses to be released on the face of the crack and the subsequent redistribution of all stresses in the body. A further increment in crack length would then release not the original residual stresses but now the post-redistribution stresses. How to keep track of all that redistribution and correctly calculate everything? In 1958, Hans Bueckner proved the superposition principle that allows one to calculate K_I and deformations using only the *original* stresses on cut plane [24].

Figure 4.1 shows an illustration of Bueckner's principle as applied to residual stress. The first published illustration of Buckner's principle in this form was given by Barenblatt [25] although Paris also published a similar figure apparently independently of Bueckner [26]. In Fig. 4.1, A is the body in its original state with residual stresses and this is taken as the undeformed state. B is the deformed state of the body after the introduction of a crack. This is the state where the fracture mechanics community would want to know K_I, and the residual stress community would want to know the deformations. One can get back the A state by adding the state in B to a state (stresses and displacements) calculated by applying the original stresses on the cut plane as surface tractions to a cracked but unstressed and undeformed body. The second line of Fig. 4.1 shows then that by simple re-arrangement B can be found by adding the original state A to a calculated state where one applies the *original residual stresses along the crack plane* to a the faces of the crack. Since the state A is undeformed and has a $K_I = 0$ (no crack so no stress singularity), only the calculated state is needed! This principle is so simple and non-intuitive that it is widely misunderstood and some mistakenly believe it does not calculate the redistribution correctly [27].

Conversely, Bueckner's is used incorrectly sometimes. For considering local plasticity effects in residual stress measurements, Bueckner's is the wrong approach because the vonMises stress is not zero in state A, so one cannot just use C by itself to examine the cracked state. Instead of using Bueckner's, one should initialize the full residual stress field [23]. In either case (Bueckner's or initial stress), one also has to extend the crack, slit or hole incrementally in order to capture the path dependence of plasticity effects.

Bueckner's principle is used ubiquitously in residual stress measurements. Because of the stress redistribution issue, an inverse procedure is necessary to calculate a residual stress profile from measured strains [28, 29]. To perform the inverse, one needs calibration coefficients that tell you the strain that would be measured if you knew the residual stress. Those coefficients are calculated using Bueckner's principle for the slitting method [17], hole drilling [30, 31], and other relaxation methods.

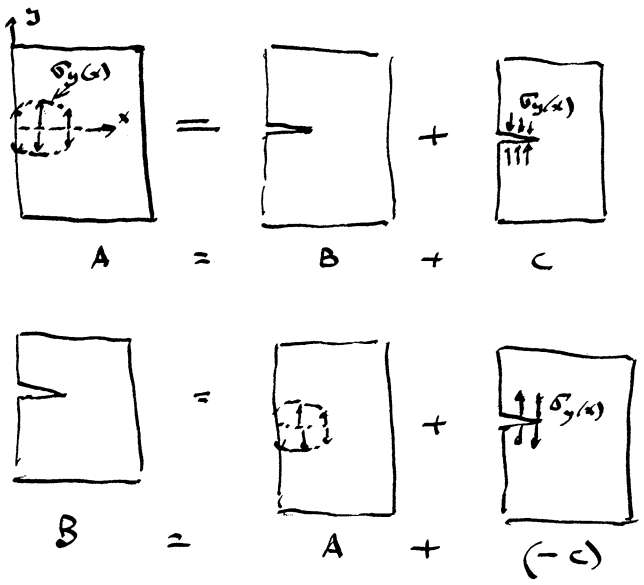

Fig. 4.1 An illustration of Bueckner's superposition principle from a paper copy of Iain Finnie's course notes at U.C. Berkeley [39]

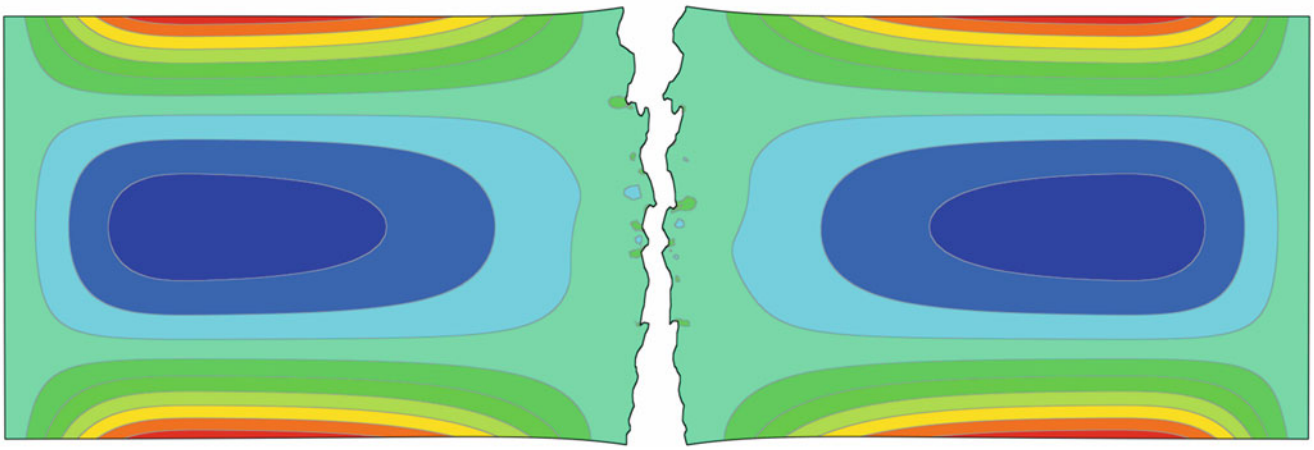

Fig. 4.2 The mismatch between otherwise mating fracture surfaces can be used to calculate the residual stresses that existed prior to the fracture. *Blue* represents compressive residual stress and *red* is tensile

The one relaxation method that avoid the cumbersome inverse calculation does so by further exploiting Bueckner's principle [32–34]. In the contour method, a part is cut in two and the shape (contour) after cutting is measured on the cut surface (B in Fig. 4.1 but with the part cut all the way through) and then applied in a calculation to the cut surface (C in Fig. 4.1 but displacements instead of stresses) to calculate the original residual stresses directly. In another relationship with fracture, we also find that bulge and plasticity errors with the contour method are best estimated using K_{Irs} than using simple stress magnitudes [35–37].

A final application of Bueckner's principle allows one to solve what almost sounds like an unsolvable problem. With no measurements or data prior to a fracture, is there any way to take the failed part and "measure" what the residual stresses were prior to fracture on the plane of the fracture? Since the stresses normal to the cut plane were relaxed by the fracture, it would seem there is nothing left to measure. But if stresses were relaxed by the fracture, there will be a geometric mismatch between the fracture surfaces, as illustrated in Fig. 4.2, and the mismatch is sufficient to uniquely calculate the original residual stresses on the cut plane. This method was demonstrated experimentally on fractured aluminum forging and independently validated using neutron diffraction [38].

Acknowledgements Los Alamos National Laboratory, an affirmative action/equal opportunity employer, is operated by the Los Alamos National Security, LLC for the National Nuclear Security Administration of the U.S. Department of Energy under contract DE-AC52-06NA25396. By approving this article, the publisher recognizes that the U.S. Government retains nonexclusive, royalty-free license to publish or reproduce the published form of this contribution, or to allow others to do so, for U.S. Government purposes. Los Alamos National Laboratory requests that the publisher identify this article as work performed under the auspices of the U.S. Department of Energy. Los Alamos National Laboratory strongly supports academic freedom and a researcher's right to publish; as an institution, however, the Laboratory does not endorse the viewpoint of a publication or guarantee its technical correctness.

References

1. Withers, P.J., Bhadeshia, H.K.D.H.: Residual stress. Part 2 – Nature and origins. Mater. Sci. Technol. **17**(4), 366–375 (2001). doi:10.1179/026708301101510087
2. Schajer, G.S.: Practical Residual Stress Measurement Methods. Wiley, Chichester (2013)
3. Withers, P.J.: Residual stress and its role in failure. Rep. Prog. Phys. **70**(12), 2211–2264 (2007)
4. James, M.N.: Residual stress influences on structural reliability. Eng. Fail. Anal. **18**(8), 1909–1920 (2011)
5. Bush, S.H.: Failure mechanisms in nuclear power plant piping systems. J. Press. Vessel. Technol. **114**(4), 389–395 (1992)
6. Cuellar, S.D., Hill, M.R., DeWald, A.T., Rankin, J.E.: Residual stress and fatigue life in laser shock peened open hole samples. Int. J. Fatigue. **44**, 8–13 (2012). doi:10.1016/j.ijfatigue.2012.06.011
7. Liu, K.K., Hill, M.R.: The effects of laser peening and shot peening on fretting fatigue in Ti-6Al-4 V coupons. Tribol. Int. **42**(9), 1250–1262 (2009)
8. Wilson, G.S., Grandt Jr., A.F., Bucci, R.J., Schultz, R.W.: Exploiting bulk residual stresses to improve fatigue crack growth performance of structures. Int. J. Fatigue. **31**(8–9), 1286–1299 (2009)
9. Citarella, R.G., Carlone, P., Lepore, M., Palazzo, G.S.: A FEM-DBEM investigation of the influence of process parameters on crack growth in aluminum friction stir welded butt joints. Key Eng. Mater. **554–557**, 2118–2126 (2013)
10. Albuquerque, C.M.C., Miranda, R.M.C., Richter-Trummer, V., Figueiredo, M.A.V.D., Calçada, R., Castro, P.M.S.T.D.: Fatigue crack propagation behaviour in thick steel weldments. Int. J. Struct. Integr. **3**(2), 184–203 (2012)
11. Stuart, D.H., Hill, M.R., Newman Jr., J.C.: Correlation of one-dimensional fatigue crack growth at cold-expanded holes using linear fracture mechanics and superposition. Eng. Fract. Mech. **78**(7), 1389–1406 (2011)
12. Bucci, R.: Lessons learned – Effect of residual stress on material durability/damage tolerance capability assessment: coupon-to-component issues, problems and cures. Paper presented at the ASTM-E08 Workshop on Residual Stress Effects on Fatigue and Fracture Testing and Incorporating Results into Design, Pittsburgh, 8 May 2002
13. Bucci, R.: Effect of residual stress on fatigue crack growth rate measurement. In: Roberts, R. (ed.) Fracture Mechanics. ASTM International, Philadelphia (1981)
14. Lados, D.A., Apelian, D.: The effect of residual stress on the fatigue crack growth behavior of Al-Si-Mg cast alloys – mechanisms and corrective mathematical models. Metall. Mater. Trans. A-Phys. Metall. Mater. Sci. **37A**(1), 133–145 (2006)
15. JE, V.D., Hill, M.R.: Evaluation of residual stress corrections to fracture toughness values. J. ASTM Int. **5**(8), JAI101713 (2008)
16. Hill, M.R., VanDalen, J.E., Prime, M.B.: Assessment of residual stress in fracture mechanics coupons. In: ASME Pressure Vessels and Piping Conference, Baltimore, Materials and Fabrication, Parts A and B, vol. 6, pp. 421–426. (2011). doi:10.1115/pvp2011-57768
17. Cheng, W., Finnie, I.: Residual Stress Measurement and the Slitting Method Mechanical Engineering Series. Springer Science + Business Media, New York (2007)
18. Hill, M.R.: The slitting method. In: Schajer, G.S. (ed.) Practical Residual Stress Measurement Methods, pp. 89–108. Wiley (2013). doi:10.1002/9781118402832.ch4
19. Schindler, H.J., Cheng, W., Finnie, I.: Experimental determination of stress intensity factors due to residual stresses. Exp. Mech. **37**(3), 272–277 (1997)
20. Schindler, H.J.: Determination of residual stress distributions from measured stress intensity factors. Int. J. Fract. **74**(2), R23–R30 (1990)
21. Prime, M.B.: Measuring residual stress and the resulting stress intensity factor in compact tension specimens. Fatigue Fract. Eng. Mater. Struct. **22**(3), 195–204 (1999)
22. Vaidyanathan, S., Finnie, I.: Determination of residual stresses from stress intensity factor measurements. Trans. ASME Ser. D J. Basic Eng. **93**(2), 242–246 (1971)
23. Prime, M.B.: Plasticity effects in incremental slitting measurement of residual stresses. Eng. Fract. Mech. **77**(10), 1552–1566 (2010). doi:10.1016/j.engfracmech.2010.04.031
24. Bueckner, H.F.: The propagation of cracks and the energy of elastic deformation. Trans. Am. Soc. Mech. Eng. **80**, 1225–1230 (1958)
25. Barenblatt, G.I.: The mathematical theory of equilibrium cracks in brittle fracture. In: Dryden, H.L., von Kármán, T., Kuerti, G., van den Dungen, F.H., Howarth, L. (eds.) Advances in Applied Mechanics, vol. 7, pp. 55–129. Elsevier (1962). doi:10.1016/s0065-2156(08)70121-2
26. Paris, P.C., Gomez, M.P., Anderson, W.E.: A rational analytic theory of fatigue. Trends Eng. **13**, 9–14 (1961)
27. Garcia, C., Lotz, T., Martinez, M., Artemev, A., Alderliesten, R., Benedictus, R.: Fatigue crack growth in residual stress fields. Int. J. Fatigue. **87**, 326–338 (2016). doi:10.1016/j.ijfatigue.2016.02.020
28. Schajer, G.S., Prime, M.B.: Use of inverse solutions for residual stress measurements. J. Eng. Mater. Technol. **128**, 375–382 (2006)
29. Faghidian, S.A., Goudar, D., Farrahi, G.H., Smith, D.J.: Measurement, analysis and reconstruction of residual stresses. J. Strain Anal. Eng. Des. **47**(4), 254–264 (2012). doi:10.1177/0309324712441146
30. Schajer, G.S.: Application of finite element calculations to residual stress measurements. J. Eng. Mater. Technol. **103**(2), 157–163 (1981)
31. Schajer, G.S.: Measurement of non-uniform residual-stresses using the hole-drilling method 0.1. Stress calculation procedures. J. Eng. Mater. Technol. **110**(4), 338–343 (1988)

32. Prime, M.B.: Cross-sectional mapping of residual stresses by measuring the surface contour after a cut. J. Eng. Mater. Technol. **123**(2), 162–168 (2001)
33. Prime, M.B., DeWald, A.T.: The contour method. In: Schajer, G.S. (ed.) Practical Residual Stress Measurement Methods. Wiley, Chichester. (2013). doi:10.1002/9781118402832.ch5
34. Pagliaro, P., Prime, M.B., Robinson, J.S., Clausen, B., Swenson, H., Steinzig, M., Zuccarello, B.: Measuring inaccessible residual stresses using multiple methods and superposition. Exp. Mech. **51**(7), 1123–1134 (2011). doi:10.1007/s11340-010-9424-5
35. Prime, M.B., Kastengren, A.L.: The contour method cutting assumption: error minimization and correction. In: Proulx, T. (ed.) Experimental and Applied Mechanics, Volume 6, Conference Proceedings of the Society for Experimental Mechanics Series, vol. 17, pp. 233–250. Springer, New York (2011). Available at http://www.lanl.gov/contour/. doi:10.1007/978-1-4419-9792-0_40
36. Hosseinzadeh, F., Traore, Y., Bouchard, P.J., Muránsky, O.: Mitigating cutting-induced plasticity in the contour method, part 1: experimental. Int. J. Solids Struct. **94–95**, 247–253 (2016). doi:10.1016/j.ijsolstr.2015.12.034
37. Muránsky, O., Hamelin, C.J., Hosseinzadeh, F., Prime, M.B. Evaluation of a self-equilibrium cutting strategy for the contour method of residual stress measurement. Int. J. Press. Vessel. Pip. (2017, submitted)
38. Prime, M.B., DeWald, A.T., Hill, M.R., Clausen, B., Tran, M.: Forensic determination of residual stresses and KI from fracture surface mismatch. Eng. Fract. Mech. **116**, 158–171 (2014). doi:10.1016/j.engfracmech.2013.12.008
39. Dharan, C., Kang, B., Finnie, I.: Finnie's Notes on Fracture Mechanics. Springer Science + Business Media, New York (2016). doi:10.1007/978-1-4939-2477-6

Chapter 5
Designing Brittle Fracture Specimens to Investigate Environmentally Assisted Crack Growth

Sunday Aduloju, Wenjia Gu, Timothy Truster, John Emery, Dave Reedy, and Scott J. Grutzik

Abstract Subcritical crack growth can occur in a glass when the stress intensity factor is less than the fracture toughness if water molecules are present. A novel bi-material beam specimen is proposed to investigate environmentally assisted crack growth (EACG). Two materials with different coefficients of thermal expansion are diffusion bonded at high temperature and cooled to the room temperature which introduces residual stress in the beam. A Finite element (FE) model is developed and initially validated with an analytical model. Steady-state crack (SSC) depth at which mode II stress intensity factor (K_{II}) is zero and the corresponding mode I stress intensity factor (K_I) value are obtained for different material pairs and thickness ratios of the top and bottom materials using the FE model. Crack propagation path is also predicted. We finally modify the geometry of the specimen to generate non-constant K_I values as the crack propagates.

Keywords Steady-state • Crack growth • Self-loading • Stress intensity factor

5.1 Introduction

Under inert conditions, a crack in a brittle material will only grow when the stress intensity factor at the crack tip equals the fracture toughness. If water is present (as it is in almost all practical environments), water molecules can interact with the material at the crack tip to cause slow crack propagation at lower stresses [1, 2]. Relative humidity and temperature both enhance this phenomenon. EACG is a type of sub-critical crack growth and can cause flaws that would otherwise be stable to grow to a point where they become critical.

As such, EACG is an important factor in determining service life or shelf life of a component.

In the past, EACG has been studied under a variety of conditions but specimens have always required a load to be externally applied [3–5]. The most common setup requires a double cantilever beam specimens subjected to a constant external loading or bending moment were crack extension are measured as a function of time using optical equipment. Crack velocities that range from 10^{-10} to 10^{-2} m/s could be collected through this method [6]. Even with simple dead loading, it can be difficult to guarantee that the load will remain constant over a test that could last months or years.

We propose a new type of specimen consisting of a bimaterial beam where the two materials have slightly different coefficient of thermal expansions (CTEs). If both materials are glass, they can be diffusion bonded at a temperature of around 400–600 °C. As they cool to room temperature the two materials will contract by different amounts according to their CTE values. Because they are constrained to be the same length along the interface, this puts the composite beam in bending with tensile stresses in the material with the smaller CTE value. Figure 5.1 shows the schematic description of the entire bonding process. In this way, the specimen is "self-loaded" by the residual stress resulting from the bonding process. This creates a very stable stress field that is ideal for long-term strength experiments.

The objective of this research is to design such a specimen. The bonding temperature and the size of each side of the bimaterial beam need to be picked to provide SIFs between approximately 0.5 and $0.9K_{IC}$ where K_{IC} is the fracture toughness of the material in tension under pure Mode I (tensile) crack opening. The goal is to have SIFs low enough to be sub-critical

S. Aduloju • T. Truster
Department of Civil and Environmental Engineering, University of Tennessee, Knoxville, TN, 37996, USA

W. Gu
Department of Civil and Environmental Engineering, Cornell University, Ithaca, NY, 14850, USA

J. Emery • D. Reedy • S.J. Grutzik (✉)
Component Science and Mechanics, Sandia National Laboratories, Albuquerque, NM, 87185, USA
e-mail: sjgrutz@sandia.gov

J. Carroll et al. (eds.), *Fracture, Fatigue, Failure and Damage Evolution, Volume 7*, Conference Proceedings of the Society for Experimental Mechanics Series, DOI 10.1007/978-3-319-62831-8_5

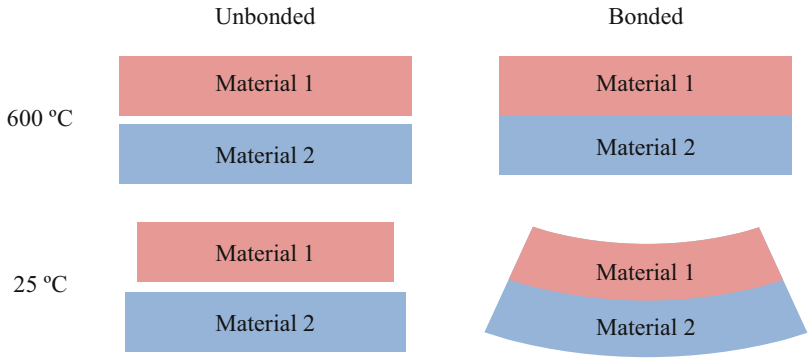

Fig. 5.1 Schematic of unbonded and bonded materials cooling from 600 °C to 20 °C with CTE values CTE_1 and CTE_2 where $CTE_1 > CTE_2$

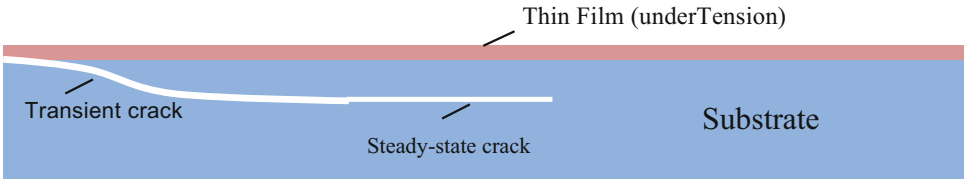

Fig. 5.2 Crack propagation in a system consisting of thin film deposited on a substrate

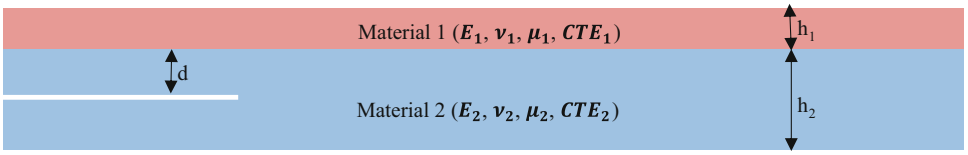

Fig. 5.3 Bimaterial beam

(less than K_{IC}) but still high enough for propagation to occur in a reasonable amount of time. An important factor to consider is to make sure that once a crack starts to propagate the propagation is stable. Suo and Hutchinson [7] have shown that in this geometry a crack will propagate in the material with smaller CTE and parallel to the interface along a path where $K_{II} = 0$. Figure 5.2 shows an unstable crack that started at the interface between the film and the substrate and grew until it became stable in the substrate when $K_{II} = 0$.

For a bonded specimen in Fig. 5.3, the expression for relative SSC depth λ is shown in Eq. (5.1) and the thickness ratio τ could be expressed as the ratio of the thickness of material 1 to material 2 in Eq. (5.2).

$$\lambda = \frac{d}{h_1} \tag{5.1}$$

$$\tau = \frac{h_1}{h_2} \tag{5.2}$$

Where d represents the cracking depth, h_1 is the thickness of the top material and h_2 is the thickness of the bottom material.

5.2 Finite Element Model

The specimen needs to designed such that the crack reliably starts from a favorable location near this $K_{II} = 0$ path. We develop a Finite Element (FE) model to find the relative cracking depth (λ) which gives $K_{II} = 0$ and tune the thickness ratio (h_1/h_2) for a given h_1 and ΔT so that K_I at this location has the desired magnitude of about 0.5 $0.9K_{IC}$ for different combinations of the two materials of the specimen. The understanding of the elastic mismatch between the two materials is very significant in providing accurate modeling of SSC. The elastic mismatch of the two materials could be expressed in terms of two Dundurs' parameters α and β. The parameters are expressed in Eqs. 5.3 and 5.4.

$$\alpha = \frac{\Gamma(\kappa_2 + 1) - (\kappa_1 + 1)}{\Gamma(\kappa_2 + 1) + (\kappa_1 + 1)} \tag{5.3}$$

$$\beta = \frac{\Gamma(\kappa_2 - 1) - (\kappa_1 - 1)}{\Gamma(\kappa_2 + 1) + (\kappa_1 + 1)} \tag{5.4}$$

where $\Gamma = \mu_1/\mu_2$, $\kappa = 3 - 4\nu$ for plane strain and $\kappa = (3 - \nu)/(1 + \nu)$ for plane stress, μ is the shear modulus and ν is the Poisson's ratio. The First Dundurs' parameter α is the measure of the difference in the stiffness of the upper material to the bottom material of the bimaterial beam. $\alpha > 0$ when the top material is stiffer than bottom material of bimaterial beam and $\alpha < 0$ when the top material is more compliant than the bottom material. The sign of α is reversed when material 1 and material 2 are interchanged. The α parameter can be seen to be between −1 and 1 by letting one of the stiffness values go to zero [8]. Suo and Hutchinson [7] show that sub-interface cracking is only weakly dependent on the second Dundur's parameter so the current parameter study focuses on α only.

It has been shown that α parameter can easily be simplified by expressing it in terms of Elastic moduli of the two materials that makes up the bonded material [9]. The simplified form of α is expressed in Eq. (5.5).

$$\alpha = \frac{E_2^+ - E_1^+}{E_2^+ + E_1^+} \tag{5.5}$$

Where the expression for E_i^+ is given in Eq. (5.6).

$$E_i^+ = \begin{cases} \frac{E_i}{(1-\nu_i^2)} & \text{(plane strain)} \\ E_i & \text{(plane stress)} \end{cases} \tag{5.6}$$

E_i , ν_i (for $i = 1, 2$) represent the elastic moduli and Poisson's ratios of the material components of the bonded material.

2 dimensional (2D) plane stress finite element simulations were performed using FE modeling capabilities of the commercial FEA code ABAQUS [10]. The materials chosen for this research were only selected based on the availability of material data and required values of α parameter. The material properties required for the FE modeling are Elastic moduli, Poisson's ratios, and CTEs. These materials' data were obtained from Sandia National Laboratories and from relevant literature. Each of the material was assumed to be isotropic and linearly elastic and initial crack length of 15 mm was assumed to be present in the substrate. Boundary conditions were applied to restrict rigid body modes and displacements were otherwise free.

All FE models were discretized using quadratic Quadrilateral (Q8) elements with a mesh focused mesh structure and quadratic quarter point elements at the crack tip. The method of J contour integral was applied the to evaluate stress intensity factors.

For earlier validation of the Finite element model, the SSC in brittle substrates beneath adherent films were modeled for α values of −0.8, −0.6, −0.4, −0.2, 0, 0.2, 0.4, 0.6 and 0.8 and were compared to the analytical results obtained from [7]. Substrate dimensions used in the analysis were 150 mm length by 25.4 mm thick and the initial crack length of 15 mm was used for all models. The film and the substrate have equal length while the thickness of the film was gradually increased by increasing the film to substrate thickness ratio τ from 0 up to 0.1. The SSC depth and K_I when $K_{II} = 0$ were determined and the results were compared to the Analytical results.

The FE model was extended to study SSC in the bottom material of bimaterial beam shown in Fig. 5.3. The materials used for this study were Schott B270 (a variant of soda-lime glass) as the top material and standard soda-lime glass as the bottom material. The material properties are shown in Table 5.1. It is important to note $\alpha = 0$ for the bimaterial beam because the Elastic moduli of the component are very close. The material components were picked because of the ready availability of the materials. The FE modeling of the bimaterial beam was accomplished by increasing the thickness ratio τ from 0.1 to 1 while retaining the initial crack length, thickness and length of the bottom material as15, 25.4 and 150 mm. The SSC depth and K_I when $K_{II} = 0$ were determined.

Table 5.1 Material property for the biomaterial beam

Material	Schott B270	Soda-lime
Elastic modulus (GPa)	71.5	74
Poisson's ratio	0.22	0.24
CTE (20–600 °C)	1.11185×10^{-5}	1.0156×10^{-5}

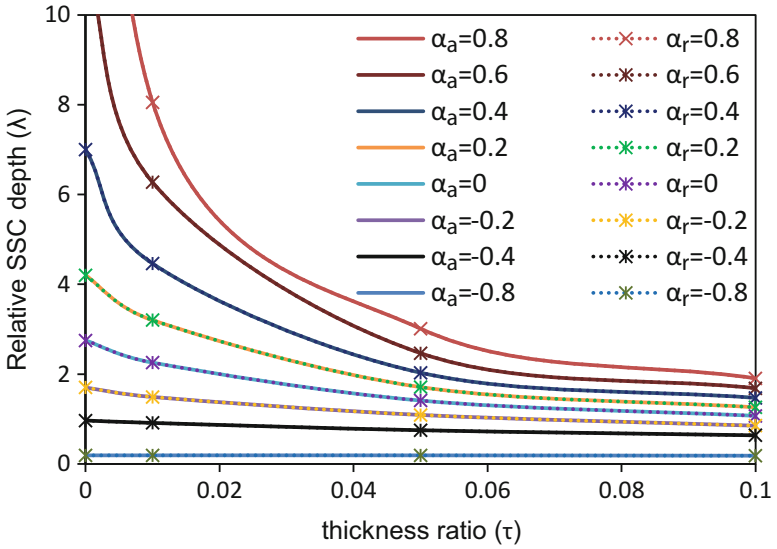

Fig. 5.4 Relative SSC depth as function of film/substrate thickness

The SSC depth and K_I for bimaterial for different α parameters were explored and four additional bimaterial specimen designs were made to obtain K_I that changes with propagation length so that crack velocities values rather than a single point be obtained. This could be realized by developing bimaterial specimens with varying thickness across its length.

FRANC3D [11, 12] code receives a mesh model as input and performs adaptive mesh restructuring to incrementally advance a crack. The SSC propagations for the five new specimens were performed using Franc3D code interfaced with Abaqus. 3D geometry and initial Finite element discretization using quadratic quadrilateral elements were done in ABAQUS FE code while the initial crack lengths were specified in the Franc3D code. The 3-dimensional models for the five designs were realized by extruding the 2D model through a thickness of 1 mm. Finer discretization of the geometry with a high concentration of elements near the crack tip was done and stress intensity factors were calculated by the M-integral method [11, 12]. The local direction of the crack growth was predicted using the maximum Tensile stress criterion.

5.3 FE Model Validation

Suo and Hutchinson's analytic model was used as a benchmark to check the accuracy of the FE model. This was done by comparing the results obtained from studying the SSC in a system consisting of a thin film deposited on a glass substrate in Fig. 5.2.

h_1 represents the thickness of the film and h_2 the thickness of the glass substrate. Figure 5.4 shows the relative SSC depth obtained for different film/substrate thickness ratio τ. These values were obtained for eight different bonded materials where α_a and α_r represent the choice of first dundurs' parameter for analytical and FE models. Figure 5.5 shows the effect of the difference in the Elastic mismatch on the relative SSC where τ_a and τ_r represent the choice of the thickness ratio used for analytical and FE models. The results obtained from the FE model in Figs. 5.4 and 5.5 compared well with the results obtained from Suo and Hutchinson analytic model [13].

5.4 Bi-material Beam Finite Element Model

The FE model was used to study SSC in the bottom material of bimaterial beam. h_1 represents the thickness of the Schott B270 glass and h_2 the thickness of the soda-lime glass. Figure 5.6 shows the axial stress contour plot across the bimaterial beam for $h_1 = h_2 = 25.4$mm and the initial crack depth of length 15 mm located at $\lambda = 0.5$., The cooling of the bimaterial beam from the bonding temperature puts the composite beam in bending because they are constrained to be the same length along the interface. The bottom material has lower CTE and contracts lesser than the top material. The contraction of the top material results in compressive stresses on the bottom material at the interface and the bottom material exert tensile stresses on the top material at the interface.

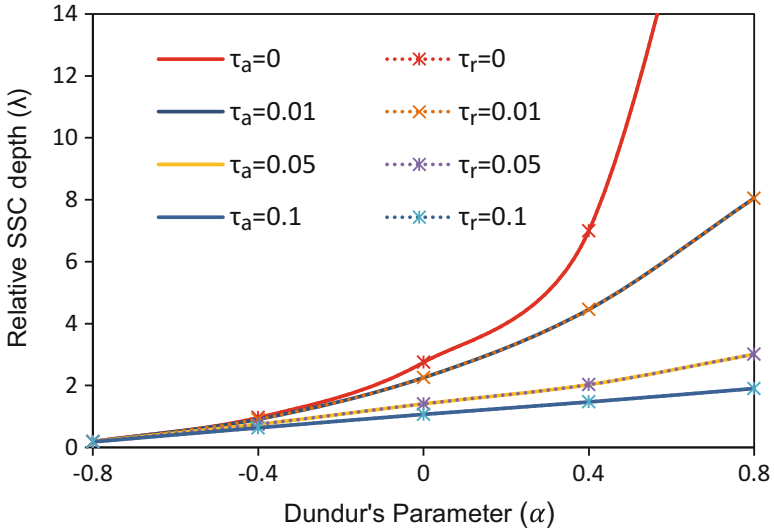

Fig. 5.5 Relative SSC depth as a function of Dundurs' parameter, (α)

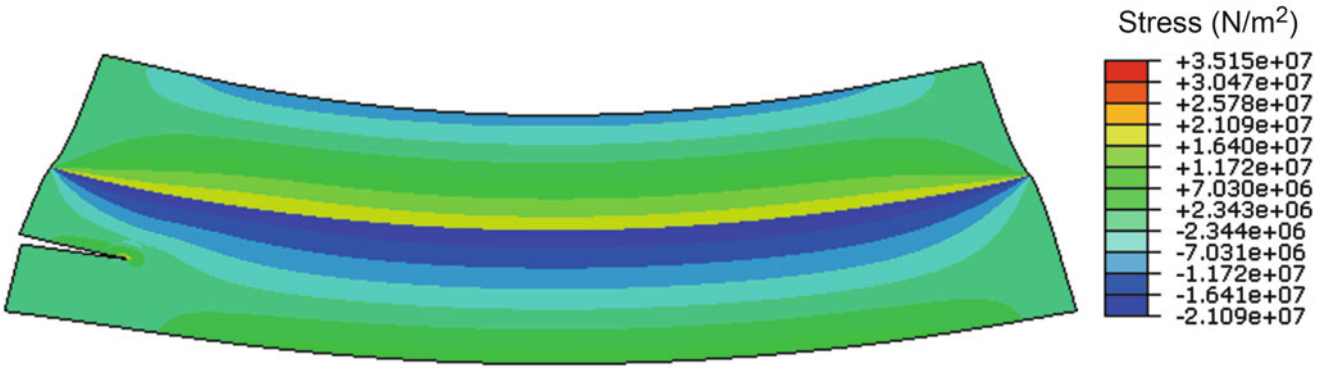

Fig. 5.6 The stress contour plot across the bimaterial beam

The increase in the Top-Bottom material thickness τ for the bimaterial beam leads to decrease in both the relative SSC depth and K_I in Fig. 5.7a. This was because the SIFs were evaluated at the new SSC depths which were farther away from the interface and as we would show later the K_I profile across the bottom material is such that it decreases as crack depth location moves farther away from the interface. Figure 5.7 shows the divergence of the analytical Suo and Hutchinson model from the full FEA solution with increasing top layer thickness. The results obtained from the FE model were compared to the analytical methods which show that the relative SSC depth obtained for the two models were the same for both thin film/substrate and bimaterial beam models but the analytical method underestimates the mode I stress intensity factor K_I for the bimaterial beam. The long crack assumption used in the Suo and Hutchinson model [7] works well for crack propagation in a system with a thin top material because the end affected region is small. This assumption no longer holds for the case where top and bottom thickness are approximately equal.

The effect of the choice of the materials for the bimaterial beam on the SIF was shown in Fig. 5.8. The specimen was designed such that the thickness and length of the bottom material remained as 25.4 and 150 mm, respectively, and the top material dimensions were the same as the bottom material. This represents a case study of $\tau = 1$.

Results show top material with higher stiffness would produce higher K_I and lower K_{II} in the bottom material. There exists a depth such that $K_{II} = 0$. Steady state propagation will happen at this depth. As such, the $K_{II} = 0$ depth and K_I at this depth are the quantities of interest for this problem. Adjusting specimen design to vary K_I at the $K_{II} = 0$ depth gives a level of control for the duration of the experiment.

We further explored the K_I at SSC for different thickness ratios τ. This makes it possible to pick top material thickness and initial crack position as a function of elastic mismatch between the materials. These two quantities can be determined from Fig. 5.9a, b. Given a material of interest for EACG, one needs only pick a top layer material with appropriate CTE value and the values for τ and crack depth to produce the desired K_I.

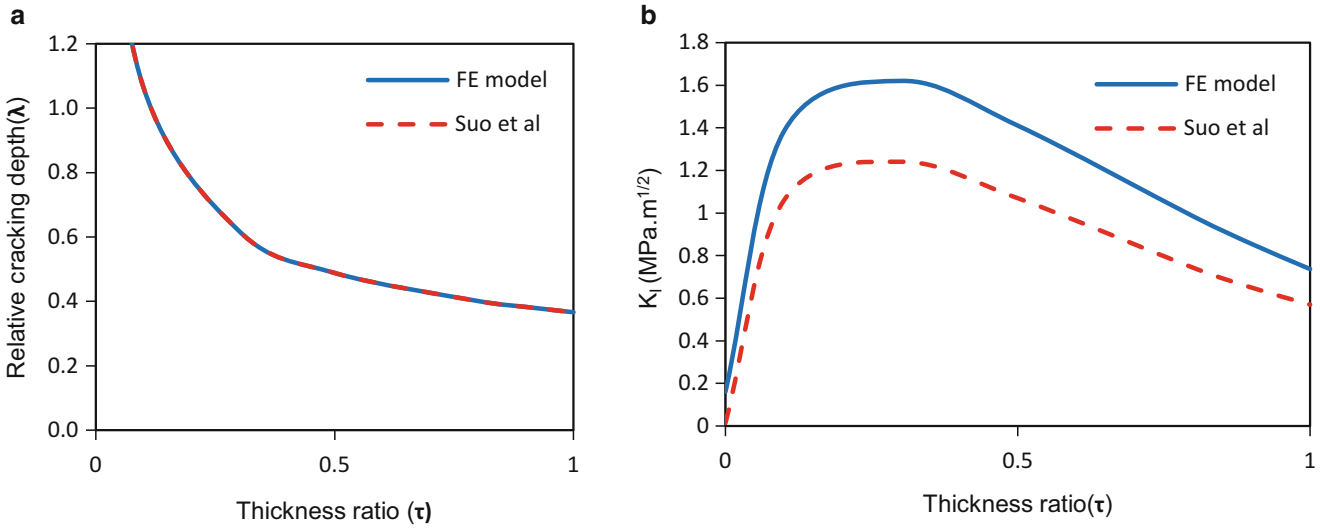

Fig. 5.7 Comparison between the FE model and the analytical model (**a**) Relative cracking depth (**b**) K_I when $K_{II} = 0$

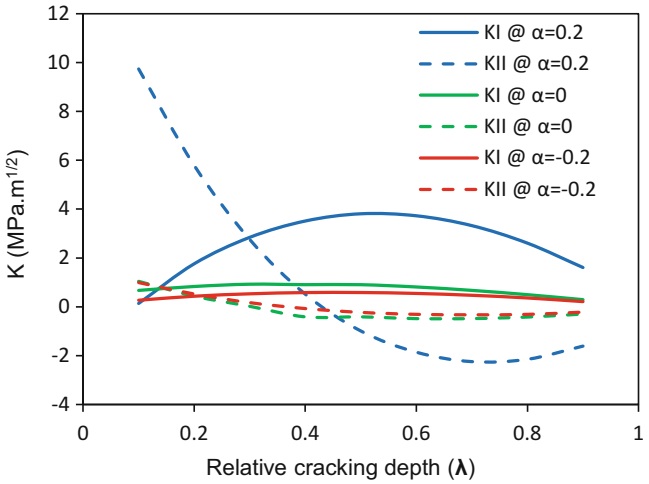

Fig. 5.8 The effect of the material Elastic mismatch on the SIF

5.5 Steady State Cracking in Schott B/Soda-Lime Glass Rectangular Bimaterial Beam

We here study subcritical crack growth in Soda-lime glass for Design 1 in Fig. 5.10. Design 1 is a rectangular bimaterial beam with $\tau = 1$ which has the same specimen design used to generate Fig. 5.8 but used in this section to study the K_I as the crack grows through the entire length of the specimen. In fact, it is a special case of $\alpha = 0$ in the study in Fig. 5.8 because Schott B270 and Soda-lime glass have the same elastic properties. Figure 5.11 shows the SSC in soda lime glass and Fig. 5.11 demonstrates that K_I obtained from this design is constant as the crack propagates through the length of the bimaterial beam. The effect of the initial value of crack length has a negligible effect on the K_I and a constant value of $K_I = 0.57$ MPa.m$^{1/2}$ at SSC depth of 9.3 mm was obtained. This value which represents $0.76K_{IC}$ of Soda-lime glass though lower than the KIC of Soda-lime (0.75 MPa.m$^{1/2}$) but high enough for the study is observed to be constant along the crack path. Hence, the crack will grow at 10^{-3} m/s [14].

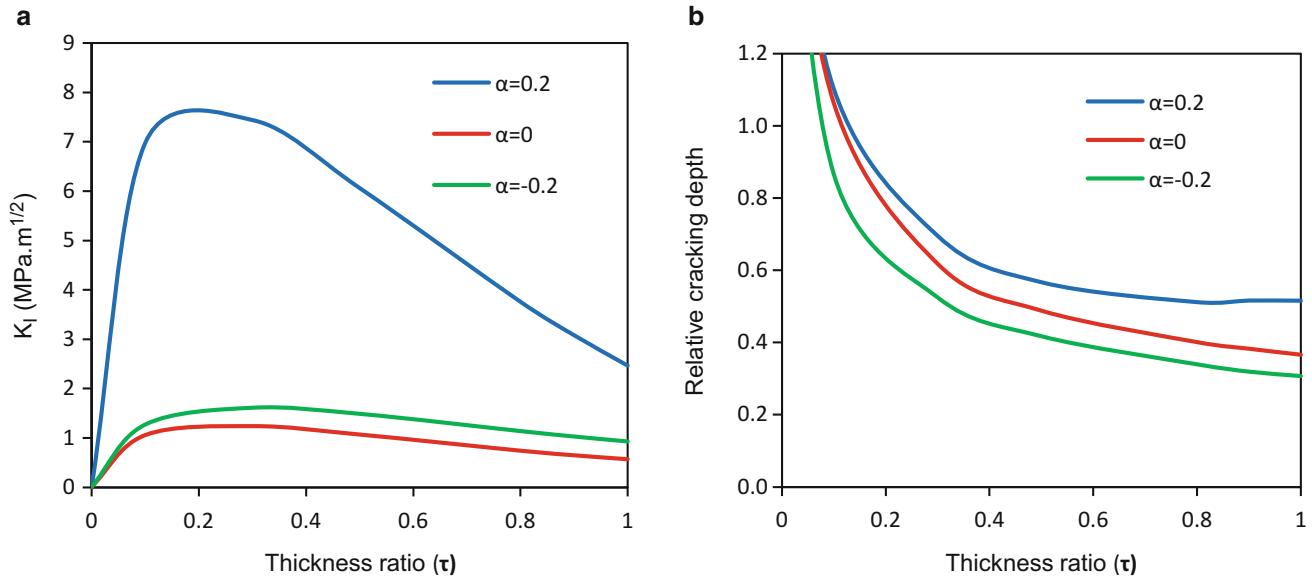

Fig. 5.9 SSC specimen design for EACG (**a**) K_I (**b**) Relative cracking depth

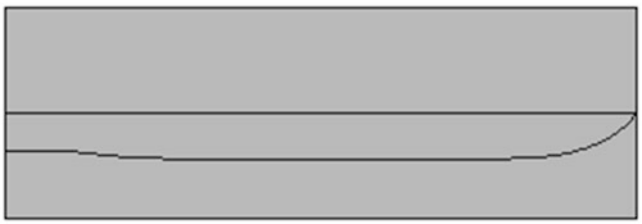

Fig. 5.10 SSC growth in design 1

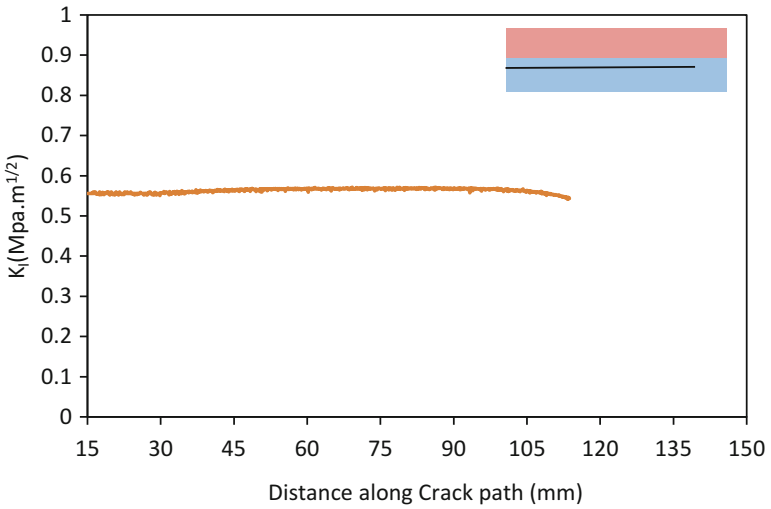

Fig. 5.11 K_I at SSC along crack path in a rectangular bimaterial beam

5.6 Geometry Design for non-constant SIF

The earlier specimen design was modified so that K_I changes with propagation length. Figure 5.12 shows SSC growth across the length of the possible specimen design. Specifically, the dimensions of design 1 was modified to obtain designs 2–5 by reducing either the thickness of the bottom material or both materials thicknesses to half of its original thickness as shown in Fig. 5.12.

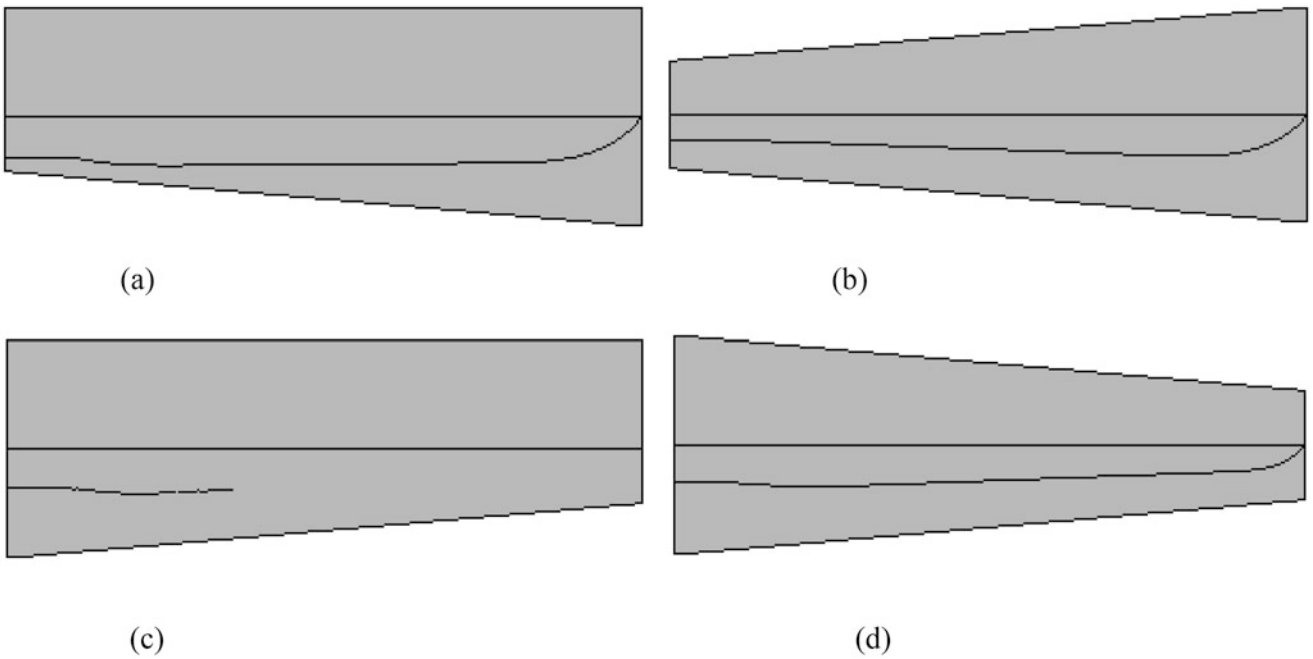

Fig. 5.12 SSC growth in possible specimen designs (**a**) design 2 (**b**) design 3 (**c**) design 3 (**d**) design 4

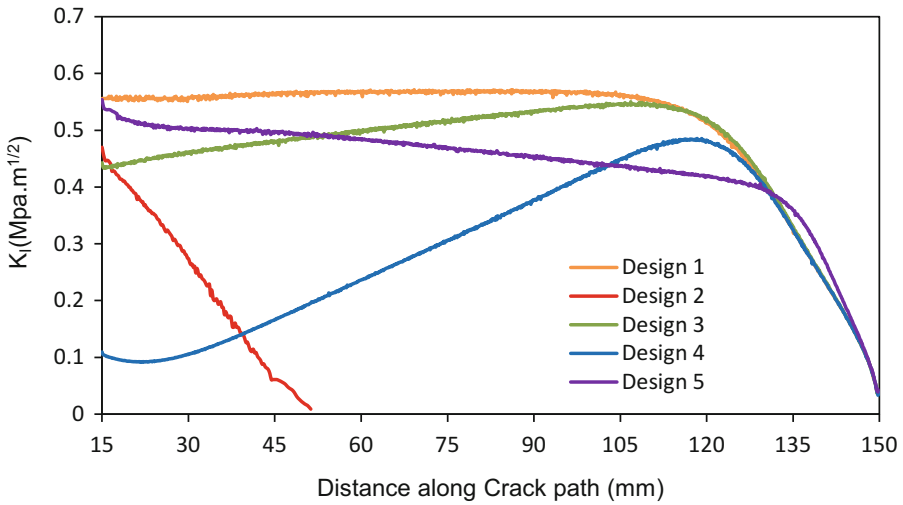

Fig. 5.13 The K_I plots along SSC path for possible specimen designs

Since the vertical edges have traction free surface, the traction free boundary condition affects the stress response in the region close to the edges in Fig. 5.6 thereby affecting the calculation of the K_I and K_{II} and it is responsible for change the direction of the crack growth. The zone of influence of the traction boundary conditions with respect to the stress field in the vicinity of the crack tip are not relevant towards the decision on how to design EACG experiment. SSC modeling assumption are restricted to the region of the specimen which is not influenced by the boundary condition. The K_I values obtained from the crack growth from initial crack length (15 mm) to 120 mm are considered valid for the design of EACG.

Designs 3 and 5 have small difference between the lowest K_I and highest K_I while designs 2 and 4 have greater difference between the lowest K_I and highest K_I. The most suitable specimen design choice for investigating EACG would be design 2 because it has the highest gap of K_I from the initial crack length to the final crack length among all the specimen designs considered.

The data obtained from such a design can then populate a range of crack velocity values rather than a single point in Fig. 5.13. If we design the specimen such that K_I decreases with propagation, it makes it more likely a notch will survive the

bonding process without propagating unstably. In addition, by observing the K_I value at which the crack tip effectively stops propagating we can obtain a threshold K_1, analogous to the threshold stress concept in fatigue failure, below which a crack will not propagate even in the presence of water. Increasing K_1 can be achieved simply by starting a crack at the opposite end of the specimen.

For study involving bimaterial with varied thickness, h_1 represents the maximum edge thickness of the top material and h_2 represents the thickness of the edge with the initial crack. The Relative SSC depths (λ) of 0.37, 0.37, 0.24, 0.37 and 0.34 were recorded for Designs 1, 2, 3, 4 and 5. The reduction of the thickness of the bottom material on either side does not change the location λ rather λ was reduced when the thickness of the top material was reduced and the lowest λ was recorded from design 3.

5.7 Conclusion

We have analyzed and performed a modest design optimization of a brittle fracture specimen for investigating EACG. We developed a FEM model which was validated by an analytical model by studying SSC in a substrate beneath adherent thin films. Results show that the FEM model gave the same results from the analytical model. We showed the analytic model was unable to predict correct K_I values for SSC in the bimaterial beam. We extend the FEM model to study the cracking in bimaterial beam. This was possible because of the robust computational framework of the FEM to model crack propagation in stress-induced specimen irrespective of whether the driving force is tensile or bending. Five specimen designs were considered and the best design for performing the study is the Design 2.

Acknowledgements Sandia National Laboratories is a multimission laboratory managed and operated by National Technology and Engineering Solutions of Sandia LLC, a wholly owned subsidiary of Honeywell International Inc. for the U.S. Department of Energy's National Nuclear Security Administration under contract DE-NA0003525. This project was completed as part of the Nonlinear Mechanics and Dynamics (NOMAD) Institute, co-hosted by Sandia National Laboratories and the University of New Mexico. The authors would like to thank Fracture Analysis Consultants (Ithaca, NY) for complimentary use of the Franc3D software.

References

1. Freeman, S.W.: Effects of chemical environments on slow crack growth in glasses and ceramics. J. Geophys. Res. **89**(B6), 4072–4076 (1984)
2. Frieman, S.W., Widerhorn, S.M.M.J.J.: Environmentally enhanced fracture of glass: a historical perspective. J. Am. Ceram. Soc. **98**(7), 1371–1382 (2009)
3. Wiederhorn, S.M.: Moisture assisted crack growth in ceramics. Int. J. Fract. Mech. **4**(2), 171–177 (1968)
4. Wiederhron, S.M., Bolz, L.H.: Stress corrosion and static fatigue of glass. J. Am. Ceram. Soc. **53**(10), 543–548 (1970)
5. Dill, S.J., Bennison, S.J., Dauskardt, R.H.: Subcritical crack-growth behavior of borosilicate glass under cyclic loads: evidence of a mechanical fatigue effect. J. Am. Ceram. Soc. **80**(3), 773–776 (1997)
6. Freiman, S.W.: Effects of chemical environments on slow crack growth in glasses and ceramics. J. Geophys. Res. Solid Earth. **89**(B6), 4072–4076 (1984)
7. Suo, Z., Hutchinson, J.W.: Steady-state cracking in brittle substrates beneath adherent films. Int. J. Solids Struct. **25**(11), 1337–1353 (1989)
8. Bogy, D.B.: On the problem of edge-bonded elastic quarter-planes loaded at the boundary. Int. J. Solids Struct. **6**(9), 1287–1313 (1970)
9. Hutchinson, J.W., Suo, Z.: Mixed mode cracking in layered materials. Adv. Appl. Mech. **29**, 63–191 (1991)
10. SIMULIA: Abaqus Analyis User's Guide, 6.14 edn. (2014) Dassault Systemes Simulia Corp, Providence
11. Fracture Analysis Consultants, Inc.: FRANC3D Reference Manual, 7th edn. (2016) Fracture Analysis Consultants, Ithaca
12. Wawrzynek, P.A., Carter, B.J., Ingraffea, A.R.: Advances in simulation of arbitrary 3D crack growth using FRANC3D NG. In: ICF12, Ottawa 2009 (2012)
13. Schmauder, S., Meyer, M.: Correlation between Dundurs' parameters and elastic constants. Z. Metallkd. **83**(7), 525 (1992)
14. Freiman, S.W., White, G.S., Fuller, E.R.: Environmentally enhanced crack growth in soda-lime glass. J. Am. Ceram. Soc. **68**(3), 108–112 (1985)

Chapter 6
Flexible Energy Harvesting/Storage Structures for Flapping Wing Air Vehicles

Alex Holness, Hugh A. Bruck, and Satyandra K. Gupta

Abstract Morphing structures are needed for many challenging missions for flapping wing air vehicles (FWAVs), but they will increase electrical power consumption in order to drive actuation systems and will require additional support systems to deliver and control the power. These power demands and associated support systems will comprise the ability of FWAVs to operate for longer periods of time without opportunities for refueling. Harvesting energy, such as solar, and increasing energy storage capacity appears to be an attractive solution to address this challenge. Although research has been conducted on integrating powering existing into aerospace components such as the body, tail and wings, they are typical rigid and can reduce performance because of parasitic mass. We envision compliant multifunctional skins with built-in capabilities for harvesting and storing energy can be used in highly compliant aerospace components, such as morphing wings. These skins will be able to deform and conform to the underlying structure, much like the way skins have evolved to work with components of biological actuation systems such as muscle and bone. They will increase the range of operation by utilizing readily available solar energy to increase electrical power and also increase storage capacity for excess electrical power conversion. Compliant multifunctional structure-energy harvesting-power concepts, once completely developed, may have an enormous impact not only on FWAVs, but on the field of UAVs in general, because of the current energy limitations that exist for these flight platforms. Once energy sources are no longer limited, the field of UAVs, especially Micro Air Vehicles (MAVs), should be able to expand exponentially.

Keywords Multifunctional wing structures • Flexible solar cells • Flexible batteries • Multifunctional performance analysis

6.1 Introduction

Skin materials can provide an interface for an underlying structure to interact with the surrounding environment. In aerospace applications, skins are made out of materials that have the appropriate friction, corrosion, and isolation characteristics that optimize durability and flight performance, while minimizing mass. Skin thicknesses are selected to ensure they provide adequate thermomechanical performance, since they are typically subjected to significant thermomechanical strain due to their location on the structure surface.

Challenging air force missions are requiring electrically-powered systems to operate for longer period of times without opportunities for refueling. Harvesting solar energy and increasing energy storage capacity appears to be an attractive solution to address this challenge. Although research has been conducted into using batteries and solar cells in existing aerospace components such as the body, tail and wingspan, simply attaching solar cells and batteries to these rigid structures does not necessarily improve system performance.

We envision multifunctional skins with built-in capabilities for harvesting and storing energy can cover or replace highly compliant aerospace components, such as morphing wings, while enhancing system performance. The compliant skins will be able to deform and conform to the underlying structure, and will increase the range of operation by utilizing readily available solar energy to increase electrical power and also increase storage capacity for excess electrical powerconversion.

A. Holness • H.A. Bruck (✉)
Department of Mechanical Engineering, University of Maryland, College Park, MD, USA
e-mail: bruck@umd.edu

S.K. Gupta
Department of Mechanical and Aerospace Engineering, University of Southern California, Los Angeles, CA, USA

J. Carroll et al. (eds.), *Fracture, Fatigue, Failure and Damage Evolution, Volume 7*, Conference Proceedings of the Society for Experimental Mechanics Series, DOI 10.1007/978-3-319-62831-8_6

Multifunctional structure-energy harvesting-power concepts, once completely developed, may have an enormous impact on the field of UAVs because of the current energy limitations that exist. Once energy sources are no longer limited, the field of UAVs, especially MAVs, should be able to expand exponentially.

By exploiting recent advances in flexible electronics, including thin film batteries and thin film solar cells, as well as multifunctional structure, it can be possible to develop multifunctional skin materials for aerospace applications. These skins will have the capability to harvest energy and store it. The electronic circuits for performing voltage conversion will be incorporated into the skins. These skins will be capable of delivering the desired structural properties. These multi-functional skins typically need to be 1–4 mm in thickness. The envisioned skins will be useful in a large number of applications for the Air Force, particularly fixed morphing wing air vehicles.

Realizing multifunctional skins is challenging due to the following reasons:

- Many different underlying building blocks (e.g., flexible circuits, thin film batteries, thin film solar cells, and structural materials) need to be integrated together to realize the multifunctional compliant skins. These building blocks need to be compatible with each other and a low-cost fabrication process for integrating them into a single sheet of skin material. We will need to systematically investigate performance and compatibility of the underlying building blocks and determine the feasible combinations. We will also need to identify the right types of interfaces between building blocks for proper functioning of the skin and a feasible fabrication process for realizing them.
- Multifunctional skin materials will be highly heterogeneous in nature. We will need to characterize their performance to figure out their behavior. We will be interested in knowing how these materials will deform under aerodynamic loading. We will also be interested in knowing how the loading will influence energy harvesting and storage efficiency. We will also need to characterize how thermal interactions among components during the operation will affect the performance.

Multifunctional materials will be utilized in complex aerospace structures [1–7]. Spatial variation in material property can be beneficial to match the skin response to the desired behavior. Spatial variation in material properties can be achieved by figuring out the right placement of the building blocks within the skin. We will need to develop computationally-efficient synthesis tools to design skin materials with the right material property variations.

6.2 Multifunctional Materials Research Related to Flexible Wings for FWAVS

6.2.1 Integration of Power Systems into Morphing Wings

Power systems for morphing wings largely consist of electrical sources. For electrical based systems, the primary consideration is the energy density of the storage material, and the replacement of energy by energy harvesting materials, such as piezoelectrics and solar cells. However, energy sources must be able to deliver energy at power levels when needed and at desired levels. Battery materials have been the desired power source for electrical systems. They can be used to drive highly efficient motors (>80% efficiency), to directly morph wing structures, or indirectly through pneumatic/hydraulic systems. However, they are largely considered independent of the morphing wing, and have not been fully integrated into them due to their stiffness. As a result, new flexible electronic concepts using thin film battery and solar cell materials are allowing for the direct integration of materials for energy systems into morphing wing structures. These require new manufacturing approaches, such as the additive manufacturing approach seen in Fig. 6.1.

Recently, solar cells have been added into the highly deformable wings of a flapping wing air vehicle (FWAV) known as “Robo Raven” [8–11] (Fig. 6.1). Robo Raven is a unique FWAV with wings that are independently controlled by programmable servo motors, which allows for dynamic shape control. The deformed wing shape and aerodynamic lift/thrust loads were characterized throughout the flapping cycle using 3D Digital Image Correlation (DIC) and a novel test stand we developed in order to understand the wing mechanics. A multifunctional performance analysis was also developed to understand how integration of solar cells into the wings influences flight performance under two different operating conditions: (1) directly powering wings to increase operation time, and (2) recharging batteries to eliminate need for external charging sources. Experimental data was used in the analysis to identify a performance index for assessing benefits of multifunctional compliant wing structures. The resulting platform, Robo Raven III, was the first demonstration of a robotic bird that flew using energy harvested from solar cells (Fig. 6.2). It was also determined from experiments that residual thrust was correlated to shear deformation of the wing induced by torsional twist, while biaxial strain related to change in aerodynamic shape correlated to lift. Furthermore, it was also found that shear deformation of the solar cells induced changes in power output directly correlating to thrust generation associated with torsional deformation. Thus, it was determinedthat

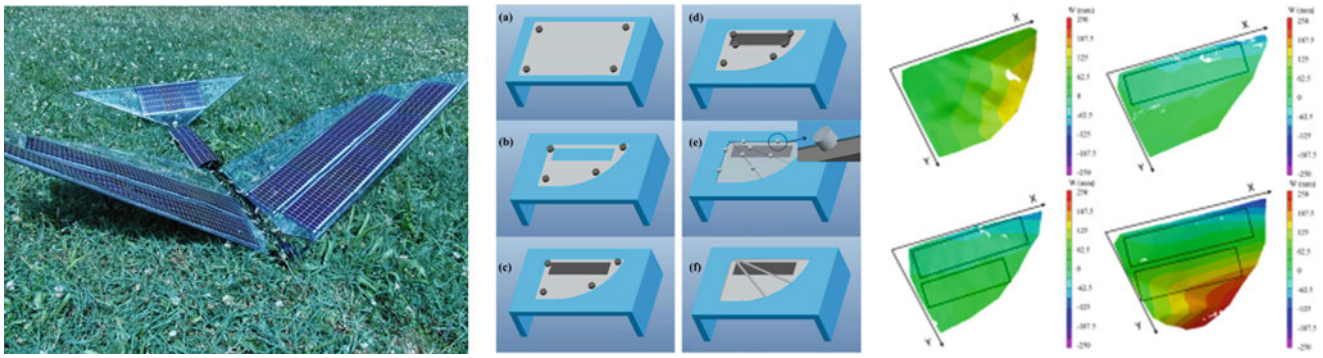

Fig. 6.1 (*left*) Robo Raven III: a flapping wing air vehicle with solar cells integrated in wings using (*middle*) new additive manufacturing process for integrating energy and power systems into morphing wing and (*right*) 3D DIC characterization of deformation changes due to outlined solar cell configurations [9, 10]

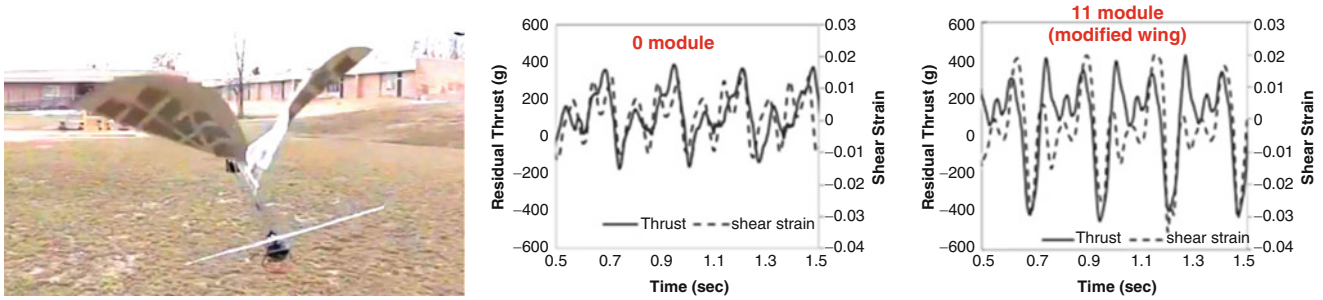

Fig. 6.2 Robo Raven III in flight showing the capability of harvesting solar power for energy while experience large shape deformations that morphing wings can experience (*left*), whose aerodynamic forces and shapes have been characterized and compared for a regular wing design with no solar cell modules (*center*) and a modified design with 11 solar cell modules [9]

morphing wings with energy harvesting elements such as solar cells may be capable of three functions: (1) lightweight and flexible structure to generate aerodynamic forces, (2) energy harvesting to extend operational time and autonomy, and (3) sensing of an aerodynamic force associated with wing deformation.

6.2.2 *System Model for Multifunctional Wings in FWAVs*

During flapping flight, thrust and lift undergo periodic, yet inconsistent, variations. A common modeling approach is to use a quasi-steady state assumption [12, 13]. Quasi-steady state wing theory assumes that the forces on a moving wing are equivalent to the sum of the forces on a fixed wing over a sequence of attitudes that track the wing motion. This model neglects acceleration forces and unsteady aerodynamic effects [14]. In very small intervals of time, the flight is considered level with no acceleration. This implies that the forces in all directions must be equal during steady state flight, assuming no change in mass.

Forces must sum to zero to maintain level, steady and unaccelerated flight along the vertical. Assuming no loss of mass or body forces aside form gravity for steady state flight conditions, the lift force, F_L, must offset the weight, W = mg. as follows [15]:

$$F_L = mg \tag{6.1}$$

The aerodynamic lift is given by:

$$F_L = \frac{1}{2}\rho S V^2 C_L \tag{6.2}$$

Where C_L is the coefficient of lift, ρ is the density of air, S is the planform area, and V is the forward velocity. Substituting Eq. 6.2 into Eq. 6.1 yields:

$$\frac{1}{2}\rho S V^2 C_L = mg \tag{6.3}$$

In the horizontal direction, the thrust force, F_T, must be equal to the drag force, F_D, during steady state flight:

$$F_T = F_D \tag{6.4}$$

where the drag force is defined using the coefficient of drag, $C_{D,P}$:

$$F_D = \frac{1}{2}\rho V^2 S C_{D,p} \tag{6.5}$$

Substituting Eq. 6.5 into Eq. 6.4 yields:

$$F_T = \frac{1}{2}\rho V^2 S C_{D,p} \tag{6.6}$$

A proposed flapping wing model for the thrust is the following:

$$F_{FT} = k_F f^2 S \Delta\alpha \tag{6.7}$$

This is produced with insight gained from [16] which notes that thrust increases with flapping frequency, f, and amplitude of oscillation, Δα. An advance ratio, J, was previously defined for FWAVs as follows [12, 17, 18]:

$$J = \frac{V}{2\Delta\alpha f b} \tag{6.8}$$

where b is the wing span.

Additionally it is noted in [17] that the upper limit of the flapping is based on the mechanical structure of the system, which consists of the actuators involved and the structure of the wings. The lower flapping frequency limit is, in the case for most birds, in slow forward flight or hovering where forward velocity is limited and is dominated on the induced velocity, w, the airflow speed in the wake right beneath the animal. And the weight, W = mg, of the FWAV must be balanced by the lift as follows [17]:

$$mg = F_L = \frac{1}{2}\rho w^2 S C_L \tag{6.9}$$

where the induced velocity, w, is the airflow speed in the wake right beneath the FWAV, as follows:

$$f_{w,min} \sim \omega_{min} = \frac{w}{\iota} \rightarrow w \sim f_{w.min} l \tag{6.10}$$

Where *fw* is the wing beat frequency and l is characteristic length. Therefore:

$$mg = F_L \sim \frac{1}{2}\rho (f_{w,\min} l)^2 C_L \tag{6.11}$$

In light of this, it is proposed that, in the case of forward flight, the forward velocity must be produced by the oscillatory wing motion as follows:

$$f \sim w = \frac{v}{l} \rightarrow V \sim fl \tag{6.12}$$

Recalling the relationship between thrust and drag Eq. 6.6. Thrust governs the offsetting drag force value and dictates the forward velocity as follows:

$$F_T = \frac{1}{2}\rho V^2 S C_{D,p} \tag{6.13}$$

Replacing the velocity term, V, with the product of frequency and characteristic length, l, yields:

$$F_{FT} = \frac{1}{2}\rho (fl)^2 S C_{D,p} \rightarrow \frac{1}{2} p f^2 l^2 S\, C_{D,p} \tag{6.14}$$

The characteristic length, l, squared is represented by the product of a new characteristic length for the span of the wing and the amplitude, as follows [16]:

$$l^2 \sim l_1 \Delta\, \alpha \tag{6.15}$$

Replacing $l2$ in Eq. 6.15 yields:

$$F_{FT} = \frac{1}{2}\rho f^2\, (l_1 \Delta\alpha)\, S D_{D,p} \tag{6.16}$$

Gathering constants (including l_1) and considering aeroelastic interactions, especially stiffness effects determined from prior work [18, 19], a new coefficient, k_F, can be defined such that Eq. 6.16 becomes:

$$F_{FT} = k_F f^2 S \Delta\alpha \tag{6.17}$$

Since it is possible to relate thrust to lift using the velocity, Eq. 6.6 can be rearranged, and solving for V 2 yields:

$$V^2 = \frac{2F_t}{\rho S C_{D,p}} \tag{6.18}$$

Substituting Eq. 6.18 into Eq. 6.2 yields:

$$F_L = \frac{C_L}{C_{D,p}} F_T \tag{6.19}$$

Because the average thrust is generated using the flapping wings Substituting the thrust generated bμ flapping Eq. 6.7 in Eq. 6.19 results in:

$$F_L = \frac{C_L}{C_{D,p}} k_f f^2 S \Delta\alpha \tag{6.20}$$

Substituting this lift into Eq. 6.3 yields the maximum flight weight for a FWAV, as follows:

$$\frac{C_L}{C_{D,p}} k_f f^2 S \Delta\alpha = mg \tag{6.21}$$

Thrust governs the offsetting drag force value by dictating the velocity in the relationship given in Eq. 6.6 (if all else remains constant). An increase in velocity benefits lift generation by way of aerodynamic lift, as seen in Eq. 6.2. Given this, thrust and lift are directly related via their drag coefficients, as seen in Eq. 6.19. These relationships provide insight into ways to increase performance by increasing thrust production in a FWAV.

6.2.3 Multifunctional System Analysis for Design Optimization

As mentioned previously, there are tradeoffs in the performance of morphing wing structures using multifunctional materials. Reducing compliance can increase actuation force required to morph wings, while decreasing compliance can increase the actuation force needed to resist aerodynamic forces [9]. As a result, new multifunctional system analysis approaches for modeling performance tradeoffs are needed in order to optimize the design of morphing wings with multifunctional materials. These analyses can be used to determine compliance distributions in morphing wings and layered architectures for multifunctional materials integrated with the wings that will minimize mass and minimize power consumption for a given distribution of aerodynamic loads and displacements over a wing. The ultimate performance metric will be the flight time, which is critical to morphing wing application such as autonomous UAVs. For example, the following flight time analysis, *T'*, developed for integration of flexible solar cells and batteries into FWAV multifunctional wing structures:

$$T' = k_b \left(C_L k_F f^2 S \Delta\alpha / C_{D,pg} - M_m - M_s\right) / \left(P - k_s M_s\right) \tag{6.22}$$

where:

k_b = flexible battery coefficient (energy capacity of batt./mass of batt.)
k_s = flexible solar cell Coefficient (power generated/mass of cells)
F_l = aerodynamic lift
M_m = Mass of MAV
$M_{s.}$ = Mass of Solar Cells
P = Average Power consumption of MAV

6.3 Experimental Results for Multifunctional Wings

6.3.1 Effects of Integrating Power Elements into Wings on System Model Predictions

Experiments were conducted to validate the system performance model to determine the effects of integrating the flexible solar cells and batteries on the aerodynamic forces, as well as the flapping frequency for the FWAV. Since the effects are similar for aerodynamic lift and thrust forces, only the thrust forces were analyzed using a test stand that we had previously developed [20]. Furthermore, only results for the solar cell wings were analyzed, although we previously reported results for wings with flexible, ultrathin galvanic cell batteries [21]. Servos were run to generate a flapping amplitude of 95 degrees. At low frequency (2 Hz or less), the servos are able to follow the demanded signal. This is true for both the multifunctional wings and the regular wing design. As the flapping frequency is increased beyond 2 Hz, the servos are unable to achieve the commanded flapping amplitude and decreases as seen in Figs. 6.3a and 6.4a. These findings are consistent with those presented in [18], and were overcome by developing a mixed mode flight platform known as "Robo Raven V", which uses propeller assistance to generate more thrust and recover lift [22]. Beyond 2 Hz the achievable peak to peak amplitude for the heavier, multifunctional wings drops considerably compared to the lighter regular wings. This difference can be seen more clearly in the comparisons plot, Fig. 6.5a. When the wings are demanded to reach half of the demanded amplitude the amplitude remains largely constant in both cases as seen in Figs. 6.3c and 6.4c.

When the angle is uncorrected, assuming $\Delta\alpha$ in Eq. 6.7 is a constant value until 2 Hz, the thrust should be the data series in each of the thrust plots (Figs. 6.3b, d and 6.4b, d) labeled *Model-Constant Amplitude*, which assumes that the wings continually deform in a similar manner at high frequencies as they do at low frequencies. When the amplitude correction is applied, using the data shown in each of the corresponding amplitude plots for each frequency, the series labeled *Model-Amplitude Corrected* is generated which directly mirrors the proposed model given in Eq. 6.7. Finally, the series labeled *Measured* is simply the measured data. When the full amplitude is demanded, the model with a constant value of $\Delta\alpha$ has a high prediction of performance after the amplitude declines beyond 2 Hz in boththe case of flexible wings and high mass

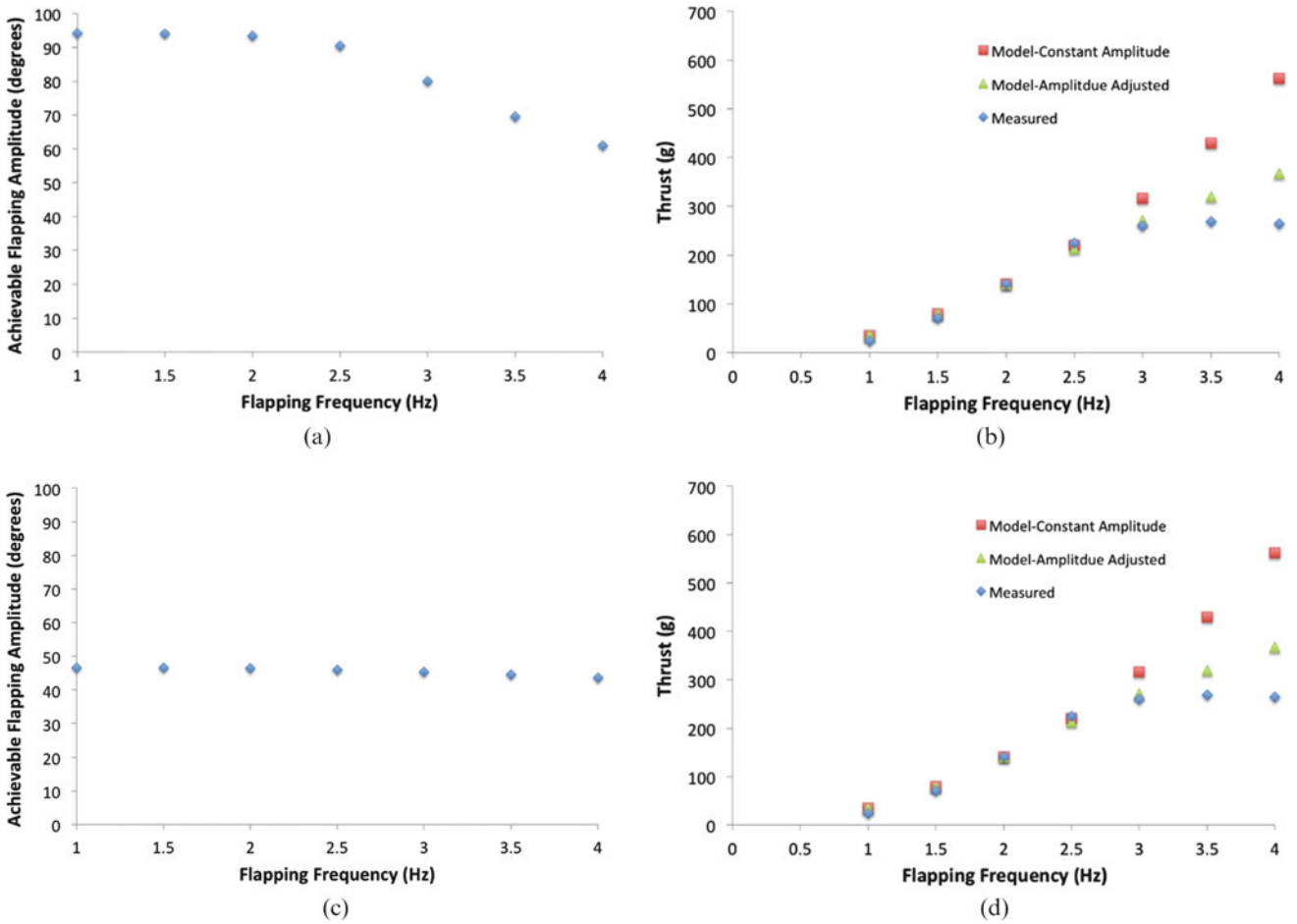

Fig. 6.3 Testing results for regular wings. (**a**) Achievable amplitude with full amplitude commanded. (**b**) Modeled and measured thrust at full commanded amplitude. (**c**) Achievable amplitude with half amplitude commanded. (**d**) Modeled and measured thrust at half commanded amplitude

multifunctional wings. When the amplitude correction is applied the agreement is greater until 3 Hz in both the case of the flexible wing and the multifunctional wing when full flapping amplitude is demanded. After 3 Hz there is a departure between the model and the measured values as there appears to be saturation of the thrust values. The departure starts a bit sooner for the multifunctional wings. When the commanded amplitude is half of the full range, the servos are able to largely follow the commanded signal and the results collapse on top of each other, however, the measured results actually outperform the models slightly as seen in Figs. 6.3d and 6.4d. What is notable is that the thrust generated by the stiffer wings is higher than the thrust generated at 2 Hz as seen in Fig. 6.5. This changes at all frequencies above this as it seems that the amplitude effects and stiffness saturate the thrust produced.

6.3.2 Predicted Effects from Integrating Flexible Solar Cells and Batteries into Wings for FWAVs

Using the experimental results, it was then possible to predict the effects on flight time from integrating the solar cells and batteries into the wings. To perform this analysis, the payload capacity of the platform with solar cells and batteries were predicted from the test stand aerodynamic lift and thrust measurements. The resulting payload capacity was assumed to be used to carry conventional LiPo batteries in order to predict the flight time. The results are shown in Table 6.1. It is interesting to note that integrating the flexible ultrathin galvanic cell batteries and flexible solar cells produce similar increases in flight time of approximately 3.4×, but that the combination can produce a potential increase of17.4×.

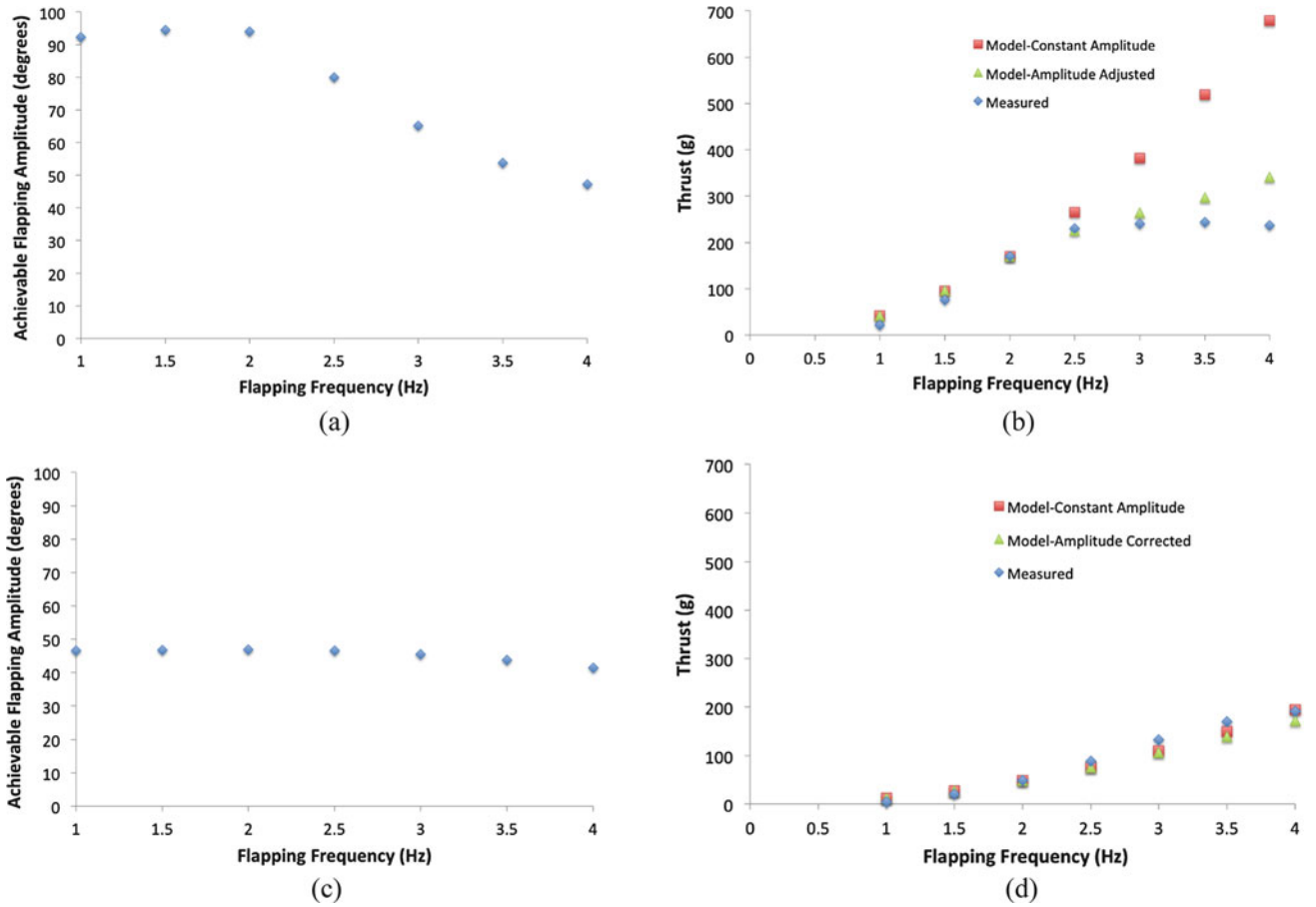

Fig. 6.4 Testing results for solar cell wings. (**a**) Achievable amplitude with full amplitude commanded. (**b**) Modeled and measured thrust at full commanded amplitude. (**c**) Achievable amplitude with half amplitude commanded. (**d**) Modeled and measured thrust at half commanded amplitude

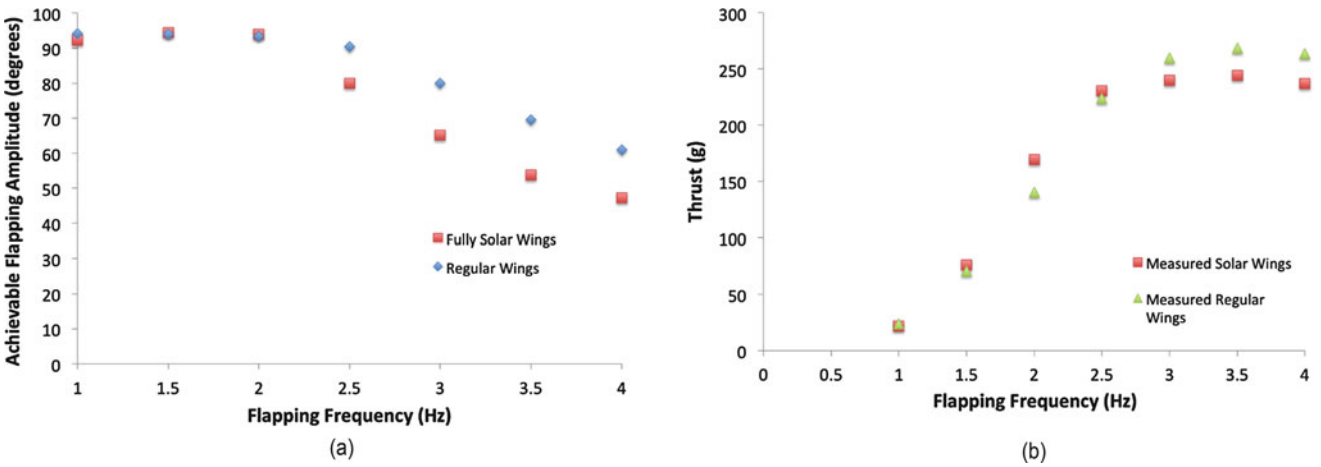

Fig. 6.5 Amplitude and thrust of regular wings compared to solar cell wings. (**a**) Achievable amplitude with full amplitude commanded. (**b**) Modeled and measured thrust at full commanded amplitude

Table 6.1 Comparison of the effects on predicted payload capacity and subsequent predicted flight time from using multifunctional wings with integrated solar cells and batteries for a FWAV

Wing type	Predicted payload capacity (g)	Predicted flight time (s)
Regular	74.5	860
Flexible battery	79.5	3800
Flexible HE solar cell	50.6	3810
Flexible HE solar cell + battery	50.6	15,800

6.4 Conclusions

In summary, the fundamental power and energy research issues for using multifunctional materials in morphing wings for applications such as FWAVs require new configurations and subsequent analyses that can address the following:

- How does adding the mass of the power system to wings affect the flight time for aerospace systems using morphing wings
- How does replacing current power sources with power sources in the wings increase lift and decrease power consumption to increase flight time
- For skins designed to cover existing morphing wing structures, can models developed for integrated energy and power systems be extended by characterizing the change in lift and thrust when the wings are covered by the skins due to change in wing morphology, change in optimal angle of attack, and subsequent changes in trailing edge performance of deformable structures such as ailerons

A system model was developed to predict the effect on lift and thrust forces from changes in flapping amplitude due to torque limitations of the servos. The results from the system model were then used in a previously developed multifunctional model for predicting flight time of a FWAV. Subsequent measurements of thrust forces generated by regular and solar cell wings were used to validate the system model. Using current and previous experimental results, the multifunctional model could predict the payload capacity due to the integration of solar cells and batteries into the wings of FWAV, as well as the subsequent flight time that would be expected if the payload capacity were used to carry conventional LiPo batteries. An increase in flight time of 3.4× is anticipated from integrating flexible batteries or solar cells, while the combination could produce an increase of 17.4×.

While the primary emphasis for flexible energy harvesting/storage structures has been on enhancing the endurance of FWAV, it is possible that the principles that have been developed can be extended to other applications that can benefit from self-powered materials. For example, inflatable structures could be easily deployed to harvest/store solar energy in remote environments. Because of the mechanical and electrical constraints of the flexible power components, a hierarchically-structured material would need to be designed that accommodates the functional constraints while possessing the geometric complexity required for accordion-style folding and unwinding with interfaces that can maintain functionality under large deformations. Figure 6.6 shows how such an envisioned structure can be used to create energy harvesting balloons. If the weather gets adverse, these can be easily retracted.

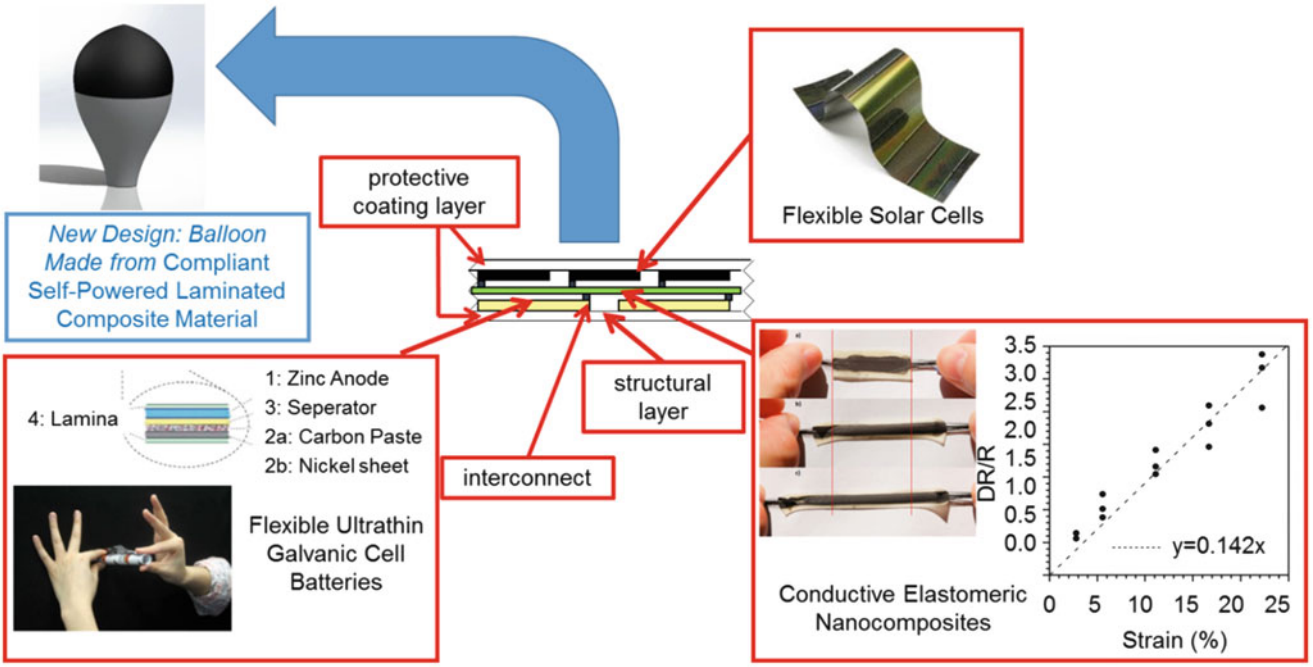

Fig. 6.6 An example of a solar balloon concept based on self-powered materials

Acknowledgements This work was sponsored by AFOSR grant FA9550-15-1-0350 with Dr. Byung-Lip "Les" Lee program manager. Opinions expressed are those of the authors and do not necessarily reflect opinions of the sponsors.

References

1. Yang, L.J., Hsu, C.K., Ho, J.Y., Feng, C.K.: Flapping wings with PVDF sensors to modify the aerodynamic forces of a micro aerial vehicle. Sensors Actuators A Phys. **139**(1), 95–103 (2007)
2. Hsu, C.K., Ho, J.Y., Feng, G.H., Shih, H.M., Yang, L.J.: A flapping MAV with PVDF-Parylene composite skin. In: Proceedings of the Asia-Pacific Conference of Transducers and Micro-Nano Technology, Singapore (2006)
3. Nemat-Nasser, S., Plaistead, T., Starr, A., Amirkhizi, A.: Multifunctional materials. In: Bar-Cohen, Y. (ed.) Biomimetics: Biologically Inspired Technologies. CRC Press, Boca Raton (2005)
4. Thomas, J.P., Qidwai, M.A.: The design and application of multifunctional structure-battery materials systems. JOM. **57**(3), 18–24 (2005)
5. Ma, K.Y., Chirarattananon, P., Fuller, S.B., Wood, R.J.: Controlled flight of a biologically inspired, insect-scale robot. Science. **340**(6132), 603–607 (2013)
6. Thomas, J.P., et al.: Multifunctional structure-plus-power concepts. In: AIAA, 43rd AIAA/ASME/ASCE/AHS/ASC Structures, Structural Dynamics, and Materials Conference, Denver, Colorado (2005)
7. Wissman, J., Perez-Rosado, A., Edgerton, A., Levi, B.M., Karakas, Z.N., Kujawski, M., Phillips, A., Papavizas, N., Fallon, D., Bruck, H.A., Smela, E.: New compliant strain gauges for self-sensing dynamic deformation of flapping wings on miniature air vehicles. Smart Mater. Struct. **22**(8), 085031 (2013)
8. Perez-Rosado, A., Griesinger, A.J., Bruck, H.A., Gupta, S.K.: Performance characterization of multifunctional wings with integrated solar cells for unmanned air vehicles. In: ASME International Design Engineering Technical Conferences and Computers and Information in Engineering Conference, Volume 5A: 38th Mechanisms and Robotics Conference (2015). doi:10.1115/DETC2014-34719
9. Perez-Rosado, A., Gelhar, R.D., Nolen, S., Gupta, S.K., Bruck, H.A.: Design, fabrication, and characterization of multifunctional wings to harvest solar energy in flapping wing air vehicles. Smart Mater. Struct. **24**, 065042 (2015)
10. Perez-Rosado, A., Bruck, H.A., Gupta, S.K.: Integrating solar cells into flapping wing air vehicles for enhanced flight endurance. ASME. J. Mech. Robot. **8**(5), 051006 (2016). doi:10.1115/1.4032411
11. Gerdes, J., Holness, A., Perez-Rosado, A., Roberts, L., Greisinger, A., Barnett, E., Kempny, J., Lingam, D., Yeh, C.-H., Bruck, H.A., Gupta, S.K.: Robo Raven: a flapping-wing air vehicle with highly compliant and independently controlled wings. Soft Robot. **1**(4), 275–288 (2014)
12. Shyy, W., Aono, H., Kwon Kang, C., Liu, H.: An introduction to flagging wing aerodynamics. Cambridge University Press, Cambridge Books Online, Cambridge (2013)
13. Madangopal, R., Khan, Z.A., Agrawal, S.K.: Biologically inspired design of small flapping wing air vehicles using four-bar mechanisms and quasi-steady aerodynamics. J. Mech. Des. **127**(4), 809–816 (2004)
14. Muijres, F., Johansson, L., Barfield, R., Wolf, M., Spedding, G., Hedenström, A.: Leading-edge vortex improves lift in slow-flying bats. Science. **319**(5867), 1250–1253 (2008)

15. Anderson, J.D.: Introduction to Flight, 7th edn. McGraw Hill, New York (2012)
16. Platzer, M.F., Jones, K.D., Young, J., Lai, J.S.: Flapping wing aerodynamics: progress and challenges. AIAA J. **46**(9), 2136–2149 (2008)
17. Shyy, W., Berg, M., Ljungqvist, D.: Flapping and flexible wings for biological and micro air vehicles. Prog. Aerosp. Sci. **35**(5), 455–505 (1999)
18. Ho, S., Nassef, H., Pornsinsirirak, N., Tai, Y.-C., Ho, C.-M.: Unsteady aerodynamics and flow control for flapping wing flyers. Prog. Aerosp. Sci. **39**(8), 635–681 (2003)
19. Zhao, L., Huang, Q., Deng, X., Sane, S.P.: Aerodynamic effects of flexibility in flapping wings. J. R. Soc. Interface. (2009). doi:10.1098/rsif.2009.0200
20. Gerdes, J.W., Cellon, K.C., Bruck, H.A., Gupta, S.K.: Characterization of the mechanics of compliant wing designs for flapping-wing miniature air vehicles. Exp. Mech. **53**(9), 1561–1571 (2013)
21. Holness, A., Steins, E., Bruck, H.A., Peckerar, M., Gupta, S.K.: Performance characterization of multifunctional wings with integrated flexible batteries for flapping wing unmanned aerial vehicles. In: ASME 2016 International Design Engineering Technical and Computers and Information in Engineering Conference, Charlotte, pp. 1–10. (2016). doi: 10.1115/DETC2016-60379
22. Holness, A., Bruck, H., Gupta, S. K.: Design of propeller-assisted flapping wing arid vehicles for en- hanced aerodynamic performance. In: ASME IDETC/CIE, 39th ASME Mechanism and Robotics Conference, ASME, Boston, pp. 1–10, (2015). doi:10.1115/DETC2015-47577

Chapter 7
The Influence of Formulation Variation and Thermal Boundary Conditions on the Near-Resonant Thermomechanics of Mock Explosives

Allison R. Range, Nicole R. McMindes, Jaylon B. Tucker, and Jeffrey F. Rhoads

Abstract The thermomechanics of energetic and inert particulate composite materials are of pronounced interest in the defense community. This work seeks to further characterize the macroscale, thermal and mechanical response of these materials under various near-resonant mechanical excitations. The fabrication of mock energetic samples based on the PBXN-109 formulation, comprised of hydroxyl-terminated polybutadiene (HTPB) binder with 85% solids loading and varying additive content (0%, 15%, and 30%) of sucrose and/or spherical aluminum crystals, enabled a systematic investigation into the effect of formulation variation on the thermal and mechanical response. Experiments were also performed on insulated plate samples of identical composition to examine the effect of varying thermal boundary conditions. In each of these experiments, the samples were mechanically excited using an electrodynamic shaker, while their thermal and mechanical responses were recorded using an infrared camera and scanning laser Doppler vibrometer, respectively. The investigation of these responses aids in the effort to characterize and understand the behavior of polymer-bonded explosives under mechanical excitation.

Keywords Energetic materials • Explosives • Thermomechanics • Vibration • Viscoelastic materials

7.1 Introduction

Energetic and inert particulate composite materials are of pronounced interest in the defense community due to their prevalent use in improvised explosive devices and munitions systems, which must be properly detected or handled to ensure public safety and national security. These materials present unique challenges in regards to their thermomechanical behavior. For example, the combination of solid particles with elastic binder results in phenomenon such as hot spot formation and particle de-bonding at the crystal-binder interface [1]. It has also been observed that these polymer-bonded materials exhibit stiffening as their age increases [2], an effect not accounted for in classic behavioral models. The materials also exhibit dramatically varying bulk thermal and mechanical moduli with particle/binder ratio and can rapidly decompose, both thermally and mechanically, under comparatively weak external loads [3–6].

Although mechanically-induced heat generation is a well-studied effect for pure materials and alternative composites, there exists an appreciable literature gap related to the influence of mechanical vibrations on particulate composite materials such as polymer-bonded explosives. The works of Loginov [7, 8] provide useful insight into the phenomenological nature of the vibration-induced heating of energetic materials. Initial investigations by this investigator and collaborators sought

A.R. Range • N.R. McMindes
Ray W. Herrick Laboratories, Purdue University, 47907, West Lafayette, IN, USA

School of Mechanical Engineering, Purdue University, 47907, West Lafayette, IN, USA

J.B. Tucker
School of Mechanical Engineering, Purdue University, 47907, West Lafayette, IN, USA

J.F. Rhoads (✉)
Ray W. Herrick Laboratories, Purdue University, 47907, West Lafayette, IN, USA

School of Mechanical Engineering, Purdue University, 47907, West Lafayette, IN, USA

Birck Nanotechnology Center, Purdue University, 47907, West Lafayette, IN, USA
e-mail: jfrhoads@purdue.edu

J. Carroll et al. (eds.), *Fracture, Fatigue, Failure and Damage Evolution, Volume 7*, Conference Proceedings of the Society for Experimental Mechanics Series, DOI 10.1007/978-3-319-62831-8_7

to characterize the initiation of explosives under vibration, citing important features such as inelastic deformation and non-uniform temperature distributions. Their later experiments focused on the structural and physicochemical changes in RDX crystals under vibrational excitation, concluding that vibration accelerates the formation of crystal defects, thus allowing the progression of inelastic deformation, fracture, and dispersion. Although they capture the essential phenomena of decomposition at a coarse level, these works neglected investigation of the role of various material or structural properties, such as material formulation. The influence of thermal boundary conditions on heat generation has also not been significantly investigated in prior work.

The objectives of this work are to observe and characterize the thermal and mechanical behavior of mock energetic particulate composite plates comprised of hydroxyl-terminated polybutadiene (HTPB) binder, sucrose particles ($C_{12}H_{22}O_{11}$), and spherical aluminum powder under inertial excitation at comparatively low frequencies (10–1000 Hz). This work serves as an extension to prior experiments conducted on beam and plate samples comprised of ammonium chloride (NH_4Cl) and HTPB [9, 10] by highlighting the effects associated with thermal boundary conditions and formulation variations. The plates, serving as mechanical mocks for polymer-bonded explosives, were mounted directly to an electrodynamic shaker in an effort to isolate the thermal and mechanical responses. Heat generation within the sample was measured through infrared thermography at the respective resonant frequency of each plate under convective and insulated boundary conditions. This investigation of the effects of thermal boundary condition and formulation variation on the thermomechanical behavior of the particulate composite plates will increase the knowledge base associated with polymer-bonded explosives.

7.2 Experimental Techniques

7.2.1 Sample Preparation

The samples of mock explosive material were prepared using an HTPB binder, sucrose particles, and spherical aluminum powder. The sucrose particles, sieved to a diameter range of 106–355 μm, are comparable in size to particles of RDX, a common energetic material. The spherical aluminum powder has an average particle diameter of 25 μm. In real world applications, the weight ratio of particles to binder can vary drastically, motivating the investigation of various formulations.

To fabricate the test samples, the HTPB binder was combined with a curing agent, isophorone diisocyanate (IPDI), and other constituents. The binder was then mixed in a Resodyn™ acoustic mixer for 5 min to ensure a homogeneous mixture. This was then degassed in a vacuum chamber to remove unwanted gasses from the liquid mixture and prevent bubbles from forming in the final sample. The solid constituents were then added to the binder mixture and the Resodyn™ was again used to mix the constituents for 5 min. For samples with low particle-to-binder weight ratios, the sample was again degassed, after which the particle and binder mixture was poured into a custom plate mold. The plates were cured in an oven for a period of 7 days at 60°C. The final dimensions of each plate were 25.4 cm by 17.8 cm by 1.27 cm.

The formulation variations are based upon the PBXN-109 formulation given by Lochert et al. [11], substituting sucrose particles as RDX to render the plate inert. A summary of this base formulation is given in Table 7.1.

Table 7.1 PBXN-109 mock formulation

Constituent	Weight percent
RDX/Sucrose	64.00
Aluminum	20.00
R45-HT (Hydroxyl-terminated Polybutadiene Resin)	7.346
Dioctyl Adipate (DOA)	7.346
Antioxidant 2246	0.100
Dantocol DHE	0.260
Triphenylbismuth	0.020
Isophorone Diisocyanate (IPDI)	0.950

Table 7.2 Plate sample characteristics

Solids loading-additive content-sample	Mass (kg)	Density (kg/m^3)
85-00-1	0.7025	1225
85-00-2	0.6400	1275
85-15-1	0.8148	1421
85-15-2	0.8027	1400
85-30-1	1.0392	1611
85-30-2	0.9200	1604

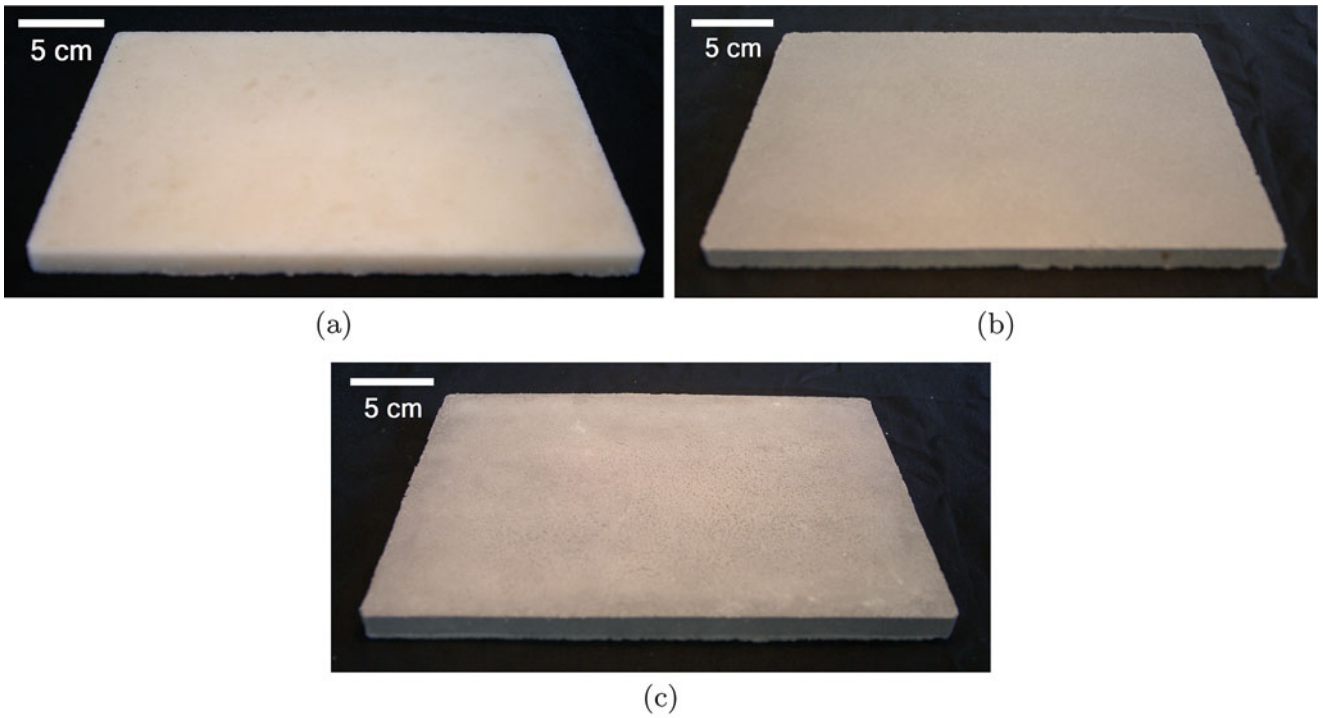

Fig. 7.1 Representative plate samples of 85% solids loading with (**a**) 0% (**b**) 15% and (**c**) 30% additive content

Plates were prepared with 85% solids loading. Three variations were made with 0%, 15%, and 30% weight ratios of aluminum additive content. Solids loading provides the weight ratio of solid crystals to polymer binder in the overall formulation. Additive content provides the weight ratio of spherical aluminum powder to mock RDX crystals (sucrose) in the solids. The mass and density of each plate is presented in Table 7.2.

Each plate was tested under convective conditions 43 days after curing to avoid inconsistencies due to aging effects of the polymer composite in the observed mechanical responses. The data presented in the following sections applies to the plates pictured in Fig. 7.1a–c.

7.2.2 Experimental Setup

Experiments were performed according to the methodology detailed in Miller et al. [9]. A TIRA 59335/LS AIT-440 electrodynamic shaker was used to mechanically excite the plates at low excitation levels. The parallel short ends of the plate were clamped to the shaker using a plate fixture to simulate clamped-free-clamped-free (CFCF) mechanical boundary conditions with an unsupported sample area of 22.9 cm by 17.8 cm. An accelerometer mounted to the shaker head provided direct feedback to the VibeLab VL-144 vibration controller. The thermal response was recorded using a FLIR A325 thermal camera with a temperature sensitivity of 0.07°C at 30°C and an accuracy of ± 2°C or ± 2%. A Polytec PSV-400 scanning laser Doppler vibrometer was used to record the frequency response of each plate.

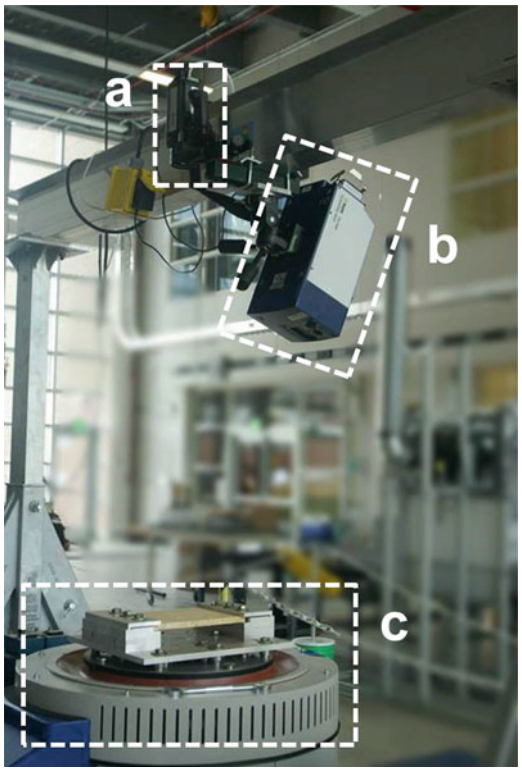

Fig. 7.2 The experimental setup with a (*a*) FLIR A325 infrared camera and (*b*) Polytec PSV-400 scanning laser Doppler vibrometer positioned above a plate mounted to the (*c*) TIRA shaker by the CFCF clamping mount

Frequency responses were obtained in response to broadband (10–1000 Hz) white noise applied at three forcing levels, 1.0, 1.9, and 2.4 g RMS. H1 estimators were used to estimate the system frequency response by comparing the cross spectral density between the accelerometer and the differentiated vibrometer reading to the measured power spectral density of the accelerometer. All of the H1 frequency response estimators were calculated at both the geometric center of the plate and at an offset point. The offset point represented half of the distance from the free and clamped edges to the center of the plate, measured as 4.4 and 5.7 cm, respectively.

A forcing level of 2 g was used to obtain the thermal response at the top surface of the plates under two different boundary conditions; the first of which is characterized by convection with the open air on the four largest surfaces and conduction with the aluminum clamping fixture on the remaining small ends, which is referred to herein as the 'convective' condition. Each plate was excited at the first resonance for a 60 min time period, during which the frequency was held constant. The aforementioned FLIR camera recorded the transient and steady-state thermal responses at the surface of the samples. Note that the emissivity of each sample was calibrated by determining the reflected apparent temperature of a perfect emitter and then calibrating the sample temperature to that of a known emissivity. The ambient temperature was also recorded during the test and then subtracted from the experimental temperature data in order to account for variations caused by the surrounding environment. The experimental set up is presented in Fig. 7.2.

The effect of an insulated boundary condition was also investigated with a forcing level of 2 g at the first resonant frequency for a 60 min time period. In contrast to above, the second thermal boundary condition, referred to as 'insulated', included an insulated boundary offset by approximately 2.5 cm from all sides of the plates. A thermally-insulated box (Fig. 7.3) was constructed to roughly simulate the insulated environment. The structural integrity of the box was maintained by acrylic panes with a 3.8 cm clearance relative to the top surface of the plate, and additional thermal insulation was provided by 1.9 cm thick foam insulation with a K-factor of 0.25 at 24°C attached on all sides. The box attached to the outside of the clamping fixture of the plate and moved with the shaker head during the course of experimentation.

Due to the non-transparent nature of the insulated box, the transient temperature profile as a function of time was not able to be obtained with the infrared thermal camera as described above. As a result, the thermal camera was used to collect a snapshot of data at the beginning and end of the 60 min time interval. The temperature increase of the plate was determined as the difference between the two recorded temperature values.

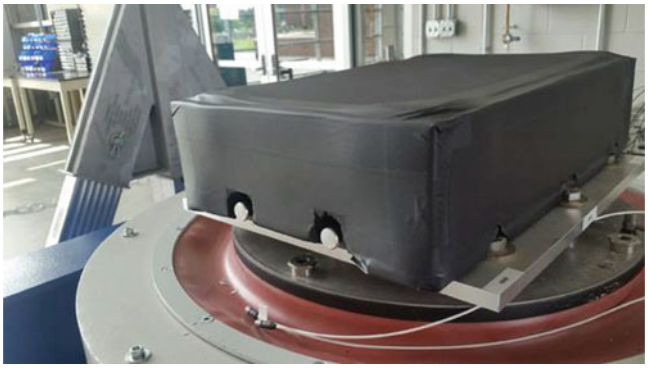

Fig. 7.3 The acrylic box with foam insulation used to simulate insulated boundary condition for the plates

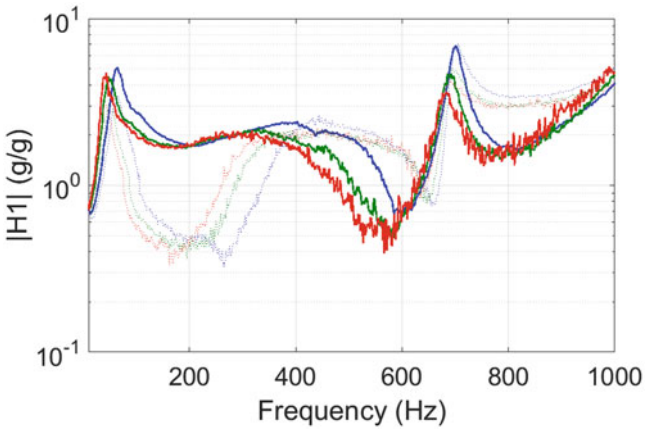

Fig. 7.4 Experimental H1 mechanical frequency response estimator of a 85% solids loading – 0% additive plate at three levels of excitation. The *red*, *green*, and *blue curves* depict responses at 2.44, 1.86, and 1 g RMS, respectively. *Solid lines* represent data from the geometric center, and *dashed lines* represent data from the offset point. Data is presented for the first 85–0% plate

7.3 Results and Discussion

7.3.1 Experimental Results

7.3.1.1 Mechanical Response

The H1 frequency response estimators for representative plates of 85% solids loading with 0, 15 and 30% additive content in response to three levels of excitation are presented as Figs. 7.4, 7.5, and 7.6. Frequency response estimators for the additional plates of identical formulation ratios are not presented here for the sake of brevity but appear qualitatively similar to those presented. All of the plates exhibit clear resonant behavior at multiple frequencies within the excited range of 10–1000 Hz. Softening behavior is also exhibited in all of the formulation variations, as evident by the decrease in both frequency and amplitude with increased forcing levels. In regards to sample variation, the amplitude and general trend of each H1 frequency response appears similar for each of the three additive content levels. It should be noted that signal return from the laser Doppler vibrometer improved with the addition of aluminum due to its increased reflectivity.

The experimentally-obtained peak frequencies and estimated quality factors for each plate (measured from the highest excitation level utilized in the random vibration tests) are presented in Table 7.3. The H1 magnitude at the first resonant frequency for plates with identical formulation ratios appear to coincide, suggesting that the sample fabrication was consistent across various mixing days. The quality factors indicate a distinct modal response in each of the plates, which is verified by the qualitative sharpness of the first resonant peaks in the frequency response functions.

Interestingly, each of the frequency response estimators presented above exhibit a significant peak in amplitude at approximately 700 Hz that was not expected based upon previous experiments. In an attempt to characterize the high

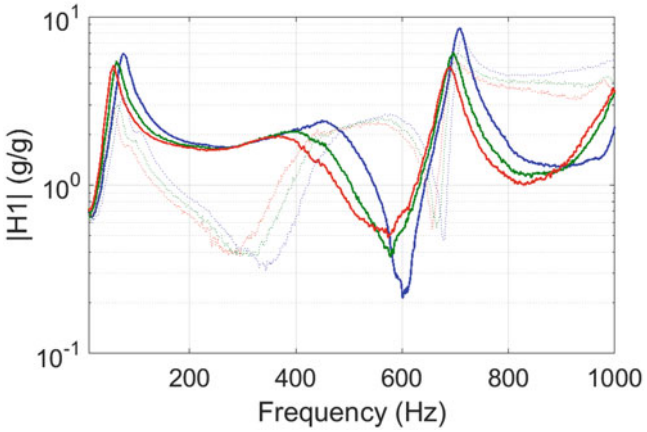

Fig. 7.5 Experimental H1 mechanical frequency response estimator of a 85% solids loading – 15% additive plate at three levels of excitation. The *red*, *green* and *blue curves* depict responses at 2.44, 1.86, and 1 g RMS, respectively. *Solids lines* represent data from the geometric center, and *dashed lines* represent data from the offset point. Data is presented for the first 85–15% plate

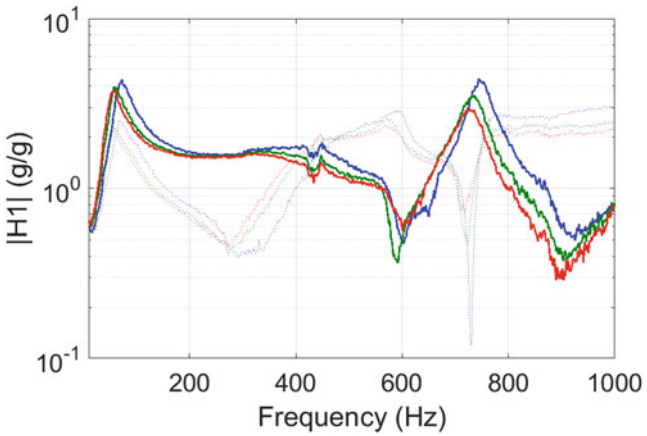

Fig. 7.6 Experimental H1 mechanical frequency response estimator of a 85% solids loading – 30% additive plate at three levels of excitation. The *red*, *green*, and *blue curves* depict responses at 2.44, 1.86, and 1 g RMS, respectively. *Solid lines* represent data from the geometric center, and *dashed lines* represent data from the offset point. Data is presented for the first 85–30% plate

Table 7.3 First resonant frequencies and associated quality factors for all of the plates

Solids loading-additive content-sample	f_{11} (Hz)	Q_{11}
85-00-1	39.2	2.33
85-00-2	37.5	2.50
85-15-1	55.2	2.56
85-15-2	56.1	2.37
85-30-1	51.6	1.67
85-30-2	52.1	1.77

frequency resonance, the operational deflection shape was recorded in response to a 6 g mechanical excitation for plates of 85% solids loading with 0% and 30% additive content using the laser Doppler vibrometer. Deflection behavior in each case can be approximated as a 3-1 plate mode, identified by 3 distinct peaks in the longitudinal direction with 1 row of peaks in the transverse direction.

7.3.1.2 Thermal Response

The spatial average and maximum surface temperature of each plate over the 60 min window at the first resonant frequency under convective boundary conditions are presented in Fig. 7.7a, b, respectively. The data appears to asymptotically approach

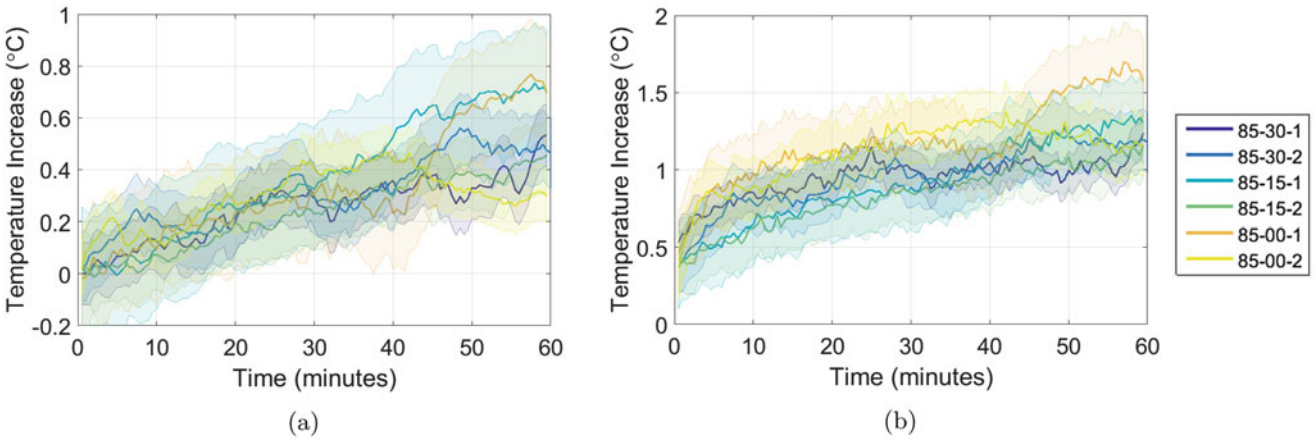

Fig. 7.7 A comparison of the experimentally-obtained plate surface temperature versus time in response to a 2 g harmonic excitation near the first resonant frequency for all of the plates. *Solid lines* indicate experimental data. The colored envelope indicates one standard deviation for each trial. Data are presented for the (**a**) mean and (**b**) maximum plate surface temperatures versus time. The legend indicates: solids loading – additive content – sample number

Table 7.4 A comparison of mean and maximum temperature increase under convective and insulated thermal boundary conditions for the minimum and maximum additive content samples

Solids loading-additive content-sample	Mean surface temperature (°C)		Maximum surface temperature (°C)	
	Convective	Insulated	Convective	Insulated
85-00-01	0.52	1.26	0.90	1.51
85-30-01	0.81	1.60	0.97	1.77

steady state within the duration of the data measurement as desired. Each plate exhibits a similar upward trend, but little distinction can be drawn between the various levels of additive content. Note that the negative lower bound of average temperature increase at the start of the experiment can be attributed to minor discrepancies between the spatial average temperature of the plate and the ambient temperature recorded on a reference material in close proximity to the experiment. Mean and maximum plate surface temperature increases by approximately 0.5°C and 1.2°C, respectively. The magnitude of temperature increase does correlate well with trends exhibited by plates of high solids loading content in prior work [9].

Application of the insulated boundary condition to the various plates yielded increased heat generation as expected. The comparison between convective and insulated temperature increases for a single plate of minimum and maximum additive content is given in Table 7.4. As previously noted, due to the non-transparent nature of the insulated box, it was not possible to obtain the transient temperature profile. The values presented are determined as the temperature difference between the initial and final profiles recorded using the infrared camera. Note that the temperature increases presented for the 85-00 plate sample are modeled in the following section. However, inconsistencies were present between the experimental results and simple bulk-scale heat transfer models, which are attributable to either experimental error within the thermal measurements or, more likely, the particulate composite nature of the material itself.

7.3.2 Thermal Simulation

In order to model the experimental temperature responses outlined above, a thermal simulation was performed with a commercial finite element package using convective and insulated conditions. The theory and assumptions used to model the simulation are outlined in Miller et al. [9] in which the heat source is given by

$$r_{avg} = \frac{\omega}{2\pi} \int_{t_0}^{t_0 + \frac{2\pi}{\omega}} \sigma \frac{\partial \epsilon}{\partial \tau} d\tau = \pi_0 (\eta \omega) \tag{7.1}$$

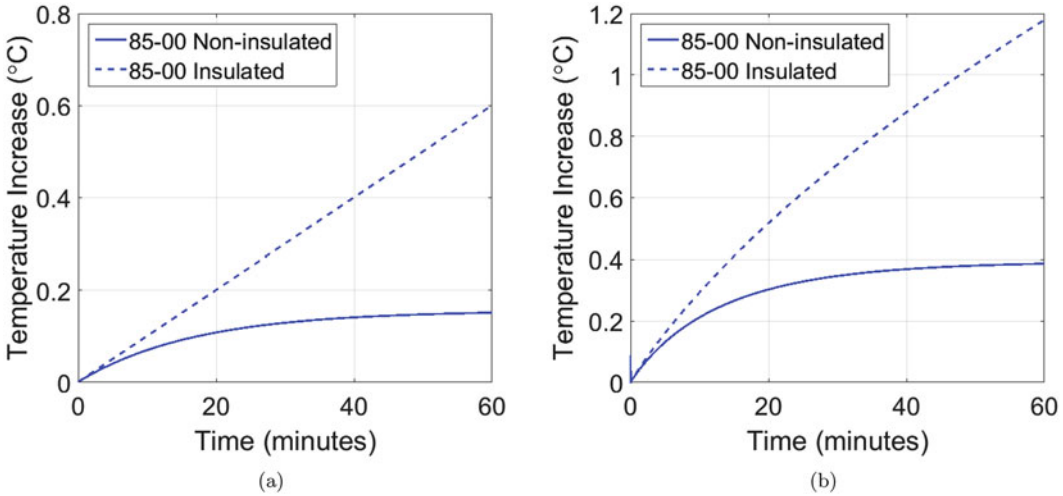

Fig. 7.8 Numerically simulated plate surface temperatures versus time in response to a 2 g excitation near the first resonant frequency for a representative plate of 85% solids loading with 0% additive content. *Solid lines* indicate insulated boundary conditions on all surfaces. *Dotted lines* indicate convective boundary conditions. Data are presented for the (**a**) mean and (**b**) maximum plate surface temperatures versus time

where η is the loss factor, ω is the frequency of excitation, and π_0 is the strain energy density given by

$$\pi_0 = \frac{E' \epsilon_0^2}{2\,(1-\nu^2)} \tag{7.2}$$

where E' is the real part of the dynamic modulus of the plate, ν is Poisson's ratio, and ϵ_0 is the strain magnitude. The dynamic modulus was obtained using a system identification approach developed by Paripovic [2]. Specifically, the technique uses acceleration data from uniaxial compression tests to estimate stiffness and damping coefficients that are then used to identify dynamic mechanical properties. Transient thermal properties for each representative plate were determined using the transient plane source technique [12]. The dynamic modulus (E'), thermal conductivity (k), and thermal diffusivity (α) were measured as 3.02 MPa, 0.35 W/(m-K), and 2.84×10^{-7} m^2/s, respectively, for a representative plate of 85% solids loading with 0% additive content. The density of 1250 kg/m^3 was taken as the average of the two 85-00 plate sample densities given in Table 7.2, and the structural loss factor was estimated as the inverse of the experimental quality factors for the two 85-00 plate samples given in Table 7.3.

Thermal behavior for a representative plate of the minimum additive content formulation was simulated in response to the heat source in Eq. (7.1). Convective simulations assumed insulated clamped ends with convective boundary conditions on all other surfaces. Insulated boundary condition simulations assumed all of the surfaces to be perfectly insulated. The transient average and maximum simulated temperature response for a representative plate of 85% solids loading with 0% additive content over the 60 min time period is presented in Fig. 7.8a, b. Note that the assumption of perfectly insulated plate boundaries provides an upper bound of temperature increase for the experimental results presented above. As expected, the insulated surface assumption results in significantly greater temperature rise than the convective condition.

Interestingly, the thermal simulation under-predicts the temperature increase in both mean and maximum surface temperature for the simulated 85-00 plate, as evident by the comparison of the first row of Table 7.4 with the final magnitude of the curves in Fig. 7.8a, b. This suggests the potential presence of particle-scale interactions that are not accounted for in the derivation of the model, such as friction between particles or de-bonding at the particle-binder interface [1, 13].

7.4 Conclusions

The thermal and mechanical responses of particulate composite, mock energetic plates, comprised of varying ratios of HTPB binder, sucrose particles, and spherical aluminum powder, under contact excitation have been presented. Clear resonant behavior was observed in each of the three formulation variations, differing solely based on the amounts of additive content.

The reported transient surface temperature patterns appear to approach steady state over the 60 min window of harmonic excitation, resulting in temperature increases on the order of 0.5–1°C, as expected from prior work with high solids loading composite materials [9]. The comparison of temperature profiles of different aluminum additive content plates yielded variations on the order of 0.5°C, suggesting that increased additive content does not result in drastically increased heat generation at a forcing level of 2 g. However, the effect may be more evident as the forcing level is increased.

The insulated boundary condition resulted in a temperature increase approximately 0.7°C higher than the corresponding convective experiment in all of the plate formulations, as expected. However, the observed trends appear to be inconsistent with simple bulk-scale heat transfer models. Future efforts will investigate whether this is due to experimental error (i.e., measuring small temperature changes via an infrared camera), or, as is more likely, directly attributable to the particulate composite nature of the material.

Thermal simulation of the heat generation within a sample of 85% solids loading with 0% additive content resulted in temperature increases significantly lower than experimentally-observed values. This also may be attributable to particle-particle interactions at the micro-scale, such as friction and de-bonding between the particle and the binder, which are not accounted for in the current heat generation model.

Future work will seek to further characterize the particulate composite material with specific attention focused on particle-scale interactions, increased excitation levels, and the impact of structural defects.

Acknowledgements This research is supported by the Air Force Research Laboratory through Grant No. FA8651-16-D-0287 entitled "Hysteretic Heating of Polymer Crystal Composites through Mechanical Vibration". The authors wish to acknowledge Jelena Paripovic and Professor Patricia Davies for their assistance with mechanical property measurements, and Jason Gabl and Professor Timothée Pourpoint for their assistance with thermal property measurements.

References

1. Roberts, Z.A., Mares, J.O., Miller, J.K., Gunduz, I.E., Son, S.F., Rhoads, J.F.: Phase changes in embedded HMX in response to periodic mechancial excitation. Chall. Mech. Time Depend. Mater. **2**, 79–86 (2017)
2. Paripovic, J., Davies, P.: A model identification technique to characterize the low frequency behaviour of surrogate explosive materials. J. Phys. Conf. Ser. **744**(1), 012124 (2016)
3. Arefinia, R., Shojaei, A.: On the viscosity of composite suspensions of aluminum and ammonium perchlorate particles dispersed in hydroxyl terminated polybutadiene—new empirical model. J. Colloid Interface Sci. **299**(2), 962–971 (2006)
4. Fu, S.Y., Feng, X.Q., Lauke, B., Mai, Y.W.: Effects of particle size, particle/matrix interface adhesion and particle loading on mechanical properties of particulate–polymer composites. Compos. Part B: Eng. **39**(6), 933–961 (2008)
5. Wakashima, K., Tsukamoto, H.: Mean-field micromechanics model and its application to the analysis of thermomechanical behaviour of composite materials. Mater. Sci. Eng. A **146**(1), 291–316 (1991)
6. Lewis, T.B., Nielsen, L.E.: Dynamic mechanical properties of particulate-filled composites. J. Appl. Polym. Sci. **14**(6), 1449–1471 (1970)
7. Loginov, N.P., Muratov, S.M., Nazarov, N.K.: Initiation of explosion and kinetics of explosive decomposition under vibration. Combust. Explos. Shock Waves **12**(3), 367–370 (1976)
8. Loginov, N.P.: Structural and physicochemical changes in RDX under vibration. Combus. Explos. Shock Waves **33**(5), 598–604 (1997)
9. Miller, J.K., Woods, D.C., Rhoads, J.F.: Thermal and mechanical response of particulate composite plates under inertial excitation. J. Appl. Phys. **116**(24), 244904 (2014)
10. Woods, D.C., Miller, J.K., Rhoads, J.F.: On the thermomechanical response of HTPB-based composite beams under near-resonant excitation. J. Vib. Acoust. **137**(5), 054502 (2015)
11. Lochert, I.J., Dexter, R.M., Hamshere, B.L.: Evaluation of Australian RDX in PBXN-109. Technical report, Australian Government DSTO (2002)
12. Flueckiger, S., Zheng, Y., Pourpoint, T.: Transient plane source method for thermal property measurements of metal hydrides. In: The ASME 2008 Heat Transfer Summer Conference, Jacksonville, vol. 1, pp. 9–13 (2008)
13. Field, J.E., Bourne, N.K., Palmer, S.J.P., Walley, S.M., Sharma, J., Beard, B.C.: Hot-spot ignition mechanisms for explosives and propellants. Philos. Trans. R. Soc. Lond. A: Math. Phys. Eng. Sci. **339**(1654), 269–283 (1992)

Chapter 8
Detecting Fatigue Crack Closure and Crack Growth Delays After an Overload Using DIC Measurements

G.L.G. Gonzáles, J.A.O. González, J.T.P. Castro, and J.L.F. Freire

Abstract The closure and crack growth behaviors of a fatigue cracked DC(T) 4340 steel specimen before and after a single 100% overload on the stress intensity factor (SIF) peak, applied over an otherwise mode I loading with quasi-constant SIF range and load ratio, was studied using Digital Image Correlation (DIC) and strain gage techniques. A significant retardation in the post-overload fatigue crack growth rate was observed, and it recovered its pre-overload value only after the crack grew a distance much larger than the Irwin plastic zone induced by the overload. This behavior is attributed to discontinuous closure, since high values of crack opening loads were observed even outside the overload plastic zone. Full-field displacements and strains determined ahead of the crack tip and crack flank opening displacements measured at points along the crack faces from DIC analysis, as well as redundant back-face strain-gage measurements, support this claim.

Keywords Digital image correlation • Crack propagation • Overload • Crack closure • Discontinuous closure

8.1 Introduction

Elber [1, 2] in his pioneer works observed that a fatigue crack subjected only to tensile load cycles can remain partially closed until a certain load level is reached at which the crack fully opens at the opening load P_{op}. This behavior can be observed in load versus strain measurements from a strain gage bounded at the back face of a cracked body, see Fig. 8.1.

According to Elber, plasticity-induced crack closure is promoted by the tensile residual plastic wake left behind the fatigue crack tip by the monotonic plastic zone that always follows it [3]. Moreover, Elber assumed that due to crack closure, the part of the cyclic load below P_{op} does not contribute to crack growth, because only if $P > P_{op}$ the crack tip would be stressed. Thus, the fatigue crack growth (FCG) rate would not be controlled by the full range $\Delta K = K_{max} - K_{min}$ of the applied stress intensity factor (SIF), but instead by $\Delta K_{eff} = K_{max} - K_{op}$, the effective SIF range during which the crack is fully opened, where K_{op} is the SIF caused by P_{op}. This idea became popular because it could explain load order effects in FCG, such as significant delays and even arrests in FCG rates observed after overloads (OL). In fact, it seems reasonable to assume that P_{op} should increase, and thus ΔK_{eff} should decrease, as the crack grows through the hypertrophied plastic zone pz_{OL} created by the OL. Furthermore, it is expected that the OL-induced delay effects should gradually decrease as the crack tip crosses pz_{OL}.

This idealized behavior has been confirmed by many works, see e.g. [4–8]. However, some authors related OL-induced delay effects at distances much larger than pz_{OL} [9–12]. Such behavior has been associated to discontinuous closure, first identified by Fleck [13]. In it the crack surface is open near the tip, but remains closed near the OL location during a large part of the loading cycle. The present paper reports a similar behavior observed in fatigue tests of a 4340 steel Disk Shaped Compact DC(T) specimen with thickness 4.4 mm, after an OL applied over otherwise quasi-constant ΔK and R loading conditions. Delayed FCG rates were observed even after the crack has grown outside pz_{OL}. The presence of discontinuous closure was detected by DIC analyses made using the VIC-3D software [14], which has been related to the over-stretched material ahead the crack tip location where the overload was applied.

G.L.G. Gonzáles (✉) • J.A.O. González • J.T.P. Castro • J.L.F. Freire
Pontifical Catholic University of Rio de Janeiro, PUC-Rio, Rua Marquês de São Vicente 225, Gávea, Rio de Janeiro, RJ, Brazil
e-mail: gonzalesglg@aaa.puc-rio.br

J. Carroll et al. (eds.), *Fracture, Fatigue, Failure and Damage Evolution, Volume 7*, Conference Proceedings of the Society for Experimental Mechanics Series, DOI 10.1007/978-3-319-62831-8_8

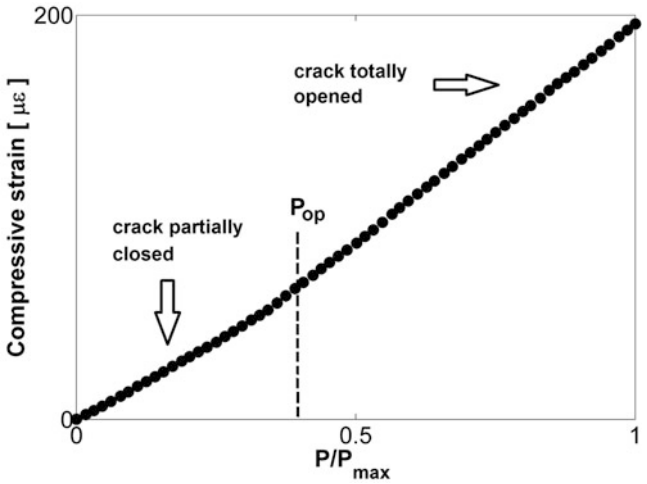

Fig. 8.1 Load versus strain curve used to determine the crack opening load P_{op} from strain gage readings made at the back face of a cracked fatigue specimen (P_{op} is measured at the beginning of the linear stretch this graph)

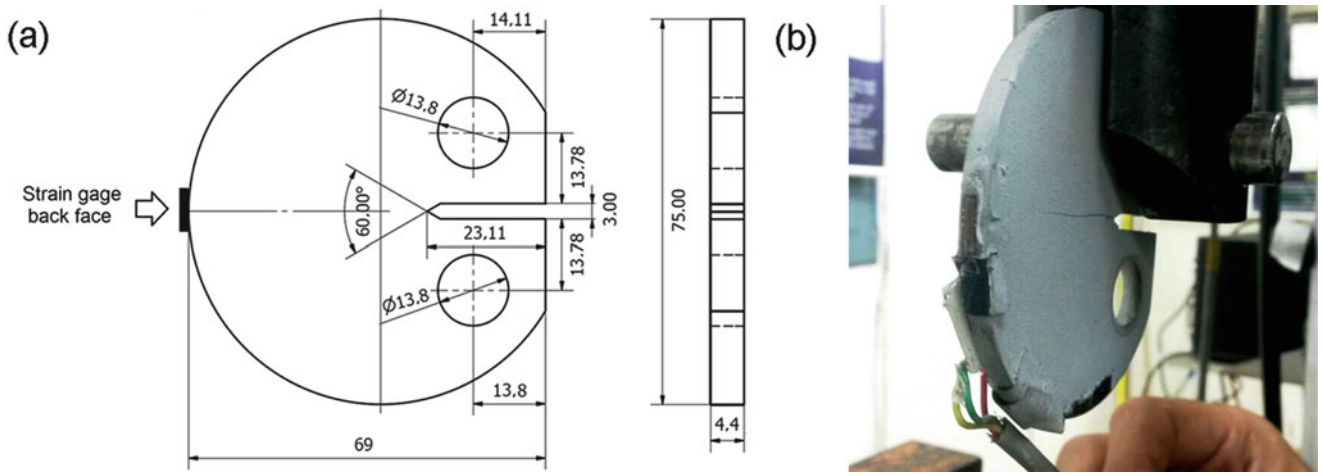

Fig. 8.2 (**a**) DC(T) specimen geometry (dimensions in mm). (**b**) Specimen used for investigation

8.2 Experimental Details

Fatigue tests were conducted following ASTM E647 procedures, using a DC(T) specimen of AISI 4340 steel with 200 HV and $S_Y = 440$ MPa, where SY is the yield strength of the material, see Fig. 8.2a. Figure 8.2b shows the strain-gage bonded at the back face of the specimen. DIC measurements were performed in one of the DC(T) surfaces, which was previously white painted and then sprayed with small black dots, see Fig. 8.2b. A traveling microscope was placed in front of the other (polished) surface of the specimen, to measure the crack length. The fatigue crack was grown under quasi-constant $\Delta K_I = 32$ MPa$\sqrt{\text{m}}$ and 0.1 loading conditions, in an Instron 8501 servo-hydraulic testing machine, under (sinusoidal) load control at 10 Hz. The nominal SIF values were calculated using the standard ASTM E999 equation:

$$K_I = \frac{P}{t\sqrt{w}} \cdot \frac{(2 + a/w)}{(1 - a/w)^{1.5}} \cdot \left[0.76 + 4.64 \cdot a/w - 11.58 \cdot (a/w)^2 + 11.43 \cdot (a/w)^3 - 4.08 \cdot (a/w)^4\right] \tag{8.1}$$

where w and t are the specimen width and thickness, a is the crack length (measured from the load line), and P is the load.

The DIC system uses two high resolution 2248 × 2048 pixels CCD cameras, high-quality Tamron SP AF180mm F/3.5 lenses, a fiber optic light source, calibration grids, and the software VIC-3D from Correlated Solutions Inc. [13]. The cameras were placed in front the specimen in a stereo configuration using a tripod, resulting in a spatial image resolution of

approximately 7 μm/pixel. For image acquisition, the loading velocity was reduced to 0.05 kN/sec. The DIC analysis was conducted using a normalized-sum-of-squared-differences correlation algorithm with optimized 8-tap interpolation, subset size of 35 pixels, step size of 7 pixels, and strain window size of 15.

8.3 Results and Discussion

Figure 8.3 illustrates the FCG behavior before and after a single 100% tensile overload on K_{max}. The crack was first propagated for about 6 mm until achieving a quasi-constant FCG rate of approximately $8{\cdot}10^{-5}$ mm/cycle, and then the OL was applied at point A, see Fig. 8.3. For convenience, the crack length is assumed negative before and positive after that point. After the OL the FCG rate continuously decreases until reaching its minimum value at a region about 2–3 mm ahead of the OL application point, a considerable distance compared with $pz_{OL} \cong (1/\pi)\cdot[2\cdot\Delta K/(1-R)/S_Y]^2 \cong (1/\pi)\cdot(2\cdot 32/0.9\cdot 440)^2 \cong 8.3\ mm$, assuming Irwin's estimate for the monotonic plastic zone in plane stress limiting conditions. Ideally, the maximum delay on the FCG rates should occur just after the crack tip crosses the (small) zone blunted by the OL, and then start to decrease after that point proportionally to the distance $pz_{OL} - pz$, since the effect of the increased residual strains inside pz_{OL} should disappear after the monotonic plastic zone that always follows the crack tip, $pz = pz_{OL}/4 \cong 2.1\ mm$, reaches the pz_{OL} boundary.

However, the FCG data shown in Fig. 8.3 indicates that the maximum delay region is located almost where it should ideally end, and that the OL-induced delays lasted up to about 20 mm after the OL application point, a distance much larger than would be expected from the idealized behavior based on Elber's ideas. Hence, a DIC analysis was performed to explain this behavior. Images were collected from the fatigue test at different crack lengths, and then processed using the VIC-3D software. In the analyses, one image of the specimen at the unloaded condition was taken to be used as reference image before each new image-acquisition cycle. In this way, the residual strains and stresses generated during the crack propagation as well as after overload cycles are not taken into account in the analyses. The crack-flank-opening displacements (COD) were determined using v-displacements of two symmetrical points located 2 mm behind the crack tip.

Figure 8.4 presents COD measurements made before and immediately after the OL. They clearly show crack closure effects before the OL during the initial part of the loading cycle. The crack fully opens at $P_{op}/P_{max} = 0.41$, and remains opened showing a linear variation of the COD with the applied load afterwards. A similar behavior is observed in the unloading cycle, but in this case P_{op} defines the point after which the crack starts to close. However, just after the OL no evidence of crack closure is observed in the COD values, indicating that the crack tip remains fully opened during the entire loading and unloading cycles. This behavior is compatible with OL-induced crack tip blunting caused by local plastic deformations, which decreases the Pop value. Moreover, the back gage strain readings presented in Fig. 8.4b show exactly the same behavior, providing a clear indication of their compatibility.

The full-field DIC displacements can be also used to calculate SIF values via a J-integral formulation based on Linear Elastic Fracture Mechanics (LEFM) concepts [15]. For that, a contour path sufficiently away from the crack-tip must be used, where the material can be assumed to be linear. The entire path length was 14 mm and it was located approximately 2.5 mm ahead of the crack tip, see Fig. 8.5a. The size of the plastic zone that follows the crack tip during its propagation

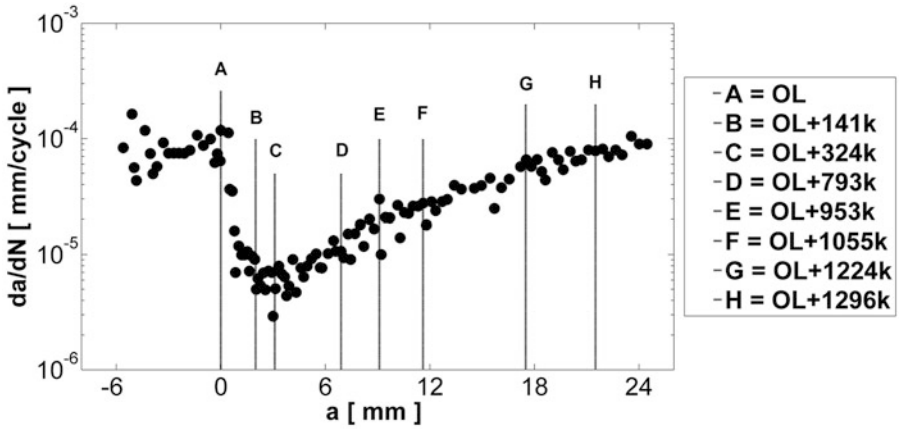

Fig. 8.3 Log of the measured FCG rate *da/dn* versus the crack length before and after the 100% overload

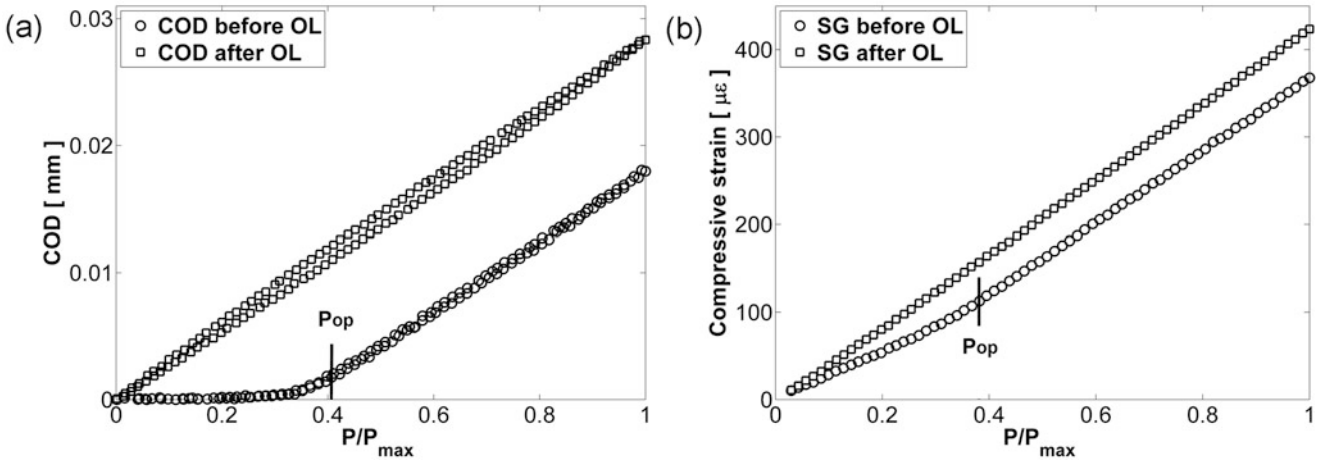

Fig. 8.4 (**a**) COD measurements at 2 mm behind the crack tip using DIC techniques; (**b**) redundant strain measurements simultaneously made at the back face of the specimen by an independent experimental system

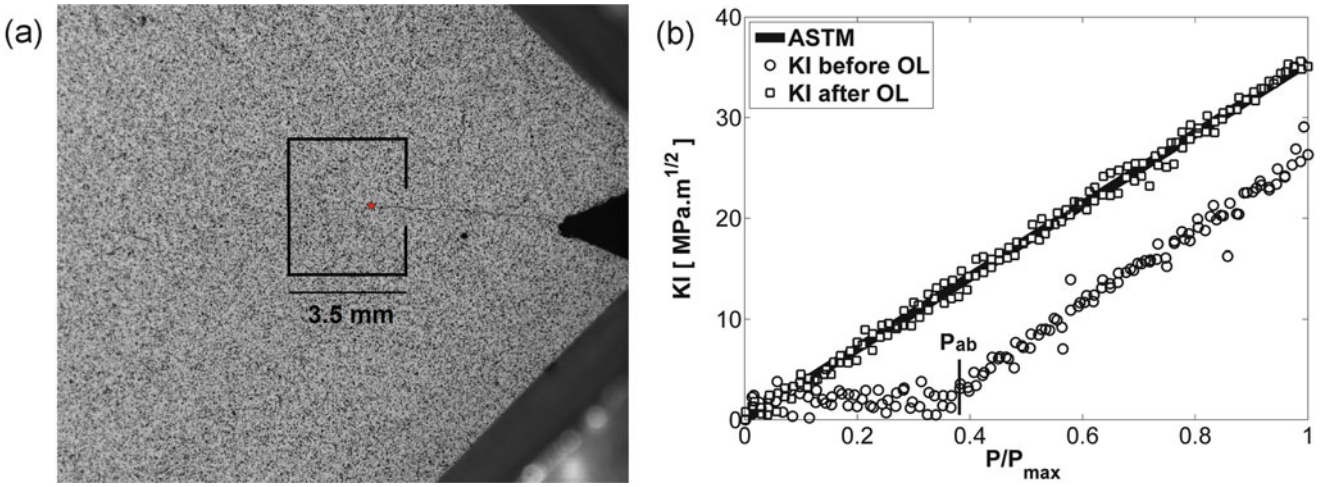

Fig. 8.5 (**a**) Elastic path used for J-integral calculation. (**b**) Mode I SIF values from J-integral formulation

can be estimated as above by $pz \cong (1/\pi) \cdot [K_{max}/S_Y)]^2 = (1/\pi) \cdot [32/(0.9 \cdot 440)]^2 \cong 2.1mm$. It is worth mentioning that, since a new reference was taken at each image-acquisition cycle, the OL-induced residual strains are not considered in this analysis.

The $K_I \times P$ behavior presented in Fig. 8.5b is similar to the COD $\times$ P behavior depicted in Fig. 8.4, and show an opening load at $P_{op}/P_{max} \cong 0.4$. Moreover, the linear part of the $K_I \times P$ curve measured before the OL follows parallel to the ASTM curve after the crack is fully opened. However, as explained in [15], these K_I values should be interpreted as pseudo-SIF calculated assuming an LE behavior. Only when the crack remains fully opened after the OL, the K_I measurements agree well with the values calculated from the ASTM formula, which do not consider the nonlinearities induced by crack closure.

Next, the COD $\times$ P behavior during the post-OL FCG phase (points A, B, C, F, G and H in Fig. 8.3) is studied. Figure 8.6a shows that the partial closure of the crack flanks increases while the crack grows inside pz_{OL} in point B, 141 kcycles after the OL, and in point C, 324 kcycles after the OL, delaying its propagation.

According to Elber, the FCG delay shown in Fig. 8.3 is due to the K_{op}/K_{max} increase after the OL was applied, and to the consequent reduction in ΔK_{eff}. Beyond point C, the crack growth rate starts to recover its initial value, but slower than expected, albeit compatibly with the P_{op} measured in points F, G, and H at 1055, 1224, and 1296 kcycles after the OL, see Fig. 8.6b. The simultaneous back-face strain readings are shown in Fig. 8.7. Once again, there is compatibility between the COD and the redundant strain P_{op} measurements. Notice that Figs. 8.6 and 8.7 present only the loading part of the loading cycles.

From this analysis, it can be concluded that OL-induced changes in P_{op} affect the FCG behavior. Moreover, it can be seen that the crack closure behavior from the COD measurements is compatible with the evolution of the FCG rate. To further

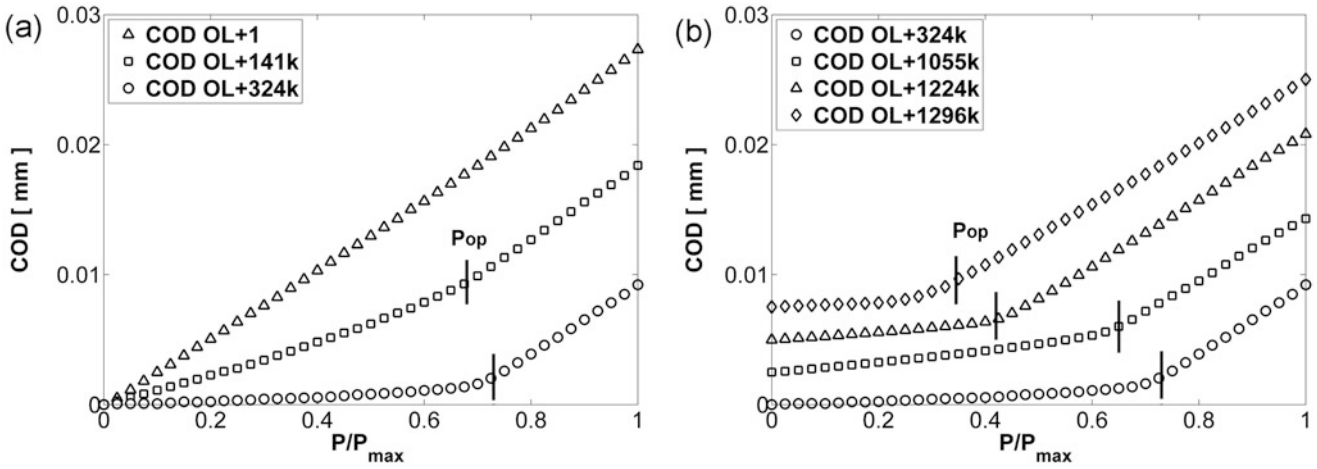

Fig. 8.6 COD measurements from DIC analysis at different crack lengths (the curves of *right* side were translated in *y*-direction for better visibility)

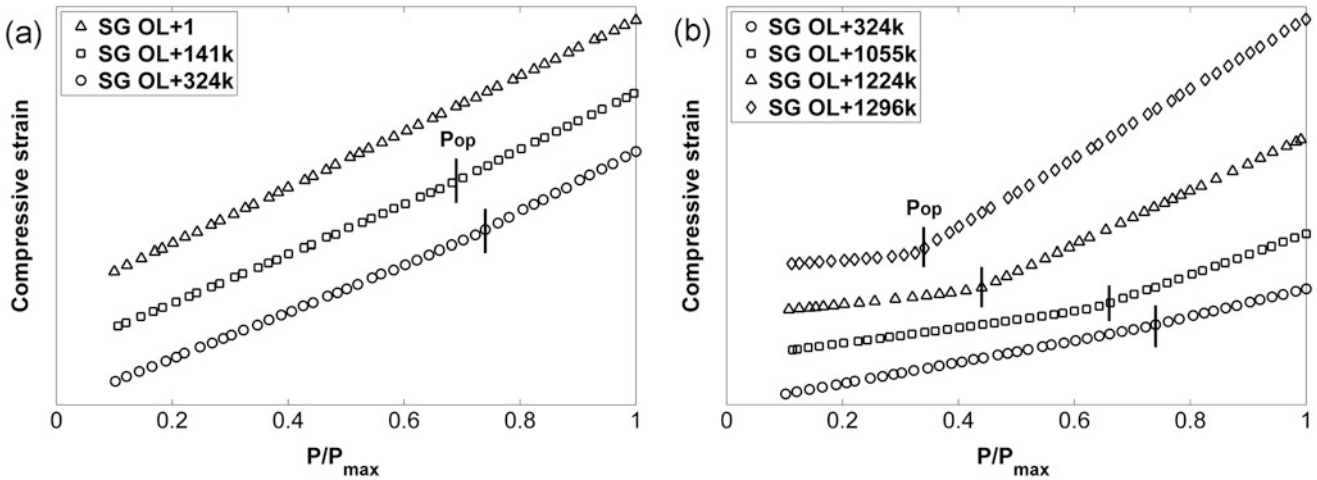

Fig. 8.7 Strain measurements from strain gage placed at back face specimen at different crack lengths (the curves were translated in *y*-direction for better visibility)

explore the post-OL FCG data after it reached its maximum delay, COD measurements at different positions along the crack flanks in points A, C, D, E and F and the corresponding full-field strain map were studied. Figure 8.8 corresponds to the point before overloading, and shows that the crack peels open from the mouth to the tip as the applied load increases. Figure 8.9 illustrates the change in COD values after the OL. Due to crack tip blunting, the crack remains fully open and there is no evidence of crack closure. Figures 8.8b and 8.9b show the corresponding strain tip fields. The data points around the crack faces and tip are excluded from the analysis to avoid their intrinsically higher noise level.

Figure 8.10 correspond to point C in Fig. 8.3, where the FCG rate reached its maximum delay. Note that the crack flanks near the tip remain completely closed during a significant portion of the load cycle. According to Elber, this behavior is explained by the larger reaction of the elastic residual ligament over pz_{OL}, as shown in the crack tip strain field of the Fig. 8.10b.

Figure 8.11 corresponds to point D, about 7 mm from the OL application point, just outside the theoretical pz_{OL}, where the FCG rate *da/dN* shows some recovery in Fig. 8.3. The COD values at points near the crack tip show a nonlinear behavior along the crack flanks. It can be seen that up to a load $0.6 \cdot P_{max}$ the portion of the crack surface near the tip (at 1, 2, and 3 mm from the crack tip) is partially open whereas the portion near the OL location (at 4 and 5 mm from the tip) remains closed.

Closure near the OL location is also observed in Figs. 8.12 and 8.13, which correspond to points E and F in Fig. 8.3, where the crack tip has propagated up to about 9 and 11.5 mm from the OL application point, respectively. COD values decrease near the OL location at 5, 6 and 7 mm from the tip in Fig. 8.12a and, at 8 and 9 mm from the tip in Fig. 8.13a. It is worth mentioning that, Figs. 8.8, 8.9, 8.10 and 8.11 used the same stereo camera configuration, whereas in Figs. 8.12 and

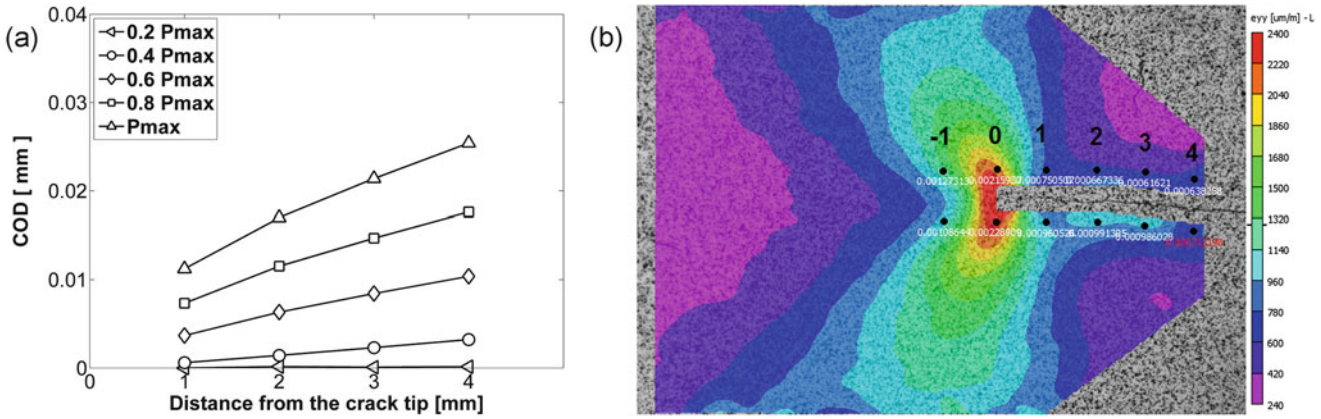

Fig. 8.8 (**a**) COD measurements along crack flanks and (**b**) strain field map for the point before the OL

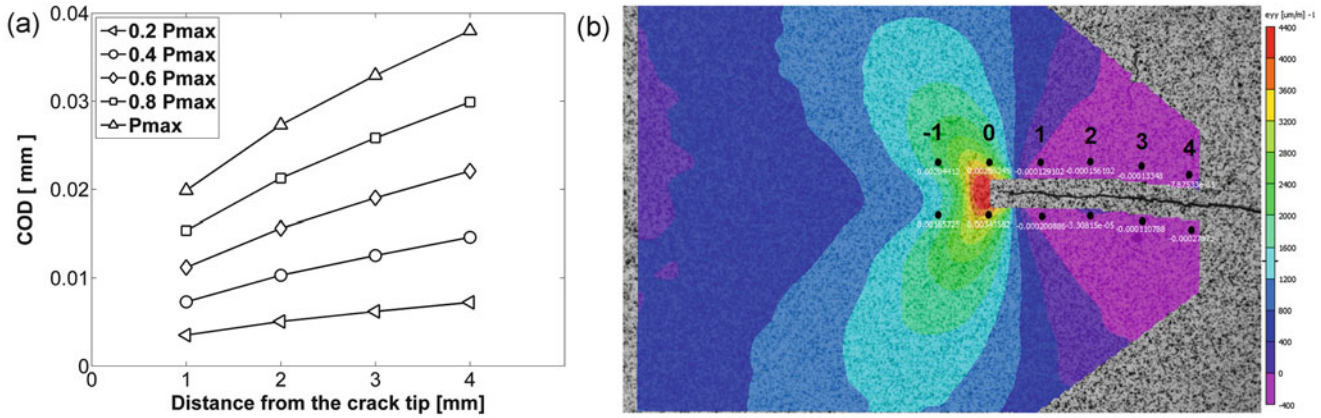

Fig. 8.9 (**a**) COD measurements along crack flanks and (**b**) strain field map for the point after the OL

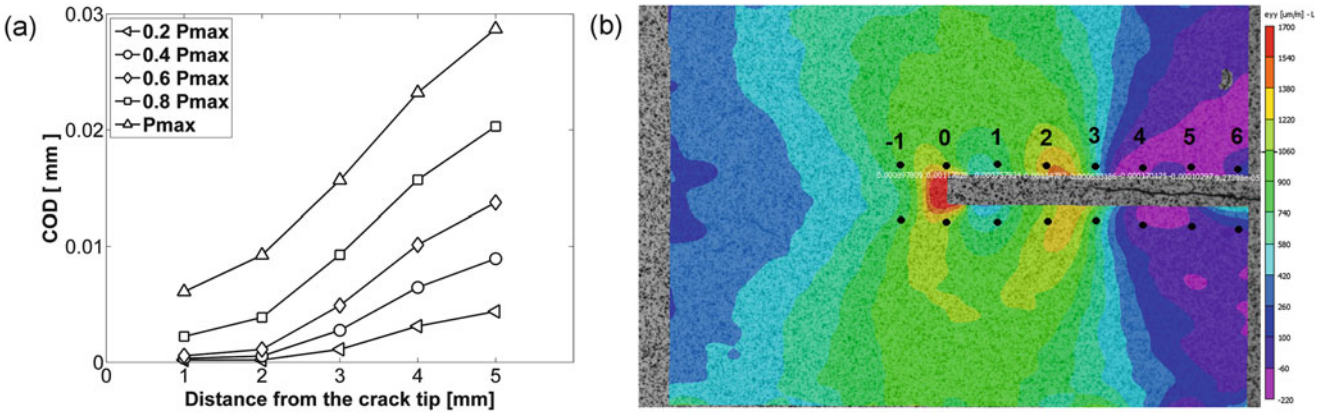

Fig. 8.10 (**a**) COD measurements along crack flanks and (**b**) strain field map for the point OL+ 324 kcycles

8.13 the cameras were moved to the left to monitor the crack growth. In this way, the OL location is outside of field of view of the cameras (right of the Figs. 8.12b and 8.13b). For each stereo camera configuration, a stereo calibration procedure was performed.

The behavior exhibited in Figs. 8.11, 8.12 and 8.13 is compatible with the phenomenon of discontinuous closure reported by Fleck [1]. Moreover, the inspection of the strain field maps extracted from DIC analysis illustrates the high crack-tip plasticity created near the OL location.

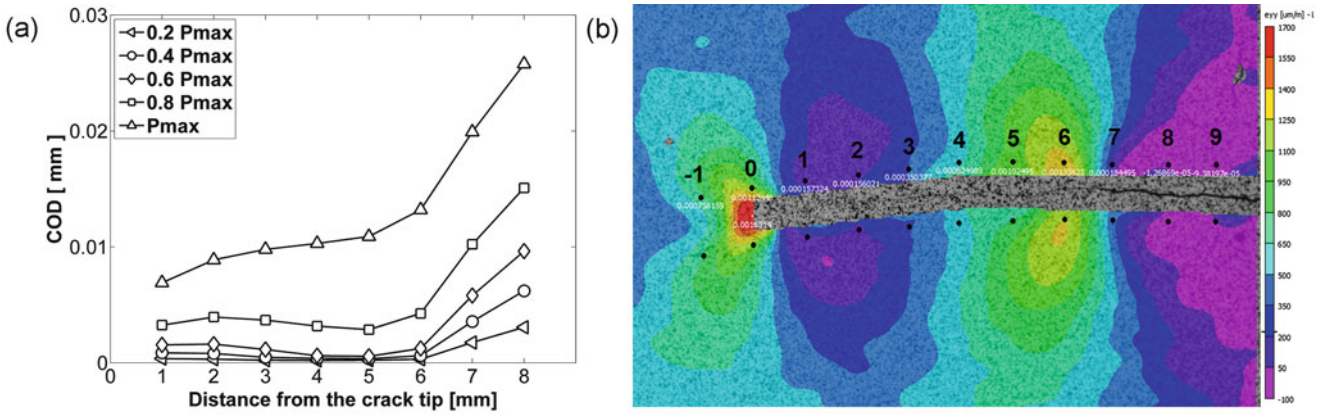

Fig. 8.11 (**a**) COD measurements along the crack flanks and (**b**) strain field map for the point OL+ 793 kcycles

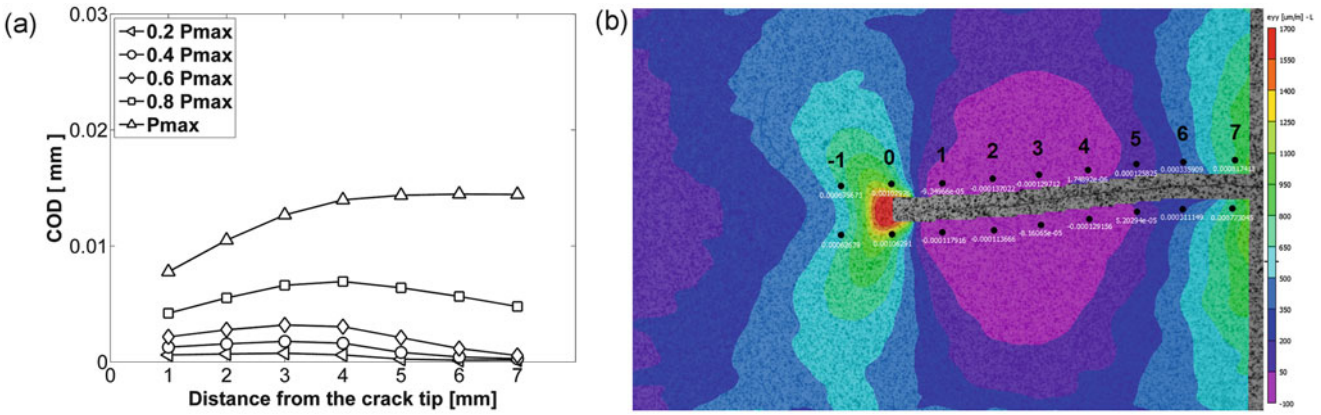

Fig. 8.12 (**a**) COD measurements along crack flanks and (**b**) strain field map for the point OL+ 953kcycles

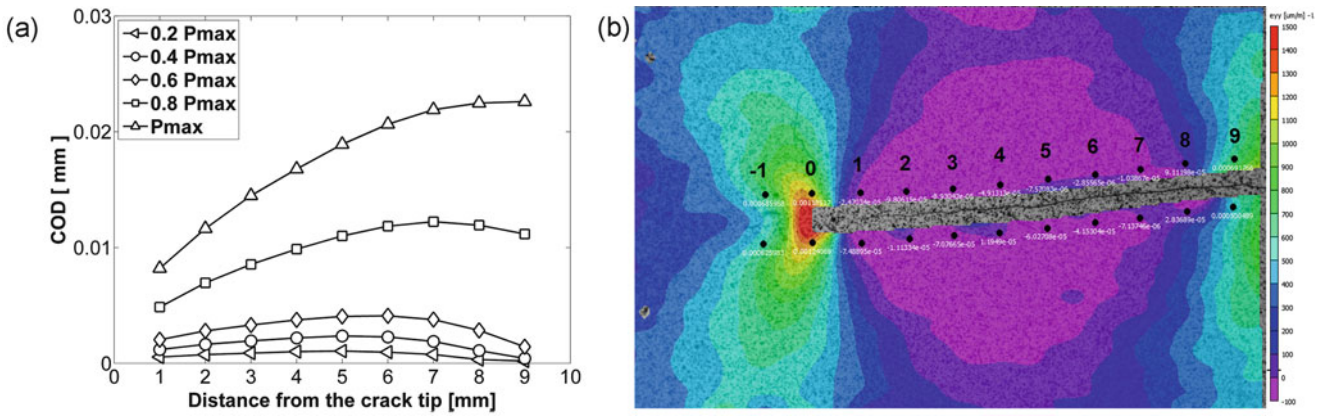

Fig. 8.13 (**a**) COD measurements along crack flanks and (**b**) strain field map for the point OL + 1055 kcycles

Figure 8.14 shows the strain behavior of the material near the OL location, for two different crack lengths. It can be seen that the strains have the same behavior and tend to stabilize at a value of 1300 $\mu\varepsilon$. In this way, the experimental results showed that the residual hump of stretched material at the OL location is the cause of the discontinuous closure observed in this fatigue test. This phenomenon leads to high levels of crack opening loads in post-overload behavior as shown in the analysis, increasing the retardation at about 3 times the theoretical OL-induced plastic zone for this case.

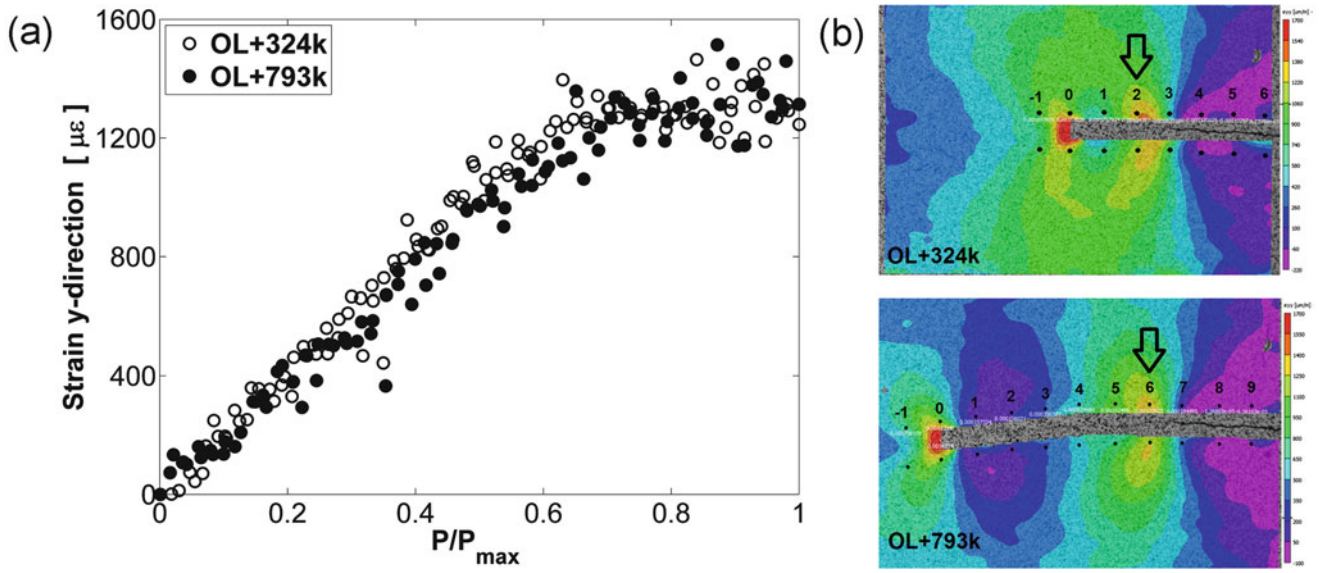

Fig. 8.14 (**a**) Strain values near the OL location (**b**) Points near the OL location used for strain evaluation

8.4 Conclusion

This paper presents an experimental study on a fatigue cracked DC(T) specimen of 4340 steel subjected to a single tensile overload in a constant ΔK test. The experimental results showed delayed FCG rates at distances much larger than the theoretical OL-induced plastic zone. With the help of DIC analysis, the presence of discontinuous closure phenomenon was clearly identified by the examination of P_{op} values from COD values and full-field strain maps in the vicinity of the crack. Moreover, the redundant measurements of P_{op} values performed by the strain gage and by the DIC analysis presented similar results confirming they both are suitable techniques to detect and measure crack opening loads, if properly interpreted.

This work shows the capability of the DIC technique in fracture mechanic problems in order to improve the understanding of crack growth under non-uniform amplitude loading, a necessary condition to elaborate appropriate models to make FCG predictions in practical applications.

Acknowledgements G.L.G. Gonzáles gratefully acknowledge the support of the CNPq–Conselho Nacional de Desenvolvimento Científico e Tecnológico, Brazil (reference 152,795/2016–2).

References

1. Elber, W.: The significance of fatigue crack closure. In: Damage Tolerance in Aircraft Structures, ASTM, Philadelphia (1971)
2. Elber, W.: Fatigue crack closure under cyclic tension. Eng. Fract. Mech. **2**, 37–45 (1970)
3. Castro, J.T.P., Meggiolaro, M.A.: Fatigue Design Techniques. Vol. 3: Crack Propagation, Temperature, and Statistical Effects. CreateSpace, Scotts Valley (2016)
4. Von Euw, E., Hertzberg, R., Roberts, R.: Delay effects in fatigue crack propagation. In: Stress Analysis and Growth of Cracks: Proceedings of the 1971 National Symposium on Fracture Mechanics: Part 1, STP34123S. ASTM International, West Conshohocken, pp. 230–259 (1972). https://doi.org/10.1520/STP34123S
5. Shin, C., Fleck, N.: Overload retardation in a structural steel. Fatigue Fract. Eng. Mate. Struct. **9**, 379–393 (1987)
6. O'Connor, S.J., Nowell, D., Dragnevski, K.I.: Measurement of fatigue crack deformation on the macro-and micro-scale: Uniform and non-uniform loading. Int. J. Fatigue. **89**, 66–76 (2016)
7. Lopez-Crespo, P., Withers, P., Yates, J., Steuwer, A., Buslaps, T., Tai, Y.: Study of overload effects in bainitic steel by synchrotron X-ray diffraction. Frattura ed Integritá Strutturale. **25**, 153 (2013)
8. Yusof, F., Lopez-Crespo, P., Withers, P.J.: Effect of overload on crack closure in thick and thin specimens via digital image correlation. Int. J. Fatigue. **56**, 17–24 (2013)
9. Brahma, K.K., Dash, P.K., Dattaguru, B.: Observation of crack closure using a crack mouth opening displacement gauge. Int. J. Fatigue. **11**, 37–41 (1989)
10. Shin, C.S., Hsu, S.H.: On the mechanisms and behaviour of overload retardation in AISI 304 stainless steel. Int. J. Fatigue. **15**, 181–192 (1993)

11. Borrego, L.P., Ferreira, J.M., Da Cruz, J.P., Costa, J.M.: Evaluation of overload effects on fatigue crack growth and closure. Eng. Fract. Mech. **70**, 1379–1397 (2003)
12. Nowell, D., De Matos, P.F.P.: Application of digital image correlation to the investigation of crack closure following overloads. Procedia Eng. **2**, 1035–1043 (2010)
13. Fleck, N.A.: Influence of stress state on crack growth retardation. In: Basic Questions in Fatigue, vol. I, ASTM STP23215S. ASTM International, West Conshohocken, pp. 157–183 (1988). https://doi.org/10.1520/STP23215S
14. VIC-3D: Correlated Solutions Inc. http://www.correlatedsolutions.com/ (2010)
15. Gonzáles, G.L.G., Diaz, J.G., González, J.A.O., Castro, J.T.P., Freire, J.L.F: Determining SIFs using DIC considering crack closure and blunting. Exp. Appl. Mech. **4**, 25–36 (2017). Springer International Publishing.

Chapter 9
In-Situ Observation of Damage Evolution in Quasi-Isotropic CFRP Laminates

Addis Tessema, Suraj Ravindran, Abigail Wohlford, and Addis Kidane

Abstract In this work, a Digital Image Correlation (DIC) impaired with high resolution optical system is applied to capture the damage evolution in composites laminates in-situ. The developed method enables to measure the local (micro scale) deformation across the thickness on the free-edge (8-plies laminate) subjected to a quasi-static tension. Three groups of specimens are prepared by arranging plies at different stacking sequence, and the formation of strain localization, initiation of matrix crack, delamination and other damages are acquired. It is obtained that matrix cracking is the primary and dominant form of damage and it usually occurred in the 90°-plies. However, the orientation and quantity of matrix cracks are highly affected by the stacking arrangement of the plies.

Keywords Damage evolution • Quasi-isotropic • Stacking sequence • Free-edge • Micro-scale

9.1 Introduction

Composite structures have a crucial role in today's engineering community. The design of composite materials has been dynamic as researchers explore new features. The mechanics of composite materials has been under study for more than six decades, and different approaches has been developed to evaluate their mechanical response. Various analytical models such as the basic classical laminate theory (CLT), meso and micro mechanics models and numerical models have been developed to analyze and predict the failure of FRC. Though, it is difficult to anticipate mechanism and the exact failure state in FRC, experimentally, it is observed that the failure is a gradual process [1–5].

It is found that the failure of a laminate starts from micro level damages and propagated within laminate. Through micromechanics models, the presence of these damages is observed to degrade the mechanical properties of the laminate and led it to the final failure. On the other hand, the macro scale failure criteria are developed and used based on the stress/strain obtained from the classical laminate theory (CLT) to estimate the form of damage. For uniaxial loading condition, The CLT is reduced in to a 2D stress formulation and this formulation fails to account the boundary/free-edge condition of the composite laminate [6]. For this matter, researcher have considered the free edges condition (i.e. formed at the edge or due to presence of holes or slots on the laminate) and established solutions for the stress at the free edges [6–10]. It was found that there is a 3D complex stress condition, and this stress condition lasts only at regions near the free edge.

According to the literatures a FRC laminate will have interlaminar stresses on the free-edges plane. These interlaminar stresses are both axial and shear stresses, where the axial is directed perpendicular to the laminate plane, while the shear is the parallel to the free-edge plane. Such a 3D stress conditions causes initiation of damages, in support, experimental works have shown that micro damages are emerged on the free-edge of a laminate coupon which is believed due to the interlaminar stresses [1, 3, 5, 11, 12]. However, there is no evidence that the magnitude and direction of these stresses are guided by the orientation of individual plies stacked in the laminate.

This study is objected to visualize the full-field strain contour over the thickness of the laminate using Digital Image Correlation (DIC). The full-field strain contours are obtained for different loading levels. Further, the gradual initiation and growth of micro damages from the free-edge is captured. By varying the stacking sequences of a quasi-static laminate, the influence of ply arrangement on the interlaminar axial and shear strain is investigated.

A. Tessema (✉) • S. Ravindran • A. Wohlford • A. Kidane
Department of Mechanical Engineering, University of South Carolina, Columbia, SC 29208, USA
e-mail: atessema@email.sc.edu

J. Carroll et al. (eds.), *Fracture, Fatigue, Failure and Damage Evolution, Volume 7*, Conference Proceedings of the Society for Experimental Mechanics Series, DOI 10.1007/978-3-319-62831-8_9

9.2 Specimen Preparation

Laminates with three different stacking arrangements are used in this study. These laminates are made from carbon fiber prepregs provided by Toray Composite Inc. Each ply in the laminate is stacked using fiber placement technique. Once the prepreg is stacked in the required orientation and arrangement, it is wrapped with vacuum plastic bags and placed in the oven to cure. Eight plies Quasi-isotropic laminates with three different laminate stacking sequences are manufactured. The three ply arrangements of laminate are $(0/-45/90/+45)_s$, $(0/-45/+45/90)_s$ and $(0/90/+45/-45)_s$. Rectangular coupon test samples are extracted from the cured laminates using a CNC water-jet cutting machine. The final coupons have a size of 150×22 mm^2 and thickness of 1.6 mm.

The side edges of the coupons are polished with different grade of sandpapers to remove any kind of flaws (i.e. notches and indentations) that are formed during water-jet cutting. Following, fiberglass tabs are glued on the width face of the coupon at the two gripping ends, as shown in Fig. 9.1a, to protect the fiber damage from the gripping pressure of the testing machine. In order to facilitate the digital image correlation, black speckle patterns are made on the white background of the specimen surface where full-field strain is acquired. The speckles are made on two distinct regions of the specimen. The first one is on the thickness edge and these are micro scale with an approximate size of 6 16 μm. The second one is on the width side of the samples and had an approximate size of 250 300 μm. The speckles on edge side are used to capture the local residual strain concentration and damage formation across the plies. On the other hand, the speckles on the width side is used to obtain the laminate global average strain.

9.3 Test Setup

Uni-axial tension test is conducted using Material Testing System (MTS 810) machine based ASTM D3479 standard. The MTS 810 machine is adjusted to perform displacement controlled loadings at a rate of 0.01 mm/min. The monotonic load is applied until the final failure of the specimen. As shown on Figs. 9.1b, 2D-DIC setup is applied for both speckled regions. These setup is used capture consecutive images of speckled regions during loading. For the micro speckled region that has an approximated area of interest 4 mm × 1 mm. A 3× magnification lens is coupled with a 9 MPixels CCD (Grasshopper) camera to capture the images at a framing rate of 1fps. For the macro speckled region, the images are acquired simultaneously with the micro speckled region using 5MPixels CCD camera incorporated with 60 mm Nikon lenses. The images of the micro and macro speckle are post processed using VIC-2D software separately. Thereby, from the micro speckle the local full-field axial, transverse and shear strain data are obtained levels.

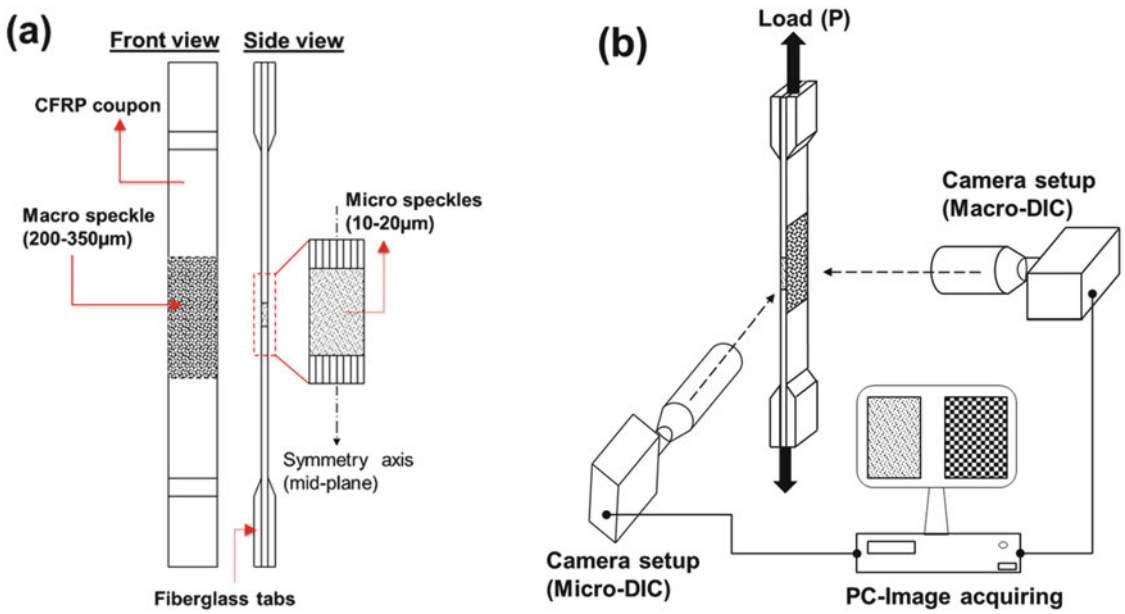

Fig. 9.1 Schematic diagram of (**a**) Test specimen and speckles and (**b**) experimental setup

9.4 Results and Discussion

9.4.1 Global Response

The typical global stress-strain plots for the three laminates are depicted in Fig. 9.2a, the stress is calculated from the load data obtained from the load cell. The global strain is obtained from the macro speckle at the surface of the specimen. As depicted, the (0/−45/90/+45) and (0/−45/+45/90) have a similar stress-strain curve. However, the failure stress and strain of the (0/90/+45/−45) are much higher. The stress-strain relation of the (0/90/+45/−45) and (0/−45/+45/90) laminates have a bilinear form. The failure stress for the (0/−45/+45/90), (0/−45/90/+45) and (0/90/+45/−45) laminates are 650 MPa, 780 MPa and 830 MPa respectively.

The stresses along with time are plotted as shown in Fig. 9.2b, distinct and nonlinear stress trend is observed for each laminate. The (0/90/+45/−45) laminate has the highest stress rate and reached to its maximum stress in shorter period (400 secs). The (0/−45/+45/90) laminate has the shortest loading time which lasts for 340 secs, whereas the (0/−45/90/+45) laminate has the largest loading duration of 590 secs. The variation in stress rate and loading duration can be taken as an indication for how the stacking arrangement facilitate the damages development and final failure of the laminate.

9.4.2 Gradual Development of Damages

The axial and shear strain contour obtained from micro speckles across the thickness of the laminate are depicted on the Fig. 9.3. The figure shows the gradual development of strain localization as a result of damage emergence in the laminate. As discussed in the introduction section, the stress condition on the free edge of the laminate is complex. Due to stress concentration, the primary damages are expected to initiate and gradually grow from the free-edge. In the (0/−45/90/+45) laminate, as shown in Fig. 9.3a, the first axial strain localization occurred in the 90°-ply around stress of 400 MPa. Later, this localization is turned to matrix/transverse cracking and number of these localizations are observed as the applied stress increased. As the loading rises, matrix cracks are observed in the +45°-plies that are located at the middle of the laminate.

As of the axial strain, certain shear strain localizations are observed in the laminate. At early stage of loading, shear strain localizations occurred in the 90°-ply and its interfaces with the neighboring plies. Moreover, the shear localizations are shown to follow the matrix cracks as seen in Fig. 9.3b. The shear contour plots have given the indication that delamination is followed as the matrix crack reached the interfaces. Moreover, the matrix cracks in the 90°-plies have a certain angle of slant and this slant is symmetrical about the mid plane of the laminate. Since the neighboring plies (+45° and −45°) have fibers oriented in opposite direction, it is expected to have a higher shear lag between the two plies, and this lead higher shear strain in the 90°-ply. It is presumed that the tilting of the matrix cracks is due to the shear lag generated from the neighboring plies.

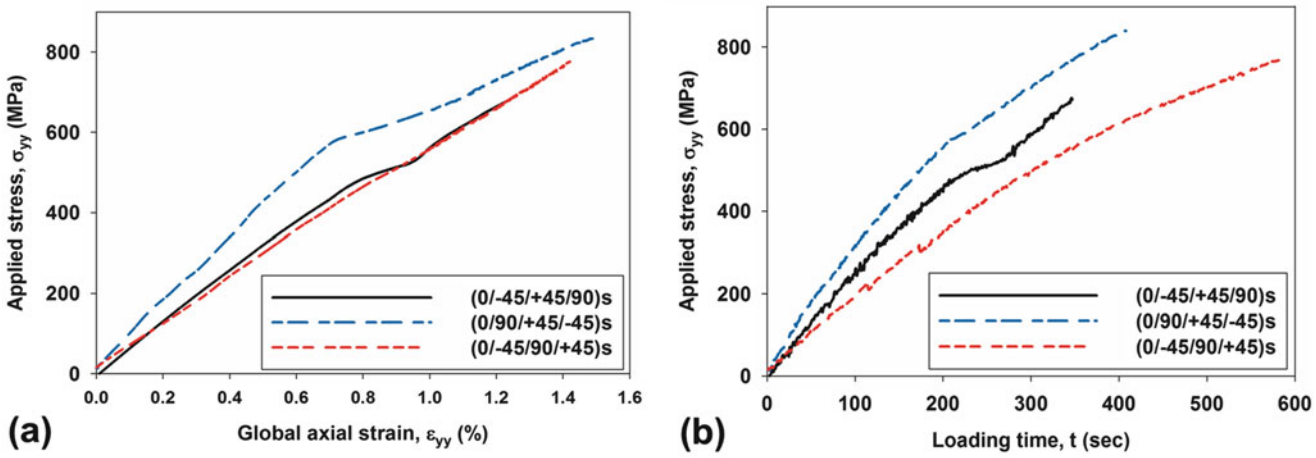

Fig. 9.2 (**a**) Stress-stress strain plot and (**b**) stress-time plot for the three laminates

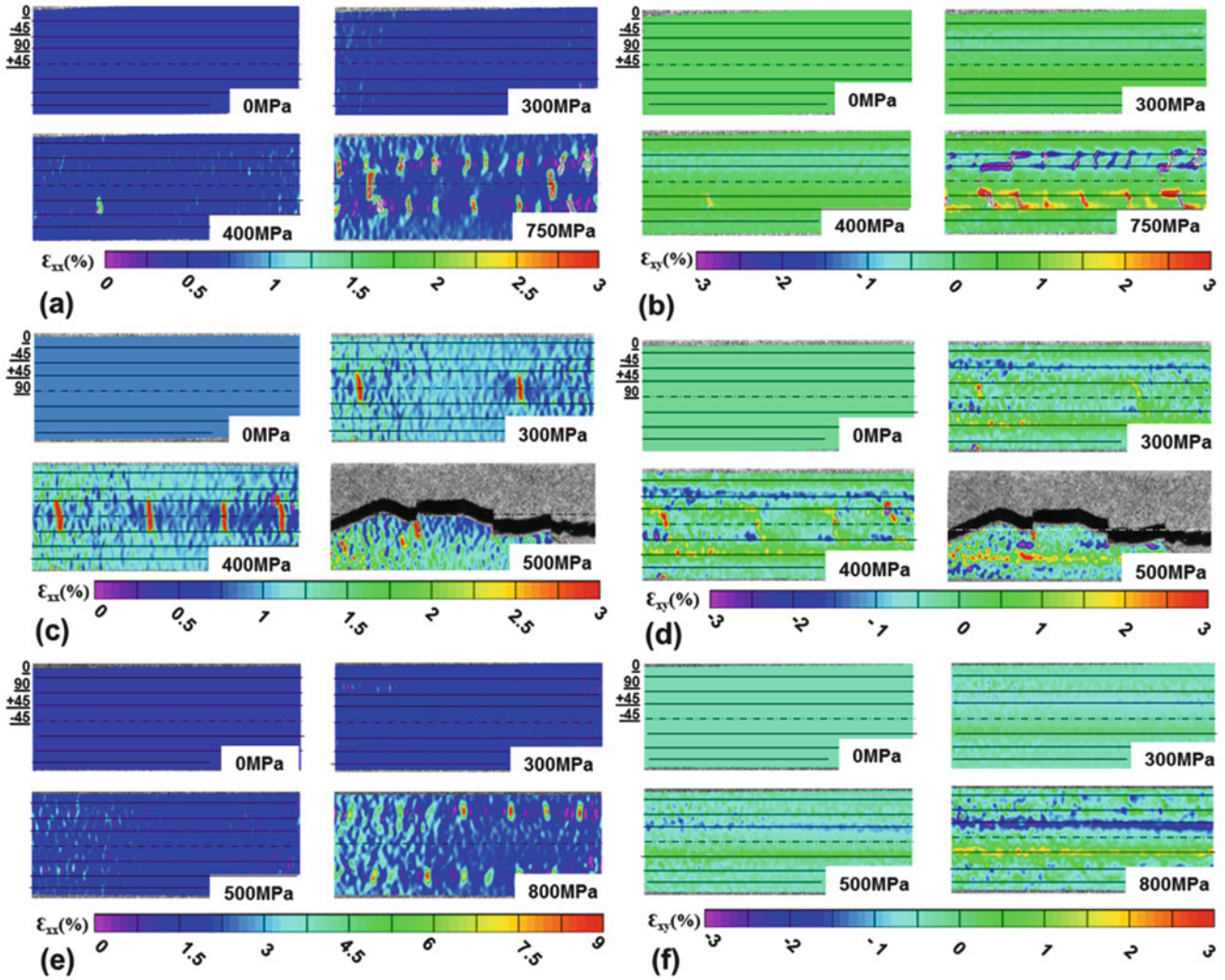

Fig. 9.3 Full-field axial and shear strain contour for (**a**, **b**) 0/−45/90/+45, (**c**, **d**) 0/−45/+45/90 and (**e**, **f**) 0/90/+45/−45 respectively

In the $(0/-45/+45/90)_s$ laminates, as seen in the Fig. 9.3c, the axial strain localization seems to occurr at early stage of the loading. The large matrix crack/localization appeared in the two 90°-plies that found at the middle of the laminate. These cracks are oriented vertically straight and have shown an interesting gradual growth and formation. It looks like that newly coming matrix cracks appeared in between two preexisting cracks, the new crack emerge near exactly at the middle of the two craks. Shear strain localizations have been observed at the interface of −45/+45 plies. As discussed earlier, these two plies have oppositely oriented fibers and during loading the two plies will have opposite inplane shear. Thus, there will be a higher relative displacement at the interface that leads to higher interlaminar shear at the interface. In addition, more shear strain localization are seen at the site where matrix crack reached the interfaces. Following, a delaminating crack has initiated at one of the location where the matrix cracks reached the interface and propagated through the interface of 90/+45 plies.

Similarly, for the (0/90/+45/−45) laminate, a number of axial strain localizations/matrix cracks appeared in the 90°-plies at higher stress. These matrix cracks have slant angles but it is not as large as the one in the (0/−45/90/+45) laminate. There was no sign matrix crack or strain localization appeared in the other plies and the matrix cracks remained in the 90°-plies. On the other hand, shear strain localizations appeared at the interfaces of −45/+45 plies. Moreover, small shear strain localization are noticed at the interface where the matrix cracks reached the interface.

Summing up, matrix cracking appeared in all of the laminates and it occurred in the 90°-plies. The stress at which the matrix cracks initiated varied for each laminate. It seems like, in the laminates where the 90°-ply is far from the mid plane the matrix cracks appeared at the higher loading than in the laminates where it is located at the mid-plane.

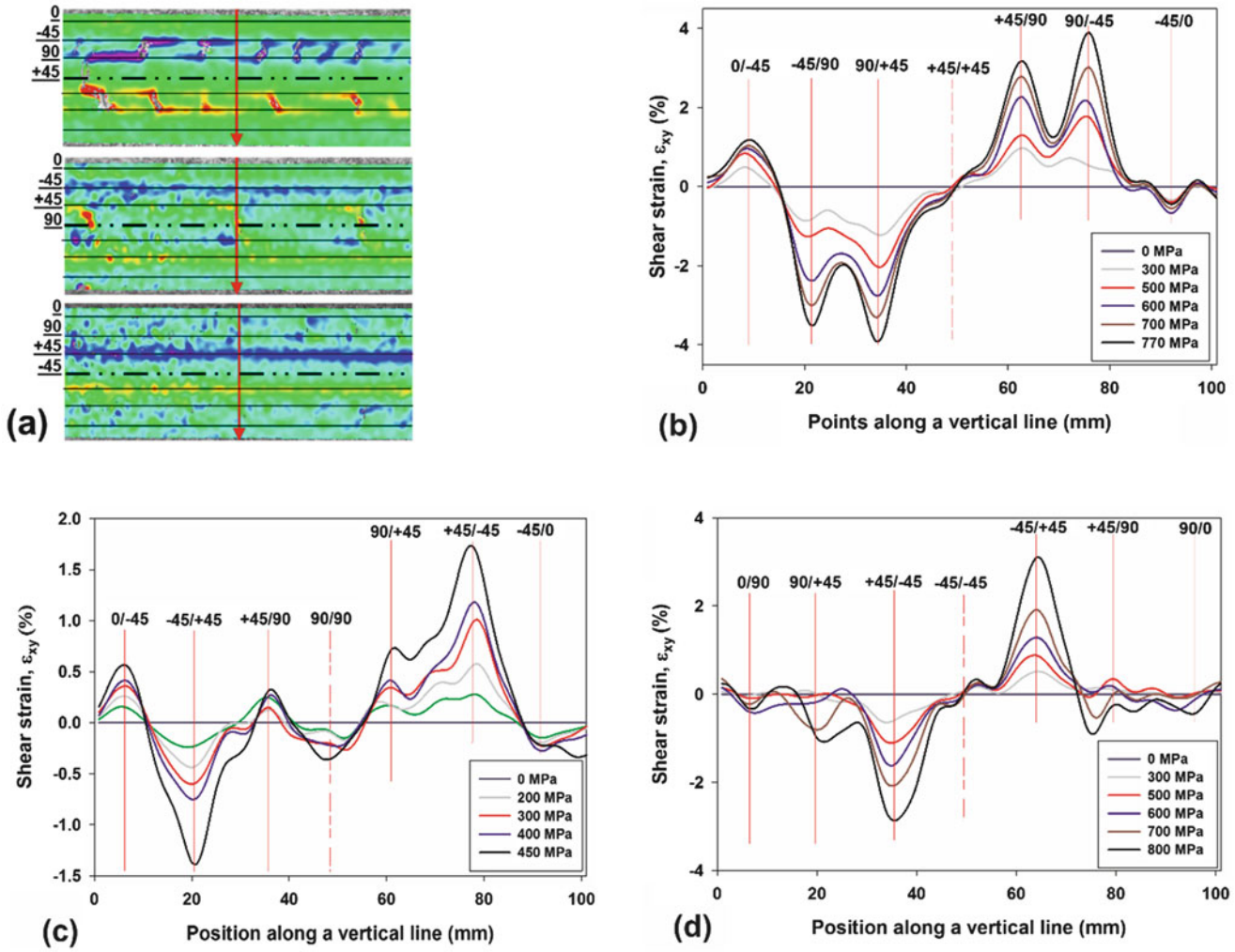

Fig. 9.4 (**a**) The shear contour with vertical line crossing all the plies, and Shear strain along the vertical line for different stresses (**b**) 0/−45/90/+45, (**c**) 0/−45/+45/90 and (**d**) 0/90/+45/−45 respectively

9.4.3 Interlaminar Shear Strain

As the arrangement plies changes in the laminate the interlaminar shear strain developed at the interfaces also varies. As shown in the Fig. 9.4, the quantity of the shear strain across all the interfaces are plotted. The plots for each laminate shows that there is a similarity on the interfaces where there is a significant interlaminar shear for the (0/90/+45/−45) and (0/−45/+45/90) laminates. In both laminates the highest interlaminar shear occurred at the interface of the +45/−45 plies and this result agrees with different numerical and analytical models [6, 13]. However, for the (0/−45/90/+45) laminate, there is no a direct contact between the +45° and −45° plies. Instead, the 90° ply is located between them, then the interlaminar shear strain due to the +45° and −45° plies also distorts the 90° ply. In addition, the matrix cracks in the 90° ply propagated to the interfaces of the neighboring plies. As it reaches the interfaces, the tip of these angled matrix cracks brings additional interlaminar strains which initiates delaminating crack across the interface. Therefore, in the (0/−45/90/+45) laminate the highest shear strain localisation occurs at the interfaces of +45/90 and 90/−45 plies.

The magnitude of the interlaminar shear strain in each laminate are seen to vary for the same amount of applied stress. The shear strain recorded for the (0/−45/90/+45) laminate is much higher than the other laminates. Relatively close results are obtained for the (0/90/+45/−45) and (0/−45/+45/90) laminates. The load transfere in laminate is through a shear lagg at the interface, thus the higher the strength and stiffness of the interface the better the load transfer between plies [14]. The amount of shear strain localisations are related with the stiffness and the quantity of shear load transferred through the interface. Regarding the stiffness, it is highly influenced by the shear property of the individual plies that make up the

interface. The interfaces in our laminate are made of 0°, 90°, +45° and −45° plies, and the 0° ply has the highest shear modulus, the +45° and −45° plies follows and the 90° ply has the least. Therefore, the ±45/0, +45/−45, ±45/90 and 90/90 interfaces have higher the stiffness accordingly.

The other factor for the shear localisation at the interface is the relative axial and shear displacement between two adjacent plies. Variation in the axial/shear displacement occurs when the two plies have different properties or fiber orientation, and this variation induces shear lagging between the two plies. Under a given axial tension load, the ±45 plies have the highest inplane shear strain. The inplane shear strains developed in the +45° and −45° plies have opposite orientations. As a result a higher shear strain localisation is expected at the interface of +45/−45, ±45/90and ±45/0 plies accordingly. The combined effect of interface stiffness and interface shear lag produces the shear strain localisations at the interfaces. The shear strain localizations obtained at each interface from this study matches the above explanation.

9.5 Summary

Uniaxial tension test is performed on three quasi-isotropic laminates with different ply arrangements. Using Digital Image Correlation (DIC) the full-filed strain across the thickness of the laminate at the free-edge of the tests coupon is captured at a different stage of loading. From the experiments, it is obtained that matrix cracking is the primary and dominant form of damage and it usually occurred in the 90°-plies. However, the orientation and quantity of matrix cracks are highly affected by the stacking arrangement of the plies. Further, shear strain localizations have been observed in most of the interfaces and the highest shear strain are obtained at the +45/−45 interfaces.

References

1. Tong, J., Guild, F.J., Ogin, S.L., Smith, P.A.: On matrix crack growth in quasi-isotropic laminates—I. Experimental investigation. Compos. Sci. Technol. **57**, 1527–1535 (1997)
2. Tessema, A., Mymers, N., Patel, R., Ravindran, S., Kidane, A.: Experimental investigation on the correlation between damage and thermal conductivity of CFRP. In: Proceedings of the American Society for Composites: Thirty-First Technical Conference, Williamsburg (2016)
3. Tessema, A., Ravindran, S., Kidane, A.: Experimental study of residual plastic strain and damages development in carbon fiber composite. Fract. Fatigue Fail. Damage Evol. **8**, 31–36 (2017). Springer
4. Shelke, A., Uddin, A., Yang, J.: Impact identification in sandwich structures using solitary wave-supporting granular crystal sensors. AIAA J. **52**, 2283–2290 (2014)
5. Berthelot, J.: Transverse cracking and delamination in cross-ply glass-fiber and carbon-fiber reinforced plastic laminates: static and fatigue loading. Appl. Mech. Rev. **56**, 111–147 (2016)
6. Mittelstedt, C., Becker, W.: Interlaminar stress concentrations in layered structures: Part I – a selective literature survey on the free-edge effect since 1967. J. Compos. Mater. **38**, 1037–1062 (2004)
7. Crossman, F.W., Warren, W.J.: Initiation and growth of transverse cracks and edge delamination in composite laminates Part 2. Experimental correlation. J. Compos. Mater. Suppl. **14**, 88–108 (1980)
8. Amrutharaj, G.S., Lam, K.Y., Cotterell, B.: Delaminations at the free edge of a composite laminate. Compos. Part B Eng. **27**, 475–483 (1996)
9. Joo, J.W.W., Sun, C.T.T.: A failure criterion for laminates governed by free edge interlaminar shear-stress. J. Compos. Mater. **26**, 1510–1522 (1992)
10. Pagano, J., Pipes, R.B.: The influence of stacking sequence laminate strength. J. Compos. Mater. **5**, 50–57 (2016)
11. Alton Highsmith, K.R.: Stiffness-reduction mechanisms in composite laminates- damage in composite materials: basic mechanisms, accumulation, tolerance, and characterization. ASTM STP. **775**, 103–117 (1982)
12. Tessema, A., Mitchell, W., Koohbor, B., Ravindran, S., Kidane, A., Van Tooren, M.: On the mechanical response of polymer fiber composites reinforced with nanoparticles. Mech. Compos. Multi-funct. Mater. **7**, 125–130 (2016). Springer
13. Ogihara, S., Takeda, N., Kobayashi, S., Kobayashi, A.: Effects of stacking sequence on microscopic fatigue damage development in quasi-isotropic CFRP laminates with interlaminar-toughened layers. Compos. Sci. Technol. **59**, 1387–1398 (1999)
14. Tessema, A., Mitchell,W., Koohbor, B., Ravindra, S., Kidane, A., Van Tooren, M.: Effects of nanoparticles on the shear properties of polymer composites. In: American Society of Composite Technical Conference (2015), Mesa Costa, California

Chapter 10
Contamination-Induced Degradation/Enhancement of Interfacial Toughness and Strength in Polymer-Matrix Composite Interfaces

Denizhan Yavas, Xu Shang, and Ashraf F. Bastawros

Abstract This study explores the effect of environmental contamination on the interfacial toughness and strength of polymer-based interfaces. Double cantilever beam, end-notched flexure, and single lap joint tests are utilized to examine the contaminated bond line behavior under different fracture modes. A typical adhesive/adherend material system exposed to a common aviation hydraulic fluid at varying contamination concentrations is examined. The mode-I fracture tests reveal a significant degradation in mode-I fracture toughness and strength with increasing contaminant concentration, whereas mode-II fracture properties are found to be insensitive to the contamination level. To the contrary, single lap joint shear strength exhibits an enhancement with increasing contaminant concentration. Such contradictory result can be attributed to nucleation vs. propagation of interfacial cracks. Contamination weakens the interfacial bonding and thereby reduces the interfacial adhesion while shielding plastic dissipation within the bond line. Whereas, contamination also reduces the plastic flow stress of the bond line and thereby increases local plastic dissipation in the SLJ geometry.

Keywords Composite materials • Adhesive joints • Adhesion • Contamination • Bond line integrity

10.1 Introduction

Polymer-matrix composites have been extensively utilized in a wide range of industrial applications, with the advantage of high strength-to-weight ratio. One of the major concerns with polymer-matrix interfaces is the environmentally induced interfacial contamination, which affects the performance and the long-term reliability of the entire structures. The behavior of the polymer-based interfaces under variety of environmental exposures, such as moisture [1, 2], chemical contaminants [3, 4], and radiation [5], have been examined by many researchers. However, these studies have represented a diverse range of joint geometries for various adhesive/adherend material combinations. Such variability may lead to numerous different degradation mechanisms, and eventually alter bond line failure mode. For example, Anderson [6] has depicted that different joint geometries can present very different sensitivity to contaminant concentrations. In addition, Davis [7] has shown that the rubber-steel peel strength can be degraded by 50% with a trace level (less than 1 $\mu g/cm^2$) of plasticizer contaminant, whereas it can be enhanced by machine oil contaminant. It is obvious that the effect of contamination on the bond line failure is controlled by many different factors (adhesive-contaminant interaction, geometry and loading conditions, etc.) [8]. Hence, a proper characterization of role of contamination on the bond line failure requires a meticulous examination of a well-defined contaminant-adhesion system under the controlled level of surface contamination for a particular bond line geometry.

This study aims to understand the effect of surface contamination on the interfacial toughness and strength of polymer-based interfaces under different modes of fracture. We examined a typical adhesive/adherend material system (Hysol EA9394/Hexcel IM7-G/8552) exposed to a common aviation hydraulic fluid (MIL-PRF-85570) at varying contamination concentrations. The desired contaminant surface concentration was controlled by the volume of the solution, and verified by performing infrared spectroscopy to be within few percent. Accordingly, double cantilever beam (DCB), end-notched flexure (ENF), and single lap joint (SLJ) tests were performed to measure the corresponding interfacial strength and toughness. Mode-I and mode-II fracture toughness of the bond line was measured by DCB and ENF tests, respectively. In addition, SLJ test, providing mixed-mode fracture state, was performed to examine the influence of contamination level on the apparent shear strength of the bond line.

D. Yavas • X. Shang • A.F. Bastawros (✉)
Department of Aerospace Engineering, Iowa State University, Ames, IA 50011-2271, USA
e-mail: dyavas@iastate.edu; bastaw@iastate.edu

J. Carroll et al. (eds.), *Fracture, Fatigue, Failure and Damage Evolution, Volume 7*, Conference Proceedings of the Society for Experimental Mechanics Series, DOI 10.1007/978-3-319-62831-8_10

10.2 Experimental Framework

The fracture DCB, ENF, and SLJ samples consist of two adherend composite panels bonded by a layer of adhesive with thickness of 400 μm. Adherend panels with a layup $\left[\pm 45^{o}, 0_5^{o}\right]_S$, were constructed by stacking 10 plies unidirectional prepregs (Hexcel IM7-G/8552) and two additional surface plies of bi-directional weaved fabric (Hexcel W3B-282). Standard fabrication of vacuum bagging and hot-press curing methods were used to produce the adherend panels. A typical aerospace-level adhesive Loctite Hysol EA9394 was examined. We utilized MIL-PRF-85570 aviation hydraulic fluid with four levels of contaminant surface concentration: 1, 3, 10, 55 μg/cm^2, which correspond to non-volatile residue cleanliness levels of A, C, G, J, respectively, defined in MIL-STD-1246C. The surface contaminant concentration was accomplished by Hexane dilution to the desired level. The diluted solution was uniformly applied on the roughened and cleaned surface of the adherend panels. The desired surface concentration was controlled by the height of the solution, and verified by performing infra-red spectroscopy to be within few percent.

All facture tests were performed under displacement control at a loading rate of 0.02 mm/s using an Instron 8862 servo-electric computer controlled testing frame, following the corresponding ASTM standards [9, 10]. Force, cross-head displacement and in-situ digital images of the interfacial crack growth were recorded simultaneously. Three samples were tested for each level of contaminant concentration. Prior to all DCB and ENF tests, an initial loading/unloading step was performed to sharpen the manufactured blunt crack-tip. Mode-I and Mode-II energy release rate curves were derived from the measured force, cross-head displacement, and instantaneous crack length obtained from DCB and ENF tests.

10.3 Results

First, DCB tests were performed to determine the mode-I fracture toughness. A representative set of force-displacement curves for the examined cases are shown in Fig. 10.1a. The slight variation in the initial loading stiffness arises from the differences in the initial crack length, being determined after an initial loading/unloading cycle to sharpen the crack tip. The control case exhibits a minor force plateau on the force-displacement curve before the start of the crack growth. To the contrary, all contamination levels have shown a linear increase up to the onset of crack growth, which can be attributed to the contamination-induced suppression of plasticity within the bond line. The bond line strength exhibits a gradual reduction with increasing the contaminant concentration. Upon reaching the critical load carrying capacity of the bond line, the measured force shows progressive drops, accompanied with successive crack propagation. The associated zig-zag pattern is attributed to the intermittent propagation and arrest of the interfacial crack or relaxation of the fracture energy, followed by building up of the fracture driving forces. The corresponding mode-I energy release rate curves calculated by modified beam theory

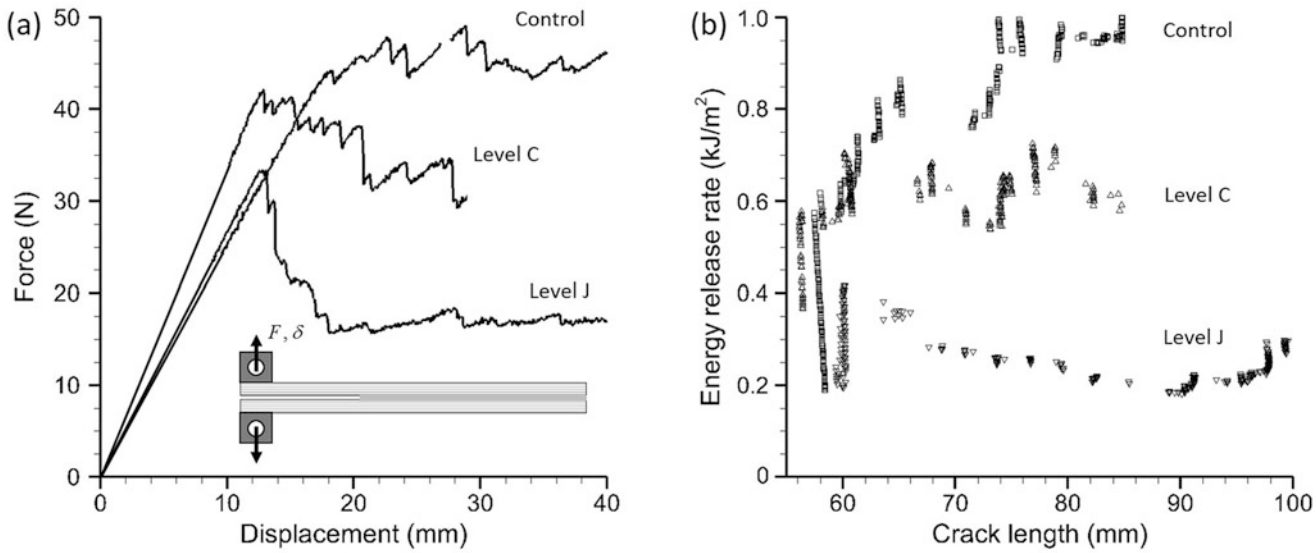

Fig. 10.1 (**a**) A representative set of force-displacement curves and (**b**) the corresponding mode-I fracture energy release rate curves, obtained from DCB experiments, for the examined cases

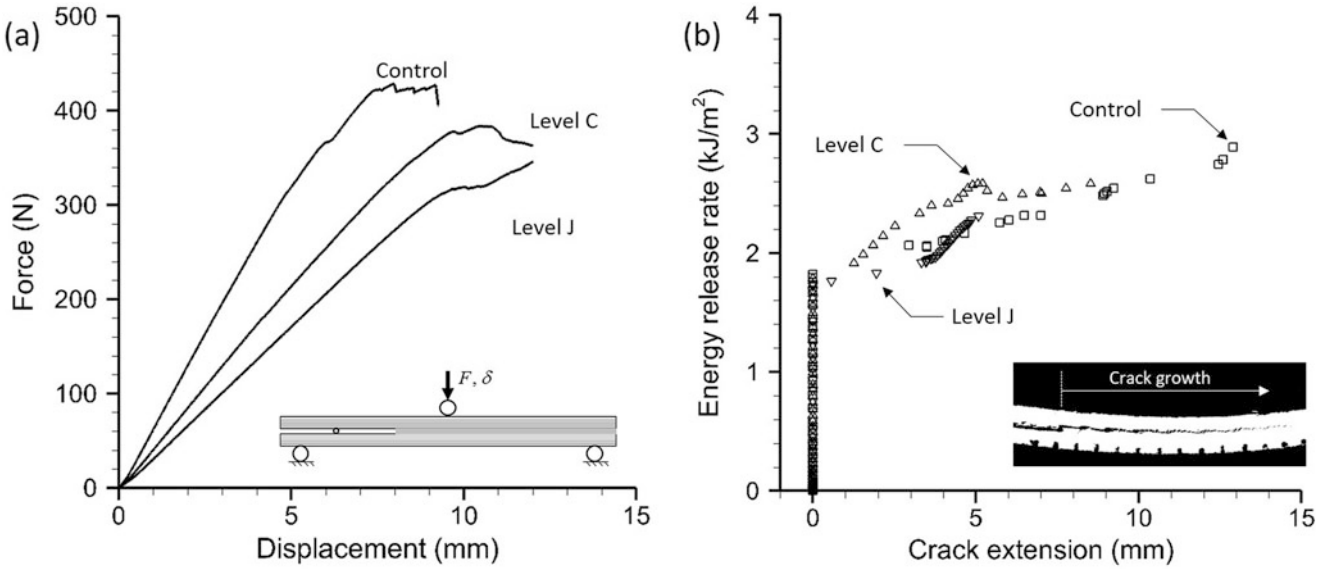

Fig. 10.2 (**a**) A representative set of force-displacement curves and (**b**) the corresponding mode-II fracture energy release rate curves, obtained from ENF experiments, for the examined cases

[9] are presented on Fig. 10.1b. Sudden jumps in the measured energy release rate of the control case clearly show the arrest and propagation of the crack, which can be attributed to the reestablishment and collapse of the plastic process zone within the bond line. To the contrary, crack growth along the contaminated surface is relatively stable. In fact, the stability of the crack growth tends to increase for increasing contamination level, which can be perceived as another evidence for the contamination-induced shielding of the plastic process zone within the adhesive layer.

Second, ENF tests were employed to characterize mode-II fracture toughness for varying contaminant concentration. Figure 10.2a depicts a representative set of force-displacement curves for the tested cases by ENF. Similarly, the variation in the initial stiffness is attributed to different initial crack length among the samples. It can be argued that, unlike mode-I bond line strength, the mode-II bond line strength is not significantly affected by increasing level of contamination. Figure 10.2b shows the corresponding mode-II energy release rate curves derived by corrected beam theory [11]. The initiation mode-II fracture energy was measured to be about 2 kJ/m^2 for all examined cases. As the crack starts to advance, the energy release rate curves exhibit a linear rise up to the same steady-state level at about 2.3 kJ/m^2. Therefore, one can note that the examined contamination does not show a notable influence on the mode-II fracture toughness and strength of the examined adhesive/adherend material system.

The steady-state level values of the energy release rate curves were considered to be the bond line toughness for the corresponding mode of fracture. Figure 10.3a, b summarizes the measured mode-I and mode-II bond line toughness as a function of contaminant surface concentration. As can be clearly seen, mode-I toughness exhibits a significant degradation with increasing concentration level, shown in Fig. 10.3a. A trace level of contamination (level C) can result in about 20–25% reduction of bond line toughness, moreover level J can further reduce mode-I toughness to the level that is an order of magnitude lower than the reference level. The authors have previously shown a correlation between mode-I bond line toughness and contaminant concentration for a different contaminant [11]. The contaminant examined in this study also causes a degradation mechanism displaying a very similar correlation with the surface concentration. In addition, the inserted images on Fig. 10.3a are optical images of the representative fracture surfaces for the presented cases. In the control case, the fabric weave periodicity completely appears on the fracture surface. This is a clear indication of fiber-tear failure, which is generally associated with enhanced ductility of the adhesive layer. To the contrary, the 55 μg/cm^2 contaminated fracture surface displays smooth adhesive surface. Such surface morphology implies that the separation occurs at the adhesive/adherend interface, which is attributed to brittle interfacial (adhesive) failure. The intermediate contamination level of 3 μg/cm^2 case exhibits a combination of both failure modes. On the other hand, mode-II bond line fracture toughness varies within few percent range of 2.2 kJ/m^2 for increasing contaminant concertation, as shown in Fig. 10.3b. It is found to be almost insensitive to the examined contamination.

Finally, SLJ tests were performed to examine the influence of the contamination on the bond line shear strength. Figure 10.4 shows a representative set of force-displacement curves for the examined cases. All cases exhibit an initial linear force rise up, which is followed by a nonlinearity commencing almost at the same force level (4 kN) for all cases. Then the failure

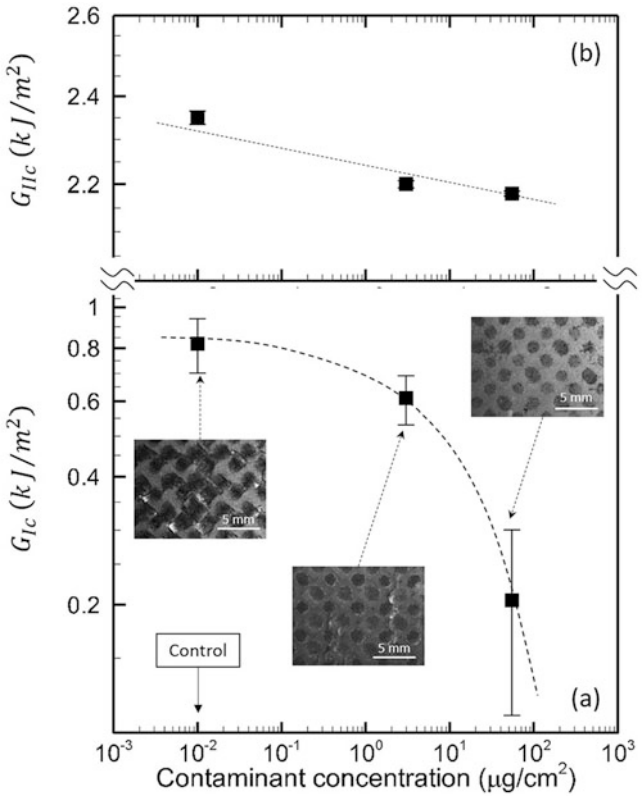

Fig. 10.3 Summary of the experimentally measured bond line mode-I (**a**) and mode-II (**b**) fracture toughness as a function of the contaminant surface concertation (both axes are on logarithmic scale). The inserted images depict the representative fracture surface morphology of the presented cases tested by DCB

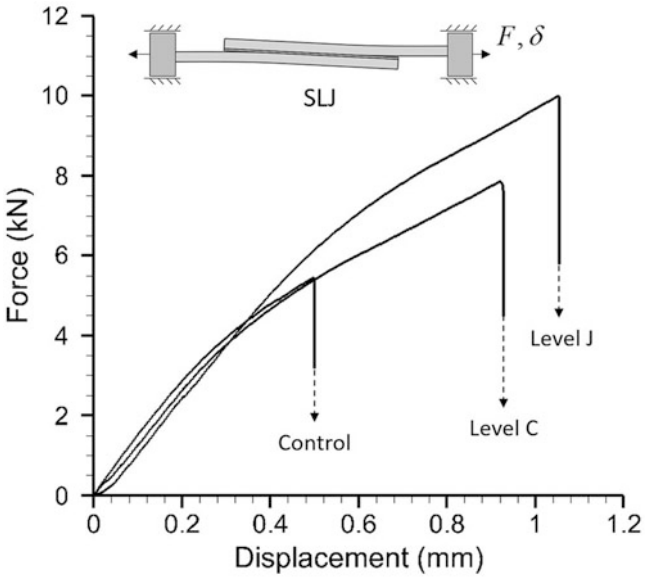

Fig. 10.4 A representative set of force-displacement curves obtained from SLJ experiments for the examined cases

takes place with an unstable crack initiation and propagation, which results in a large force drop in force-displacement curves. The failure load is measured to be about 6 and 10 kN for the control and 55 μg/cm^2 contaminated cases, respectively. Figure 10.5 summarizes the measured SLJ shear strength as a function of contaminant surface concentration on logarithmic scale. Interestingly, the joint strength exhibits an enhancement with increasing contaminant concentration. In addition, the image

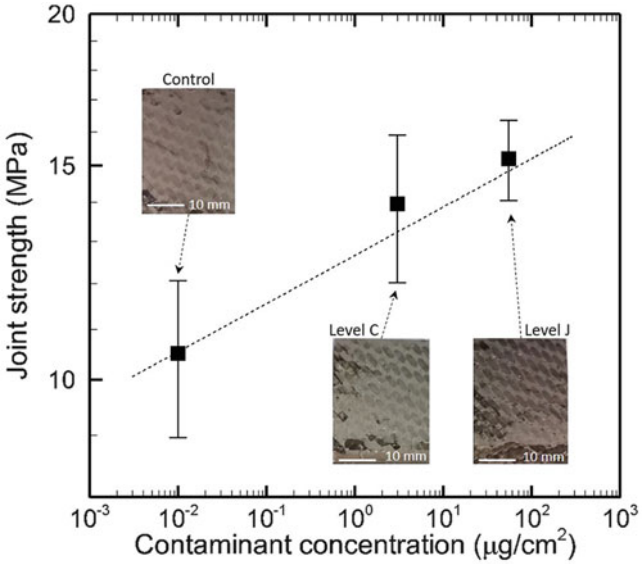

Fig. 10.5 Summary of the experimentally measured SLJ shear strength as a function of the contaminant surface concertation (both axes are on logarithmic scale). The inserted images depict the fracture surface morphology of the presented cases

inserts on Fig. 10.5 depict optical images of the representative fracture surfaces for the reported cases. Unlike the failure mode transition seen for mode-I fracture, SLJ fracture surface morphology reveals a reverse failure transition from brittle to ductile failure as the contaminant concentration increases. Such failure mode transitions can be related to enhanced plastic deformation of the adhesive layer. The authors have previously shown that the examined contaminant leads to 10–15% drop in the plastic flow stress of the examined adhesive [12, 13]. Hence, the contamination-induced softening of the adhesive layer provides improved plasticity, thereby increases the nucleation stress in the SLJ geometry.

10.4 Conclusions

The presented study revealed the effect of surface contamination on the interfacial toughness and strength of polymer-matrix interfaces. A typical adhesive/adherend material system exposed to a common aviation hydraulic fluid at varying contamination concentrations was examined. We have performed DCB, ENF, and SLJ tests to examine the behavior of the contaminated bond line under different fracture modes. Mode-I fracture toughness and bond line strength exhibited a gradual deterioration with increasing contaminant concentration. Whereas, mode-II fracture toughness and strength were found to be insensitive to the contaminant concentration. On the other hand, increasing contamination level resulted in a gradual enhancement in SLJ shear strength. Such contradictory effect can be attributed the nucleation vs. propagation of interfacial cracks. In general, bond line contamination weakens the interfacial bonding, and reduces the interfacial strength and fracture toughness, as seen for mode-I fracture tests. In addition, as a secondary effect, it reduces plastic flow stress of the adhesive layer [12, 13], which resulted in the observed increase of the local plastic dissipation in the SLJ geometry.

Acknowledgements This work was supported by NAVAIR through Redwood scientific Inc. under contract No. 104728.

References

1. Crocombe, A.D., Hua, Y.X., Loh, W.K., Wahab, M.A., Ashcroft, I.A.: Predicting the residual strength for environmentally degraded adhesive lap joints. Int. J. Adhes. Adhes. **26**(5), 325–336 (2006)
2. Katnam, K.B., Sargent, J.P., Crocombe, A.D., Khoramishad, H., Ashcroft, I.A.: Characterisation of moisture-dependent cohesive zone properties for adhesively bonded joints. Eng. Fract. Mech. **77**(16), 3105–3119 (2010)
3. Markatos, D.N., Tserpes, K.I., Rau, E., Markus, S., Ehrhart, B., Pantelakis, S.: The effects of manufacturing-induced and in-service related bonding quality reduction on the mode-I fracture toughness of composite bonded joints for aeronautical use. Compos. Part B. **45**(1), 556–564 (2013)

4. Wetzel, M., Holtmannspötter, J., Gudladt, H.-J., Czarnecki, J.V.: Sensitivity of double cantilever beam test to surface contamination and surface pretreatment. Int. J. Adhes. Adhes. **46**, 114–121 (2013)
5. Paulauskas, F.L., Meek, T.T., David Warren, C.: Adhesive bonding via exposure to microwave radiation and resulting mechanical evaluation. In: MRS Proceedings, vol. 430, p. 193. Cambridge University Press, New York (1996)
6. Anderson, G.L.: Continuum and fracture mechanical studies of contaminated bonding surfaces. J. Adhes. **41**(1–4), 129–137 (1993)
7. Davis, G.D.: Contamination of surfaces: origin, detection and effect on adhesion. Surf. Interface Anal. **20**(5), 368 (1993)
8. Olsson-Jacques, C.L., Wilson, A.R., Rider, A.N., Arnott, D.R.: Effect of contaminant on the durability of epoxy adhesive bonds with alclad 2024 aluminium alloy adherends. Surf. Interface Anal. **24**(9), 569–577 (1996)
9. ASTM D5528-13: Standard Test Method for Mode I Interlaminar Fracture Toughness of Unidirectional Fiber-Reinforced Polymer Matrix Composites. ASTM International, West Conshohocken (2013)
10. ASTM D7905/D7905M-14: Standard Test Method for Determination of the Mode II Interlaminar Fracture Toughness of Unidirectional Fiber-Reinforced Polymer Matrix Composites. ASTM International, West Conshohocken (2014)
11. Yavas, D., Bastawros, A.F.: Prediction of interfacial surface energy and effective fracture energy from contaminant concentration in polymer-based interfaces. ASME. J. Appl. Mech. **84**(4), 044501 (2017)
12. Yavas, D., Shang, X., Hong, W., Bastawros, A.F.: Utilization of nanoindentation to examine bond line integrity in adhesively bonded composite structures. Int. J. Fract. **204**(1), 101–112 (2017)
13. Yavas, D., Bastawros, A.F.: Measurement of bond line fracture toughness in adhesively bonded composite structures by nanoindentation. In: Zehnder, A., et al. (eds.) Fracture, Fatigue, Failure and Damage Evolution Conference Proceedings of the Society for Experimental Mechanics Series, vol. 8. Springer, Cham (2017)

Chapter 11
Direct and Simultaneous Extraction of Mixed-Mode Traction-Separation Relations

Chenglin Wu, Rui Huang, and Kenneth M. Liechti

Abstract Traction-separation relations can be used to represent the interactions between two surfaces during separation. In the past, characterizing these interactions, particularly under mixed-mode conditions has been tedious. In this work, a direct method is proposed to simultaneously determine the normal and shear components of traction-separation relations at any mode-mix, based solely on measurements of the initial crack length, load and load-line displacement and rotation of each adherend in a laminated beam configuration.

Keywords Mixed-mode • Interfacial fracture • Traction-separation relations • Direct extraction

11.1 Introduction

Traction-separation relations can be used to represent the interactions between two surfaces during separation. In the past, characterizing these interactions, particularly under mixed-mode conditions has been tedious. In this work, a direct method is proposed to simultaneously determine the normal and shear components of traction-separation relations at any mode-mix, based solely on measurements of the initial crack length, load and load-line displacement and rotation of each adherend in a laminated beam configuration.

A series of experiments were conducted to extract the vector traction-separation relations between silicon and epoxy over a wide range of mixed-mode conditions for positive and negative shear. A custom-built loading device was developed to provide the measurements alluded to above. Since the vector traction-separation relations are extracted in a direct manner with no a priori assumptions as to their form, it was possible to examine the applicability of potential versus non potential representations of mixed-mode traction-separation relations for this interface.

11.2 Experiments

The experimental program can be illustrated through asymmetric DCB configuration as shown in Fig. 11.1. In this configuration, the top and bottom adherends are made of different materials with different loading conditions. The target measurements are load (P_1 , P_2), end-displacement (Δ_1 , Δ_2), and end-rotation (θ_1 , θ_2).

Schematics of the apparatus and the specimen geometry are shown in Fig. 11.2a, b, respectively. The loading device is a slightly modified version of the one that was used in previous work [1]. The left end of the specimens were clamped. A 45° prism was mounted on the top surface of the top adherend above the loading point on the right end. A laser beam was projected onto the surface of the prism so that the reflection was almost parallel to the axis of the silicon and incident on a position sensing detector. Both ELS and ENF specimens were used for the experiment.

The end-rotation of the top adherend (θ_1) was then determined by the vertical movement of the laser spot on PSD (Δd) and the distance between the prism and the PSD (L) as $\theta_1 = 1/2 \arctan(\Delta d/L)$. The resolution of the end-rotation measurement is then estimated to be at 1×10^{-4} radian. A photonic sensor with a resolution of 0.1 μm was placed at a distance of a_0 toward the loaded end to measure the deflection Δ_{20} of the lower adherend. Given that the displacement of bottom adherend

C. Wu (✉)
Department of Civil, Architectural, and Environmental Engineering, Missouri University of Science and Technology, Rolla, MO 65409, USA
e-mail: chenglinwu@utexas.edu

R. Huang • K.M. Liechti
Department of Aerospace Engineering and Engineering Mechanics, University of Texas, Austin, TX 78712, USA

J. Carroll et al. (eds.), *Fracture, Fatigue, Failure and Damage Evolution, Volume 7*, Conference Proceedings of the Society for Experimental Mechanics Series, DOI 10.1007/978-3-319-62831-8_11

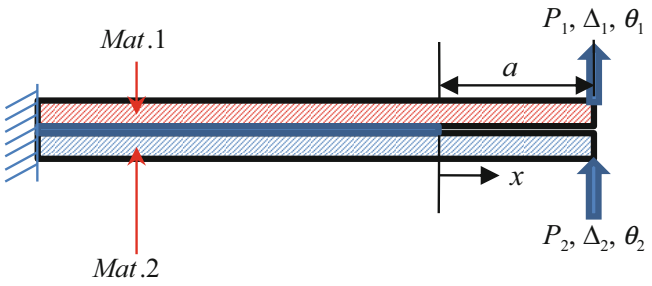

Fig. 11.1 Asymmetric DCB

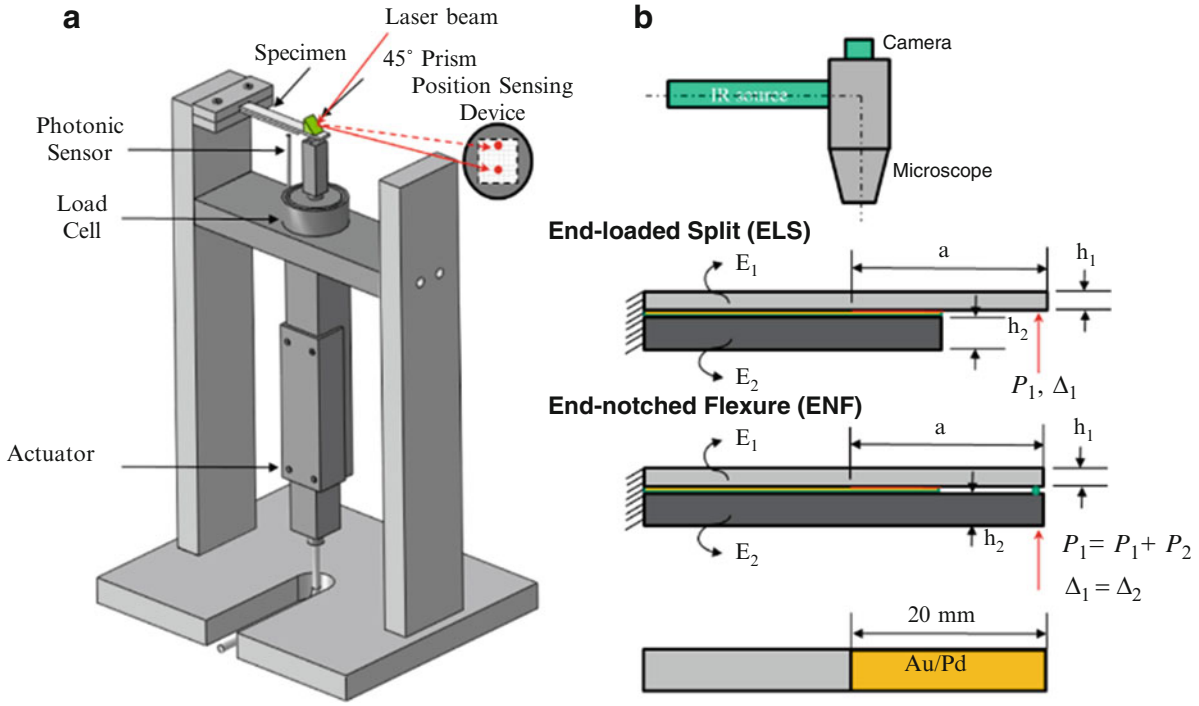

Fig. 11.2 (**a**) Schematic of loading device, (**b**) specimen configuration

at the location of the initial crack front was monitored and found to be negligible, the end-rotation of the bottom adherend was obtained as $\theta_2 = \Delta_{20}/a_0$. In addition, the end displacement of the bottom adherend was obtained as $\Delta_2 = (a/a_0)\Delta_{20}$. For the ELS specimen, only the top adherend was loaded ($P_2 = 0$), P_1 , Δ_1 were obtained from the load cell and the prescribed displacement. For the ENF configuration, the total force applied ($P = P_1 + P_2$) was measured. The force applied to each beam was obtained using the NCOD measurements which will be mentioned as follows.

Classical crack opening interferometry was used to measure the normal crack opening displacement (NCOD) as silicon is transparent to infra-red. This infrared crack opening interferometry (IR-COI) technique essentially uses the interference between the two rays reflected from the crack surfaces to determine the distance between them. The normal infra-red incident beam was provided using an infrared microscope (Olympus BH2-UMA) that was fitted with an internal beam splitter and an IR filter (1040 ± 15 nm). The images of the region near the crack front were obtained using a digital camera (Lumenera Corporation, Infinity 3) with a resolution of 1392 × 1040 pixels. The images were then processed to determine the NCOD. The IR-COI technique implemented in this work has a resolution of 20 nm in the NCOD. It should be noted here that in this experiment, all data were collected and synchronized within single Labview® control program.

For the specimens, the top adherend was made of silicon. The bottom was made of various materials including acrylic, glassy-polymer, glass-filled polymer, silicon, aluminum, copper, and stainless steel to cover wide range of mode-mix angle ($-50^\circ < \psi < 90^\circ$).The thickness of the top beam (h_1) was kept constant at 1 mm. The thickness of the specimens were controlled ($h_2 = h_1\sqrt{D_1/D_2}$, $D_i = \frac{E_i h_i^3}{12(1-\nu_i^2)}$, E_i, ν_i, $i = 1,2$, are the Young's modulus and Poisson's ratio for each adherend, respectively) to maintain a so called "balanced condition" [2].

11.3 Analysis and Results

From [2], when the balanced condition is met, the J-integral for mode I and II can be expressed in terms of the far-field measurements explicitly as

$$J_I = \widehat{D}\left(\frac{P_1}{D_1} - \frac{P_2}{D_2}\right)(\theta_1 - \theta_2)\,, \tag{11.1}$$

$$J_{II} = \frac{\widehat{A}}{4}\frac{h_1}{D_1}P\,(h_2\theta_2 + h_1\theta_1)\,, \tag{11.2}$$

where $\widehat{A} = \left(\frac{1}{A_1} + \frac{1}{A_2} + \frac{h_1^2}{4D_1} + \frac{h_2^2}{4D_2}\right)^{-1}$, $A_i = \frac{E_i h_i}{1-\upsilon_i{}^2}$.

The local CTOD can also be computed using far-field measurements through following equations,

$$\delta_n^* = (\Delta_1 - \Delta_2) + \frac{a^3}{6}\left(\frac{P_1}{D_1} - \frac{P_2}{D_2}\right) - a\,(\theta_1 - \theta_2)\,, \tag{11.3}$$

$$\delta_t^* = \frac{1}{2}\,(h_1\theta_1 + h_2\theta_2) - \frac{h_1}{4D_1}Pa^2, \tag{11.4}$$

where δ_n^*, δ_t^* are the normal and shear CTODs, respectively. Then the traction-separation relation can be obtained by taking derivatives of J-integral with respect to local CTODs. ($\sigma^* = \frac{\partial J_I}{\partial \delta_n^*}$, $\tau^* = \frac{\partial J_{II}}{\partial \delta_t^*}$). It should be noted here that for the ENF specimens, the force distributed to each beam is challenging to measure due to spatial limitations. Therefore, the NCOD were measured using IR-COI to provide force measurements on top adherend (P_1) using relationship derived from Eq. (11.3) since the total force is measured ($P = P_1 + P_2$),

$$P_1 = \widehat{D}\left\{\frac{P}{D_2} + \frac{6}{a^3}\left[\delta_n^* + (\theta_1 - \theta_2)\,a\right]\right\}. \tag{11.5}$$

The extracted TSR for mode-mix angle of $\psi = 26.97^\circ$ are shown in Fig. 11.3. In the normal TSR, an initially stiffening response was observed. In the past, the response prior to the maximum traction has been universally represented by linearly elastic behavior. Time constraints have not allowed further investigation to determine if the stiffening behavior is elastic. A stiffening response is certainly consistent with rubber-like behavior and may relate to randomly oriented polymer chains in

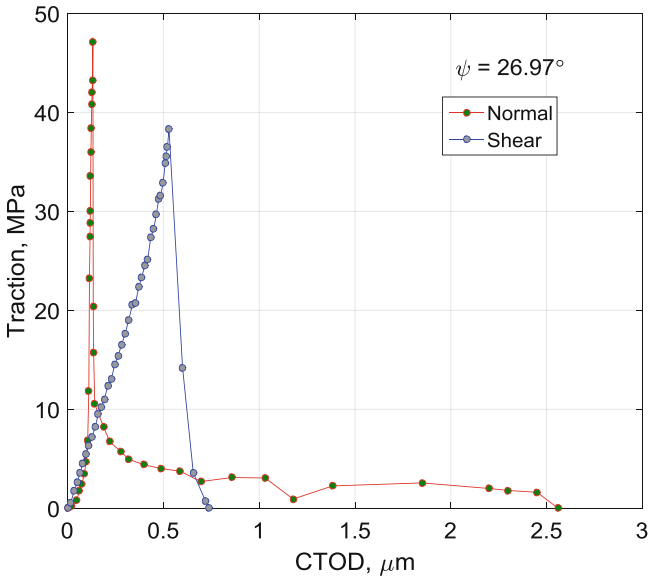

Fig. 11.3 Extracted TSR for ELS specimen with silicon as substrate ($\psi = 26.97^\circ$)

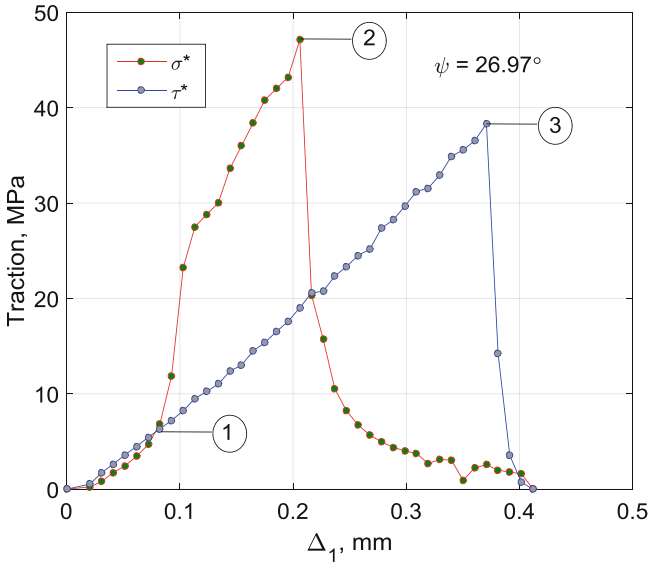

Fig. 11.4 Development of TSRs: traction versus end-displacement ($\psi = 26.97^{\circ}$)

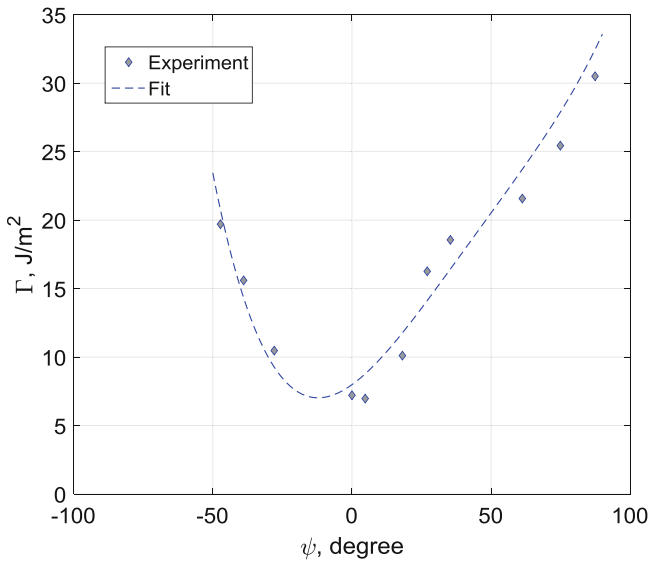

Fig. 11.5 Toughness versus phase angle

the epoxy interphase being oriented normal to the interface as the loading is increased. The normal traction reached its peak at a normal separation of approximately 130 nm which was very close to the values found in previous work [1], albeit with a different epoxy. The peak strength was about 48 MPa which was at the elastic limit of the epoxy used in present study. After the peak, the normal traction dropped suddenly and eased into a plateau with an average strength of 2 MPa, which ended at a normal separation of 2.5 μm. The descending traction also followed a power-law type function of separation, with a steeper decay than has been previously described by exponential functions. The shear TSR had an essentially linear response till the shear traction reached its peak. After the peak, the traction dropped very rapidly to zero with very small increase in separation for a shear interaction range of 0.7 μm, much smaller than the range of the normal interaction.

The development of the tractions were considered in detail (Fig. 11.4). Between zero and point ①, the response is linear for both tractions near the original crack front. After point ①, the normal traction increases much more rapidly than the linearly increasing shear traction. After point ②, the normal traction decreases sharply while the shear traction maintains its constant growth rate. However, after point ③, the shear traction rapidly decayed to zero simultaneously with the normal traction. The implication of this sequence of events is that damage in each response is not coupled as is commonly assumed.

The obtained toughness versus the mode-mix phase angle was plotted in Fig. 11.5. As shown, the variation of toughness with mode-mix can be approximated using a 4th order polynomial function. The toughness increased with increasing phase

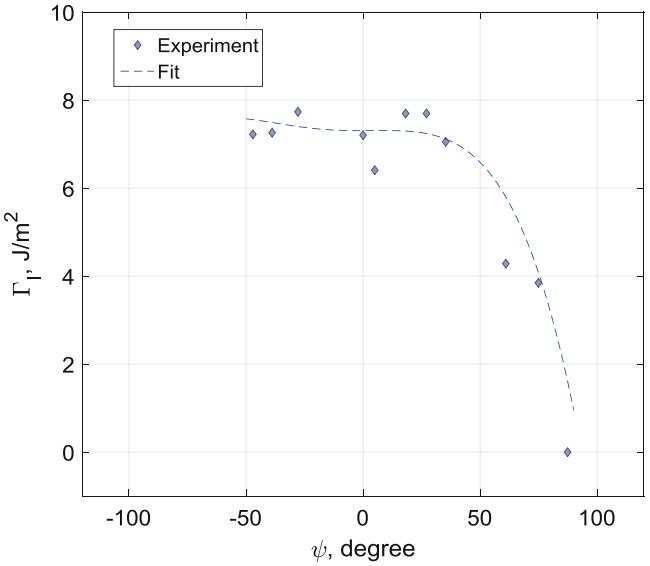

Fig. 11.6 Mode I toughness versus phase angle

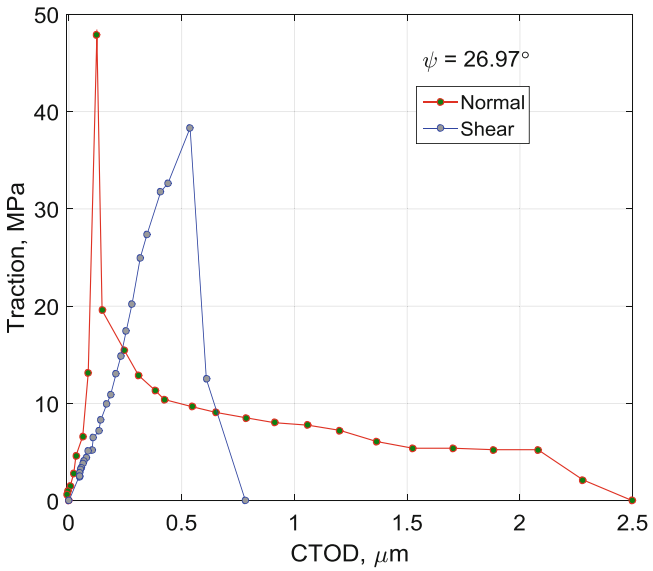

Fig. 11.7 Interfacial TSR for ELS specimen with silicon as substrate ($\psi = 26.97^{\circ}$)

angle and exhibited the same asymmetric behavior with respect to mode-mix that has been noted for the total toughness of glass/epoxy and sapphire/epoxy interfaces. The mode-I toughness was essentially constant for negative mode-mix angles (Fig. 11.6) and then dropped sharply for angles above 50°.

The extracted TSRs using the beam analysis include the behavior of epoxy layer, leaving open the question as to how much of the extracted total separation is due to the separation of the two interfaces and how much is due to the bulk epoxy. In doing so, it is recognized that it is likely that a thin interphase layer forms in the epoxy next to the silicon.

This interphase is expected and has been shown to have mechanical and fracture behavior that differs from those of the bulk epoxy. The contribution of the bulk behavior of the epoxy to the total separation was assumed to be elastic. The contribution was determined by first conducting a finite element analysis of two silicon strips with the corresponding extracted traction-separation relation active between them. This analysis established the extent of the cohesive zone and the tractions acting over it. This distribution of tractions was then applied to a strip of epoxy having the thickness of the epoxy in the experiment. The bottom of the epoxy was fixed in both directions. After removing the elastic response of the epoxy layer in the cohesive zone, the ascending part of the normal TSR has a much higher stiffness. The effect of the epoxy layer on the descending portion of the traction-separation relation is less noticeable (Fig. 11.7).

11.4 Conclusions

The vectorial interfacial TSRs for silicon/epoxy interface were extracted directly and simultaneously for a wide range of mode-mix. A decoupled normal and shear TSRs were observed. The effect of epoxy deformation was also investigated.

Acknowledgments The authors gratefully acknowledge funding of this work by Semiconductor Research Corporation.

References

1. Wu, C., Gowrishankar, S., Huang, R., Liechti, K.M.: On determining mixed-mode traction–separation relations for interfaces. Int. J. Fract. (2016). doi:10.1007/s10704-016-0128-4
2. Wu, C.: Using far-field measurements for determining mixed-mode interactions at interfaces. Dissertation, The University of Texas at Austin (2016)

Chapter 12
Damage Evolution in 304L Stainless Steel Partial Penetration Laser Welds

Sharlotte Kramer, Amanda Jones, John Emery, and Kyle Karlson

Abstract Partial penetration laser welds join metal surfaces without additional filler material, providing hermetic seals for a variety of components. The crack-like geometry of a partial penetration weld is a local stress riser that may lead to failure of the component in the weld. Computational modeling of laser welds has shown that the model should include damage evolution to predict the large deformation and failure. We have performed interrupted tensile experiments both to characterize the damage evolution and failure in laser welds and to aid computational modeling of these welds. Several EDM-notched and laser-welded 304L stainless steel tensile coupons were pulled in tension, each one to a different load level, and then sectioned and imaged to show the evolution of damage in the laser weld and in the EDM-notched parent 304L material (having a similar geometry to the partial penetration laser-welded material). SEM imaging of these specimens revealed considerable cracking at the root of the laser welds and some visible micro-cracking in the root of the EDM notch even before peak load was achieved in these specimens. The images also showed deformation-induced damage in the root of the notch and laser weld prior to the appearance of the main crack, though the laser-welded specimens tended to have more extensive damage than the notched material. These experiments show that the local geometry alone is not the cause of the damage, but also microstructure of the laser weld, which requires additional investigation.

Keywords Damage evolution • Ductile fracture • Laser weld • Computational modeling • Void nucleation

12.1 Introduction

Laser welds are a type of joint formed by the melting of two metals at a seam with a high-powered laser. Oftentimes these welds do not fully penetrate the thickness of the material to prevent damage to nearby heat-sensitive material [1]. These partial penetration laser welds have a crack-like geometry with a local stress riser, leading to failure in the weld of a component under loading. In this study, we consider 304L stainless steel (SS) partial penetration laser welds; Fig.12.1a is a cross-section of a typical butt-type laser weld in this study with approximately 0.75-mm depth in a 1.55-mm thick sheet. 304L SS is a highly ductile metal, leading to questions of whether the deformation damage mechanisms at the root of the laser weld are dominated by plastic deformation, ductile rupture, void nucleation and growth, or growth of pre-existing pores from the welding process. Previous research has considered deformation of laser welds with the unwelded ligament removed to exclude the stress riser in an initially partial penetration laser weld in 304L SS [2, 3] and quantified the variations in weld root porosity [4, 5], but this is the first experimental study to systematically characterize damage evolution in these laser welds with the full partial penetration geometry. A computational study of laser weld deformation, based on limited experimental tensile data, combined the material and geometric effects into a surrogate model to represent the laser weld deformation for a component-level analysis with some success [6]. Due to the pragmatic approach of this research, the details of different damage mechanisms were neglected. A different computational study considered the effect of porosity on deformation in laser welds with the unwelded ligament removed [3]. Recent computational efforts in conjunction with this study, with higher-fidelity modeling of full partial penetration laser weld geometry, have highlighted many of the unknowns of the damage evolution. Computational modeling of tensile loading of the local geometry of the laser weld, based on material model calibration of the tensile tests of the base material, cannot predict the early load-drop in the load-displacement behavior of the laser weld geometry. This implies that damage mechanisms based purely on the ductile rupture of the base 304L are

S. Kramer (✉) • A. Jones • K. Karlson
Sandia National Laboratories, 1515 Eubank Blvd. SE, Albuquerque, NM, 87123, USA
e-mail: slkrame@sandia.gov

J. Emery
Component Science and Mechanics, Sandia National Laboratories, Albuquerque, NM, 87185, USA

J. Carroll et al. (eds.), *Fracture, Fatigue, Failure and Damage Evolution, Volume 7*, Conference Proceedings of the Society for Experimental Mechanics Series, DOI 10.1007/978-3-319-62831-8_12

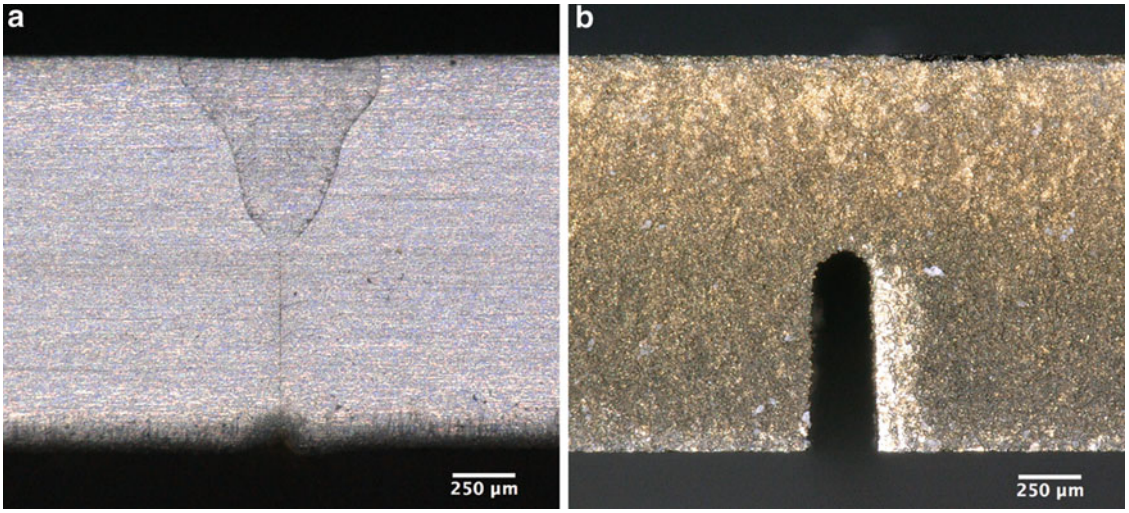

Fig. 12.1 (**a**) Cross-section of a 0.763-mm deep partial penetration laser weld in 1.532-mm thick 304L SS sheet with the laser weld having a keyhole shape and an unwelded ligament (the vertical line below the laser weld); (**b**) Cross-section of an EDM-notched 304L SS sheet with 0.236-mm notch width and a 0.789-mm notch depth that is similar to the unwelded ligament in the laser welded specimens

insufficient to characterize the damage evolution of these laser welds. Experimental evidence of the damage mechanisms is required to guide improvements in these computational models. In this study, we performed interrupted tensile tests of laser-welded 304L SS to interrogate the local deformation and damage mechanisms in the laser weld. Additionally, we performed interrupted tensile tests of EDM-notched 304L SS specimens (see Fig. 12.1b), which have a similar pre-notch depth as the unwelded ligament of the laser-welded specimens, though not the same sharp notch tip, to compare the effect of the local geometry without the complications of the pre-existing porosity, heat affected zone, or change in grain structure in the laser weld as compared to the parent material. In this paper, we detail the experimental methodology of the interrupted testing and post-test measurements of damage, present the experimental results, discuss potential competing damage mechanisms, and identify future areas of research based on these initial findings.

12.2 Methodology

The base material in this study was 304L SS sheet material, approximately 1.55-mm thick. Pairs of 76.2 × 101.6-mm plates were joined along the long edge with a single laser butt weld. These plates were cut into tensile coupons such that the laser weld was perpendicular to the tensile loading direction. In this study, the rolling direction of the parent 304L SS sheet material was along the short edge of the original plates, meaning the rolling direction of the material was in the direction of the global tensile load of the laser welded specimens. The notched tensile specimens were cut from EDM-notched plates (152.4 × 101.6-mm) of the 304L SS with the rolling direction along the tensile direction; the EDM notch was cut in the center of the plate with a nominally 0.2-mm wide EDM-wire, parallel to the short edge of the plate, resulting in a nominally 0.24-mm wide notch with a depth approximately half the thickness of the parent plate. All specimens had a nominal gage width of 6.35-mm.

We performed base material tensile tests on a custom servo-hydraulic load frame with dual, horizontal, in-line actuators, allowing the center of the specimen to be stationary, which was useful for *in situ* imaging of the local geometry of the notched and welded specimens during the interrupted tensile testing. The specimens were oriented with the width of the specimens along the vertical axis. The global displacement for the base material, notched, and laser welded 304L SS specimens was measured using a 25.4-mm gage length extensometer, attached on the thin side of the specimens; the extensometer body hung vertically below the specimen. Figure 12.2 shows the experimental setup, including the Navitar 6000 long-working distance microscope lens and CCD camera that imaged the through-thickness side of the specimens. The base material testing global actuator displacement rate was 12.7 μm/s. The tensile test global actuator displacement rate for the notched and laser welded specimens was 1.27 or 2.54 μm/s. We tested three base material specimens, one notched specimen to failure, five notched specimens to different displacement/load levels, seven laser-welded specimens to failure, and 14 laser welded specimens to different displacement/load levels. The notched specimens came from a single notched plate, but the notch depth varied slightly along the plate. The laser-welded specimens came from three different welded plates with slight

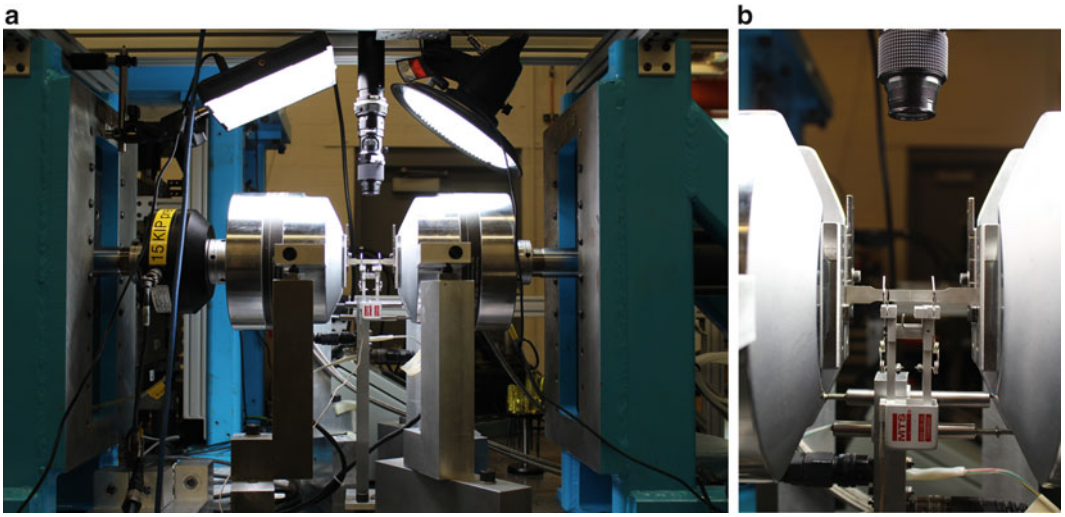

Fig. 12.2 Experimental setup for the interrupted tensile testing and base material tensile testing: (**a**) Custom horizontal, dual-actuator load frame with *in situ* imaging; (**b**) Close-up view of laser-welded specimen with extensometer and *in situ* imaging

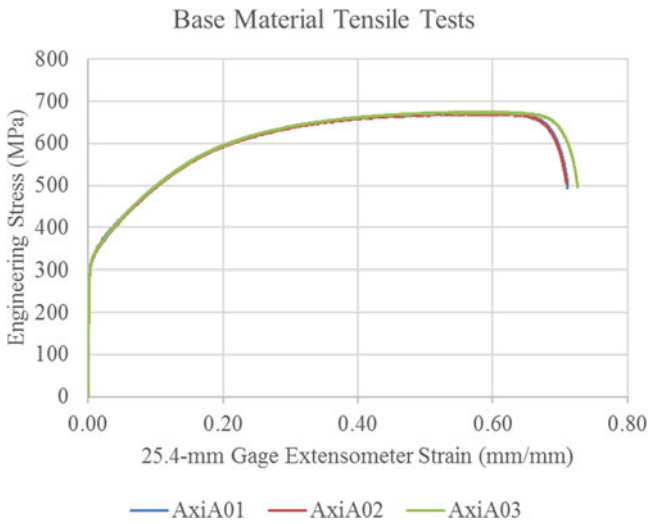

Fig. 12.3 Engineering stress-strain for three base material 304L SS tensile specimens

variations in laser weld depth. The initial interrupted tensile testing focused on loads around peak load for the notched and laser-welded specimens from Plate 4 to 5. Subsequent testing of laser-welded specimens from Plate 6 evenly distributed the tests across the load-displacement curve.

After testing, we imaged the damaged root of the welds and notches using SEM to visualize the damage along the width of the specimens. We also cross-sectioned the deformed specimens along their mid-planes to see the crack growth where there was the highest triaxiality, furthest from the surface. Some of the specimens were etched to see the laser weld structure and the main crack, while others were polished and then SEM imaged in efforts to detect void nucleation.

12.3 Results

Figure 12.3 shows the engineering stress-strain plot for the base material 304L SS, which had a modulus of 197 GPa, 0.2% offset yield stress of 309 MPa, and ultimate strength of 672 MPa. For the 25.4-mm gage length, nominally 6.35-mm gage width, and 1.55-mm thickness, the failure strain was 72% on average.

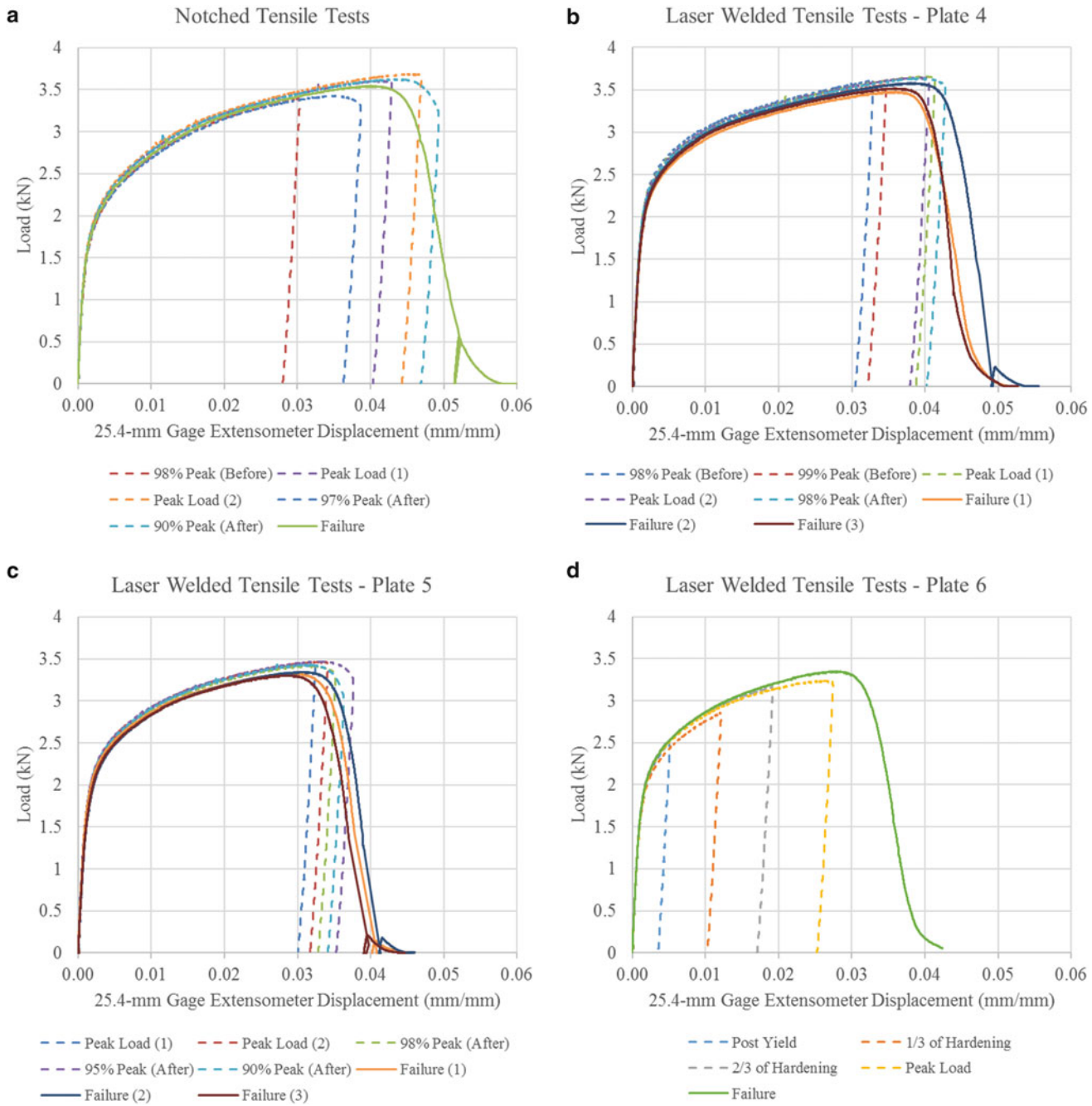

Fig. 12.4 Experimental data from interrupted tensile testing: (**a**) load vs. extensometer normalized displacement for notched specimens; (**b**) load vs. extensometer normalized displacement for Plate 4 of the laser-welded specimens; (**c**) load vs. extensometer normalized displacement for Plate 5 of the laser-welded specimens; and (**d**) load vs. extensometer normalized displacement for Plate 6 of the laser-welded specimens

The average normalized 25.4-mm gage extensometer displacements to failure for laser-welded Plates 4–6 (only one failure specimen for Plate 6) were 0.052, 0.044, and 0.046 mm/mm, respectively. The material above the notched specimens was on average 0.747 mm deep, in between the weld depths of Plates 5 and 6. The normalized 25.4-mm gage extensometer displacement to failure of the notched specimen was 0.058 mm/mm. Dividing the normalized 25.4-mm gage extensometer displacement of each interrupted test specimen by the normalized 25.4-mm gage extensometer displacement to failure of the parent plate allows us to compare the relative percent displacement to failure of each specimen.

The six notched specimen tension tests, whose load versus normalized extensometer displacement plots are shown in Fig. 12.4a, had different load goals and corresponding percent displacements to failure: 98% of the estimated peak load before

peak, 52% displacement to failure; peak load, 74% displacement to failure; a repeat of peak load, 81% displacement to failure; 97% of peak load after peak load, 67% displacement to failure; 90% of peak load after peak load, 85% displacement to failure; and complete failure. Figure 12.4b–d show the load vs. normalized extensometer displacement plots for the laser-welded specimens from Plates 4 to 6, respectively. The load goals and corresponding percent displacements to failure for the eight specimens from Plate 4 were 98% of the estimated peak load before peak, 63% displacement to failure; 99% of the estimated peak load before peak, 66% displacement to failure; peak load, 79% displacement to failure; a repeat of peak load, 77% displacement to failure; 98% of peak load after peak load, 82% displacement to failure; and three specimens to complete failure. The load goals and corresponding percent displacements to failure for the eight specimens from Plate 5 were peak load, 73% displacement to failure; a repeat of peak load, 77% displacement to failure; 98% of peak load after peak load, 79% displacement to failure; 95% of peak load after peak load, 84% displacement to failure; 90% of peak load after peak load, 82% displacement to failure; and three specimens to complete failure. The load goals and corresponding percent displacements to failure for the five specimens from Plate 6 were immediately unloaded after the initial slope change in the load-displacement curve (colloquially called "post-yield" at 76% of the estimated peak load before peak), 11% displacement to failure; one third between the initial slope change and peak load (colloquially called "1/3 of hardening" at 87% of the estimated peak load before peak), 26% displacement to failure; two thirds between the initial slope change and peak load (colloquially called "2/3 of hardening" at 96% of the estimated peak load before peak), 42% displacement to failure; peak load, 60% displacement to failure; and complete failure. Plate 4 had the deepest welds with an average of 0.794 mm; Plate 5 had an average weld depth of 0.757 mm; and Plate 6 had an average weld depth of 0.737 mm. The variation in the displacement to failure for the laser-welded specimens is likely due to weld penetration depth, where the deeper the weld, the longer the displacement to failure.

Figure 12.5 includes central cross-sections of six laser-welded specimens with increasing levels of deformation. These cross-sections, which have been etched to relieve the laser welds, show an increase in crack length with increased deformation. Notably in Fig. 12.5a, a small crack does appear after the initial change in slope of the global load-displacement curve. The crack growth dramatically increases before peak load and afterwards. Figure 12.6 has SEM images of polished central cross-sections of notched and laser-specimens with load levels just before and after peak load. The notched specimens show considerable deformation in the curved portion of the notch, but the presence of cracks is not clear before peak load

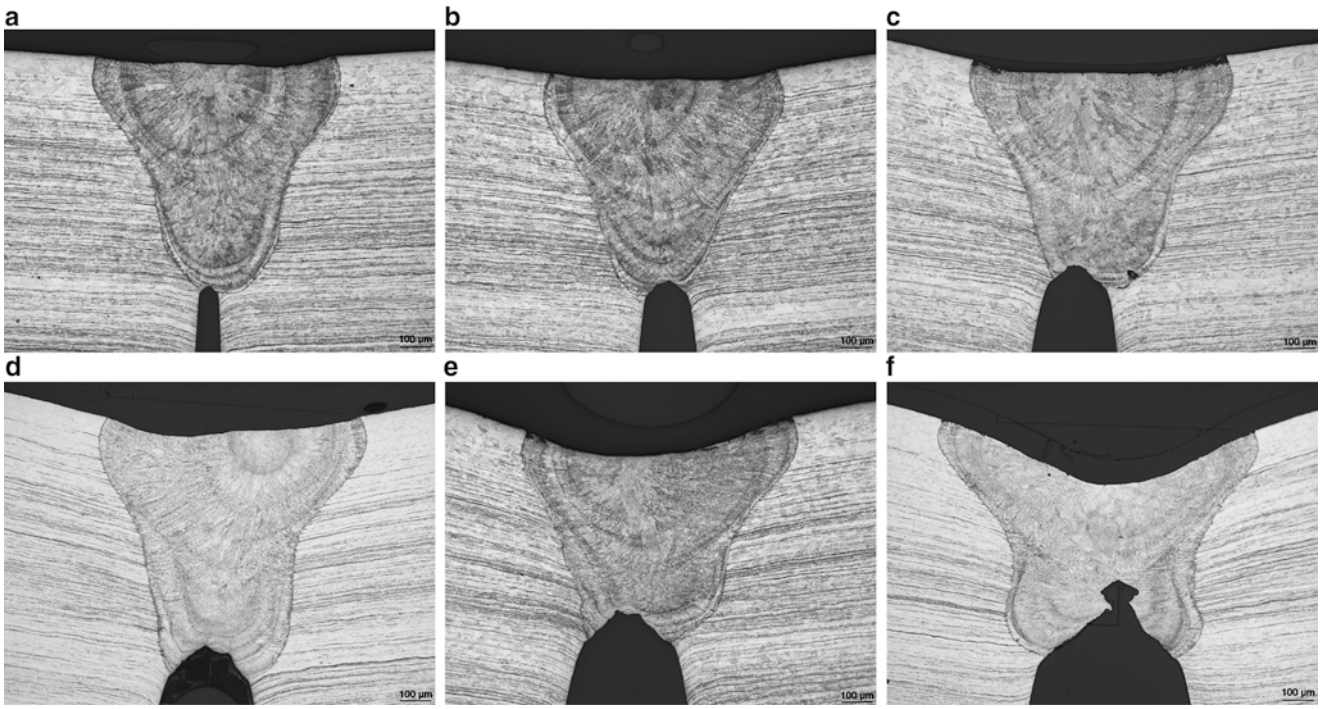

Fig. 12.5 Etched central cross-sections from select laser-welded specimens, showing increased crack growth as displacement increased: (**a**) Plate 6 "post-yield" specimen, 11% displacement to failure; (**b**) Plate 6 "1/3 of hardening" specimen, 26% displacement to failure; (**c**) Plate 6 "2/3 of hardening" specimen, 42% displacement to failure; (**d**) Plate 4 98% peak-load (before estimated peak load) specimen, 63% displacement to failure; (**e**) Plate 6 peak-load specimen, 60% displacement to failure; and (**f**) Plate 5 90% peak-load (after peak load) specimen, 82% displacement to failure

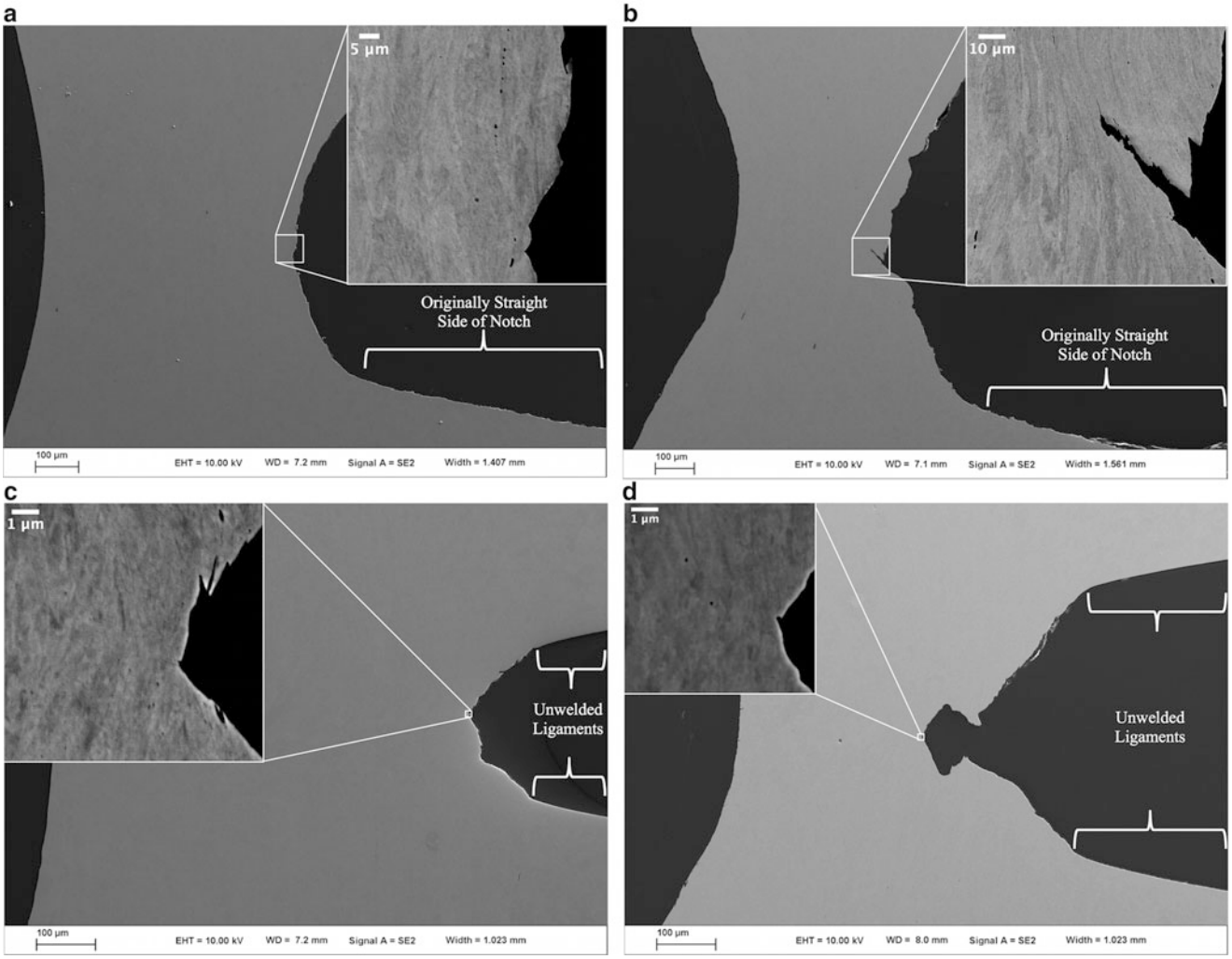

Fig. 12.6 Polished cross-sections from select notched and laser-welded specimens (oriented 90-degrees and inverted from corresponding Fig. 12.5 images), with inset electron backscatter diffraction SEM images near the crack tip to show void nucleation: (**a**) notched 98% peak-load (before estimated peak load) specimen, 52% displacement to failure; (**b**) notched 90% peak-load (after peak load) specimen, 85% displacement to failure; (**c**) Plate 4 98% peak-load (before estimated peak load) specimen, 63% displacement to failure; and (**d**) Plate 5 90% peak-load (after peak load) specimen, 82% displacement to failure

from this view. In contrast, the crack growth into laser welds is apparent in both laser-welded specimens. All four of these specimens show evidence of void nucleation ahead of the free surface in the electron backscatter diffraction (EBSD) SEM view of the root of the notch/crack tip. Figure 12.7 includes SEM images of the root of the notch or laser weld from the perspective of the advancing deformation/crack; these images were taken prior to sectioning and view the central portion of the root of the notch or laser weld. Figure 12.7a, b shows the roots of the notches of the 98% peak load (before estimated peak load) and 90% peak load (after peak load) specimens, which are the same as those in Fig. 12.6a, b. Figure 12.7a clearly shows horizontal cracks at the root of the notch; higher magnification images (not provided here) show micro-scale cracking as well. Figure 12.7b shows the crack more prominently at the root of the notch. Figure 12.7c–f shows the damage and crack propagation of laser-welded specimens with increasing global deformation [note: the image magnification changes with each successive level of deformation]. Figure 12.7c has clear evidence of ductile rupture and horizontal cracks for the least global deformation level, just beyond the slope change of the load-displacement curve; also the preexisting pores from the welding process are deforming and are cracking open, seen as the vertically elongated oval structure in the root of the weld. Figure 12.7d–f shows evidence of extensive plastic deformation, ductile rupture, and pore deformation and coalescence with the main crack.

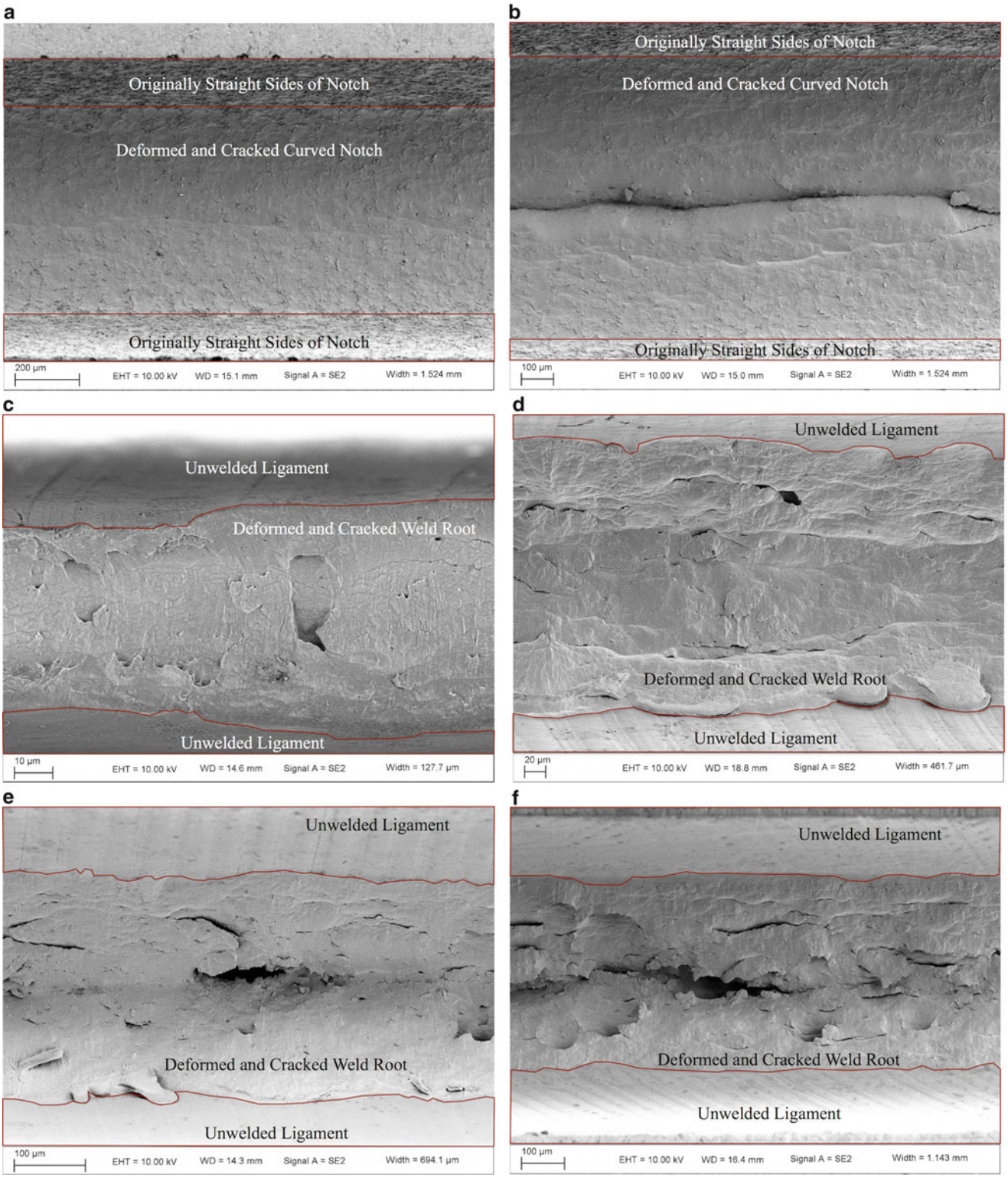

Fig. 12.7 SEM images of the root of select notched and laser welded specimens: (**a**) notched 98% peak-load (before estimated peak load) specimen, 52% displacement to failure; (**b**) notched 90% peak-load (after peak load) specimen, 85% displacement to failure; (**c**) Plate 6 "post-yield" specimen, 11% displacement to failure; (**d**) Plate 4 98% peak-load (before estimated peak load) specimen, 63% displacement to failure; (**e**) Plate 6 peak-load specimen, 60% displacement to failure; and (**f**) Plate 5 90% peak-load (after peak load) specimen, 82% displacement to failure

12.4 Discussion and Future Work

The initial hypothesis used in the computational modeling of these notched and laser-welded geometries of 304L SS was that the global load-displacement curve behavior was dominated by extensive plastic deformation and necking processes of the highly ductile 304L SS base material [6]. In contrast, this experimental study has shown that damage and crack propagation occur much earlier, just after the initial slope change of the global load-displacement curve, progress steadily through the next slope of the global load-displacement curve, and then quickly advances between peak load to failure. This observed behavior is similar to that of a single edge-notched tension (SENT) geometry specimen, but without a fatigue pre-crack; tensile loading of a SENT geometry in a ductile material can provide a J resistance curve [7]. The initial slope-change of the load-displacement curve is potentially due to the local crack growth at the root of the laser weld and not just material yielding and hardening; further research is needed to determine if the blunt notch produces the same crack growth behavior upon the initial slope change of the load-displacement curve. Nevertheless, both the notched and laser-welded specimens have considerable crack damage and void nucleation ahead of the crack tip prior to peak load of the structures.

The damage is more pronounced in the case of the laser welds as compared to the notched specimens because of the sharper notch at the root of the weld acting as a larger stress concentration as well as preexisting pores at the root of the weld. The size and distribution of these preexisting pores are yet unknown for this particular weld, but these welds have pores that can greatly vary in size from those that can be detected with micro-computed tomography (CT) on the order of 10-μm and larger [4, 5] down to smaller pores only measured through destructive sectioning and imaging of undeformed welds. A few specimens of this particular laser weld were imaged with micro-CT, showing only on the order of three to five large-scale pores over each 6.35-mm specimen width. The deformed and cracked pores in the root of the least deformed laser-welded specimen in Fig. 12.7c were likely smaller than could be detected by micro-CT. The roots of these laser-welded specimens show evidence of extensive pore growth, deformation, and cracking in several pores that were originally small, probably less than 10-μm. In contrast, the roots of the notched specimens mostly show the horizontal cracking and micro-cracks. We do not know the influence of the EDM oxide-layer surface finish on the initiation of the cracks early in the deformation, but the extensive horizontal cracks and micro-cracks after large global deformation are visible in the underlying deformed 304L SS. These same types of cracks are evident in the laser welds in locations away from the pores, so this damage is probably from the geometry, not surface effects. The void nucleation ahead of the main cracks is found in the cross-sections of both the notched and laser-welded specimens. This may be the main crack damage mechanism in the notched specimens, but the damage evolution in laser-welded specimens is more complex with the preexisting pores, void nucleation, and variation in laser weld penetration depth along the width of the specimen.

This study leads to several research opportunities to elucidate these damage mechanisms. Additional interrupted tests of notched specimens, including lower levels of deformation, could determine when cracks begin to form in the notched specimens, which, when compared to the laser-welded specimens, could determine if the native pores or void nucleation is the predominant damage mechanism at the onset of damage. Not all central cross-sections of the specimens have been polished and SEM imaged; these images of the lower deformation laser-welded specimens may also help to determine if the pores or void nucleation is the predominant damage mechanism at the onset of damage. EBSD of the deformed and undeformed notched and laser welded specimens would provide data on grain structure and evolution of plastic deformation ahead of the damage, perhaps revealing the true role of plastic deformation in these geometries. Destructive sectioning and imaging of undeformed laser-welded specimens could quantify the distribution of preexisting pores in these welds, which we suspect are a driving factor in the extensive early damage in these structures.

12.5 Summary

This study has considered the damage evolution in notched and partial-penetration, laser-welded tensile specimens of 304L SS. The experimental approach of interrupting the tensile tests at various levels of deformation and imaging the deformed specimens has allowed us to refute a previously held assumption that these structures are dominated by plastic deformation rather than damage at the stress concentrations of these geometries. The data clearly shows early crack damage with steady growth before peak tensile load of these specimens. Notched and laser-welded specimens both have crack damage prior to peak tensile load. Further research is necessary to clarify the roles of the geometry, preexisting pores in the laser weld, plastic deformation, and void nucleation have on the damage mechanisms in these structures.

Acknowledgements We would like to thank B. Boyce and J. Carroll for discussions regarding the experiments; B. McKenzie for the SEM imaging; D. MacCallum, D. Johnson, C. McConnell, and D. Pendley for specimen preparation; and A. Kilgo and C. Profazi for sectioning and imaging the specimens.

Sandia National Laboratories is a multi-program laboratory managed and operated by Sandia Corporation, a wholly owned subsidiary of Lockheed Martin Corporation, for the U.S. Department of Energy's National Nuclear Security Administration under contract DE-AC04-94AL85000.

References

1. Miyamoto, I., Knorovsky, G.A.: Laser micro welding. In: Zhou, Y. (ed.) Microjoining and Nanojoining, pp. 345–417. Woodhead Publishing, Cambridge (2008)
2. Boyce, B.L., Reu, P.L., Robino, C.V.: The constitutive behavior of laser welds in 304l stainless steel determined by digital image correlation. Metall. Mater. Trans. A. **37A**, 2481–2492 (2006)
3. Madison, J.D., Aagesen, L.K., Battaile, C.C., Rodelas, J.M., Payton, T.K.C.S.: Coupling 3D quantitative interrogation of weld microstructure with 3D models of mechanical response. Metallogr. Microstruct. Anal. **2**(6), 359–363 (2013)
4. Madison, J.D., Aagesen, L.K.: Quantitative characterization of porosity in laser welds of stainless steel. Scr. Mater. **67**, 783–786 (2012)
5. Madison, J., Aagesen, L.K., Chan, V.W.L., Thornton, K.: Advancing quantitative description of porosity in autogenous laser-welds of 304L stainless steel. Integr. Mater. Manuf. Innov. **3**(11), 1–17 (2014)
6. Emery, J.M., Field Jr., R.V., Foulk III, J.W., Karlson, K.N., Grigoriu, M.: Predicting laser weld reliability with stochastic reduced-order models. Int. J. Numer. Methods Eng. **103**, 914–936 (2015)
7. Anderson, T.L.: Fracture Mechanics: Fundamentals and Applications, 3rd edn, pp. 114–128. CRC Press, Boca Raton (2005)

Chapter 13
Cross-Axis Coupling and Phase Angle Effects Due to Multiaxial Vibration

Ed Habtour, Abhijit Dasgupta, and Sabrina Vantadori

Abstract The response of structures under combined biaxial harmonic base excitation is investigated experimentally. The effect of cross-axis coupling, especially as a function of the relative phase angle between two vibration actuators is demonstrated. The experiments are performed using a unique multiaxial electrodynamic shaker with high degree of controllability. Increasing the phase angle between the rotational and translational excitation from 0° to 135° increases the dynamic response of the structure and its nonlinear stiffness. The results are compared to both uniaxial rotational and translational vibration. The chapter provides qualitative and quantitative differences between uniaxial and multiaxial nonlinear harmonic excitation with varying phase and fatigue build up.

Keywords Multiaxial • Nonlinear • Fatigue • Precursor • Reliability

The reliability of systems exposed to multiaxial vibration environments depends on the dynamic response of the internal components. Designers utilize vibration isolators, stiffeners and dampers to reduce the transmission of stresses from the system level to the component level, without full understanding of how the loads are transmitted. Designers also rely on inadequate linear models to estimate of the reliability of complicated systems through their lifecycle [1–4]. Most mechanical systems are intrinsically nonlinear structures and consequently, the linear models are of limited value. Cost and time limitations perpetuate these design strategies in the structural reliability engineering community [1]. Multiaxial vibration conditions generate synergistic dynamic nonlinearities to a mechanical system due to cross-axes coupling [5]. However, current military and commercial standards do not address these nonlinearities. These standards call for sequential uniaxial testing as a compromise for simultaneous multiaxial excitation [3]. Additionally, studies evaluating the merits of multiaxial excitation using electrodynamic shakers are limited [2–5]. These studies have shown evidence of different failure modes for structures exposed to uniaxial and multiaxial vibration loading using multiaxial shakers [2]. To the best of our knowledge, Gregory et al. were the first research group to publish their evaluation of multi- (six) degrees-of-freedom (MDoF) electrodynamic shaker. They utilized the MDoF shaker to perform a dynamic characterization for short cantilever beams with large tip mass [6]. The beams were subjected to uniaxial and multiaxial broadband random excitations with a bandwidth of 20–2000 Hz at 0.0032 g^2/Hz acceleration spectrum density (ASD) input. The results showed substantial differences in the beam response for uniaxial and multiaxial excitations. The combination of inertial nonlinearity due to the component heavy mass and fatigue damage accumulation in the system produced dynamic softening response as well as a decrease in the components' resonance frequencies [4]. Thomas et al. observed similar softening behavior in cantilever beams exposed to nonlinear rotational vibrations [7].

The chapter focuses on understanding the effect of the phase angle variation between the different axial excitation in MDoF environment on the structural response and fatigue accumulation. We ascertain the differences in the response of a cantilever beam structure under three types of harmonic excitations: (1) single transverse, (2) single rotation, and (3) combined rotation and transverse with varying phase angle. Our focus was on the beam flexural mode. The phase angle between the rotation and transverse base excitations was varied from 0° to 135°. Uniform and straight AISI 1095 high carbon steel cantilever beams were clamped to a rigid fixture, as shown in Fig. 13.1a. The density and the elastic modulus

E. Habtour (✉)
U. S. Army Research Laboratory, APG, Adelphi, MD, 21005, USA
e-mail: ed.m.habtour.civ@mail.mil

A. Dasgupta
University of Maryland, College Park, MD, 20742, USA

S. Vantadori
Civil-Environmental Engineering and Architecture Department, University of Parma, Parco Area delle Scienze 181/A, 43124, Parma, Italy

J. Carroll et al. (eds.), *Fracture, Fatigue, Failure and Damage Evolution, Volume 7*, Conference Proceedings of the Society for Experimental Mechanics Series, DOI 10.1007/978-3-319-62831-8_13

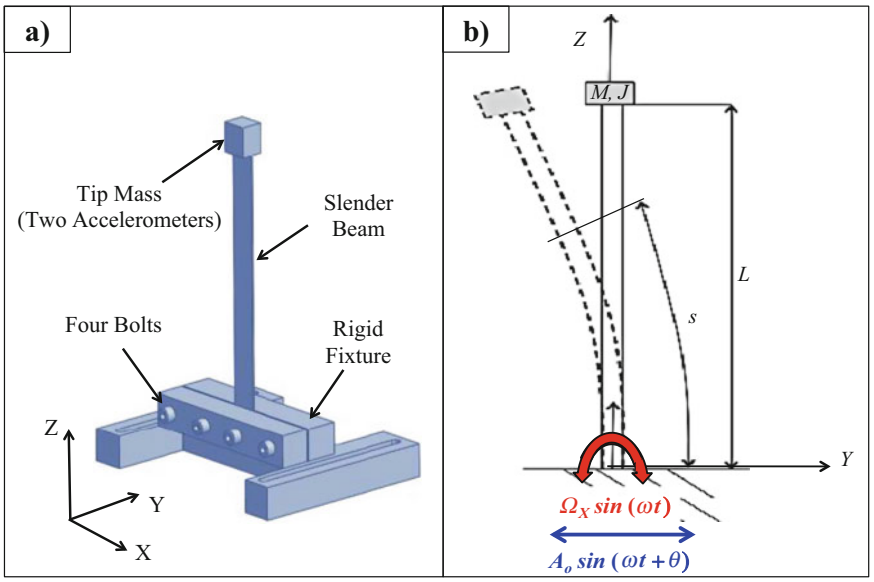

Fig. 13.1 (**a**) Beam attached to a rigid fixture, (**b**) beam transverse and rotational excitation with varying phase

Table 13.1 Nonlinear experimental cases

Case	Test	Total cycles ($\times 10^3$)	Phase (°)	Resonance (Hz)
I	1	0–41	0	40.77
	2	41–117		
	3	117–188		
	4	188–247		
II	1	0–68	45	40.28
	2	68–135		
	3	135–202		
III	1	0–68	90	40.65
	2	68–137		
	3	137–205		
IV	1	0–70	135	40.3
	2	70–140		
	3	140–210		

of the material were 7.85 g/cm^3 and 205 GPa, respectively [8]. The beam length and cross-section area were 127 mm and 15.88×1.08 mm^2, respectively. The tip mass weight was approximately 3×10^{-3} kg, which consisted of one accelerometer for each side of the beam. Four sets of experiments (Cases: I, II, III, and IV in Table 13.1) were conducted; details of each case are listed in Table 13.1. In each case, a beam was exposed to combinations of constant amplitude harmonic excitation consisting of transverse acceleration, $A_o = 0.3$ g, and rotational acceleration, $\Omega_X = 70$ rads/s^2. The reason for selecting these amplitudes was to compare the combined biaxial results to previous uniaxial rotation and transverse harmonic excitation studies [8, 9]. The angles, θ, were 0°, 45°, 90°, and 135° for Cases I, II, III, and IV, respectively. The number of applied cycles depended on the observed irreversible shift in the resonance frequency and the irreversible change in the beam tip displacement response due to material 'softening' caused by early material degradation (precursor to fatigue damage) [10, 11]. The maximum tip displacement amplitudes versus the number of fatigue cycles for Cases I, II, III, and VI are shown in Fig. 13.2. Nonlinear material 'softening' is seen to amplify the beam tip response each time the test was repeated, as shown in Fig. 13.2. The increase in the beam tip response amplitude directly correlates to the increase in the number of cycles. The experimental results also show that increasing the phase angle between the rotation and transverse input signals from 0° to 135° increased the beam tip response. Furthermore, due to the rotational excitation and the cross-axis coupling, the structural stiffness in the equation of motion became time varying and nonlinear [9]. For zero phase angle, cross-axis coupling causes a small reduction in the structural stiffness.

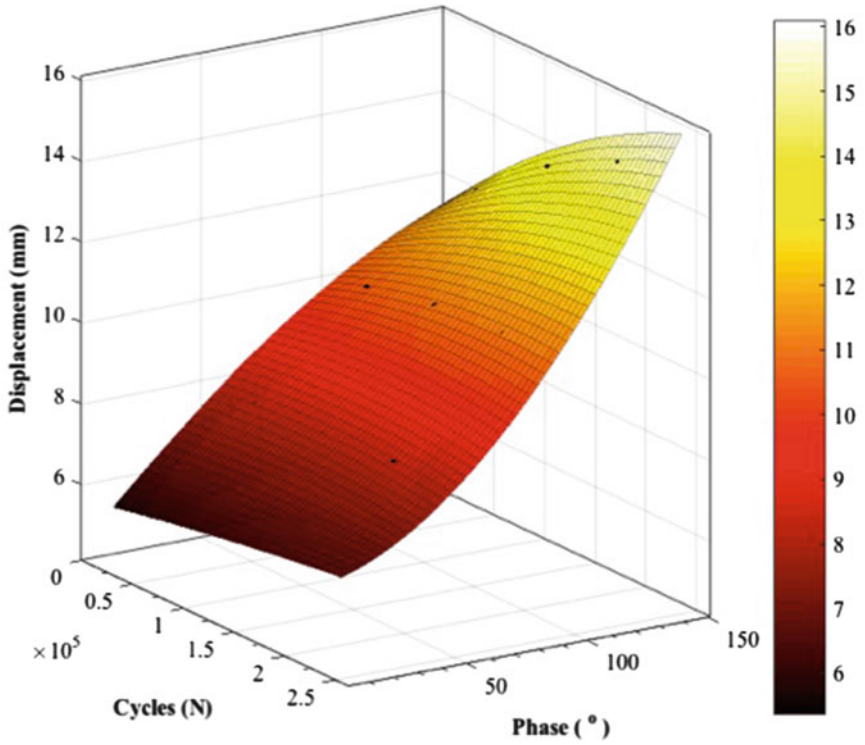

Fig. 13.2 Beam tip response as a function of cycles and phase

Understanding the coupling effects due to multiaxial base excitation was an important step in predicting the structural response and lifecycle of complex systems, which is the subject of current efforts at the Army Research Laboratory. The sensitivity of the phase angle between the rotation and transverse base excitation may broaden design space for improving reliability.

References

1. Pagnacco, E., Lambert, S., Khalij, L., Rade, D.A.: Design optimisation of linear structures subjected to dynamic random loads with respect to fatigue life. Int. J. Fatigue. **43**, 168–177 (2012)
2. Mršnik, M., Slavič, J., Boltežar, M.: Multiaxial vibration fatigue—A theoretical and experimental comparison. Mech. Syst. Signal Process. **76**(77), 409–423 (2016)
3. Habtour, E., Connon, W., Pohland, M.F., Stanton, S.C., Paulus, M., Dasgupta, A.: Review of multiaxial vibration in linear and nonlinear structures. Shock. Vib. (2014). doi:10.1155/2014/294271
4. Ernst, M., Habtour, E., Dasgupta, A., Pohland, M., Robeson, M., Paulus, M.: Comparison of electronic component durability under uniaxial and multiaxial random vibrations. J. Electron Packag. **137**(1), (2015). doi:10.1115/1.4028516
5. Ernst, M., Habtour, E., Dasgupta, A.: Examining Steinberg's Octave rule applicability for electronic systems exposed to multiaxial vibration. IEEE Trans. Compon. Packag. Manuf. Technol. **6**(4), (2016). doi:10.1109/TCPMT.2016.2519447
6. Gregory, D., Bitsy F., Smallwood, D.O.: Comparison of the response of a simple structure to single axis and multiple axis random vibration inputs. In: Shock and Vibration Symposium, Orlando, 2008
7. Thomas, O., Sénéchal, A., Deü, J.-F.: Hardening/softening behavior and reduced order modeling of nonlinear vibrations of rotating cantilever beams. Nonlinear Dyn. **86**(2), 1293–1318 (2016)
8. Habtour, E., Cole, D.P., Riddick, J.C., Weiss, V., Robeson, M., Sridharan, R., Dasgupta, A.: Detection of fatigue damage precursor using a nonlinear vibration approach. J. Struct. Health Monit. (2016). doi:10.1002/stc.1844
9. Habtour, E., Cole, D.P., Sridharan, R., Stanton, S., Dasgupta, A.: Damage precursor detection for structures under nonlinear rotational base vibration. Int. J. Nonlinear Mech. **82**, 49–58 (2016)
10. Vantadori, S., Haynes, R., Fortese, G., Habtour, E., Ronchei, C., Scorza, D., Zanichelli, A.: Methodology for assessing embryonic cracks development in structures under high-cycle multiaxial random vibrations. Fatigue Fract. Engng. Mater. Struct. (2017). doi:10.1111/ffe.12634
11. Rabiei, E., Droguett, E.L., Modarres, M.: A prognostics approach based on the evolution of damage precursors using dynamic Bayesian networks. Adv. Mech. Eng. **8**(9), (2016)

Chapter 14
Behavior of Steel-Concrete Composite Beams Under Fatigue Loads

Ayman El-Zohairy and Hani Salim

Abstract Besides the static load, the cyclic load caused by the vehicles always exists in the bridge structures. This kind of loading may cause failure even when the nominal maximum loads have not exceeded the ultimate resistance of the structure. So, the main objective of this paper is to evaluate the fatigue behavior of composite beams at the sagging moment regions. A numerical model is described to predict the fatigue response of each part of the composite section. The accuracy of the developed numerical model is validated using existing test data. Also, the transformed section method is used to evaluate the fatigue response of the composite beams in terms of deflection, strains in the concrete flange and the steel beam, plastic deformation, reduction in the static strength of the shear connectors, and residual capacity of the composite beam. The cumulative damage rule is analyzed through the S-N curve to assess the procedures presented in the design code. A rapid growth in the residual deformations of the composite beams is obtained at the starting and the end of the fatigue life with the number of cycles while a linear increase in the remaining part of the fatigue life occurs. In addition, a reduction in the static strength of the shear connectors is developed with the number of cycles and subsequently causes a drop in the monotonic beam capacity which can be calculated based on the new shear connection strength.

Keywords Composite beams • Fatigue loads • Numerical model • Post-tensioning • Residual deformation

14.1 Introduction

Recently, the steel-concrete composite beams are used widely for the construction of bridges and buildings structures in the United States due to the advantages of combining the benefits of component materials and gaining effective lightweight structural members. In the real life, bridge structures are generally exposed to cyclic loads caused by the vehicles. This kind of loading causes failure even when the peak loads are less than the ultimate resistance of the structure. Fatigue fracture of the shear connectors or concrete crushing in the compression zone are the expected modes of failure for composite beams under fatigue loads. Since the shear connectors are a vital key in the composite beams that transfer shear forces between the concrete flange and the steel beam, their fatigue resistance is significant to maintain the composite action between the two components of the composite section and needed to be well investigated.

Previous studies have been done on the fatigue behavior of steel-concrete composite beams. Experimental findings of full-scale composite beams confirmed that cracks were initiated in the concrete slab and propagation of cracks in the shear connectors led all specimens to fail [1, 2]. Fracture of the shear connectors was the fatigue failure mode of specimens, with good ductility, and the fatigue life was significantly affected by the shear stress amplitude [3]. For composite sandwich systems, a significant effect on the fatigue performance was found for a larger difference between the maximum applied load and the load range [4]. A computational model which adopted the usual mesh refinement techniques was developed to investigate the dynamic analysis of a composite bridge and to expect the distortions that related to the steel and composite bridges' service life under the effect of vehicles' dynamic actions [5]. An extended model based on a beam element whose nodal degrees of freedom are lateral deflection and rotation was presented to simulate the non-linear cyclic behavior of composite beams [6].

In addition, earlier studies have been conducted on the fatigue behavior of shear connectors in steel–concrete composite beams by using the standard push-out test device. Slutter and Fisher carried out the first fatigue tests on shear connectors and the fatigue failure of studs occurred in the welding zone between the steel plate and the shear connectors [7]. A series of experimental work with standard push-out specimens was presented to develop semi-empirical analytical methods to

A. El-Zohairy (✉) • H. Salim
Department of Civil and Environmental Engineering, University of Missouri, Columbia, MO, USA
e-mail: aeq76@mail.missouri.edu; SalimH@missouri.edu

J. Carroll et al. (eds.), *Fracture, Fatigue, Failure and Damage Evolution, Volume 7*, Conference Proceedings of the Society for Experimental Mechanics Series, DOI 10.1007/978-3-319-62831-8_14

determine the reduction in the static strength, the fatigue life, and the development of an improved damage [8, 9]. Simplified relationships for predicting the fatigue life of studs based on plenty of experimental data have been developed [7, 10]. The equations that have been developed for fatigue design of shear connectors were compared with reference to all appropriate test data on welded stud connectors. The results concluded that the reliability of design of stud connectors for fatigue is unclear and is probably inconsistent. Also, there is no experience of failures because real stress ranges are less than those calculated in design [11]. The stud spacing has a large influence on the shear force induced in the stud while the young modulus of concrete has a relatively small influence [12].

The main objective of this paper is to evaluate the fatigue behavior of composite beams at the sagging moment regions. A numerical model is described to predict the fatigue response of each part of the composite section. The accuracy of the developed numerical model is validated using existing test data. Also, the transformed section method is used to evaluate the fatigue response of the composite beams in terms of deflection, strains in the concrete flange and the steel beam, plastic deformation, reduction in the static strength of the shear connectors, and residual capacity of the composite beam. The cumulative damage rule is investigated through the S-N curve to assess the processes presented in the design code.

14.2 Numerical Model

A numerical model is proposed to implement the numerical investigation of post-tensioned steel-concrete composite beams as well as plain beams under the effect of fatigue loads by considering the fatigue damage in the concrete flange. The proposed numerical model is validated using previous experimental findings.

14.2.1 Element Selection

The steel beam is modeled by using a brick eight-node element, SOLID45, which has plasticity, stress stiffening, large deflection, and large strain capabilities. The concrete flange is idealized by using a solid element, SOLID65, that able to crack in tension and crush in compression. The connection between the steel beam and the concrete flange induced by the shear stud as a deformable shear connector is simulated using a beam element and a spring element [13]. The uniaxial beam element, BEAM23, is used to simulate the shank of the shear connector while the unidirectional spring element, COMBINE39, is used to resist the longitudinal shear force and simulate the relative movement between the steel beam and the concrete flange.

The steel rebars and the post-tensioned tendons are simulated by using a 3D-link element, LINK8. The initial post-tensioning (PT) force in the external tendons is defined by an initial strain implemented in the real constants of the link element [14]. The interaction between the two surfaces of the steel beam and the concrete flange is simulated by using contact element, CONTAC52, to maintain the physical contact and to allow the sliding between the two surfaces. The normal stiffness is the only real constant that be defined for the contact element and is calculated based on the weakest stiffness of the two surfaces in contact.

14.2.2 Material Modeling

According to the literature available, the modulus of the steel material is nearly the same with the initial elastic modulus when the composite beams subjected to fatigue loads. Modulus of elasticity (E_s) for the steel beam, tendons, shear connectors, and steel rebars used in this analysis are the same for the laboratory works. On the other hand, the modulus of the concrete material decreases obviously as the loading cycles increase, which can be calculated based on the following equation [15]:

$$E_c^f = \left[0.6515 - 0.0646 \ln\left(\frac{n}{N}\right)\right] E_c \tag{14.1}$$

where: E_c^f is the elastic modulus of concrete after a certain number of cycles (n), N is the fatigue life of shear connectors under a specific shear stress range, and E_c is the initial elastic modulus of concrete.

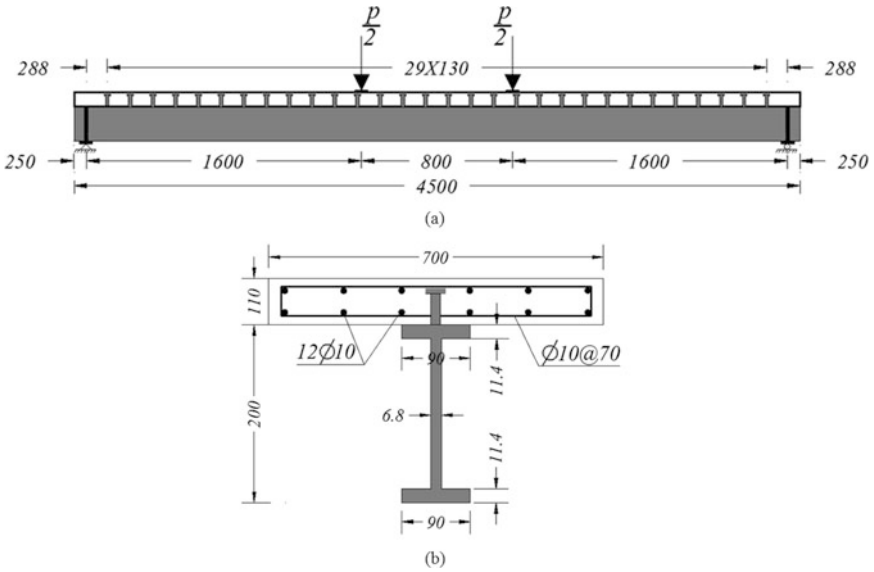

Fig. 14.1 Details of the tested specimen FSCB-2: (**a**) beam elevation and (**b**) beam cross-section

Table 14.1 Summary of the materials properties for the validated specimen

	Steel I-beam			Concrete	Shear connectors	
Model	f_y (MPa)	f_u (MPa)	E_s (MPa)	f_c (MPa)	f_y (MPa)	f_u (MPa)
FSCB-2	362.89	458.03	30,000	38.85	406.5	509

14.3 Numerical Model Validation

FSCB-2 is one of the composite beams that tested experimentally by Yu-Hang et al. [3] to obtain the residual static mechanical performance of steel–concrete composite beams after a certain number of cycles. The experimental findings of this beam are used to validate the proposed numerical model. The specimen is 4500 mm long and tested over a clear span of 4000 mm under four-point loading. The detailed geometrical dimensions of the tested specimen are shown in Fig. 14.1. To avoid the longitudinal shear failure, 10 mm in diameter transversal stirrups are provided in the concrete flange with a spacing of 70 mm along the whole beam span. The shear connection is achieved by using headed studs of a 16 mm in diameter. A summary of the materials properties for the validated specimen is listed in Table 14.1. Due to symmetry, only longitudinal half of the beam is modeled.

The load versus displacement curves of the numerical and experimental results are compared in Fig. 14.2. The general behavior of the numerical model shows good agreement with the test data; however, the numerical model shows slightly more stiffness in both the linear and nonlinear ranges. The perfect bond assumed between concrete and the steel rebars as well as between concrete and the shear connectors are the main reasons for this difference in response.

14.4 Transformed Section Method

The theory of the transformed section method is widely used and commonly established as a technique of analysis of bending stresses in a composite beam. Transformed sections introduce a visual form of a composite member that used for the analysis of that member. A material may be converted into another material based upon the modular ratio which equals to the ratio of modulus of elasticity of the two materials [15]. Damage in the concrete flange after a certain number of cycles is considered by decreasing the modulus of elasticity of concrete material obviously as the loading cycles increase. Full interaction between the concrete flange and the steel beam is assumed which means slip and slip strain are everywhere zero. Then, it can be assumed that plane sections before deformation remain plane after deformation. The process of transformation appears as a readily suitable procedure when the relationship $\sigma = M{\cdot}y/I$ and Hooke's law are used in bending. Also, the maximum elastic deflection, Δ_{max}, at mid-span of a beam under four-point loading can be calculated using the following formula:

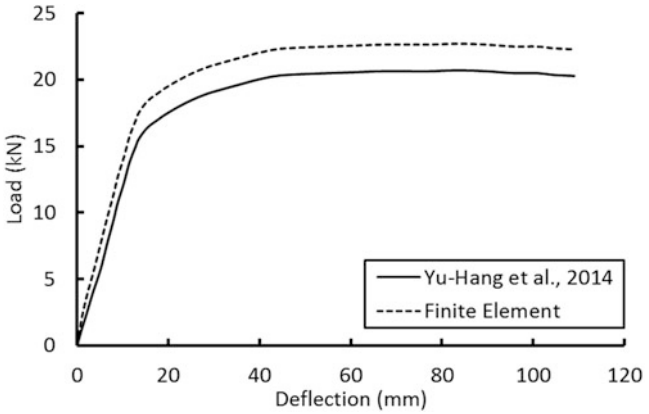

Fig. 14.2 Residual load versus deflection relationships for the numerical and experimental results

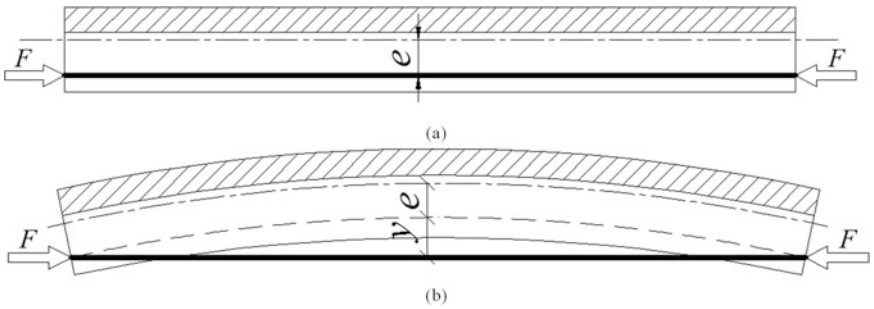

Fig. 14.3 Strengthened beam as an eccentric column: (**a**) external PT force and (**b**) initial camber

$$\Delta_{\max} = \frac{p\,a}{24\,E\,I}\left(3l^2 - 4a^2\right) \tag{14.2}$$

where: P is the point load value, a is the distance between the point load and the nearest support, and EI is the bending rigidity of the transformed section.

For composite beams with external PT force, supper position can be used to inspect the beam behavior under fatigue loads. The strengthened composite beam with externally post-tensioned tendons behaves like an eccentrically loaded column; as illustrated in Fig. 14.3. The external PT force, F, behaves like an eccentric load with eccentricity, e, from the centroidal axis of the composite beam. This eccentricity produces a primary bending moment equal to F*e that exists in addition to the usual deflection-related moment in the classical theory [16]. Like classical column buckling theory, the beam bending equation is as following:

$$\mathrm{EI}\,y'' = -\mathrm{P}\,(\mathrm{e} + \mathrm{y}) \tag{14.3}$$

The solution of the previous differential equation can be simplified to calculate the mid-span upward deflection due to the effect of the external PT force as following:

$$\delta = \mathrm{e}\left(\sec\frac{kL}{2} - 1\right) \quad \text{where} \quad \frac{kL}{2} = \frac{\pi}{2}\sqrt{\frac{F}{P_{cr}}} \quad \text{and} \quad \mathrm{P}_{cr} = \frac{\pi^2\,EI}{L^2} \tag{14.4}$$

where: δ is the maximum mid-span upward deflection due to the external PT force, $\mathrm{P_{cr}}$ is the critical buckling load, and L is the beam length.

To verify the results from the transformed section method with the numerical outcomes, additional two simply supported steel-concrete composite beams are analyzed to inspect the fatigue behavior and fatigue rigidity of composite beams with and without external PT force. The first beam is used as a reference beam without any retrofit while the other beam is strengthened with externally post-tensioned tendons to inspect the effect of external PT on the fatigue behavior of composite

beams. The overall length of the analyzed beams is 4572 mm while the clear span between supports is 4420 mm. The thickness and width of the concrete flange are 101.6 and 1143 mm, respectively. A doubled mesh, with 10 mm in diameter, is used as a steel reinforcement in the longitudinal and transverse directions to avoid the undesired longitudinal shear failure. The external PT force is 180 kN applied by two tendons extended parallel to the steel beam web through the full length of the beam. The fatigue load range is 148 kN and is applied by two point loads with a 1370 mm spacing to cause a fatigue fracture in the shear connectors after 1,000,000 cycles according to AASHTO standards [17].

Comparisons between results of the numerical model and the transformed section method are illustrated in Fig. 14.4 to show the behavior of the reference beam under fatigue loads. The initial effect of the external PT on the composite beam during the fatigue life is also investigated. The initial upward deflection, initial strain in the steel bottom flange, and initial strain in the concrete flange at mid-span are presented in Fig.14.5. Good agreement between the results of the numerical model and the transformed section method is obtained. Furthermore, additional studies are conducted on the fatigue behavior of composite beams by using the transformed section method and previous relationships to demonstrate the residual deformations and reduced static strength of the composite beams.

According to mechanics, the ability to resist longitudinal shear is the vital key for beams to develop strength and stiffness. The essence of composite action is the ability to develop this strength in the connection between the steel beam and the concrete flange [18]. The shear flow between the two main components of the composite section varies along the beam length and the required resistance could be obtained to match that variation exactly but it is more economically to provide a uniform resistance over the whole beam or over a few lengths of uniform provision.

The shear flow equation is used to calculate the longitudinal shear force range that must be resisted by the shear connectors under fatigue loads. So, the shear stress range that induced in the shear connectors can be computed based on the following equations:

$$\Delta q = \frac{\Delta Q\, S}{I_c} \tag{14.5}$$

$$\Delta \mathrm{F} = \Delta \mathrm{q} * \mathrm{spacing/n} \tag{14.6}$$

$$\Delta \tau = \Delta F/A \tag{14.7}$$

where: Δq is the shear flow range, ΔQ is the shear force range that applied on the beam, S is the first moment of area for the concrete flange, I_c is the second moment of area for the transformed section, ΔF is the induced shear force range per stud, n is the number of studs per one row, $\Delta\tau$ is the shear stress range per stud, and A is the cross-section area of one stud.

Based on the calculated shear stress range in the shear connector, the fatigue life (N) of the shear studs can be achieved by using the following equation [17]:

$$\Delta\tau = 4/\pi\ (238 - 29.51\ \mathrm{Log\ N}) \tag{14.8}$$

14.4.1 Residual Deformation

Under cyclic loading, the distribution of interface shear force between the shear studs varies with cycles of load due to the damage region that developed in the concrete flange by the shear studs and causes a loss of stiffness in the connection. Redistributions of the interface shear force from studs with larger damage to studs with smaller damage occur and change with every cycle of loading. So, incremental slippage and deflection and loss of composite action, measured by a reduction in the interface shear force, occur due to repeated loading [19]. In Fig. 14.6a, the inelastic slip related to the plastic slippage is plotted versus the number of cycles during the fatigue life. This sigmoidal relationship can be expressed in the following form [8]:

$$\delta_{pl,n} = A - B \ln\left[\frac{1}{\frac{n}{N_f}} - 1\right] \geq 0 \tag{14.9}$$

$$A = 0.104\, e^{3.95\frac{P_{max}}{P_{u,o}}} \qquad B = 0.664\,\frac{P_{min}}{P_{u,o}} + 0.029$$

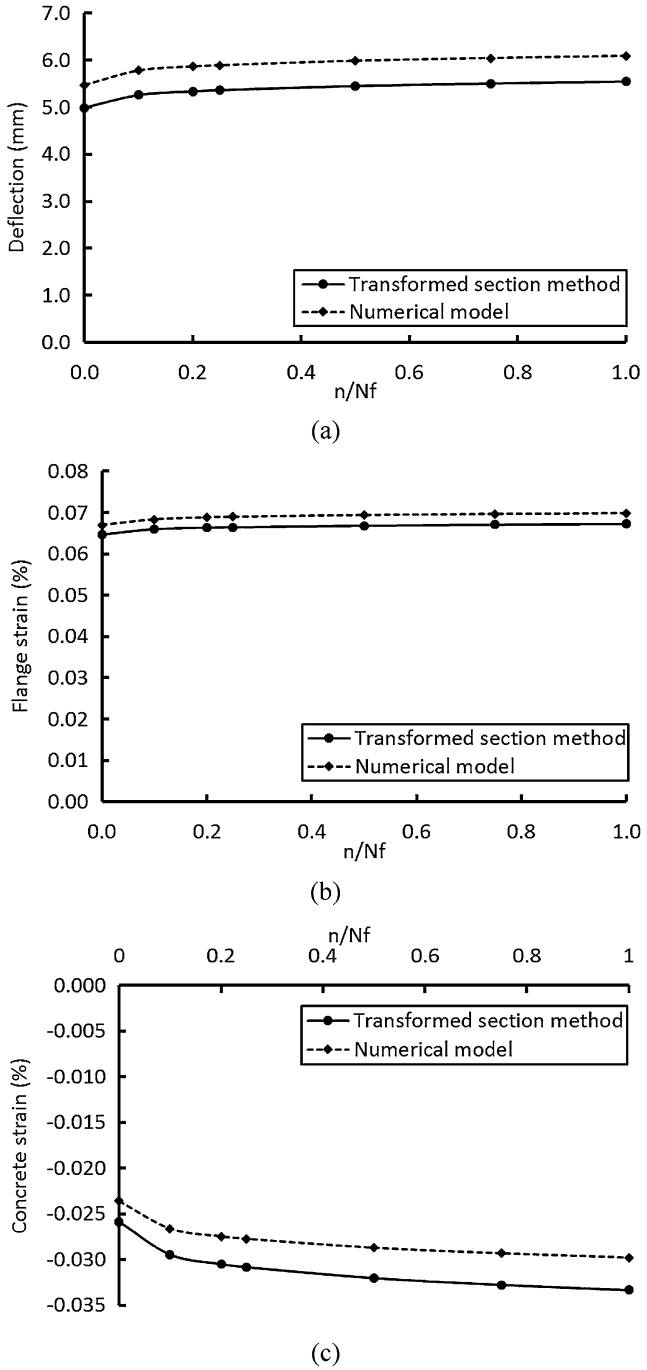

Fig. 14.4 For reference beam: (**a**) deflection, (**b**) strain in the steel bottom flange, and (**c**) strain in the concrete flange

where: $\delta_{pl,n}$ is the plastic slippage (mm), P_{max} is the maximum shear force in the stud (N), P_{min} is the minimum shear force in the stud (N), $P_{u,o}$ is the static capacity of the stud (N).

A rapid growth in the residual deformations of the composite beams, slippage and deflection, is obtained at the starting and the end of the fatigue life while a linear increase in the remaining part of the fatigue life occurs. Furthermore, the residual deflection ($f_{r,n}$) of the composite beam at mid-span can be obtained using the following formula [3]:

$$f_{r,n} = 10.11\ \delta_{pl,n}/(12h) \tag{14.10}$$

where: h is the composite section height (mm).

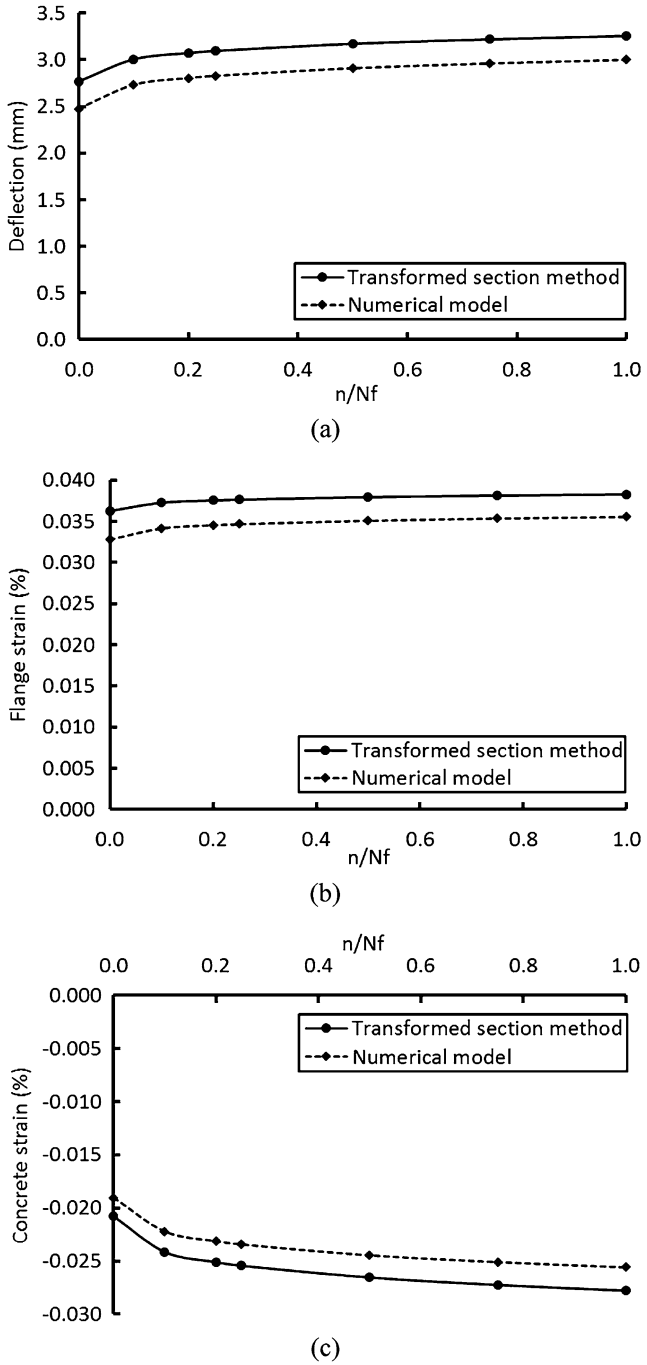

Fig. 14.5 For strengthened beam: (**a**) initial camber, (**b**) initial strain in the steel bottom flange, and (**c**) initial strain in the concrete flange

Based on the previous expression, the residual deflection of composite beams under fatigue loads depends mainly on the plastic slippage between the concrete flange and the steel beam. So, the residual deflection with the number of cycles behaves similar to the plastic slippage; as illustrated in Fig. 14.6b.

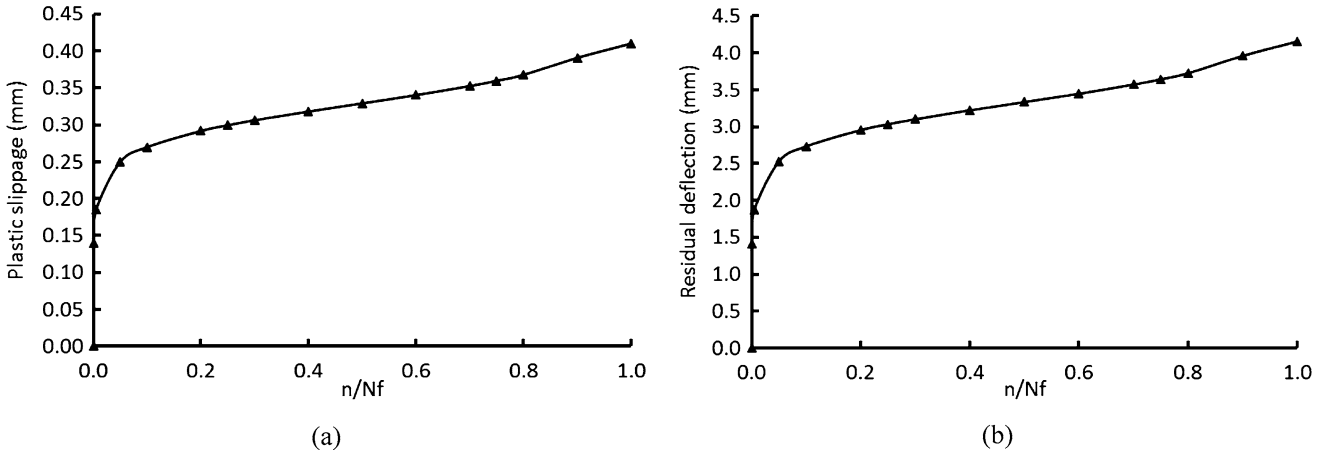

Fig. 14.6 Residual deformation of composite beam under fatigue loads: (**a**) plastic slippage and (**b**) residual deflection

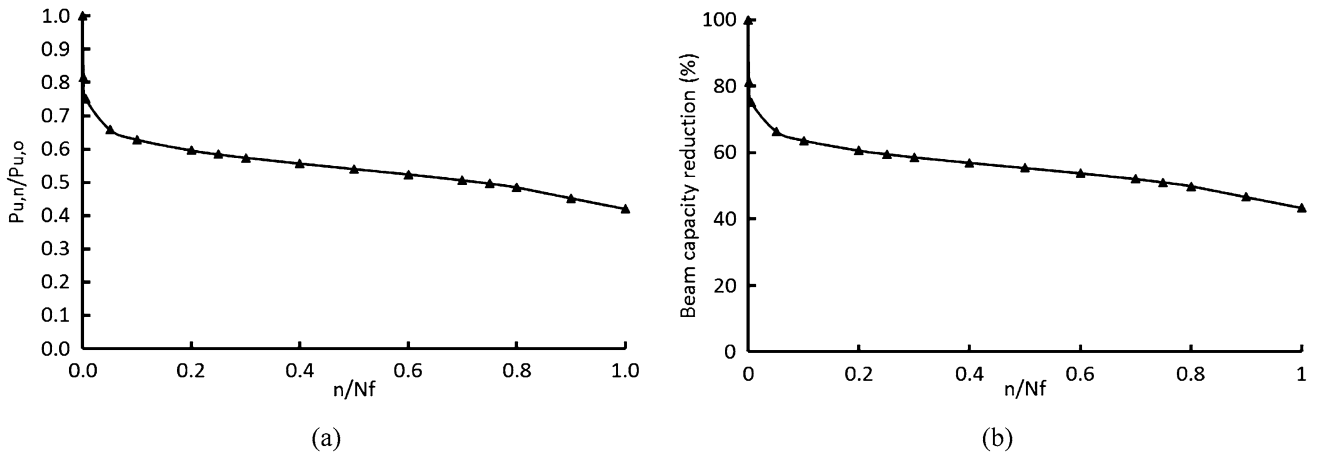

Fig. 14.7 Reduced static strength of the: (**a**) shear connectors and (**b**) composite beam

14.4.2 Reduced Static Strength

The reduction in the static strength of the shear connectors increases with the number of cycles and subsequently causes a drop in the beam capacity over the fatigue life. This reduction can be represented by a sigmoidal shape; as shown in Fig. 14.7a. Furthermore, the presented relationship can be formulated with the following expression:

$$\frac{P_{u,n}}{P_{u,o}} = K - 0.04 \ln\left(\frac{1}{1-\frac{n}{N_f}} - 1\right) \leq 1.0 \text{ and } \geq \frac{P_{max}}{P_{u0}} \tag{14.11}$$

$$K = 0.74 \frac{P_{max}}{P_{u,o}} \left(1 - \frac{\Delta P}{P_{max}}\right) + 0.54$$

where: $P_{u,n}$ is the static strength of the stud after a certain number of cycles (n) and ΔP is the shear force range in the stud ($P_{max} - P_{min}$).

The drop in the monotonic capacity of the composite beam over the lifetime can be calculated based on the new strength of the shear connection. Figure 14.7b illustrates the static strength of the composite beam with the number of cycles. A rapid reduction in the beam capacity is observed at the starting and the end of the lifetime while a linear increase in the remaining part of the fatigue life occurs.

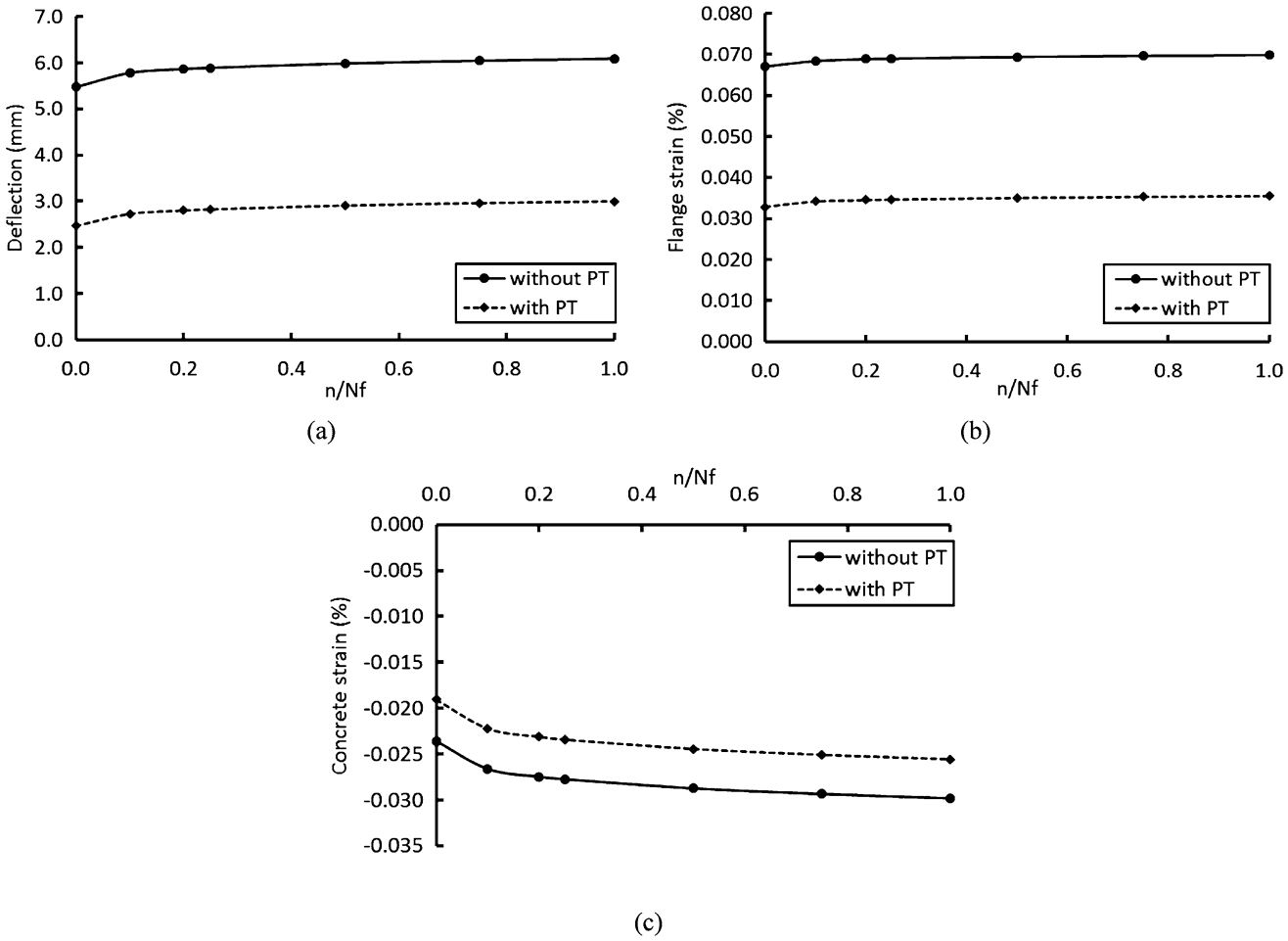

Fig. 14.8 Effect of external PT on: (**a**) deflection, (**b**) strain in the steel bottom flange, and (**c**) strain in the concrete flange

14.5 Effect of External PT

The elastic performance of composite beams under fatigue loads, represented by deflections and strains in both the steel bottom flange and concrete flange, is numerically investigated to demonstrate the effect of external PT on the fatigue behavior of composite beams. Under cyclic loads, all beams demonstrate an increasing in their mid-span deflections in the early stages of their fatigue life then the deflection slightly increases with the number of cycles. The Effect of external PT is demonstrated by a reduction in the elastic deflection during the fatigue life; as shown in Fig. 14.8a. In addition, the initial compressive strain that is experienced in the steel bottom flange helps to relieve a part of the tensile strain during the lifetime; as shown in Fig. 14.8b. Keeping the steel flange between tensile and compressive strains enhances the fatigue life of the steel beam. Also, relieving more tensile strains in the steel flange can be achieved by increasing the initial PT force. In comparison to the steel flange, the same effect of external PT is observed on the compressive strain in the concrete flange; as shown in Fig. 14.8c.

14.6 Damage Accumulation Model

A simple standard is presented by the Palmgren–Miner cumulative linear damage rule for expecting the amount of fatigue damage due to a specific block of constant amplitude cyclic loads in a loading sequence with different stress amplitudes [20]. According to this rule, the number of cyclic loads applied on an element, illustrated like a portion of the fatigue life, gives a part of the damage and the arrangement of the loading blocks does not affect the fatigue life. So, if N_j is the number of

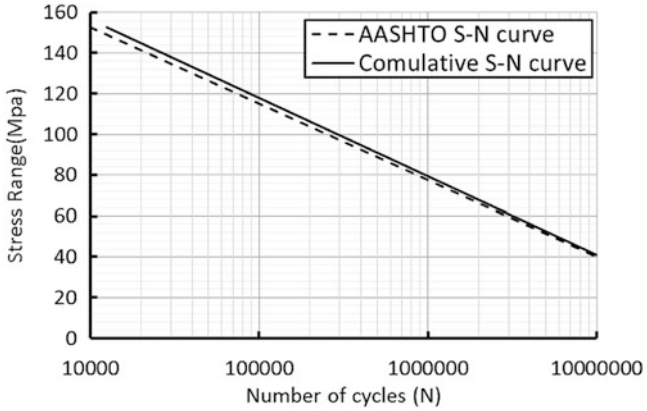

Fig. 14.9 S-N curves for AASHTO and cumulative damage model

cycles related to the j_{th} block of the same amplitude in a series of k different stress magnitudes with N_{fj} as the lifetime, the failure would occur when:

$$\sum_{j=1}^{k} \frac{N_j}{N_{fj}} = 1.0 \tag{14.12}$$

By applying this linear damage accumulation method, the S-N relationship in AASHTO is modified to a new relationship that gives an additional fatigue life to the shear connector at the same shear stress range; as shown in Fig. 14.9. This additional fatigue life increases for larger shear stress range. According to test results with different stress magnitudes, the Palmgren–Miner cumulative linear damage rule leads to an overestimation in the fatigue life of the shear connectors. The disregard of crack propagation in shear connectors and local damage in concrete for the evaluation of the residual fatigue life of shear connectors under different stress magnitudes is the main reason of the overestimated results [8].

14.7 Conclusion

The fatigue behavior of composite beams is evaluated by introducing a numerical model that considers the fatigue damage in the concrete flange during the lifetime. The accuracy of the developed numerical model is validated and results based on the transformed section method are presented. The main conclusions are:

1. The proposed numerical model is accurate enough to predict the fatigue behavior of the composite beams.
2. A rapid growth in the residual deformations of the composite beams is obtained at the starting and the end of the fatigue life while a linear increasing in the remaining part of the fatigue life occurs.
3. A reduction in the static strength of the shear connectors is developed with the number of cycles and subsequently causes a drop in the beam capacity over the fatigue life.
4. Pre-compressing the steel bottom flange reduces the tension portion of the stress range cycle and should improve the fatigue life of the steel beam.
5. Based on the Palmgren–Miner cumulative linear damage rule, additional fatigue life is added to the shear connectors in comparison to AASHTO standards.

References

1. Richard Yen, J.Y., Lin, Y., Lai, M.T.: Composite beams subjected to static and fatigue loads. J. Struct. Eng. (ASCE). **123**(6), 765–771 (1997)
2. Hanswille, G., Porsch, M., Ustundag, C.: The behaviour of steel-concrete composite beams under repeated loading. In: Nordic Steel Construction Conference, NSCC2009, Malmo, 2009
3. Yu-Hang, W., Jian-Guo, N., Jian-Jun, L.: Study on fatigue property of steel-concrete composite beams and studs. J. Constr. Steel Res. **94**, 1–10 (2014)

4. Dai, X.X., Richard Liew, J.Y.: Fatigue performance of lightweight steel-concrete-steel sandwich systems. J. Constr. Steel Res. **66**, 256–276 (2010)
5. Leitão, F.N., da Silva, J.G.S., Vellasco, P.C.G., de Andradeb, S.A.L., de Limab, L.R.O.: Composite (steel-concrete) highway bridge fatigue assessment. J. Constr. Steel Res. **67**, 14–24 (2011)
6. Hwang, J.W., Kwak, H.G.: Improved FE model to simulate interfacial bond-slip behavior in composite beams under cyclic loadings. J. Compos. Struct. **125**, 164–176 (2013)
7. Slutter, R.G., Fisher, J.W.: Fatigue strength of shear connectors. Highw. Res. **147**, 65–88 (1966)
8. Hanswille, G., Porsch, M., Ustundag, C.: Resistance of headed studs subjected to fatigue loading part I: experimental study. J. Constr. Steel Res. **63**, 475–484 (2007)
9. Dogan, O., Roberts, T.M.: Fatigue performance and stiffness variation of stud connectors in steel–concrete–steel sandwich systems. J. Constr. Steel Res. **70**, 86–92 (2012)
10. Johnson, R.P.: Shear connection for composite bridges and Euro-code 4. In: Part 2: Composite Construction Conventional and Innovative, International Conference, Innsbruck, pp. 573–578 (1997)
11. Johnson, R.P.: Resistance of stud shear connectors to fatigue. J. Constr. Steel Res. **56**, 101–116 (2000)
12. Liu, K., De Roeck, G.: Parametric study and fatigue-life cycle design of shear studs in composite bridges. J. Constr. Steel Res. **65**, 1105–1111 (2009)
13. El-Zohairy, A., Salim, H.: Parametric study for post-tensioned composite beams with external tendons. J. Adv. Struct. Eng. (2017). doi:10.1177/1369433216684352
14. Kim, U., Chakrabarti, P.R., Choi, J.H.: Nonlinear finite element analysis of unbonded post-tensioned concrete beams. In: Challenges, Opportunities and Solutions in Structure Engineering and Construction, Taylor & Francis Group, London, ISBN 978-0-415-56809-8, 99–104 (2010)
15. Hamilton, R., Tennyson, S., Hamilton, W.: Analysis by the transformed-section method. Proc. Am. Soc. Eng. Educ. Annu. Conf. Exposition. **6**(192), 1–11 (2001)
16. Malvern, L.E.: Introduction to the Mechanics of a Continuous Medium, 1st edn. Prentice-Hall, Inc., Englewood Cliffs (1969)
17. American Association of State Highway and Transportation Officials: AASHTO LRFD, Bridge Design Specifications, Washington, DC (2004)
18. Quimby, T.B.: A Beginner's Guide to the Steel Construction Manual, 2nd edn. Quimby & Associates, Alaska (2011)
19. Taplin, G., Grundy, P.: Steel-concrete composite beams under repeated load. In: Composite Construction in Steel and Concrete IV Conference, Banff, 28 May–2 June (2000)
20. Miner, M.A.: Cumulative damage in fatigue. J. Appl. Mech. **12**, 159–164 (1945)

Chapter 15
Studying the Fracture of Tropical Wood Species with the Grid Method

B. Odounga, R. Moutou Pitti, E. Toussaint, and M. Grédiac

Abstract The present study consists in studying the initiation and propagation of cracks at room temperature of three tropical species: Okume (Aucoumea Klaineana), Iroko (Pterocarpus Soyauxii) and Padouk (Malicia Excelsa). A short review of the literature shows that only few studies dealing with the fracture mechanics properties of this type of wood species are available. Similar studies are however routinely performed on temperate wood species such as Beech and Douglas, using mixed-mode crack growth (MMCG) specimens for instance [1, 2]. In this paper, tropical wood specimens are studied using the grid method [3] and such MMCG specimens, but made of the three aforementioned tropical species.

Keywords Crack growth • Fracture mechanics • Grid method • Tropical wood species • Compliance method

15.1 Extended Abstract

The present study consists in studying the initiation and propagation of cracks at room temperature of three tropical species: Okume (Aucoumea Klaineana), Iroko (Pterocarpus Soyauxii) and Padouk (Malicia Excelsa). A short review of the literature shows that only few studies dealing with the fracture mechanics properties of this type of wood species are available. Similar studies are however routinely performed on temperate wood species such as Beech and Douglas, using mixed-mode crack growth (MMCG) specimens for instance [1, 2]. In this paper, tropical wood specimens are studied using the grid method [3] and such MMCG specimens, but made of the three aforementioned tropical species.

This paper describes the wood specimens, which are subjected to an opening mode, the experimental device and the background of the grid technique used for tracking the location of the crack tip during the test. The origin and characteristics of the tropical wood species studied here are also given. The experimental results are given and compared in terms of force-displacement curves, but also in terms of energy release rate – crack length curves.

Typical MMCG specimens made of each of the three different species are shown in Fig. 15.1. The main difference between the three species is their density: Okume (density = 0.44) is less dense than Iroko (density = 0.64) and Padouk (density = 0.79). For all the specimens, the initial crack length is the same: a = 20 mm. It is located at mid-height and oriented along the fiber direction, which is horizontal here. The initial crack is completed by a notch (length: 2 mm) made with a cutter in order to initiate correctly crack propagation. A grid, with a regular pitch of 200 microns, was transferred on one face of the specimens, see Fig. 15.1d. The technique presented in [4] is used for this purpose.

The experimental device is shown in Fig. 15.2. A 200 kN Zwick/Roel testing machine was used for the tests. A camera was fixed on a tripod at a distance of 67.5 cm from the specimens in order to take images of the grid during the tests.

A small sized steel Arcan fixture was used to load the specimens. The lower part was fixed and the upper part was subjected to an imposed displacement. The testing machine was equipped with a force transducer in order to obtain the force-displacement curves, the displacement being obtained with the full-field measurements. The cross-head speed was

B. Odounga
Ecole Polytechnique de Masuku, Université des Sciences et techniques de Masuku, Franceville, BP 901, Gabon

CNRS, Institut Pascal, Université Clermont Auvergne, Clermont-Ferrand, F-63000, France

R. Moutou Pitti (✉)
CNRS, Institut Pascal, Université Clermont Auvergne, Clermont-Ferrand, F-63000, France

IRT, CENAREST, Libreville, 14070, Gabon
e-mail: rostand.moutou_pitti@uca.fr

E. Toussaint • M. Grédiac
CNRS, Institut Pascal, Université Clermont Auvergne, Clermont-Ferrand, F-63000, France

J. Carroll et al. (eds.), *Fracture, Fatigue, Failure and Damage Evolution, Volume 7*, Conference Proceedings of the Society for Experimental Mechanics Series, DOI 10.1007/978-3-319-62831-8_15

Fig. 15.1 Wooden specimens: Okume (**a**), Iroko (**b**), Padouk (**c**) and the specimen Iroko equipped grid (**d**)

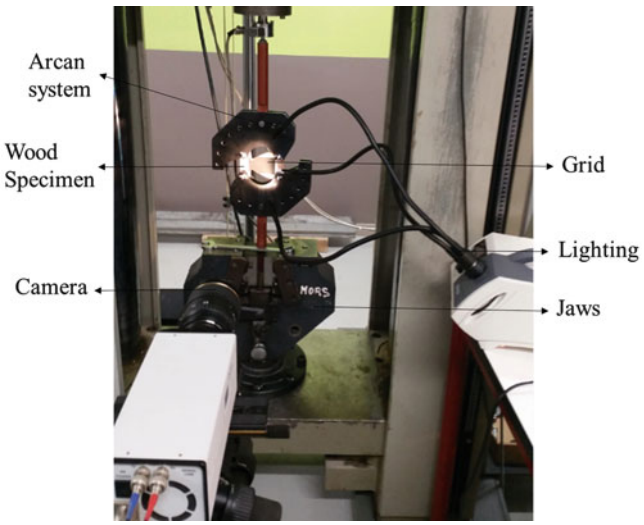

Fig. 15.2 Experimental device

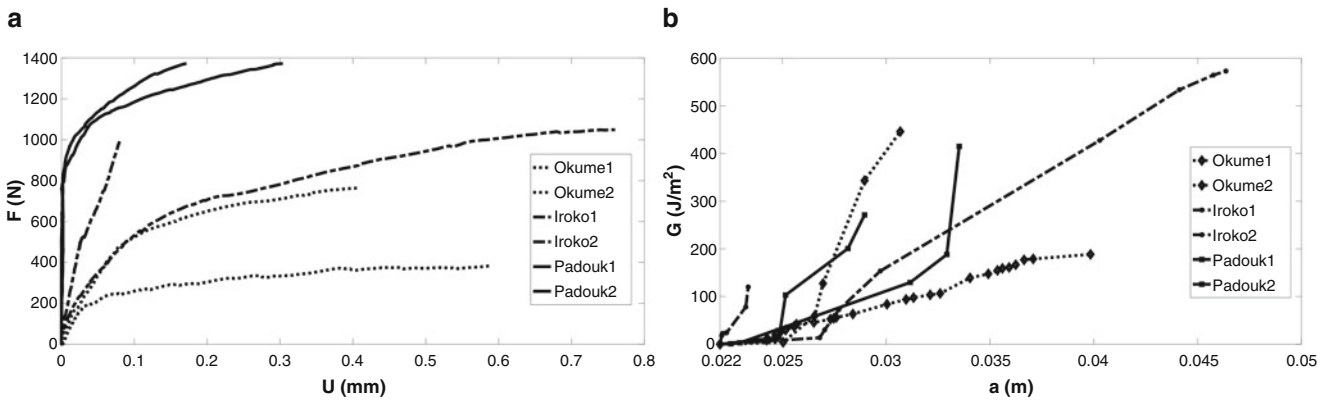

Fig. 15.3 Force-crack opening curves (**a**), evolution of G vs. crack length a (**b**) for the three woods species

0.005 mm/s, and the acquisition rate of the camera was 1.35 frames/second. The specimens were illuminated by three flexible optical arms powered by a cold light source KL 2500 LCD. A SIGMA 105 mm objective was mounted on the camera. To minimize image noise, each image was averaged over eight frames.

Two specimens per specie were tested. Figure 15.3a shows the force-displacement curves obtained for the three species, thus for the six tested specimens. Although the curves are somewhat scattered, a clear trend appears. Indeed, there is a link between force at failure and density. For Okume the mean force at failure is nearly $F_{R\,(Okume)} = 600\,N$, causing an opening of the crack $d_{Okume} = 0.035\,mm$. For Iroko this mean value is a slightly greater since $F_{R\,(Iroko)} = 1000\,N$, with $d_{Iroko} = 0.034\,mm$. For Padouk, we have $F_{R\,(Iroko)} = 1400\,N$ and $d_{Padouk} = 0.031\,mm$.

The results obtained during these tests were then used in order to obtain the critical energy release rate G, which writes as follows:

$$G_C = \frac{F_C^2}{2.b} \cdot \left(\frac{\Delta C}{\Delta a}\right)_d \tag{15.1}$$

where F_c is the so-called critical force corresponding to an increase da of the crack length a, b is the thickness of the specimen. $C = U/F$ is the compliance, where U is the crack opening, and ΔC is the increase in compliance between after and before the crack length has increased by a quantity denoted Δa.

Figure 15.3a shows the value of F as a function of the crack opening U obtained by the grid method. Figure 15.3b shows the value of G as a function of the length of crack a. The first values of G, which induce the onset of crack propagation in the material, confirm the impact of density on the fracture for the three tropical species. Much more energy is needed to initiate a crack propagation in Iroko than in Okume and still more in Padouk. Indeed, the average of G of the two test pieces of each tested of the species showed that the initiation of a crack propagation in Okume requires an energy equal to $G = 6J/m^2$. For Iroko, this value is $G = 14J/m^2$ and for Padouk, $G = 15J/m^2$.

When we consider the mean of the extreme G values, let us say to failure, we observe that the difference between the three species is no longer significant. Therefore the effect of the density is no longer observable. They revolve around $G = 350\,J/m^2$.

Tests were carried out on three tropical species: Okume, Iroko and Padouk. The grid method was applied in order to track the crack tip during the test performed in opening mode. The results showed the influence of the density on the identified fracture parameters, since the denser the material, the greater the force at failure. These results also highlight the influence of the density on the energy which is necessary to initiate the propagation of the crack in these wood species. Indeed, we observed that the first value initiating the propagation of the crack increases with the density.

References

1. Moutou Pitti, R., Dubois, F., Petit, C., Sauvat, N.: Mixed mode fracture separation in viscoelastic orthotropic media: numerical and analytical approach by the Mtv-integral. Int. J. Fract. **145**, 181–193 (2007)
2. Moutou Pitti, R., Dubois, F., Pop, O.: On a specimen providing stable mixed mode crack growth in wooden material. Comptes Rendus Mécanique. **336**(9), 744–749 (2008.) Original Research Article
3. Grédiac, M., Sur, F., Blaysat, B.: The grid method for in-plane displacement and strain measurement: a review and analysis. Strain. **52**(3), 205–243 (2016)
4. Piro, J.L., Grédiac, M.: Producing and transferring low-spatial-frequency grids for measuring displacement fields with moiré and grid methods. Exp. Tech. **28**(4), 23–26 (2004)

Chapter 16
Generalization of Integral Parameters to Fatigue Loading in Room Temperature

Rostand Moutou Pitti, Hassen Riahi, and Mulugeta A. Haile

Abstract In this paper a numerical approach coupling independent path integrals, such as M-integral, to compute the crack driving forces namely the stress intensity factors, and empirical models, for instance Paris-Erdogan's law, to assess the cumulative fatigue damage (i.e. crack size) during the crack growth process, is proposed. The M-integral derived from Nother's theorem combines the real and virtual mechanical deformation and stress fields. A finite element routine is developed in order to compute the energy release rate according to the stress intensity factors. Results are given for a simple standard Al7075-T6 tensile test specimen. Finally, numerical estimates are compared to experimental data for various crack length in order to prove the efficiency and the accuracy of the proposed model.

Keywords Material fatigue • Crack growth • M-integral • Aluminum alloys • Finite element • Experiment

16.1 Introduction

Prediction of the fatigue life of mechanical and aerospace structures, subjected to variable load amplitudes, is still a complex subject. As such, experience has shown that traditional lifing tools do not perform well with most airframe structures. In metallic structures, an unobserved initial crack or defect can propagate slowly until reaching a critical size followed by a sudden catastrophic fracture. In aluminum alloys, such as Al7075-T6 common airframe material, the crack growth life can be significant compared to the crack initiation stage duration. Hence, conservative results, in terms of fatigue life, could be obtained if the crack growth process is ill taken into account in the prediction model. The fatigue life, defined as the number of loading cycles to the failure, is computed through the integration of the commonly known crack growth laws, such as the Paris-Erdogan's one [1], which is sufficiently accurate to model a steady state crack growth behavior. Mathematically speaking, these crack growth laws, are empirical models functions of material parameters, obtained through experimental results, and Stress Intensity Factors (SIF), which are the main crack driving forces if the constitutive material has a linear elastic behavior, or the size of the yielding zone in the neighborhood of the crack tip is very small. The SIF's, which mainly depend of the geometry of the structure, the shape of the initial flaw, and the loading conditions, are computed based on the relative displacements of the crack edges. This method can be time consuming, since it requires, the use of a very small meshing around the crack tip to enhance the accuracy of the estimates, and the decomposition of the mechanical fields into symmetric and antisymmetric parts to separate the different fracture modes. In this situation, energy release rate based-method [2] seems to be a good alternative. The SIF's are derived from the evaluation of an independent path integral where a good accuracy level can be obtained based on a structured relatively coarse mesh around the crack tip.

The paper is organized as follow. Section 2 reviews the results of the experiment tests conducted on standard Al7075-T6 tensile test specimen. Section 3 formulates out the independent path based method used to compute the Stress Intensity Factors. Section 4 presents a fatigue life assessment method, coupling finite element computation and the integration of fatigue crack growth law. Finally, some conclusions and prospects are given in the last section.

R. Moutou Pitti (✉)
CNRS, Institut Pascal, Université Clermont Auvergne, Clermont-Ferrand, F-63000, France

IRT, CENAREST, Libreville, 14070, Gabon
e-mail: rostand.moutou_pitti@uca.fr

H. Riahi
LARIS, UPRES EA7315, Université d'Angers-ISTIA, 62 avenue Notre Dame du Lac, Angers, France

M.A. Haile
US Army Research Laboratory (ARL), Adelphi, MD, USA

J. Carroll et al. (eds.), *Fracture, Fatigue, Failure and Damage Evolution, Volume 7*, Conference Proceedings of the Society for Experimental Mechanics Series, DOI 10.1007/978-3-319-62831-8_16

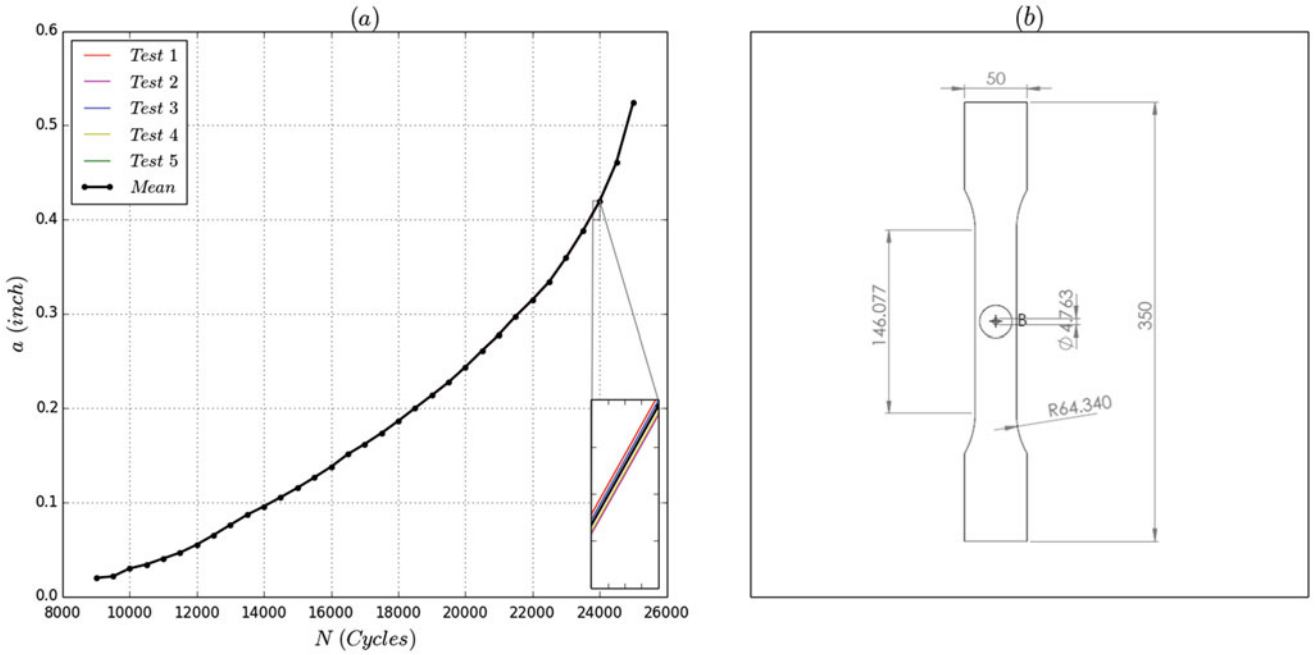

Fig. 16.1 (**a**) Fatigue crack growth tests data, (**b**) standard Al7075-T6 tensile test specimen

16.2 Experimental Results

Five fatigue crack growth tests are performed on standard Al7075-T6 tensile test specimen to determine the material properties needed to define the fatigue crack growth model.

The aluminum alloy test specimen measures 13.78 inches (350 mm) tall by 1.97 inches (50 mm) wide and 0.093 inches (1.6 mm) thick. An initial notch 0.01 inches (0.254 mm) long was made at the edge of the hole 0.187 inches (4.76 mm) diameter. A detailed drawing is shown in Fig. 16.1b. Fatigue crack growth tests were run on axial-load fatigue-testing machine which allows to applying an oscillatory load with a minimum load $P_{min} = 500\ N$ and a maximum load $P_{max} = 5000\ N$, which correspond to a tensile-tensile test with a load ratio $R = 0.1$. As the crack propagates through the specimen, the crack length is recorded every $\Delta N = 500$ loading cycles. As can be seen in Fig. 16.1a the scatter between the date of the five conducted tests is not significant. Consequently, the analysis will be performed on the mean data.

16.3 M-Integral Formulation and Finite Element Implementation

Independent path integral techniques, such as M-integral [3], seem to be a good tool to compute the fracture parameters such as energy release rate and stress intensity factors. Let us consider a cracked medium Ω subjected to mechanical loads, and $\overrightarrow{\theta}$ a continuous derivable vector field defined around the crack tip as depicted in Fig. 16.2. The M-integral reads:

$$M = \int_{\Omega} \frac{1}{2} \left[\sigma^{v}_{ij,k}\, u_i - \sigma^{u}_{ij}\, v_{i,k} \right] \theta_{k,j}\, ds + \int_{\Gamma} \frac{1}{2} F_i\, v_{i,j}\, \theta_j\, dx_1 \tag{16.1}$$

The first term is the generalized definition of the M-integral which represents the effect of mechanical loads applied far away from the crack tip, where σ^{v}_{ij} and σ^{u}_{ij} are stress components associated to the auxiliary displacement field v and the real displacement field u, respectively. The second term represents the effect of mechanical load F_i applied on the crack edges Γ. The real stress intensity factors K^{u}_{I} and K^{u}_{II}, associated to the opening and in plan shear fracture modes respectively, can be easily derived by performing two distinct computations for particular values of the auxiliary stress intensity factors K^{v}_{I} and K^{v}_{II}, such as:

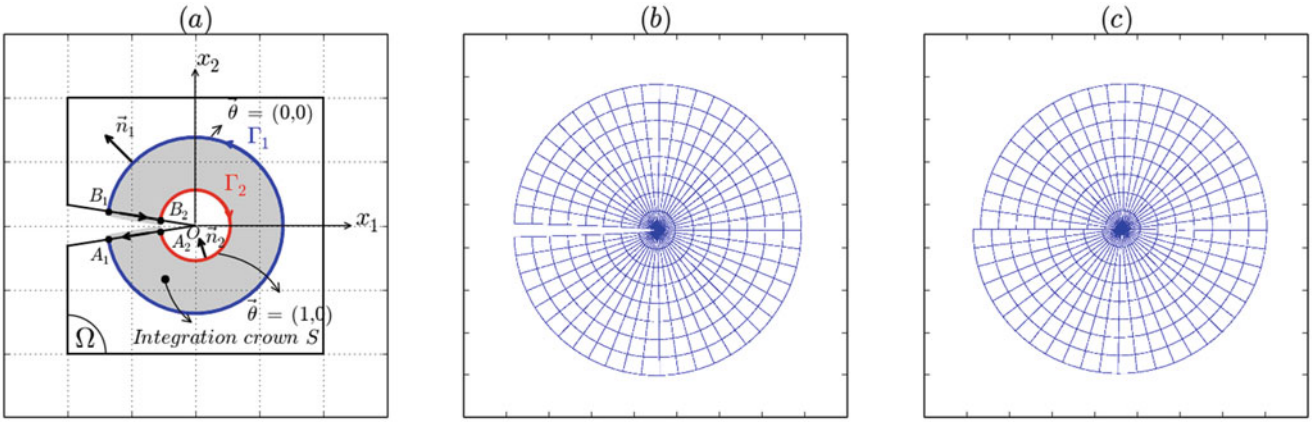

Fig. 16.2 (**a**) Integration domain S and definition of the vector field $\vec{\theta}$, (**b**) opening mode auxiliary displacement, (**c**) in plan shear mode auxiliary displacement

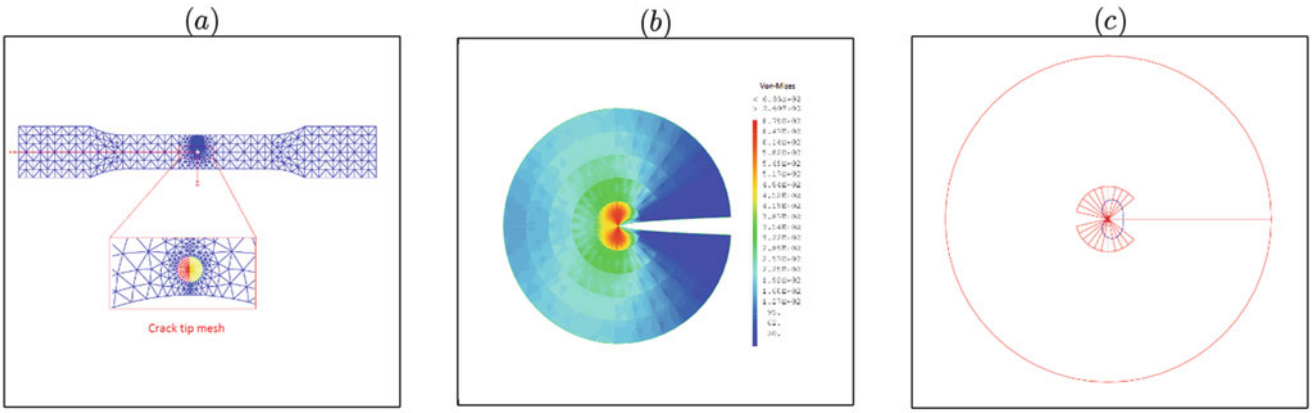

Fig. 16.3 (**a**) Finite elements mesh (**b**) Von-Mises stress around the crack tip, (**c**) Yielding zone around the crack tip

$$K_I^u = \frac{8M\left(K_I^v = 1, K_{II}^v = 0\right)}{C_1}, \quad K_{II}^u = \frac{8M\left(K_I^v = 0, K_{II}^v = 1\right)}{C_2} \tag{16.2}$$

where C_1 and C_2 are the elastic compliances associated to the opening and in plan shear fracture modes, respectively.

This analytical formulation of the M-integral is implemented in the finite elements software cast3m [4]. The standard Al7075-T6 tensile test specimen is meshed using quadratic elements. In order to have good accuracy on the estimates of the fracture parameters, a refined structured mesh is adopted in the vicinity of the crack tip, as shown in Fig. 16.3a. As can be seen in Fig. 16.3b, c, linear elastic fracture behavior hypothesis is verified since the yielding zone is confined at the crack tip. In addition, based on the deformed shape of the crack edges *(see* Fig. 16.3b*)* it is clear that the crack propagates in opening fracture mode.

Table 16.1 compares the numerical estimate of the stress intensity factor K_I with the analytical reference solutions developed by Tada et al. [5] and Grandt [6], and given by Eqs. 16.3 and 16.4, respectively. Note that the finite elements analysis is conducted under plan stress assumption.

$$K_I = \sigma \left[1 + 0.2\left[1 - \frac{a}{a+r}\right] + 0.3\left[1 - \frac{a}{a+r}\right]^6\right]$$
$$\left[2.243 - 2.64\frac{a}{a+r} + 1.352\left[\frac{a}{a+r}\right]^2 - 0.248\left[\frac{a}{a+r}\right]^3\right]\sqrt{\pi a} \tag{16.3}$$

Table 16.1 Accuracy analysis of the numerical results

	Numerical	Tada et al. [5]	Grandt [6]
$K_I \ \left(MPa\sqrt{mm}\right)$	133.24	135.10	135.77
% error		1.37	1.86

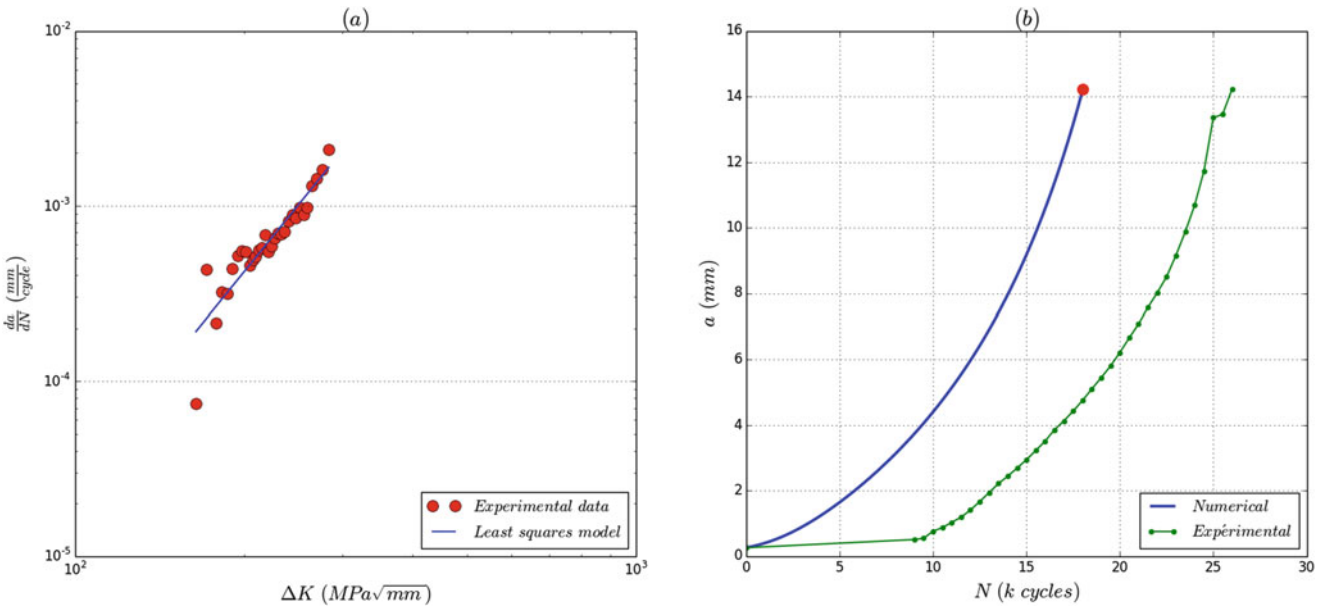

Fig. 16.4 (**a**) Paris-Erdogan's crack growth model fit to experimental data. (**b**) Comparison of fatigue life for the numerical estimates and experimental data

$$K_I = \sigma \left[\frac{0.8733}{0.3245 + \frac{a}{r}} + 0.6762\right] \sqrt{\sec(\pi a)}\ \sqrt{\pi a} \tag{16.4}$$

As can be seen, the numerical estimate of the SIF K_I is in excellent agreement with the reference solutions since the error does not exceeds 2%.

16.4 Fatigue Crack Growth Life Prediction

Many crack growth model have been developed in the literature to describe the relationship between the crack growth rate da/dN and the SIF variation ΔK_I during a loading cycle. Here, the Paris-Erdogan's model is investigated, Eq. 16.5.

$$\frac{da}{dN} = C\ \Delta K_I^m \tag{16.5}$$

Crack lengths and number of loading cycles recorded during the experimental tests, and reported in Fig. 16.1a were used to compute the crack growth rate da/dN. The SIF range ΔK_I is obtained by the M-integral numerical based approach, described in the previous section. The real constants C and m, which are material properties, were obtained using least squares linear regression after transforming the experimental data to *log-log* space. The plots in Fig. 16.4a shows the data points and the fitted model. Constants of model fit and the Root Mean Square Error (RMSE) which measures the accuracy of the regression model are given in Table 16.2. As can be seen the Paris-Erdogan's model fits well the experimental points since the RMSE is relatively small.

Figure 16.4b shows a plot of crack length versus the number of loading cycles for the numerical method and experimental data.

The numerical curve is built based on incrementally solving scheme of the Paris-Erdogan's model between an initial crack length a_i and a critical crack length a_c. As can be seen, the Paris-Erdogan's model underestimates the fatigue crack growth

Table 16.2 Paris-Erdogan's coefficients

C	m	RMSE
$3.45{\cdot}10^{-13}$	3.64	0.14

life of the standard Al7075-T6 tensile test specimen. The numerical results can be enhanced using others crack growth models which allows to take into account the crack closure and/or the mean stress effects.

16.5 Conclusions

In this paper, a numerical methodology coupling independent path integral and crack growth model is developed to evaluate the fatigue life. The results in term of SIF, given by the M-integral approach, are in good agreement with the analytical reference solutions since the relative error is very small. Unfortunately, Paris-Erdogan's model underestimates the fatigue crack growth life of the tested specimen. Thus, more accurate crack growth models, such as Walker and Forman laws, should be investigated. In addition, the coming work will be focused on the analysis of crack growth under random loading, where crack retardation phenomena will be closely investigated. Finally, probabilistic approach will be used in order to take into account the effect of uncertainties of the material properties, the crack geometry and the loading conditions, on the variability of the fatigue crack growth.

References

1. Paris, P., Erdogan, F.: A critical analysis of crack propagation laws. J. Basic Eng. **85**, 528–534 (1963)
2. Bui, H.D., Proix, J.M.: Découplage des modes mixtes de rupture en thermoélasticité linéaire par les intégrales indépendantes du contour. In: Actes du troisième colloque Tendances Actuelles en Calcul de Structure, Bastia, pp. 631–643 (1985)
3. Riahi, H., Moutou Pitti, R., Dubois, F., Chateauneuf, A.: Mixed-mode fracture analysis combining mechanical thermal and hydrological effects in an isotropic and orthotropic material by means of invariant integrals. Theor. Appl. Fract. Mech. **85**(Part B), 424–434
4. Suo, X.G., Combescure, A.: On the application of the Gθ method and its comparison with the Lorenzi's approach. Nucl. Eng. Des. **135**, 207–224 (1992)
5. Tada, H., Paris, P.C., Irwin, G.R.: The Stress Analysis of Crack Handbook, 3rd edn. ASME, New York (2000)
6. Grandt Jr., A.F.: Stress intensity factors for some through-cracked fastener holes. Int. J. Fract. **11**(2), 283–294 (1975)

Chapter 17
Fracture Behavior of Unidirectional Composites Analyzed by Acoustic Emissions Technique

C. Barile and C. Casavola

Abstract The aim for delamination tests is to obtain reliable results, simulating in-situ cracking and giving a fracture toughness value that can consistently characterize materials for structural applications. Standardized organizations developed and adopted similar standards to carry out tests by using proper load fixture possibly combined with optical instruments, to allow the real monitoring of delamination growth for the whole duration tests. In this work, the fracture behavior of unidirectional composites is experimentally analyzed by using acoustic emissions technique too. Sensor was placed on the sample to monitor the evolution of the acoustical events during the tests. Data obtained, in terms of energy, number of hits and hits derivative were critically analyzed to assess the capability of the technique in following the evolution of the damage process and giving information about the toughness values compared with the standardized calculation methods.

Keywords Fiber composites • Delamination test • Fracture toughness • Acoustic emission • Mechanical characterization

17.1 Introduction

The use of high performance laminated composites in several engineering applications is largely growing in the last years due to the possibility to properly design them for specific purpose. Carbon fiber reinforced plastics (CFRP) have many advantages such as high specific strength, specific stiffness, etc. and for this reason they are used in structures used especially in automotive and aerospace fields. In contrary, these materials suffer from different damage mechanisms. One of the most dangerous is the delamination. Delamination is a serious damage mode, not only because it will cause the structure split into two or more pieces along the interfaces of layers at the end of the damaging process, but because it can reduce the laminate strength such a point that it becomes unusable in service. The design of composite materials to account for delamination and other forms of damage includes the definition of damage resistance, that represents the capability of a material to resist the initial occurrence of damage. Knowledge of a laminated composite material's resistance to interlaminar fracture is useful for product development and material selection [1].

In real laminated composite structures, delamination may occur under different loading modes named as mode I, mode II and mixed mode. Mode I is the most common delamination that occurred in the structures, due to lower energy which is required for the initiation process [2]. Commonly, delamination tests aim to evaluate the fracture toughness G_I of composite material according to ASTM D5528–01 [3]. Based on the energy release rate failure criterion for mode I loading condition, crack growth begins when the available energy release rate, G_I, is equal to or greater than a critical value, G_{IC}. Accurate determination of G_{IC} is an important aspect to better understand the damage tolerances and durability of the laminated composites. In this paper, in addition to the ASTM D5528–01 [3] recommended procedures, innovative approaches based on the acoustic emission (AE) information and the combination of mechanical and AE data are represented for evaluation of the crack initiation. These new methods were already applied especially for Glass Fiber Reinforced Plastic (GFRP) [4, 5], but no many results are reported in scientific literature for CFRP materials [6].

This paper tries to investigate the delamination initiation and propagation in the unidirectional carbon/epoxy laminated composites. The acoustic emission technique is applied to achieve this purpose. It is a non-destructive technique with good applicability to examine delamination damage [7–10]. The AE signal is a natural phenomenon described by a transient wave resulting from damage mechanisms that occurs, for example, during the initiation and propagation of delamination failure causing a sudden release of energy inside the material. First, the behavior of the delamination is studied using combination of the AE signals and the mechanical experimental data. Load-displacement graph is compared with crack growth-displacement

C. Barile (✉) • C. Casavola
Dipartimento di Meccanica, Matematica e Management, Politecnico di Bari, viale Japigia 182, 70126, Bari, Italy
e-mail: claudia.barile@poliba.it

J. Carroll et al. (eds.), *Fracture, Fatigue, Failure and Damage Evolution, Volume 7*, Conference Proceedings of the Society for Experimental Mechanics Series, DOI 10.1007/978-3-319-62831-8_17

graph to better clarify the failure mechanism. Then three different graphs (*cumulative hits/time, cumulative energy/time, derivative hits-time/time*) obtained by manipulating acoustic emission data were critically analyzed to explain the whole delamination process of composite specimens. The importance of observing and manipulating the number of hits to obtain information about the state of material was confirmed by several studies that combine the acoustic emission technique with different sources of stress as high power laser heating [11] or mechanical fatigue tests [12].

The principal aim of this preliminary analysis is to properly combine these data and test on the next samples the reliability of sentry function [13], successfully applied on glass/epoxy composite materials. This function had acceptable results in predicting the residual torsional strength of a composite laminate after impact load, to predict the initiation stage, and to evaluate the fracture toughness of the laminated composites subjected to mode I delamination [14, 15].

17.2 Materials and Methods

Experimental campaign involves 9 *double cantilever beam* (DCB) specimens made of epoxy resin reinforced by carbon unidirectional fibers. According to ASTM standard [3], the laminates contain an even number of plies and the delamination growth occurring in the 0° direction. A non-adhesive insert has been inserted at the midplane of the laminate during layup to form an initiation site for the delamination. The film thickness was no greater than 13 μm and is 45 mm long. Specimens have rectangular shape section and uniform thickness (25 × 3 mm), and they are 125 mm long.

Tests were carried out at environmental controlled conditions, 23 °C, and at constant displacement rate of 1 mm/min on a servo hydraulic loading machine, *Instron 1342*. Figure 17.1 reported the schematic sample and the load fixture used for the execution of the mode I delamination test.

Instead of creating a manual reference system to live monitor the crack growth, a digital grid was created and calibrated before each test. It was overlapped on live recorded images acquired by CCD camera Marlin AVT (Fig. 17.2). It is a firewire camera, black and white having 1636 × 1252 number of pixels and a frequency of 12.75 frames per seconds. Since the insert is not visible by the camera, its nominal length and the length of the hinge were considered to create a first blue grid, corresponding to the length of the insert after the pin of the hinge, and then the red grid for evaluating the real crack growth. According to ASTM standard [3] the blue grid, named a_0, represents the initial delamination length.

The optical set-up laid in front of the testing machine is reported in Fig. 17.3. It recorded images during the entire duration test of each specimen.

Acoustic emission events were recorded by using Acoustic Emission software AEWin and a data acquisition system Physical Acoustics Corporation (PAC) PCI-2. To detect Acoustic Emissions one piezoelectric sensor [16, 17] was coupled with the sample by a silicone gel. The AE sensor is a resonant-type, single-crystal piezoelectric transducer from PAC. Its main characteristics are reported in Table 17.1:

Acoustic emissions acquisition frequency was chosen in consideration of the duration of the test and set to 100 kHz. While a threshold value of 35 dB was chosen because preliminary tests demonstrated that it efficiently reduces background noise without altering the main features of the signal. The signal was detected by the sensor and enhanced by a 20/40/60-AST preamplifier. The gain selector of the preamplifier was set to 40 dB.

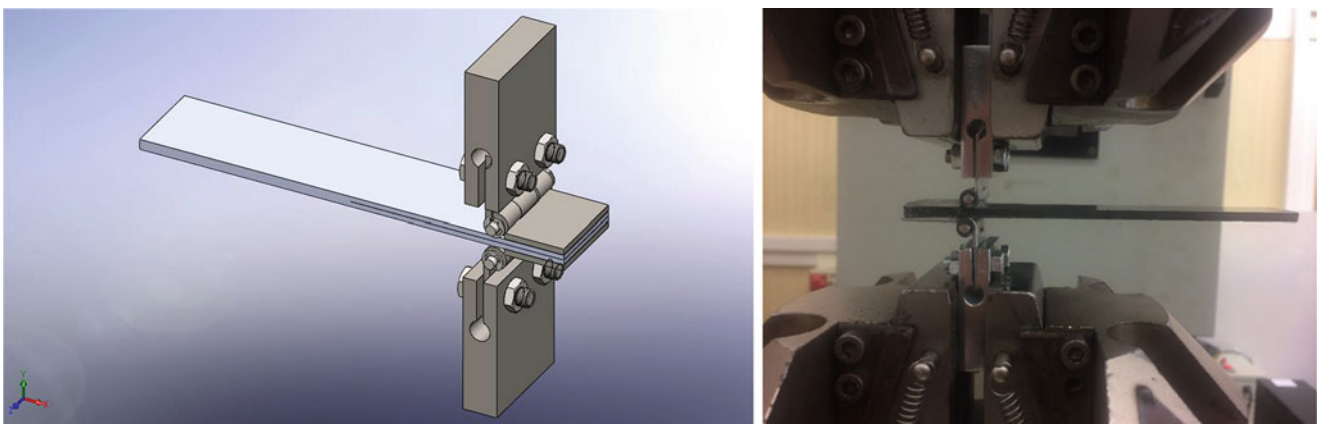

Fig. 17.1 Schematic loading fixture for mode I delamination test

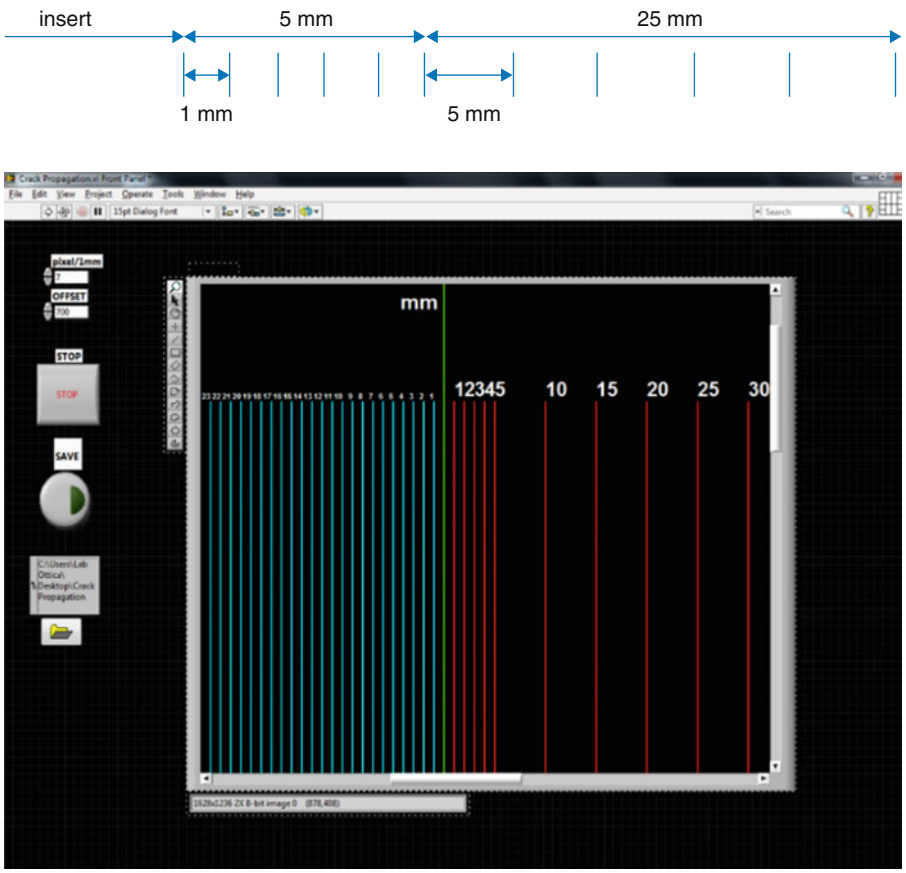

Fig. 17.2 Manual mark VS digital marks to evaluate cracks growth

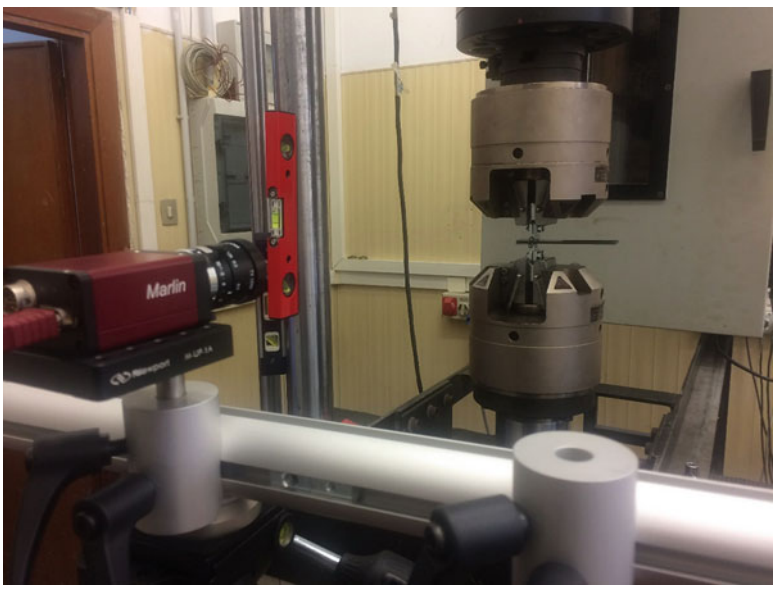

Fig. 17.3 Optical set-up recording delamination growth

The delamination mechanism in a body characterized by linear elastic behavior provides a strain energy release rate (G) that is expressed by Eq. (17.1):

$$G = -\frac{dU}{Bda} \tag{17.1}$$

Table 17.1 Pico sensor main characteristics

Characteristics of the pico sensor	
Peak sensitivity	54 dB
Operating frequency range	200–750 kHz
Resonant frequency	250 KHz
Temperature range	−65 to 177 °C
Dimension	5 × 4 mm

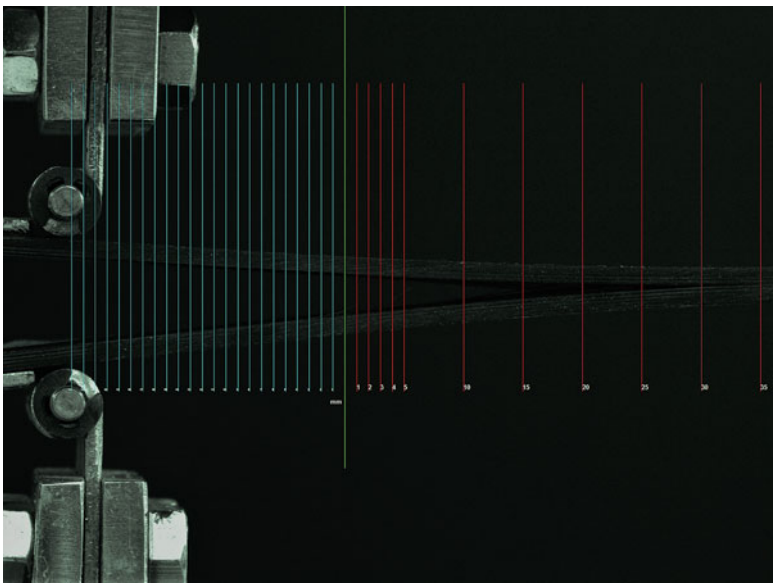

Fig. 17.4 Final recorded image of CCD camera of one representative delaminated specimen

where a is the crack length, B is the specimen width and U represents the total elastic strain energy of the specimen.

Energy release rate for Mode I DCB test is evaluated according to standardized formula referring to the beam theory as follows:

$$G_I^{BT} = \frac{3P\delta}{2Ba} \tag{17.2}$$

where P is the maximum load and δ is the deflection in correspondence of the load.

In Fig. 17.4 is reported a representative image of delaminated specimen recorded by CCD camera. The image reported also the time information used to identify the maximum load for fracture toughness evaluation.

17.3 Results and Discussion

In this work, the DCB specimens were loaded according to the procedures represented in ASTM D5528 so as to investigate the delamination in carbon/epoxy composites under mode I loading.

Figure 17.5 shows a representative *load-displacement* graph overlapped on *crack-growth displacement* diagram for one of the 9 specimens.

As can be seen from Fig. 17.5 by increasing load up to 98 N, strain energy is accumulated in the specimen. When load reaches to 98 N, stored strain energy in the specimen (G_I) reaches to the critical value (G_{IC}) and delamination initiates. Beyond the maximum load, the nonlinearity is considerable. Initial growth of the delamination seems not to be affected by fiber bridging phenomenon that generally occurred behind the crack tip in glass fiber reinforced plastics (GFRP) [4]. It is interesting to note in the crack growth trend that after the maximum load there is a heavily increasing slope of the curve during the loading, confirming that delamination occurs.

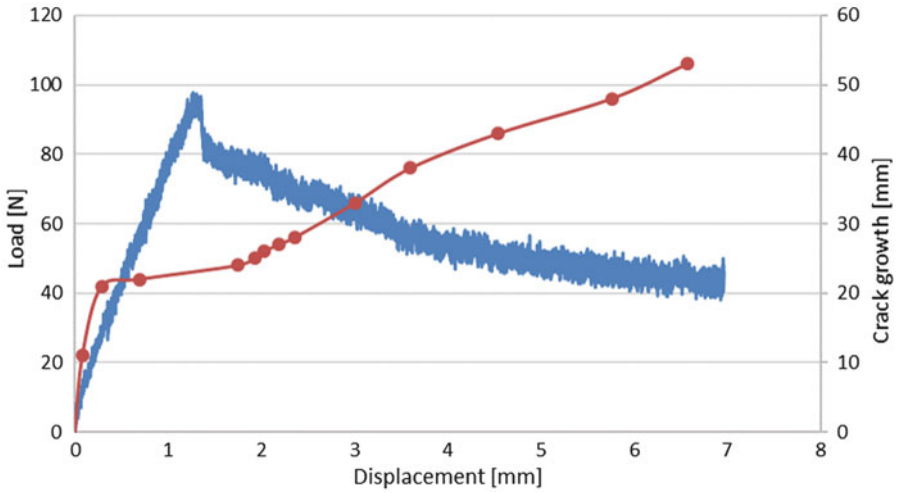

Fig. 17.5 The load displacement and crack length displacement diagrams

Another important aspect to be considered is the possibility to detect the crack initiation in the specimen by observing three different graphs obtained by only analyzing the acoustic emission data. In Fig. 17.6 it is possible to observe the *cumulative hits vs time* graph, the *cumulative energy vs time* graph and the *derivative hits/time vs time* graph of one representative specimen of the 9. In all of diagrams it is possible to identify three different regions representing three different states of material.

In the I region, a low level of hits, energy and derivative of hits is accounted. The time range compared with the camera images recorded corresponds to the crack growth inside the insert. Then the crack initiation phase starts and so the slopes of both cumulative hits and energy deeply grow; moreover, the *derivative hits/time* graph shows a very interesting result since it underlines an intense acoustic emission activity in a limited period (90–110 sec) which includes the instant correspondent to the maximum load used to calculate G_{IC} (101 sec) and the visual observation crack according to ASTM standard [3]. Then the III region is identified, it represents the crack propagation phase characterized by a relevant acoustic emission activity but lower to the previous region. This trend is confirmed by both the cumulative hits and energy graphs in which the third slope of the curve is lower than the II region but higher than the I region. The more accuracy in detecting crack initiation respect to the crack propagation was tested in previous works but only referring to fatigue crack propagation on aluminum [18], steel [19, 20] and titanium [21, 22] specimens. For this reason, this result represents an important breakthrough for the scientific literature since it allows to obtain truthful information on non-homogenous material.

This observation confirms the importance of using acoustic emission technique in monitoring delamination fractures since it allows to obtain predictive information about the state of material more accurately than the visual observation used according to ASTM 5528–01. It is important to underline that more visible results are obtained observing the derivative graph of hits respect to the cumulative one, but these are more confidently for the crack initiation phase than for the crack propagation.

17.4 Conclusion

In this work, the acoustic emission technique is applied on DCB mode I delamination tests. The approach was used to obtain predictive information about the state of material. Significant results were obtained by manipulating acoustic data and observing three different kind of graphs: *cumulative hits/time, cumulative energy/time, derivative hits/time*. It results that the last one graph seems to be the more promising representation for predict initiation crack delamination and that the initiation phase, as verified in metallic materials, is better relieved than the propagation stage. Future works have been planned to identify a good method to follow the crack propagation and to evaluate the fracture toughness by using the sentry function as already done for GFRP.

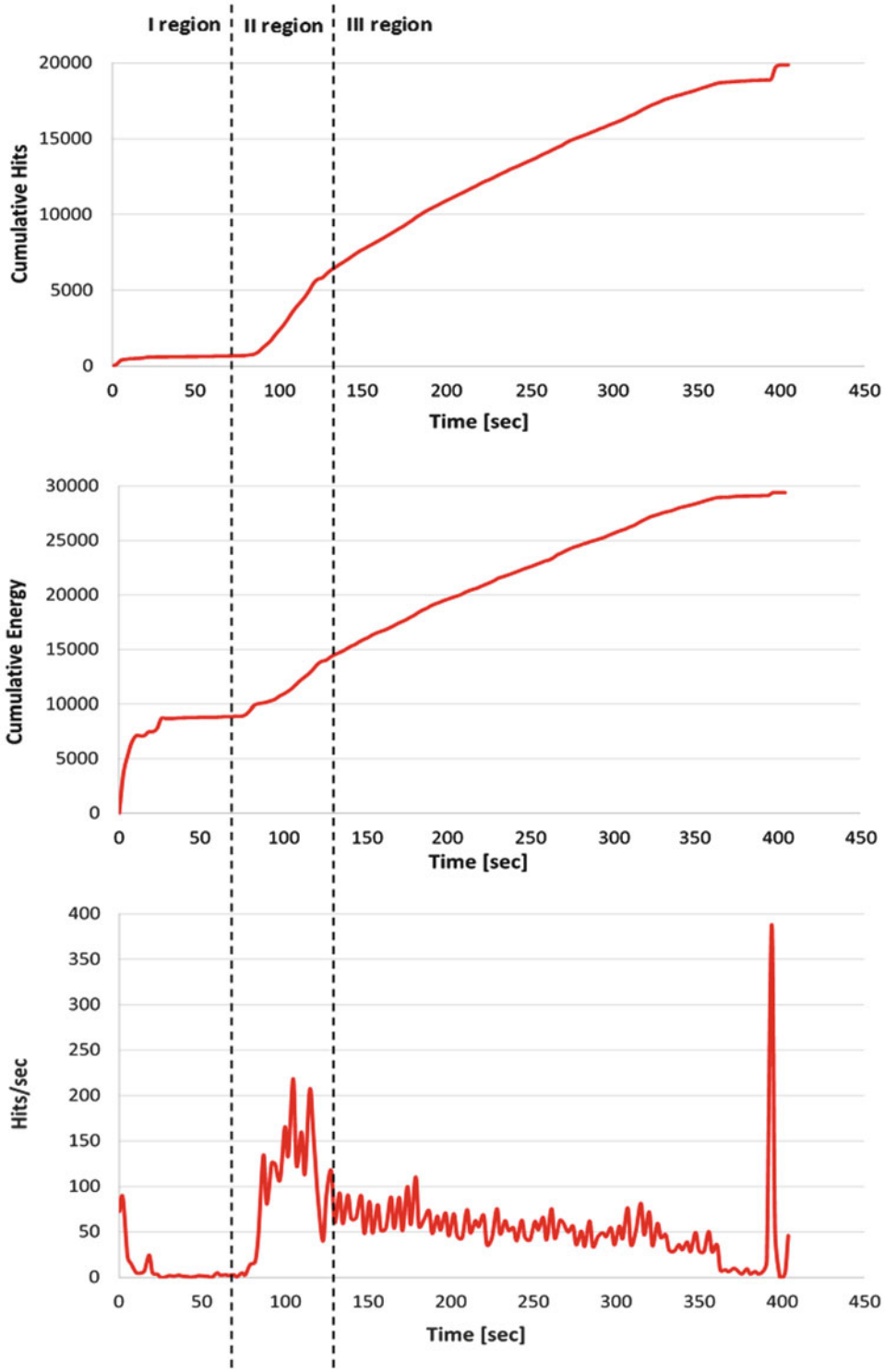

Fig. 17.6 Three different regions distinguished in (*up*) cumulative hits-time graph, (*middle*) cumulative energy-time graph and (*down*) derivative hits-time graph

References

1. Oskouei, A.R., Zucchelli, A., Ahmadi, M., Minak, G.: Using acoustic emission to evaluate fracture toughness energy release rate (GI) at mode I delamination of composite materials. In: Sikorski, W. (ed.) Acoustic Emission (2012). ISBN 978–953–51-0056-0
2. Silversides, I., Maslouhi, A., LaPlante, G.: Acoustic emission monitoring of interlaminar delamination onset in carbon fibre composites. Struct. Health Monit. **12**(2), 126–140 (2013)
3. ASTM D5528–01: Standard Test Method for Mode I Interlaminar Fracture Toughness of Unidirectional Fiber-Reinforced Polymer Matrix Composites. ASTM International, West Conshohocken (2007)
4. Saeedifar, M., Fotouhi, M., Najafabadi, M.A., Toudeshky, H.H., Minak, G.: Prediction of quasi-static delamination onset and growth in laminated composites by acoustic emission. Compos. Part B. **85**, 113–122 (2016)
5. Fotouhi, M., Najafabadi, M.A.: Acoustic emission-based study to characterize the initiation of delamination in composite materials. J. Thermoplast. Compos. Mater. **29**(4), 519–537 (2016)
6. Mohammadi, R., Saeedifar, M., Toudeshky, H.H., Najafabadi, M.A., Fotouhi, M.: Prediction of delamination growth in carbon/epoxy composites using a novel acoustic emission-based approach. J. Reinf. Plast. Compos. **34**(11), 868–878 (2015)
7. Barile, C., Casavola, C., Pappalettera, G., Pappalettere, C.: Acoustic emission analysis in titanium grade 5 samples during fatigue test. Conf. Proc. Soc. Exp. Mech. Ser. **9**, 87–91 (2016)
8. Ono, K.: Trends of Recent Acoustic Emission Literature. J. Acoust. Emission. **12**, 177 (1994)
9. Dornfeld, D.A.: Application of acoustic emission techniques in manufacturing. NDT Int. **25**, 259–269 (1992)
10. Barile, C., Casavola, C., Pappalettera, G., Pappalettere, C.: Fatigue damage monitoring by means of acoustic emission and thermography in Ti grade 5 specimens. Procedia Eng. **114**, 487–492 (2015)
11. Barile, C., Casavola, C., Pappalettera, G., Pappalettere, C.: Acoustic emission analysis of aluminum specimen subjected to laser annealing. Conf. Proc. Soc. Exp. Mech. Ser. **8**, 309–315 (2014)
12. Barile, C., Casavola, C., Pappalettera, G., Pappalettere, C.: Considerations on acoustic emissions in Ti grade 5 during fatigue test. Procedia Eng. **109**, 320–326 (2015)
13. Cesari, F., Dal Re, V., Minak, G., et al.: Damage and residual strength of laminated carbon–epoxy composite circular platesloaded at the centre. Compos. Part A. **38**, 1163–1173 (2007)
14. Refahi Oskouei, A., Zucchelli, A., Ahmadi, M., et al.: An integrated approach based on acoustic emission and mechanical information to evaluate the delamination fracture toughness at mode I in composite laminate. Mater. Des. **32**, 1444–1455 (2011)
15. Minak, G., Zucchelli, A.: Damage evaluation and residual strength prediction of CFRP laminates by means of acoustic emission techniques. In: Durand, L.P. (ed.) Composite Materials Research Progress, pp. 165–207. Nova Science Publishers Inc, New York (2008)
16. Enoki, M., Kishi, T., Kohara, S.: Determination of microcracking moment tensor of quasi-cleavage facet by AE source characterization. In: Progress in Acoustic Emission III, Proceedings of the Eighth International Acoustic Emission Symposium, The Japanese Society for Non-Destructive Inspection, pp. 763–770 (1983)
17. www.mistrasgroup.com
18. Barile, C., Casavola, C., Pappalettera, G., Pappalettere, C.: Hybrid thermography and acoustic emission testing of fatigue crack propagation in Aluminum Samples. Conf. Proc. Soc. Exp. Mech. Ser. **66**(5), 247–252 (2015)
19. Barile, C., Casavola, C., Pappalettera, G., Pappalettere, C.: Analysis of crack propagation in stainless steel by comparing acoustic emissions and infrared thermography data. Eng. Fail. Anal. **69**, 35–42 (2016)
20. Nemati, N., Metrovich, B., Nanni, A.: Acoustic emission assessment of through-thickness fatigue crack growth in steel members. Adv. Struct. Eng. **16**, 269–282 (2015)
21. Barile, C., Casavola, C., Pappalettera, G., Pappalettere, C.: Acoustic sources from damage propagation in Ti grade 5. Meas. **91**, 73–76 (2016)
22. Vlasic, F., Nohal, L., Mazal, P., Liskutin, P.: Study of high-cycle fatigue behaviour of titanium alloy using acoustic emission method. Conf. Proc. Metal. 1423–1430 (2014). ISBN 978-80-87294-52-9